UNIVERSIDAD DE BURGOS

FACULTAD DE CIENCIAS

Interaction with Biomolecules and Biological Activity of Metal Complexes and Silver Atomic Quantum Clusters

PhD Thesis

Cristina Pérez Arnaiz

Burgos, 2018

La **Dra. Begoña García Ruiz**, Catedrática de Química Física del Departamento de Química de la Universidad de Burgos y la **Dra. Natalia Busto Vázquez**, Investigadora postdoctoral del Departamento de Química de la Universidad de Burgos

CERTIFICAN:

Que la siguiente memoria titulada **"Interaction with biomolecules and biological activity of metal complexes and silver atomic quantum clusters"** ha sido realizada por Cristina Pérez Arnaiz, Licenciada en Química, en el Departamento de Química de la Universidad de Burgos bajo su dirección y autoriza su presentación para que sea calificada como Tesis Doctoral con mención de Doctor Internacional.

En Burgos, a 16 de abril de 2018

Fdo. Begoña García Ruiz
Directora

Fdo. Natalia Busto Vázquez
Codirectora

AGRADECIMIENTOS

No imaginas el día que comienzas un doctorado ese momento en el que estarás escribiendo estas líneas, los agradecimientos a todas las personas que has encontrado en el camino y que han dejado su huella en tu trabajo y tu vida a lo largo de los años. Hay algo maravilloso en la investigación, y es que echando la vista atrás puedo asegurar que de todas y cada una de esas personas he aprendido algo. Todas esas aportaciones aparecen reflejadas de alguna forma en esta tesis, desde la guía basada en la experiencia de quien la tiene hasta los consejos e ideas que surgen alrededor de una simple taza de café. Sé que este trabajo no existiría sin ellas y, por ello, quiero daros las gracias.

En primer lugar quiero agradecer a mi directora de tesis, Begoña García, no solo por su confianza en mí desde el principio de este viaje, sino por ser un ejemplo de lucha y trabajo. No es un secreto que la investigación es un mundo de luces y sombras, ilusionante pero muy duro en algunas ocasiones. Por ello quiero agradecer su guía en estos primeros años.

A Natalia Busto le doy las gracias por ser mi codirectora para enseñarme y mi amiga para apoyarme. Siempre tuve la inquietud de aprender a trabajar en esa interfase entre la química y la biología, y qué es el doctorado sino la oportunidad de experimentar, equivocarse y (alguna vez que otra) acertar para encontrar tu camino. Natalia estuvo allí para que yo pudiera encontrar el mío.

También quiero agradecer especialmente a José María Leal por su atención, siempre dispuesto a ayudarnos concienzudamente con cualquier problema en todo momento.

En esta etapa de mi vida hay un grupo de personas con las que seguramente he compartido más tiempo que con mi propia familia: mis compañeros. Recuerdo como si fuera ayer cuando entré en el laboratorio. Allí ya estaban Jesús y Héctor. En esa época aprendí sobre valoraciones, dicroísmos y viscosidades, y también a echar la quiniela. No fui la nueva por mucho tiempo, Matteo llegó poco después, así como Javi y Ana Rosa, mi compañera de pasillo, lloros y risas estos últimos años. Porque la verdad es que no solo hay ciencia en un doctorado, hay mucho más, y por eso doy las gracias a mis compañeros de viaje y a las últimas en llegar, Carolina y Nathalie, con quienes también he compartido estos últimos pasos. Sé lo afortunada que soy por haber sido parte de un grupo como este.

También he sido afortunada durante las estancias en otros centros. Las pocas semanas que pasé al comienzo de mi doctorado con el grupo de Martín Martínez Ripoll y José M. Mancheño en el Instituto CSIC de Química Física Rocasolano me ayudaron a perder el miedo a lo que nos es aún desconocido y a salir de nuestra zona de confort y, a pesar de los años que han pasado, recuerdo a Martín como una de las personas que marcó para siempre mi concepto de la investigación y la ciencia.

Al Prof. Ramón Vilar del Imperial College en Londres, que me acogió durante unos meses como a un miembro más de su equipo, le agradezco enormemente aquella oportunidad. Durante esta estancia no solo aprendí nuevas técnicas, sino también otras formas de trabajar, cómo funcionan otros grupos y se organizan los recursos en otras instituciones. Quiero agradecer especialmente al Dr. Jorge González su ayuda en ese periodo, sin la cual no habría podido desarrollar aquel trabajo. Y es que realizar una estancia es como llegar ante una gran puerta cerrada tras la que hay numerosas oportunidades esperando, y ambos abrieron esa puerta para que pudiera aprovechar mi estancia al máximo.

Al Prof. Fernando Domínguez del CiMUS (Centro de Investigación en Medicina Molecular y Enfermedades Crónicas) en Santiago de Compostela le agradezco su confianza para acogerme en su grupo y sus valiosos consejos en un mundo que me era prácticamente desconocido. Agradezco la ayuda de todo su grupo y sobre todo de Mabel, que tuvo infinita paciencia conmigo y me ayudó siempre en todo lo que pudo.

Además quiero dar las gracias a las personas que de distintas formas han hecho posible con su trabajo y colaboración el desarrollo de esta tesis, especialmente al Prof. Arturo López Quintela de la Universidad de Santiago de Compostela, al Prof. Gustavo Espino de la Universidad de Burgos y a los Prof. Blanca R. Manzano y Prof. Félix A. Jalón de la Universidad de Ciudad Real. También a la financiación recibida por el Ministerio de Educación, Cultura y Deporte por la concesión de la ayuda de Formación del Profesorado Universitario (FPU13/00180).

Finalmente quiero agradecer a todas esas personas que son también parte de este trabajo aunque no pertenezcan a este curioso mundo de la investigación, ya que en muchas ocasiones es su apoyo lo que me ha permitido avanzar, en especial a mis padres y mi hermana, y a Pablo, que incluso hizo el esfuerzo de leerse algún que otro trocito de esta tesis. Seguramente en nuestra etapa como doctorandos todos hemos oído la famosa pregunta “¿Pero tú exactamente qué es lo que estás haciendo?”, y a pesar de que a veces resulte difícil de contestar, son nuestra familia y amigos los que siempre están ahí. Yo no hubiera podido hacerlo sin ellos.

¡Gracias!

ÍNDICE

LISTADO DE ABREVIATURAS... 11

PRÓLOGO.. 15

CAPÍTULO I: INTRODUCCIÓN... 19

1. El cáncer 19

1.1. ¿Qué es el cáncer? 19

1.2. El cáncer en cifras: un problema mundial 20

1.3. La ciencia y el cáncer 20

1.4. Tratamientos contra el cáncer... 21

1.4.1. Quimioterapia 22

1.4.2. Terapia Fotodinámica 22

2. Los ácidos nucleicos... 23

2.1. El ADN como diana contra el cáncer. 23

2.2. Estructura de los ácidos nucleicos. 25

2.2.1. Estructura primaria 25

2.2.2. Estructura secundaria... 27

2.2.3. Estructura terciaria... 31

3. Interacción de ligandos con ácidos nucleicos 33

3.1. Interacción de ligandos con ADN en doble hélice 33

3.1.1. Interacciones covalentes.. 34

3.1.2. Interacciones no covalentes... 34

3.2. Interacción de ligandos con ADN en cuádruple hélice 36

4. Consecuencias biológicas de la interacción droga - ADN 37

4.1. El ciclo celular.. 38

4.2. Efectos biológicos del enlace a ADN en doble hélice............... 39

4.3. Efectos biológicos del enlace a G-cuádruplex.......................... 40

5. Otras dianas contra el cáncer... 40

CAPÍTULO II: METODOLOGÍA EXPERIMENTAL 45

1. Metodología Química - Física... 45

1.1. Reactivos 45

1.1.1. Disolvente 45

1.1.2. Ligandos comerciales 45

1.1.3. Ligandos no comerciales 45

1.1.4. Polinucleótidos 46

1.1.5. Proteínas 48

1.2. Técnicas Experimentales... 48

1.2.1. Medidas de pH.. 48

1.2.2. Espectrofotometría de absorción 48

1.2.3. Fluorescencia.. 53

1.2.4. Dicroísmo circular (CD).. 57

1.2.5. Calorimetría de Valoración Isotérmica (ITC) 60
1.2.6. Calorimetría Diferencial de Barrido (DSC) 62
1.2.7. Desnaturalización térmica por FRET 65
1.2.8. Viscosidad 67
1.2.9. Relajación por salto de temperatura: T-Jump. 69

2. Metodología Biológica. 71

2.1. Electroforesis 71
2.1.1. Electroforesis horizontal de agarosa 71
2.1.2. Electroforesis vertical de poliacrilamida (PAGE) 73
2.2. Polymerase Stop Assay (PSA) 74
2.2.1. Procedimiento experimental 77
2.3. Cultivo celular 77
2.4. Citotoxicidad: ensayo MTT 78
2.4.1. Procedimiento experimental 78
2.5. Captación celular mediante ICP-MS 79
2.5.1. Procedimiento experimental 79
2.6. Microscopía Confocal de Fluorescencia 79
2.6.1. Ensayos de colocalización celular 80
2.7. Microscopía Time Lapse 81
2.7.1. Activación de caspasas 82
2.8. Citometría de flujo 82
2.8.1. Estudio del ciclo celular 83
2.8.2. Estudios de viabilidad celular 84
2.8.3. Acumulación de especies reactivas de oxígeno (ROS) 85
2.8.4. Estudio de la cardiolipina oxidada 86

PARTE 1:

Aim of Part 1 91

CAPÍTULO III: MECANISMO DE LA INTERACCIÓN ENTRE EL AGENTE ANTITUMORAL DOXORRUBICINA Y EL ADN.

Summary 95
Article: “*New insights into the mechanism of the DNA/doxorubicin interction*”... 97

CAPÍTULO IV: EFECTOS DE LA INTERACCIÓN DE CLÚSTERES ATÓMICOS DE PLATA CON EL ADN.

Summary 107
Article: “*Interaction of silver atomic quantum clusters with living organisms: bactericidal effect of* Ag_3 *clusters mediated by disruption of topoisomerase-DNA complexes*” 109

CAPÍTULO V: INTERACCIÓN CON ADN Y PROTEÍNAS DE COMPLEJOS DE PLATINO CON LIGANDOS N^N DADORES. CONSECUENCIAS EN SU CITOTOXICIDAD.

Summary **123**
1. **Introduction** **125**
2. **Results and discussion** **126**
    2.1. Stability in DMSO and aqueous solution 126
    2.2. DNA binding 127
    2.3. Cytotoxicity studies 130
    2.4. Protein binding 131
    2.5. Cellular uptake 132
3. **Conclusions** **133**

PARTE 2:

Aim of Part 2 .... **137**

CAPÍTULO VI: PROCESOS INTRAMOLECULARES DE LA G-CUÁDRUPLEX DE ADN TELOMÉRICO.

Summary **141**
Article: "*New microsecond intramolecular reactions of human telomeric DNA in solution*" 143

CAPÍTULO VII: INTERACCIÓN DE LA G-CUÁDRUPLEX DE ADN TELOMÉRICO CON EL LIGANDO TMPyP4.

Summary **151**
Article: *"Kinetic evidence for interaction of TMPyP4 with two different G-quadruplex conformations of human telomeric DNA*" 153

CAPÍTULO VIII: INTERACCIÓN DE COMPLEJOS DE Ni, Cu Y V CON DIFERENTES SECUENCIAS DE G-CUÁDRUPLEX.

Summary **169**
1. **Introduction** **171**
2. **Results and discussion** **173**
    2.1. pK_a studies 173
    2.2. Aggregation studies 175
    2.3. FRET melting assay 176
    2.4. Spectrophotometric titrations. 177
    2.5. ITC measurements 178
    2.6. Polymerase Stop Assay 180
3. **Conclusions** **183**

PARTE 3

Aim of Part 3 187

CAPÍTULO IX: ACTIVIDAD ANTICANCERÍGENA DE COMPLEJOS CICLOMETALADOS DE Ir(III) Y Rh(III). ¿QUÉ PAPEL JUEGA EL CENTRO METÁLICO?

Summary 191
1. **Introduction 193**
2. **Results and discussion 195**
    2.1. pK_a study 195
    2.2. Photophysical properties 195
    2.3. In vitro cytotoxicity 197
    2.4. Cellular uptake 197
    2.5. Cell cycle arrest 198
    2.6. Induction of apoptosis 199
    2.7. Cellular localization 200
    2.8. Effect on the mitochondrial membrane potential 202
    2.9. Intracellular ROS detection 202
    2.10. Oxidized cardiolipin study 204
    2.11. Photodynamic activity. 204
3. **Conclusions 205**

CONSIDERACIONES GENERALES 209

ARTÍCULOS Y CONGRESOS 211

BIBLIOGRAFÍA 213

LISTADO DE ABREVIATURAS

[D]	Concentración de ligando en el equilibrio
[P]	Concentración de polinucleótido en el equilibrio
AQC	Clústeres cuánticos atómicos
Atm	Atmósferas (presión)
BP	Pares de bases
BSA	Seroalbúmina bovina
C_D	Concentración analítica de ligando
CD	Dicroísmo circular
C_D/C_P	Relación molar droga/polinucleótido
CL	Cardiolipina
C_p	Capacidad calorífica
C_P	Concentración analítica de polinucleótido
ctDNA	ADN Calf Thymus
D	Ligando o droga
DHE	Dihidroetidio
DMEM	Dulbecco's Modified Eagle's Medium
DMSO	Dimetilsulfóxido
DOX	Doxorrubicina
DSC	Calorimetría diferencial de barrido
dsDNA	ADN en doble hélice
EB	Bromuro de Etidio
FAM	Amidita de fluoresceína
FBS	Suero bovino fetal
FRET	Transferencia de energía de resonancia de Förster
H2DCFDA	2',7'- diclorofluoresceína diacetato
HBSS	Hank´s Balanced Salt Solution
HSA	Seroalbúmina humana
I	Fuerza Iónica
ICP-MS	Espectrometría de Masas con Plasma Acoplado Inductivamente
ITC	Calorimetría de valoración isoterma
kb	kilobases (1.000 bases nitrogenadas)
LiCaC	Cacodilato de litio ($(CH_3)_2AsO_2Li$)
MA	Molécula aceptora
MD	Molécula dadora
min	Minutos
NaCaC	Cacodilato de sodio ($(CH_3)_2AsO_2Na$)
P	Macromolécula (polinucleótido o proteína)
PBS	Tampón fosfato salino
PDT	Terapia Fotodinámica
PI	Yoduro de Propidio
PS	Agente fotosensibilizador
qPCR	Real Time Quantitative PCR
s	Segundos
SD	Desviación estándar
T	Temperatura
TAMRA	Tetrametilrodamina

TBE	Tampón electroforético (Tris, borato y EDTA).
TEM	Microscopio Electrónico de Transmisión
T_m	Temperatura de desnaturalización o de “melting”
TMPyP4	*meso*-5,10,15,20-Tetrakis-(N-methyl-4-pyridyl)porphine
UV	Ultravioleta
Vis	Visible
V	Voltios (voltaje)
ε	Coeficiente de extinción molar
λ	Longitud de onda
τ_f	Tiempo de vida medio del estado excitado
Φ	Rendimiento cuántico de emisión

Prólogo

“Nothing in life is to be feared, it is only to be understood. Now is the time to understand more, so that we may fear less.”

Maria Skłodowska-Curie, Nobel Prize in Physics, 1903, and in Chemistry, 1911.

PRÓLOGO

El cáncer es una de las principales causas de muerte en el mundo, por lo que desde hace décadas distintas ramas de la ciencia han intentado aunar esfuerzos en la lucha contra esta enfermedad. Actualmente la quimioterapia es una de nuestras principales armas para desarrollar esta lucha, y un amplio abanico de drogas de distinta naturaleza se emplean en el tratamiento contra el cáncer. Sin embargo, a pesar de los avances en los últimos años, aún nos enfrentamos a retos como la mejora de la eficacia de los tratamientos, la supresión de los nocivos efectos secundarios inducidos por estas drogas y la superación de la resistencia adquirida a las mismas.

Para conseguir estos objetivos es fundamental comprender los mecanismos a través de los cuales ejercen su actividad biológica los compuestos anticancerígenos, aunque esto no es una tarea sencilla. A día de hoy sabemos que la amplia mayoría de estos compuestos clínicamente en uso ejercen su actividad a través de su enlace al ADN, aunque los modos de acción exactos son difíciles de precisar. Dado el papel de los ácidos nucleicos en procesos vitales como son la replicación o la transcripción, no es de extrañar que constituyan la principal diana terapéutica contra el cáncer. Es por ello que una de las primeras etapas básicas en la investigación contra el cáncer consiste en el estudio detallado de los modos de interacción de estas drogas con los ácidos nucleicos, con el fin de entender qué factores son determinantes en su actividad biológica. Así, compuestos como el cisplatino presentan actividad antitumoral a través de la formación de enlaces covalentes con el ADN, mientras que otras drogas como la doxorrubicina forman enlaces de naturaleza no covalente.

En esta tesis se ha estudiado la interacción de especies de naturaleza orgánica y metálica así como complejos metálicos con distintas biomoléculas, incluyendo ácidos nucleicos y proteínas, con el fin de relacionar las características de esta interacción con su actividad biológica. Para ello, por una parte se ha empleado una serie de técnicas de caracterización termodinámica y cinética que nos permiten determinar los tipos de interacción y las fuerzas que los gobiernan: medidas de absorción y de fluorescencia, dicroísmo circular, viscosimetría, calorimetría diferencial de barrido, calorimetría de valoración isoterma, ensayos de desnaturalización térmica por FRET y la técnica de relajación química T-Jump. Por otra parte, se han realizado distintos ensayos biológicos, incluyendo ensayos de inhibición de actividad de enzimas y ensayos de citotoxicidad, entre otros.

Esta tesis se divide en tres partes:

- **Parte 1**. La **Parte 1**, que incluye los **Capítulos III**, **IV** y **V**, se centra en el estudio de la interacción de distintos compuestos con ADN en doble hélice. Entre las especies estudiadas se encuentra un compuesto de naturaleza orgánica: la doxorrubicina; una especie de naturaleza íntegramente metálica: clústeres atómicos de plata; y una familia de complejos metálicos de platino.

- **Parte 2**. En la **Parte 2**, que incluye los **Capítulos VI**, **VII** y **VIII**, también se estudia la interacción de distintas especies con ácidos nucleicos, pero esta vez nos centramos en un tipo de estructura secundaria concreta: la cuádruple hélice de ADN o ARN, también conocida como G-cuádruplex. De nuevo, el estudio se realizó con una molécula orgánica, la porfirina TMPyP4, así como con una familia de complejos metálicos con centros de níquel, cobre y vanadio.
- **Parte 3**. En la **Parte 3**, constituida por el **Capítulo IX**, se explora el modo de acción de una familia de complejos metálicos con centros de iridio y de rodio con actividad anticancerígena que no presentan como diana el ADN, sino la mitocondria, lo cual constituye una nueva vía alternativa a los clásicos agentes antitumorales.

Dado que algunos de los Capítulos anteriormente enumerados, a saber **Capítulos III**, **IV**, **VI** y **VII** ya se encuentran publicados en revistas científicas indexadas y con revisión por pares, estos artículos se han incluido en su versión original junto con un resumen del trabajo realizado en cada Capítulo. En todos los casos se han cumplido las normas de derecho de propiedad intelectual establecidas por las distintas editoriales (American Chemical Society, Royal Society of Chemistry y Elsevier) relativas a la inclusión de artículos completos publicados en tesis doctorales.

Por otra parte, los resultados obtenidos durante esta tesis presentados en el **Capítulo V** forman parte de un artículo que se encuentra en pruebas de imprenta aceptado para publicación en la revista Inorganic Chemistry, y los presentados en los Capítulos **VIII** y **IX** forman parte de artículos que se encuentran en distintas fases de envío.

Además, dado que se opta a la Mención de Doctorado Internacional, que exige la escritura del trabajo de tesis en al menos dos idiomas, los **Capítulos I** y **II** han sido escritos en castellano, mientras que todo el contenido referente a resultados, discusión y conclusiones (**Partes 1, 2 y 3**) se presenta íntegramente en inglés.

Capítulo I

Introducción

“Tumors destroy men in a unique and appalling way, as flesh of his own flesh which has somehow been rendered proliferative, rampant, predatory and ungovernable. They are the most concrete and formidable of human maladies, yet despite more than 70 years of experimental study they remain the least understood.”

Francis Peyton Rous, Nobel Prize in Medicine, 1966

1. El cáncer.

1.1. ¿Qué es el cáncer?

Cáncer es un término genérico que engloba un amplio grupo de dolencias que pueden afectar a cualquier parte del cuerpo. Sin embargo, existen ciertas características comunes: los "sellos distintivos del cáncer", recogidos en la **Figura 1** [1]. Estas marcas distintivas que comparten todas las células cancerígenas incluyen el mantenimiento de la señalización proliferativa, la evasión de los supresores de proliferación, resistencia a la muerte celular, inmortalidad replicativa, la inducción de la angiogénesis, y la activación de mecanismos de invasión y metástasis.

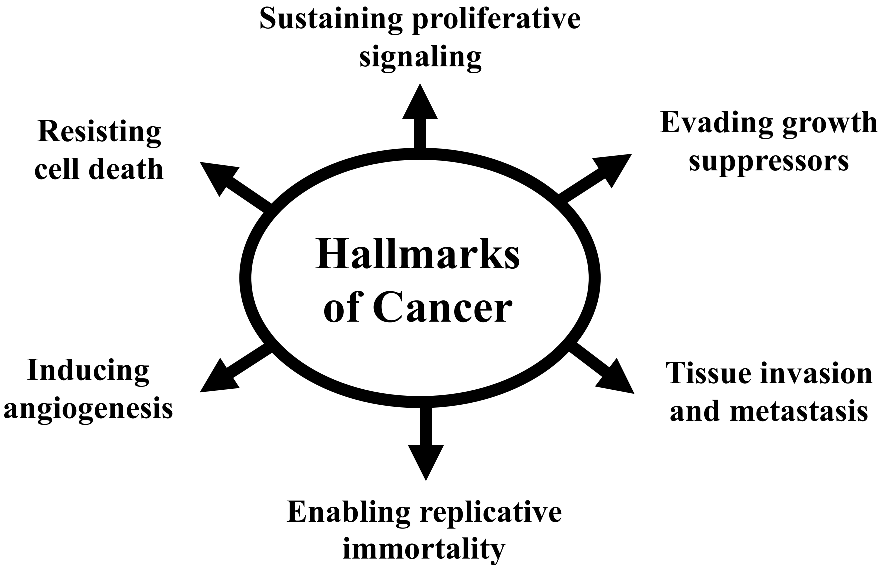
Sustaining proliferative signaling
Evading growth suppressors
Resisting cell death
Hallmarks of Cancer
Inducing angiogenesis
Tissue invasion and metastasis
Enabling replicative immortality

Figura 1. Los sellos distintivos del cáncer (de ref. [1]).

Todas estas características surgen debido a determinadas mutaciones en el ADN, especialmente en genes que controlan los procesos de crecimiento y división celular. Estas anomalías pueden ser heredadas, producirse como resultado de errores en el proceso de replicación del ADN o bien ser causadas por agentes externos (especies químicas, radiación UV, rayos X, etc.). En muchos tipos de cáncer estas características tienen como consecuencia última la generación de tumores sólidos, que pueden crecer sin control invadiendo tejidos cercanos y afectando a su funcionalidad. Estas células tumorales pueden ser capaces de inducir la formación de capilares sanguíneos para abastecer de nutrientes y oxígeno al propio tumor, proceso conocido como angiogénesis. En ocasiones, células cancerígenas de estos tumores pueden desprenderse y viajar por el sistema circulatorio y linfático asentándose y originando nuevos tumores lejos del tumor inicial, lo que se denomina metástasis.

1.2. El cáncer en cifras: un problema mundial.

El cáncer se encuentra entre las principales causas globales de muerte con más de 8 millones de defunciones al año [2]. Esto significa que una de cada seis muertes en el mundo están relacionadas con esta enfermedad, y según la Organización Mundial de la Salud el futuro no se presenta más esperanzador: se estima una cifra de hasta 24 millones de muertes para el año 2035. Estos datos explican por sí solos la magnitud del esfuerzo que la comunidad científica dedica al estudio del cáncer, a nivel tanto de ciencia básica como aplicada. Cabe destacar que aunque el cáncer ha sido considerado comúnmente como “la enfermedad del primer mundo”, lo cierto es que los datos aportados por el proyecto Globocan 2012, que presentó los datos de mortalidad y prevalencia del cáncer a nivel global, muestran un cambio de tendencia preocupante, ya que en las últimas décadas se ha producido un incremento de la incidencia del cáncer en países menos desarrollados. Tanto es así que en la actualidad cerca del 57 % de los casos de cáncer se concentran en estas regiones menos favorecidas. Además, si bien el cáncer es uno de los grandes problemas de las sociedades en países desarrollados, en las regiones sin recursos el drama es aún mayor, debido a la imposibilidad de acceder a tratamientos adecuados. Esto hace que, de hecho, el 65 % de las muertes causadas por esta enfermedad en el mundo se produzcan en países en vías de desarrollo [3].

A pesar de los esfuerzos invertidos durante décadas, son muchos los retos a los que se enfrenta la ciencia frente a esta enfermedad. A día de hoy la “cura” del cáncer no existe, muchos de los nuevos tratamientos que podrían implementar mejoras respecto de los ya existentes presentan costes que hacen que su aplicación sea insostenible a largo plazo o sencillamente inasumible por las personas con menos recursos y los datos de incidencia y mortalidad de la misma son desalentadores…

… y, sin embargo, la historia del ser humano está repleta de desafíos superados.

1.3. La ciencia y el cáncer.

La primera descripción escrita sobre el cáncer data del antiguo Egipto (1600 a. C.). Se trata del “papiro de Edwin Smith”, en el que se describen ocho casos de tumores de mama y se concluye que para esta dolencia “no existe tratamiento”. No fue hasta el siglo XVIII cuando se realizó la primera propuesta de tratamiento contral el cáncer: el cirujano John Hunter sugirió entonces que la cirugía podría usarse para curar determinados tumores [4].

En los últimos 200 años nuestro conocimiento en esta materia ha aumentado considerablemente, para lo cual ha sido vital el papel de la ciencia básica, pilar sin el cual el progreso de la ciencia resulta imposible. En 1962 Watson y Crick recibieron el Premio Nobel por el descubrimiento de la estructura de la doble hélice de ADN a partir de las imágenes de difracción de rayos X de Rosalind Franklin [5]. Desde entonces, el conocimiento en este área de la ciencia creció de forma imparable: aprendimos que el ADN es la base del código genético, contenedor de toda la información por la que se rigen los procesos en los seres vivos, y llegamos a comprender lo que se conoce como **dogma central de la biología molecular** (**Figura 2**), que explica cómo se produce el flujo de información genética en los seres vivos. Esencialmente, esta información contenida en el ADN puede replicarse para generar una copia de sí misma o transcribirse a ARN para ser después traducido en proteínas [6].

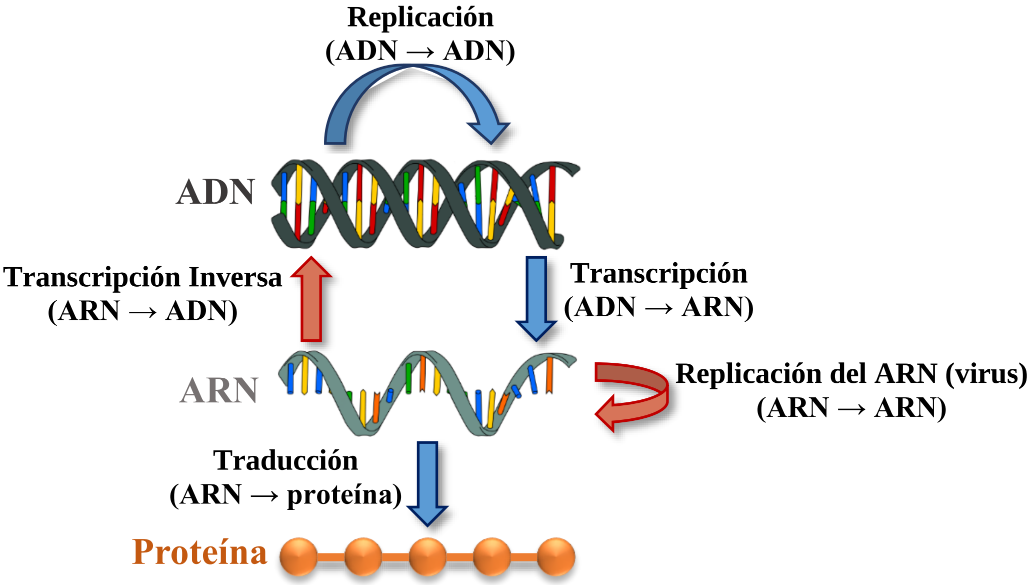

Figura 2. Esquema del dogma central de la biología molecular. Las flechas azules indican los procesos denominados “generales” formulados inicialmente por F. Crick (1958) [7]. Las flechas rojas indican algunos de los procesos llamados “especiales”, añadidos con posterioridad [6].

Según avanzaba el conocimiento sobre la función de los ácidos nucleicos se comenzaron a esclarecer las causas que iniciaban los procesos cancerígenos. Durante los años 70 se descubrieron dos importantes familias de genes relacionados con el cáncer: oncogenes y genes supresores de tumores. Modificaciones en este tipo de genes causados por agentes químicos o radiación, la presencia de determinadas anomalías heredadas de los progenitores en los mismos o la introducción de nuevas secuencias de ADN por determinados tipos de virus, pueden iniciar procesos cancerígenos. Además, el descubrimiento de diferentes tipos de tratamiento también experimentó avances a pasos agigantados, sobre todo en las décadas de los 60 y 70, con el desarrollo de la cirugía, quimioterapia y radioterapia. En los últimos años nuevas rutas están siendo exploradas, como la inmunoterapia y la terapia dirigida [8,9]. A día de hoy aún queda un largo camino por recorrer en este ámbito, lo cual se evidencia en el gran esfuerzo actual de la comunidad científica dirigido a luchar contra esta enfermedad.

1.4. Tratamientos contra el cáncer.

Los tratamientos más antiguos y de uso más extendido son principalmente tres: cirugía, quimioterapia y radioterapia. Otras vías incluyen la terapia hormonal, la inmunoterapia, la terapia dirigida o la terapia fotodinámica, y existen un amplio número de líneas de investigación abiertas en todas estas áreas [10–12]. En este trabajo nos centramos precisamente en el ámbito de la quimioterapia. Para ello se han estudiado distintos tipos de sistemas, incluyendo tanto agentes antitumorales orgánicos como complejos metálicos, con el fin de obtener conclusiones sobre el tipo de acción biológica según las características físico-químicas de los compuestos y de su interacción con distintas biomoléculas. También se ha explorado el potencial como agentes para terapia fotodinámica de nuevos complejos metálicos.

1.4.1. Quimioterapia.

La quimioterapia se basa en el uso de drogas anticancerígenas con el fin de detener o disminuir el crecimiento de las células tumorales. Sin embargo, estos compuestos no solo afectan a las células cancerígenas, sino que también actúan sobre las células sanas, lo cual acarrea graves efectos secundarios. Por ello en la actualidad la investigación en quimioterapia se centra no solo en el desarrollo de nuevos tratamientos con mejor eficacia, sino también en suavizar la repercusión de estos efectos secundarios.

La era de la quimioterapia comenzó en la década de 1940, cuando se descubrieron las propiedades antineoplásicas del famoso gas mostaza, toxina que había sido empleada en la I Guerra Mundial [13]. A lo largo de las siguientes décadas se produjeron grandes avances en el estudio de nuevas drogas antitumorales, principalmente de naturaleza orgánica, como los taxanos, camptotecinas o antraciclinas [14]. En 1978 la FDA aprobó el uso del cisplatino, el primer complejo metálico en ser usado como agente antitumoral [15]. Muchas de las drogas antitumorales tienen como diana celular el ADN, aunque otras dianas como la mitocondria, centro del metabolismo celular, están siendo exploradas [16].

1.4.2. Terapia Fotodinámica.

La terapia fotodinámica (PDT) es un tipo de tratamiento que emplea una droga, llamada agente fotosensibilizador (PS), que al ser expuesta a una luz de una determinada longitud de onda es capaz de generar especies radicales citotóxicas (**Figura 3**) [17].

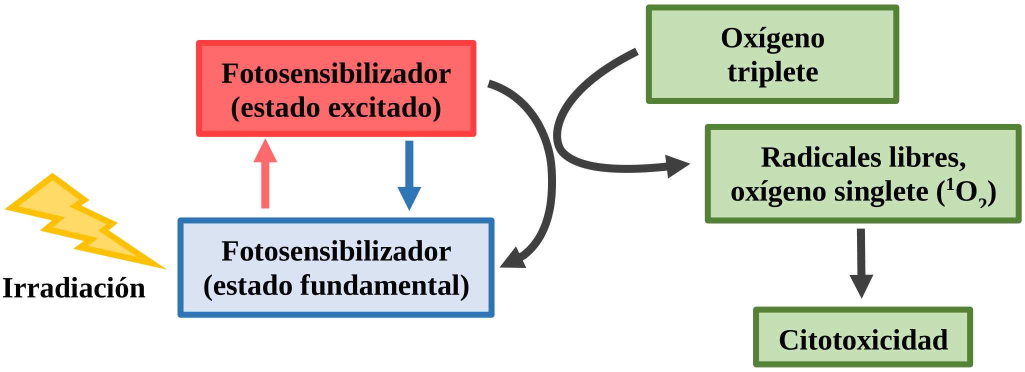
Oxígeno triplete
Fotosensibilizador (estado excitado)
Radicales libres, oxígeno singlete ($^1O_2$)
Irradiación
Fotosensibilizador (estado fundamental)
Citotoxicidad

Figura 3. Esquema del mecanismo de acción de la PDT (adaptado a partir de ref. [17]).

Idealmente este agente PS presenta citotoxicidad nula en la oscuridad [18]. Al ser irradiado puede pasar al estado singlete excitado ($^1PS^*$), y a partir de un cruce entre sistemas alcanzar el estado triplete excitado ($^3PS^*$) [19]. En este punto pueden darse dos tipos de reacciones, que se recogen en la **Figura 4** [20]. En las reacciones de tipo I el PS en su estado triplete excitado puede reaccionar a través de un proceso de transferencia protónica o electrónica con un sustrato biológico, dando lugar a determinadas especies radicales altamente reactivas. En las reacciones de tipo II se produce una transferencia de energía entre el estado triplete del PS al oxígeno molecular, que también se encuentra en estado triplete ($^3O_2$) siendo por tanto una transición permitida, pasando a oxígeno singlete ($^1O_2$). Esta especie es altamente oxidante y reactiva por lo que puede provocar la muerte celular por diversas vías.

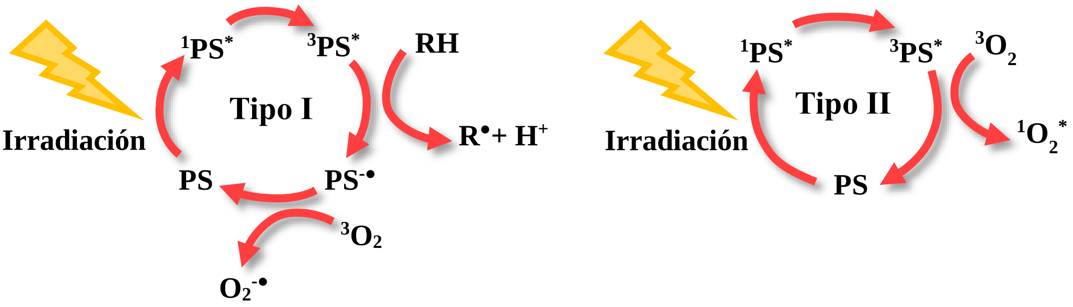

Figura 4. Esquema de los mecanismos fotoquímicos tipo I y tipo II en PDT (adaptado a partir de ref. [20]).

2. Los ácidos nucleicos.

2.1. El ADN como diana contra el cáncer.

El ADN es la diana molecular de muchas de las drogas antitumorales existentes [21]. En este sentido, la mayoría de agentes quimioterapéuticos en uso son inespecíficos, ya que afectan tanto a células cancerígenas como a células sanas. Esta es la razón de que todos los agentes antitumorales de que disponemos hoy en día sean potencialmente tóxicos y su uso conlleve importantes efectos secundarios. Como puede verse en la **Figura 5**, la investigación en este campo está en continua evolución. Los primeros agentes anticancerígenos descubiertos a principios del siglo XX interaccionan con el ADN a través de la formación de enlaces covalentes (cross-linking), modo de enlace que comparten algunas drogas antitumorales en uso actualmente, como es el caso del complejo metálico cisplatino [22]. En las décadas siguientes surgió el interés por las familias de agentes intercalantes, como las antraciclinas, entre los que se incluye la doxorrubicina, compuesto estudiado en la **Parte 1** de esta tesis [23,24]. Otros mecanismos de acción, como es la rotura de la doble cadena del ADN, el reconocimiento de determinadas secuencias de ADN por parte del agente antitumoral con el fin de incrementar la selectividad o el reconocimiento de complejos proteína-ácido nucleico, han sido también ampliamente investigados.

Por otra parte, una de las vías de estudio más recientes se basa en aprovechar la diversidad estructural de los ácidos nucleicos. Como se recoge de nuevo en la **Figura 5**, uno de los mejores ejemplos en este ámbito son las drogas selectivas de cuádruples hélices de ADN (G-cuádruplex). Las G-cuádruplex pueden formarse únicamente en regiones ricas en residuos de guanina y su existencia se conoce desde la década de 1960 [25], aunque se consideraron durante años como una simple singularidad estructural de los ácidos nucleicos sin relevancia biológica. Este tipo de estructuras presenta un altísimo grado de polimorfismo y su función es aún objeto de discusión, pero se piensa que pueden jugar un papel clave en procesos celulares tan importantes como la transcripción [26–28]. Además, se han encontrado más de 700.000 regiones en el genoma humano con posibilidad de formar G-cuádruplex [29]. Muchas de estas regiones se localizan precisamente en promotores de conocidos oncogenes, como el c-Myc, así como en los telómeros, que se encuentran en los extremos de los cromosomas [30,31]. Esta es la razón por la cual el interés por las G-cuádruplex como posible diana terapéutica contra el cáncer se ha intensificado en los últimos años, tema que trataremos en la **Parte 2** de esta tesis.

En resumen, la interacción de compuestos, tanto de naturaleza orgánica como complejos metálicos, con diferentes tipos y estructuras de ácidos nucleicos acarrea importantes implicaciones biológicas que pueden ser aprovechadas en la lucha contra el cáncer. Para ello resulta imprescindible comprender las características estructurales de la propia molécula de ADN, ya que estas van a definir el tipo de interacción con las distintas drogas. También es importante recalcar que, si bien la mayor parte de las drogas antitumorales en uso tienen como diana terapéutica el ADN, existen otras muchas posibles vías de acción que son cada vez más relevantes. Algunos ejemplos de dianas alternativas al ADN son la membrana celular o el funcionamiento de determinados orgánulos como la mitocondria, como veremos en la **Parte 3** de esta tesis.

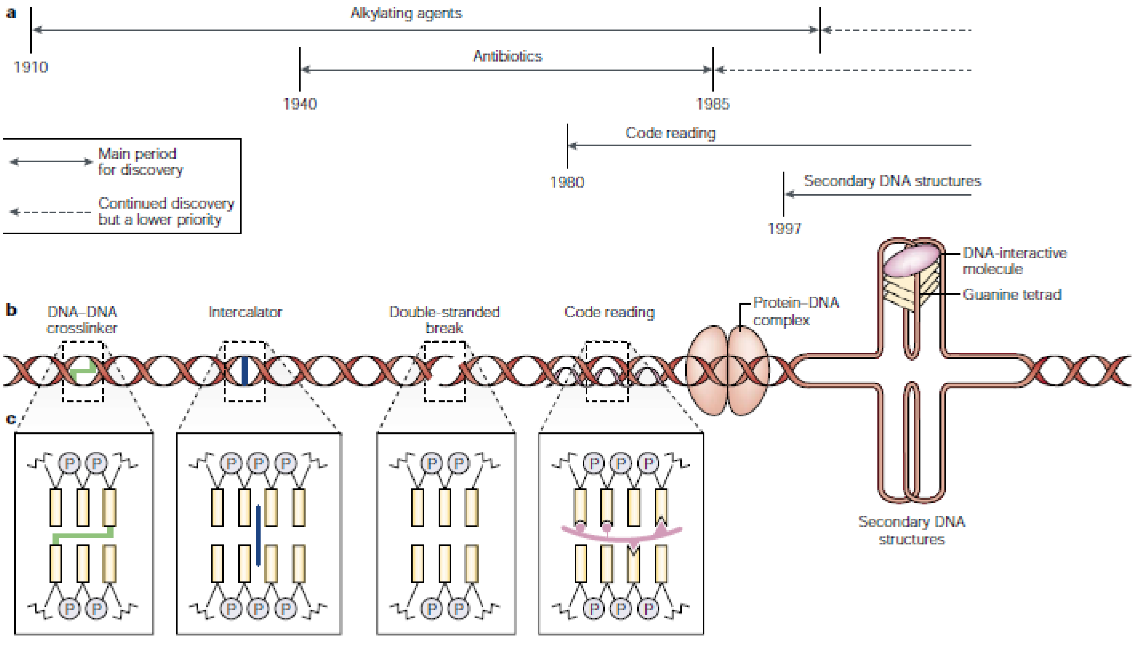
a
Alkylating agents
1910
Antibiotics
1940
1985
Code reading
1980
Secondary DNA structures
1997
Main period for discovery
Continued discovery but a lower priority
b
DNA–DNA crosslinker
Intercalator
Double-stranded break
Code reading
Protein–DNA complex
DNA-interactive molecule
Guanine tetrad
Secondary DNA structures
c
P

Figura 5. Tipos de agentes capaces de interaccionar con el ADN y su modo interacción molecular (de ref. [21]). **A)** Cronograma del descubrimiento de los tipos de drogas que actúan a nivel de ADN y su evolución con el tiempo. **B y C)** Ilustración de los distintos tipos de interacción con ADN, incluyendo cross-linking, intercalación, ruptura de la doble cadena de ADN y reconocimiento de secuencia. Además, la doble hélice de ADN está frecuentemente asociada a proteínas como la Topoisomerasa II, y en forma de estructuras secundarias, como las G-cuádruplex.

2.2. Estructura de los ácidos nucleicos.

2.2.1. Estructura primaria.

Los ácidos nucleicos son polímeros constituidos por nucleótidos sucesivos unidos covalentemente entre sí. Un nucleótido presenta tres componentes característicos: (1) una base nitrogenada (pirimidínica o purínica), (2) una pentosa (ribosa en el ARN o desoxirribosa en el ADN) y (3) uno o más grupos fosfato (**Figura 6**).

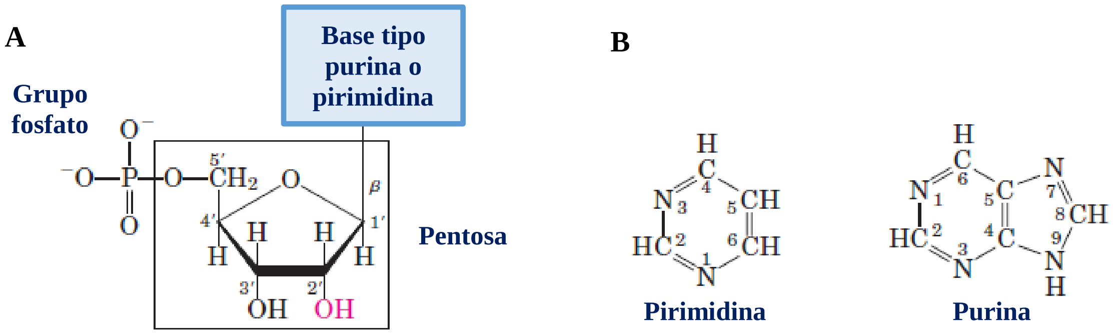
A
Base tipo purina o pirimidina
B
Grupo fosfato
Pentosa
Pirimidina
Purina

Figura 6. A) Estructura general de un ribonucleótido (ARN) con la numeración adoptada para describir las pentosas. En el caso de los desoxiribonucleótidos (ADN), el grupo –OH en el carbono 2’ (rojo) está reemplazado por un grupo –H. **B)** Tipos de bases nitrogenadas: pirimidina y purina (imagen adaptada de ref. [32]).

Tanto el ADN como el ARN presentan dos tipos de bases nitrogenadas tipo purina: adenina (A) y guanina (G). En cuanto a las bases pirimidínicas, ADN y ARN presentan citosina (C), pero la segunda base pirimidínica es diferente: timina (T) en el ADN y uracilo (U) en el ARN. En la **Figura 7** aparecen representadas las estructuras de los nucleótidos presentes en el ADN.

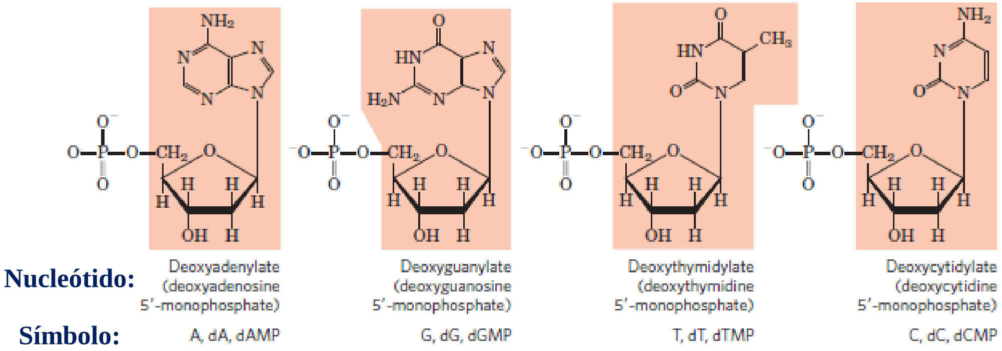
Nucleótido:
Deoxyadenylate (deoxyadenosine 5′-monophosphate)
Deoxyguanylate (deoxyguanosine 5′-monophosphate)
Deoxythymidylate (deoxythymidine 5′-monophosphate)
Deoxycytidylate (deoxycytidine 5′-monophosphate)
Símbolo:
A, dA, dAMP
G, dG, dGMP
T, dT, dTMP
C, dC, dCMP

Figure 7. Nucleótidos presentes en el ADN (imagen original de ref. [32]).

Los sucesivos nucleótidos se unen entre sí de forma covalente mediante enlaces fosfodiéster, en los que el grupo fosfato en 5’ de un nucleótido se une al grupo hidroxilo en 3’ (ver **Figura 6.A**) del siguiente, tal y como se representa en la **Figura 8**. De esta forma se generan las cadenas de ADN y ARN, en las que se alternan residuos fosfato y pentosa unidos covalentemente, con las bases nitrogenadas sobresaliendo de forma lateral. A pH fisiológico los grupos fosfato del esqueleto covalente están totalmente ionizados y cargados negativamente. Estas cadenas de nucleótidos constituyen una estructura lineal que se conoce como estructura primaria de los ácidos nucleicos. La secuencia nucleotídica se indica, por convenio, en dirección 5’ → 3’.

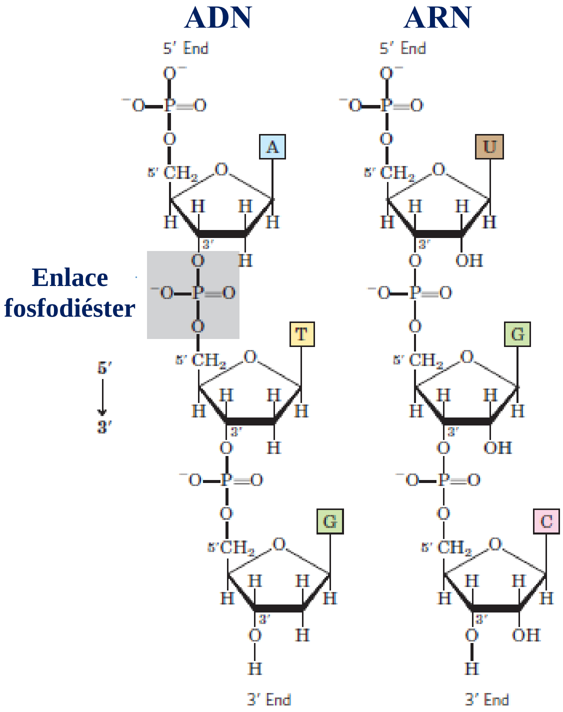

Figura 8. Cadena de desoxirribonucleótidos (ADN) y de ribonucleótidos (ARN) unidos mediante enlaces fosfodiéster (imagen adaptada a partir de ref. [32]).

En la cadena de ADN, la conformación de un nucleótido está afectada por la rotación de hasta siete enlaces (**Figura 9.A**). Uno de ellos es el enlace entre la base nitrogenada y el C de la posición 1’ de la pentosa. En las purinas, debido a impedimentos estéricos esta rotación puede dar lugar únicamente a dos tipos de configuraciones: conformación anti o syn. En las pirimidinas, los impedimentos estéricos hacen que generalmente solo la conformación anti esté presente (**Figura 9.B**).

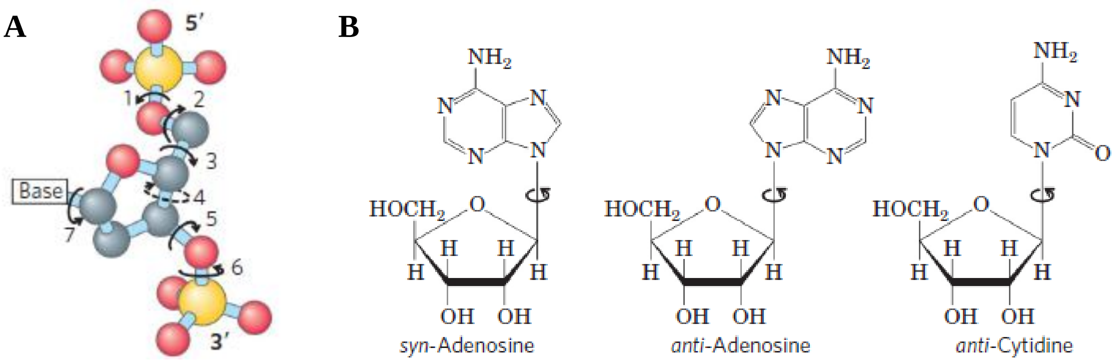

Figura 9. A) La conformación de un nucleótido en el ADN está afectada por la rotación de hasta siete enlaces diferentes. **B)** En las bases purínicas existen dos conformaciones estéricamente posibles: anti o syn. En las bases pirimidínicas únicamente se encuentra la conformación syn (de ref. [32]).

2.2.2. Estructura secundaria.

La estructura secundaria de los ácidos nucleicos se refiere al ordenamiento espacial de nucleótidos cercanos entre sí. En el ADN, la forma predominante consiste en una estructura en doble hélice, descrita por Watson y Crick en 1953 [5], aunque existen otras estructuras como las G-cuádruplex o los i-motifs. En el caso del ARN, este suele aparecer en la naturaleza en forma de cadena sencilla, por lo que la estructura secundaria cuando aparece es local, solo en determinadas regiones de la molécula.

- La doble hélice de ADN.

Este modelo tridimensional consiste en dos cadenas antiparalelas de polinucleótidos enrolladas entre sí de forma helicoidal alrededor de un eje imaginario. La complementariedad existente en los pares de bases, entre G y C y entre A y T, es la base de la estructura en doble hélice. Esta complementariedad surge del establecimiento de tres enlaces de hidrógeno entre las bases G y C, y de dos enlaces de hidrógeno entre A y T, tal y como se representa en la **Figura 10.A**. Por tanto, las dos cadenas de la doble hélice tienen secuencias de bases complementarias. Ambos pares de bases (G-C y A-T), al estar formados por una pirimidina y una purina, presentan un tamaño similar. Se disponen apilados en paralelo con poca separación entre ellos (3.4 Å) y cada par de bases gira 36° con respecto del anterior en sentido dextrógiro, es decir, hacia la derecha. Este apilamiento da lugar a una hélice de 20 Å de diámetro como la que aparece representada en la **Figura 10.B**, la cual presenta en su superficie un surco mayor y un surco menor. Esta estructura se conoce como forma B-ADN y es la más común en la naturaleza. Sin embargo, también se conocen otras estructuras en doble hélice, como son las formas Z y A [33].

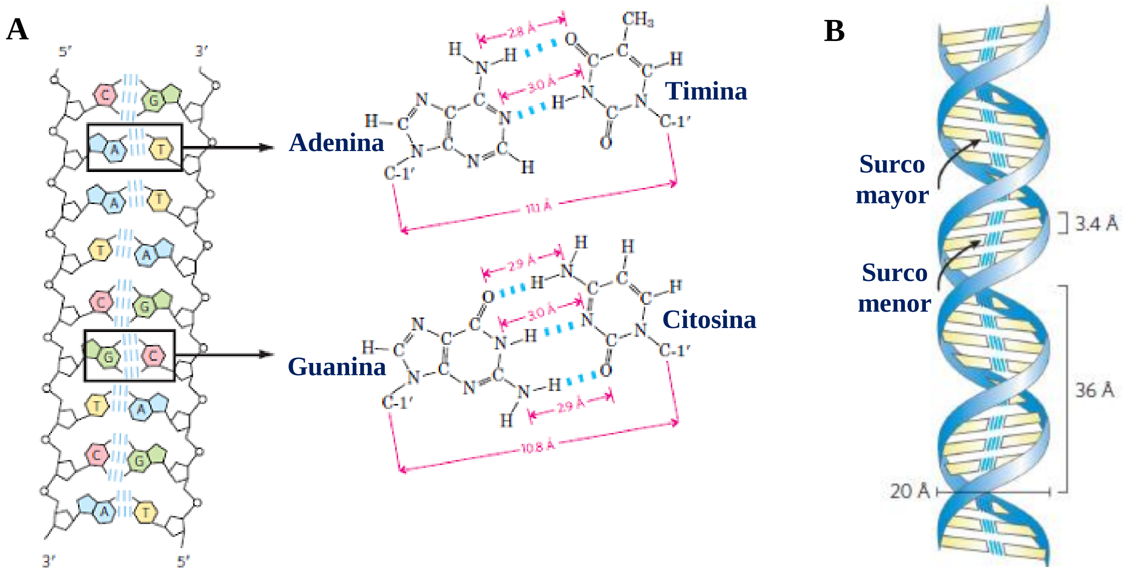

Figura 10. A) Esquema representando la complementariedad de las bases nitrogenadas en una doble cadena de ADN y puentes de hidrógeno establecidos entre dichas bases. **B)** Modelo de la estructura de la doble hélice de B-ADN (imagen adaptada a partir de ref. [32]).

La forma Z del ADN fue descubierta en 1979 a partir de experimentos de difracción de rayos X de una doble cadena complementaria de ADN de composición d(CG)$_3$ (**Figura 11**). Inmediatamente atrajo la atención de la comunidad científica por tratarse de una hélice levógira, en lugar de la esperada hélice dextrógira conocida hasta la fecha [34]. La disposición resultante de las bases nitrogenadas hace que la cadena de residuos fosfato tenga forma de zig-zag, como se representa en la **Figura 12**. Esta estructura del ADN aparece a concentraciones muy altas de sales y en presencia de determinados cationes multivalentes *in vitro* [35,36], e *in vivo* bajo la acción de determinadas proteínas que favorecen la transición de la forma B a la forma Z [37].

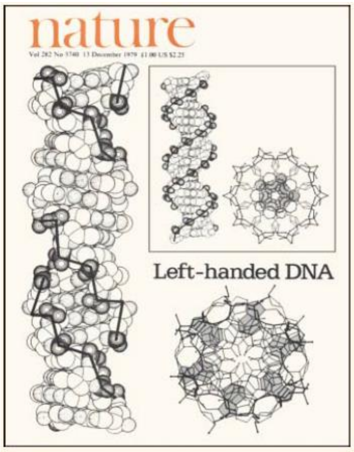

Figura 11. Portada de Nature: descubrimiento del Z-ADN [34].

En el A-ADN, la doble hélice es dextrógira y más ancha que la forma B-ADN, con un diámetro de 26 Å (**Figura 12**). Los pares de bases no son perfectamente perpendiculares con respecto del eje de la hélice, haciendo que el surco mayor sea más profundo y el surco menor menos profundo. Esta forma aparece favorecida en condiciones de baja hidratación del ADN [38].

En conclusión, la B-ADN es la forma de ADN de menor energía bajo condiciones fisiológicas [37], por lo que no es de extrañar que sea la forma predominante en la naturaleza. Es de resaltar que, a pesar de que la información genética viene definida por la secuencia de nucleótidos, la estructura de este polímero juega un papel crucial en todos los procesos biológicos en los que participa. Así, la doble hélice B-ADN permite el empaquetamiento, accesibilidad y replicación de la información genética de forma eficaz [39]. Sin embargo, la presencia tanto en procariotas como en eucariotas de otras formas como el Z-ADN [40], y el hecho de que parezcan estar involucradas en la expresión de determinados genes, pone de manifiesto la importancia y la necesidad de investigar y comprender la diversidad estructural de los ácidos nucleicos.

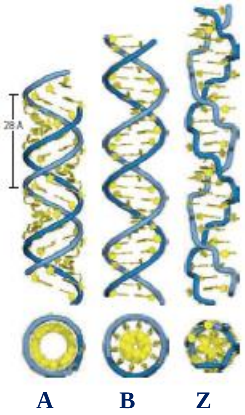

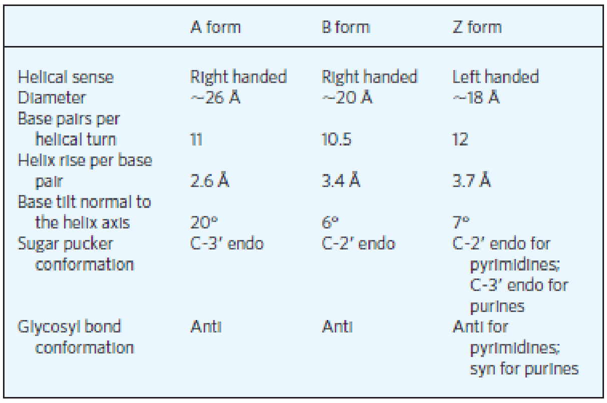

	A form	B form	Z form
Helical sense	Right handed	Right handed	Left handed
Diameter	~26 Å	~20 Å	~18 Å
Base pairs per helical turn	11	10.5	12
Helix rise per base pair	2.6 Å	3.4 Å	3.7 Å
Base tilt normal to the helix axis	20°	6°	7°
Sugar pucker conformation	C-3′ endo	C-2′ endo	C-2′ endo for pyrimidines; C-3′ endo for purines
Glycosyl bond conformation	Anti	Anti	Anti for pyrimidines; syn for purines

Figura 12. Comparación entre las formas A, B y Z del ADN. Las estructuras mostradas presentan 36 pares de bases, con las ribosas y bases en amarillo y el esqueleto en azul. La tabla recoge algunas de las propiedades de estas formas del ADN (de ref. [32]).

- La triple hélice de ADN.

A pesar de que la doble hélice es la forma más conocida del ADN, existen otras formas que involucran no dos, sino tres o cuatro cadenas de ADN. Los nucleótidos que participan en un par de bases pueden formar puentes de hidrógeno adicionales con otros nucleótidos cercanos. Por ejemplo, un residuo de cisteína protonado puede interaccionar con un residuo de guanina de un par G-C, y un residuo de timina con uno de adenosina de un par A-T, como se muestra en la **Figura 13.A**. Estas interacciones, diferentes de los tradicionales pares de Watson y Crick, se denominan apareamientos de Hoogsteen. Estos apareamientos permiten la formación de triples hélices de ADN (**Figura 13.B**) [41,42].

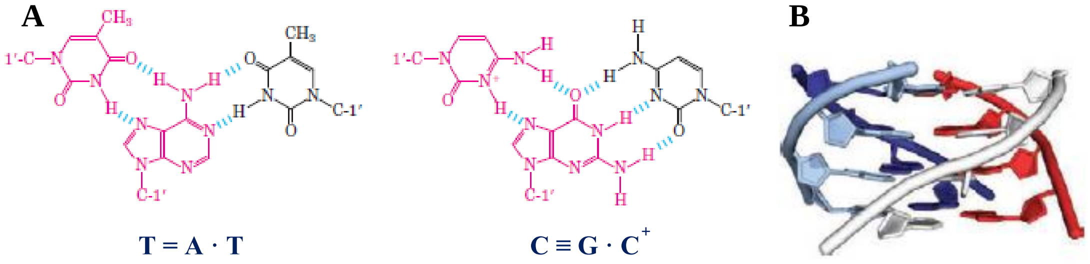

Figura 13. A) Pares de Hoogsteen (en rosa) presentes en el ADN en triple hélice. **B)** Representación de una triple hélice de ADN (de ref. [32]).

- La cuádruple hélice de ADN.

La formación de cuádruples hélices de ADN o ARN, también conocidas como G-cuádruplex, se basa en el establecimiento de enlaces de hidrógeno tipo Hoogsteen entre cuatro guaninas dispuestas en una tétrada plana, como se representa en la **Figura 14.A**. Dos o más tétradas pueden apilarse una encima de otra, estableciendo interacciones de stacking entre ellas y dando lugar a las cuádruples hélices de ADN o ARN [43,44]. Estas estructuras se estabilizan mediante la inserción en el centro de las mismas de cationes monovalentes como el Na$^+$ o K$^+$ (**Figura 14.B**). Estos cationes se encuentran en el canal iónico, coordinados a los ocho átomos de oxígeno expuestos de las guaninas circundantes [45].

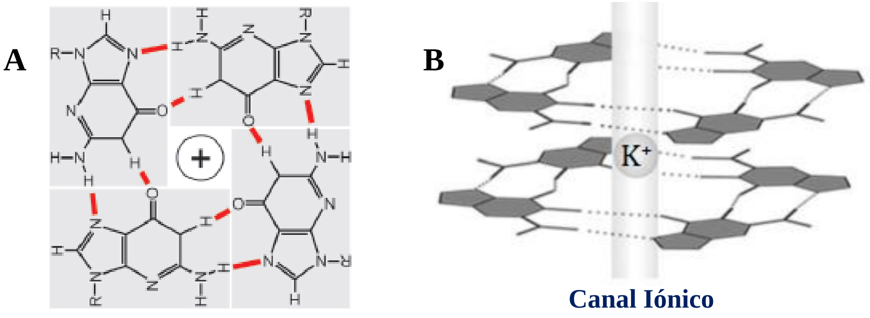

Figura 14. A) Las unidades estructurales básicas de las G-cuádruplex son las tétradas, compuestas por cuatro guaninas interaccionando a través de enlaces de Hoogsteen. **B)** El apilamiento de dos o más tétradas da lugar a las G-cuádruplex, establizadas tanto por interacciones de stacking entre los planos de guaninas como por la presencia de cationes monovalentes en el canal iónico formado en el centro de estas estructuras (imagen adaptada a partir de ref. [46]).

Las estructuras de G-cuádruplex presentan un altísimo grado de polimorfismo [45], ya que se han caracterizado un elevado número de diferentes topologías o conformaciones que dependen de:

(1) La secuencia de nucleótidos.

(2) La composición del disolvente: naturaleza de los cationes monovalentes presentes en el medio, pH, etc.

De esta forma, una misma secuencia de nucleótidos rica en guaninas puede plegarse bajo diferentes conformaciones de G-cuádruplex según las condiciones del medio, o incluso pueden coexistir en disolución diferentes conformaciones de una misma secuencia en equilibrio [47], lo cual refleja la complejidad del estudio de estos sistemas. Por ello existen diferentes formas de clasificación de las cuádruples hélices [46]. Así, pueden clasificarse teniendo en cuenta si la estructura se forma a partir de una o varias hebras de ADN (**Figura 15**):

A) **G-cuádruplex intramolecular:** plegamiento de una sola hebra sobre sí misma.

B) **G-cuádruplex intermolecular:** plegamiento de dos, tres o cuatro hebras.

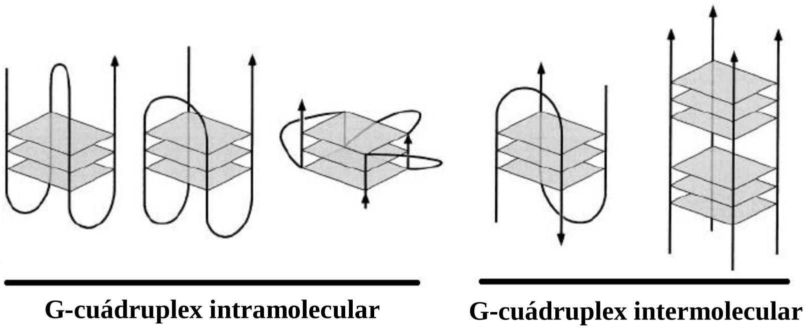

Figura 15. Representación esquemática de algunos ejemplos de G-cuádruplex intramolecular e intermolecular. Las tétradas se representan como rectángulos grises y la cadena de ADN como líneas negras. La dirección de las flechas se corresponde con la dirección 5’ → 3’ de la cadena de ADN.

También la polaridad u orientación de las hebras (5’ → 3’) determina el polimorfismo estructural de las G-cuádruplex [48], como se refleja en la **Figura 16**.

A) **4 hebras paralelas**: conformación paralela.

B) **3 hebras paralelas:** conformación híbrida.

C) **2 hebras paralelas:** conformación antiparalela.

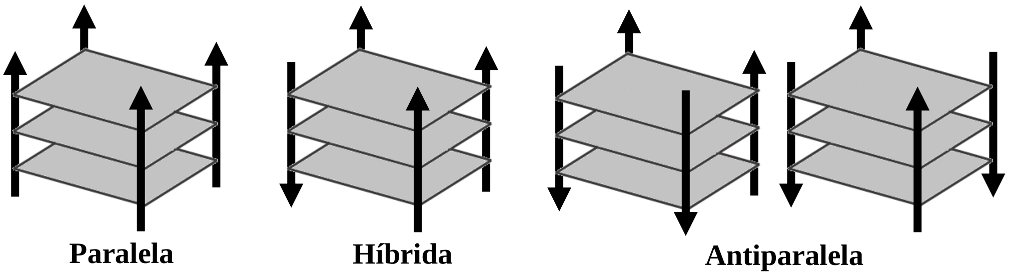

Figura 16. Representación esquemática de las diferentes posibilidades existentes en la orientación de las hebras en las G-cuádruplex.

Finalmente, tanto de la polaridad de las hebras como del tipo de plegamiento dependen el número y características de los “loops”, que son las cadenas que sobresalen externas a la estructura formada por las tétradas de guaninas apiladas. En la **Figura 17** se representan los tipos de loops que pueden encontrarse en las G-cuádruplex: tipo hélice, lateral y diagonal.

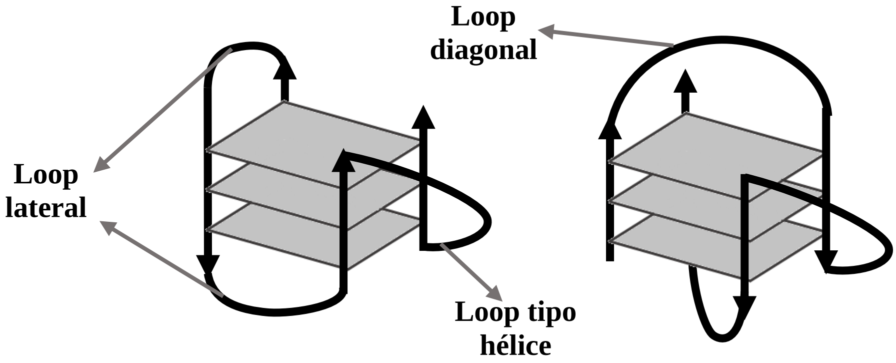

Figura 17. Tipos de loops que pueden encontrarse en las G-cuádruplex.

Todas las características anteriormente descritas ponen de manifiesto la variedad y complejidad estructural de las cuádruples hélices de ADN. Existe un campo de estudio muy activo en este ámbito, y ya han sido caracterizadas estructuralmente las conformaciones de G-cuádruplex de muchas secuencias de interés en el genoma humano, como es el caso del ADN telomérico o regiones de protooncogenes como el c-Myc o el Bcl-2 [47,49,50]. Este gran interés por la resolución de las conformaciones de las diferentes cuádruples hélices de ADN reside en que sus características estructurales pueden determinar la interacción con determinadas drogas específicas de G-cuádruplex, como veremos en el **apartado 3.2** de este **Capítulo I.**

2.2.3. Estructura terciaria.

El empaquetamiento del ADN en virus, procariotas y eucariotas presenta diferentes grados de complejidad y da lugar a la estructura terciaria del ADN. Cuanto más complejo es el genoma, como en el caso de las eucariotas, mayor es el grado de organización del material genético, como veremos a continuación [51].

- **Virus.** Muchos virus consisten básicamente en una cadena sencilla de ADN o ARN rodeada por una carcasa proteica. Sin embargo, otros ADNs virales tienen una topología circular covalentemente cerrada, al igual que el ADN de muchos procariotas.

- **Procariotas.** El ADN en doble hélice en procariotas suele encontrarse en forma circular covalentemente cerrada y se encuentra anclado en la cara interna de la membrana plasmática. Al tratarse de una molécula circular cerrada, puede adquirir diferentes estructuras por medio de superenrollamientos de la doble hélice sobre sí misma. A esta estructura se la conoce como genóforo o cromosoma procariota (**Figura 18**). En muchas bacterias además del cromosoma pueden encontrarse otros elementos extracromosómicos llamados plásmidos, constituidos por pequeñas moléculas de ADN circular que están libres en el citosol y que son responsables, entre otras cosas, de la resistencia a antibióticos. Por ejemplo, plásmidos con el gen que codifica la enzima β-lactamasa confieren resistencia a antibióticos como la penicilina, ampicilina y amoxicilina [52].

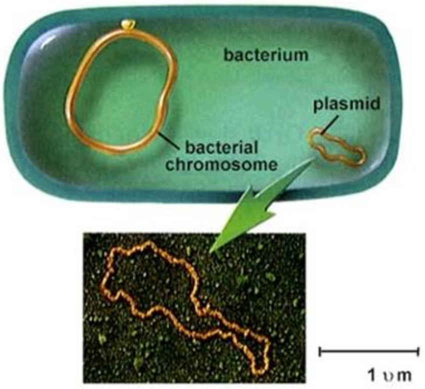

Figura 18. Representación del cromosoma bacteriano y de un plásmido, junto con una imagen este último obtenida mediante TEM (Microscopio Electrónico de Transmisión), en una bacteria (imagen de “ScienceSourceimages”).

- **Eucariotas**. La organización del material genético en eucariotas presenta un grado de complejidad mucho mayor que en procariotas y se distribuye en cromosomas, cuyo número difiere mucho de unas especies a otras. Cada cromosoma en las células eucariotas está formado por una única molécula de ADN en doble hélice, cuyo nivel de compactación es altísimo. Esta compactación se produce tanto por procesos de superenrollamiento, similares a los presentes en procariotas, como por asociación con proteínas específicas. Estas proteínas son del tipo histona, que presentan bajo peso molecular y son ricas en aminoácidos básicos, arginina y lisina, disponiendo así de gran cantidad de cargas positivas que favorecen la interacción con los grupos fosfato del ADN.

En la **Figura 19** se presenta un esquema con las etapas del empaquetamiento del ADN en eucariotas. La unidad fundamental de organización del cromosoma en eucariotas es el nucleosoma, que consiste en un octámero de histonas alrededor del cual el ADN da dos vueltas. Estos nucleosomas se unen entre sí por un fragmento de ADN de unos 200 pares de bases, dando lugar a una estructura que se conoce como “collar de perlas”. El siguiente nivel de compactación consiste en una asociación helicoidal de los nucleosomas, dando lugar a una estructura llamada fibra de 30 nm, la cual mediante asociación a proteínas de tipo no histona se compacta aún más formando las fibras de cromatina. Finalmente, mediante la formación de bucles y superenrollamientos se forman los cromosomas, que solo son visibles durante la división celular.

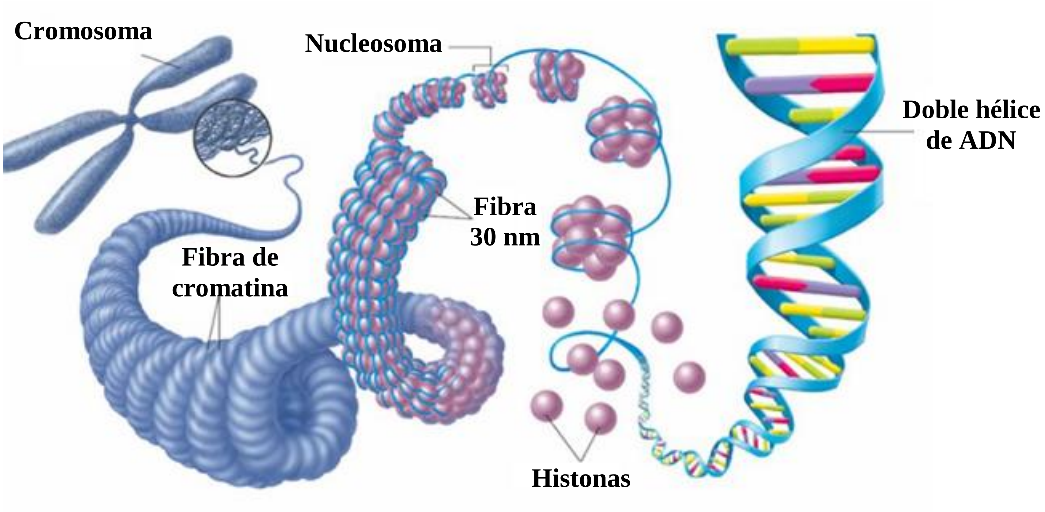

Figura 19. Esquema de las etapas del empaquetamiento del ADN en eucariotas (adaptado a partir de ref. [32]).

3. Interacción de ligandos con ácidos nucleicos.

Los ácidos nucleicos, especialmente el ADN, son dianas terapéuticas claves de muchas drogas empleadas contra afecciones como el cáncer y las enfermedades infecciosas [53]. Esto es debido al papel que estos biopolímeros juegan en diferentes procesos biológicos vitales (ver **Figura 2, apartado 1.3, Capítulo I**), y que pueden verse alterados o inhibidos debido al enlace de ciertos ligandos. Entender las características de la interacción de estos ligandos con el ADN y su implicación biológica es un área de investigación en la que se involucran áreas de la química, la biología molecular y la medicina. En esta tesis se ha hecho especial énfasis en el estudio de la interacción de pequeños ligandos con dos estructuras del ADN: la doble y la cuádruple hélice de ADN. Aunque existen muchas características comunes, las diferencias estructurales tienen importantes consecuencias en la interacción con ligandos. Por ello, a continuación se clasifican y describen brevemente los tipos de interacción ligando – ADN, en doble y cuádruple hélice, que pueden presentar los agentes anticancerígenos que actúan a nivel de ADN.

3.1. Interacción de ligandos con ADN en doble hélice.

Los modos de enlace de ligandos al ADN pueden clasificarse en dos grandes grupos: covalentes y no covalentes.

3.1.1. Interacciones covalentes.

Muchas de las drogas anticancerígenas en uso hoy en día ejercen su actividad terapéutica gracias a la formación de enlaces covalentes irreversibles, por ejemplo, a través de la alquilación o del cross-linking. Los agentes alquilantes son, de hecho, la clase más antigua de agentes antitumorales [21]. Estos agentes suelen reaccionar con los residuos de guanina del ADN, aunque pueden afectar a otras bases, introduciendo grupos alquilo como el metilo e impidiendo de esta forma el reconocimiento entre bases A-T y G-C en los pares de bases del ADN, lo cual provoca un desajuste conocido como “miscoding” [54]. El resultado último consiste en la fragmentación de la molécula de ADN por la acción de las enzimas de reparación, producido cuando estas tratan de reemplazar las bases alquiladas sin éxito. Sin embargo, los agentes más potentes y eficaces dentro de este grupo actúan a través de la formación de “cross-linking”, proceso en el cual dos bases nitrogenadas se unen entre sí a través de un agente bifuncional con dos sitios de unión al ADN [55]. El cross-linking puede ser intracatenario, cuando se produce entre dos bases de una misma hebra de ADN, o intercatenario, entre dos cadenas diferentes de ADN (**Figura 20**). Esto impide la lectura del ADN tanto para ser duplicado como para sintetizar el correspondiente ARN y, por tanto, los procesos de replicación y transcripción resultan inhibidos provocando la muerte celular [22,56]. Además, el enlace covalente al ADN puede producirse también a través de un solo sitio de unión, dando lugar a monoaductos. El cisplatino es un ejemplo típico de agente anticancerígeno capaz de formar distintos tipos de enlaces covalentes con el ADN, en el que el metal, Pt, puede coordinarse a las posiciones N7 de los residuos principalmente de guanina, como se representa en la **Figura 20** [57,58].

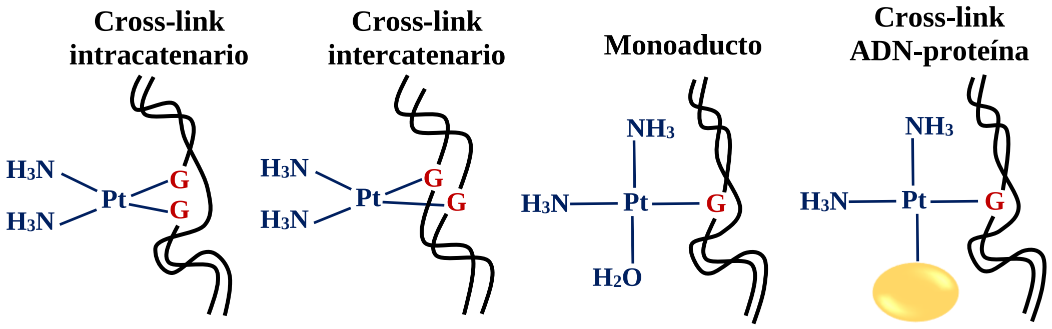

Figura 20. Tipos de enlaces covalentes con ADN formados por el compuesto cisplatino.

3.1.2. Interacciones no covalentes.

Existen varios tipos de interacciones no covalentes entre ligando y ADN basadas en el establecimiento de enlaces de hidrógeno, fuerzas de van der Waals, interacciones electrostáticas y/o hidrofóbicas. Al contrario que las interacciones covalentes, estas son reversibles, y sus efectos biológicos más relevantes están relacionados principalmente con la inducción de cambios conformacionales en la molécula de ADN y la interferencia en interacciones proteína-ADN como en el caso de las topoisomerasas. Los modos de interacción no covalente se clasifican en tres tipos: intercalación, unión al surco y enlace externo (**Figura 21**).

- **Intercalación.**

Las drogas intercalantes son moléculas capaces de insertarse entre dos pares de bases adyacentes de la doble hélice, sin llegar a romper los enlaces de hidrógeno entre las bases A-T y G-C. Todas ellas tienen una característica común: presentan unidades aromáticas planas en su estructura [59]. El complejo ADN-intercalador está estabilizado por interacciones π-π stacking entre la región aromática del intercalador y las bases nitrogenadas del ADN [60]. Por esta razón, este tipo de complejos son menos sensibles a los cambios de fuerza iónica del medio que las uniones al surco y los enlaces externos que veremos a continuación. Entre los efectos que los agentes intercalantes provocan sobre la molécula de ADN destacan el alargamiento y desenrollamiento parcial de la doble cadena debido a la inserción de la molécula entre los pares de bases [61,62]. Además, las interacciones de stacking establecidas estabilizan la estructura en doble hélice. Estas modificaciones estructurales tienen importantes consecuencias en la funcionalidad de la molécula de ADN, ya que pueden desencadenar la inhibición de los procesos de replicación, transcripción y reparación del ADN [63]. Algunos ejemplos clásicos de drogas intercalantes son el bromuro de etidio o miembros de la familia de las antraciclinas como la doxorrubicina [23,64].

- **Unión al surco.**

Los conocidos como "groove binders" son moléculas capaces de interaccionar con los surcos de la doble cadena de ADN estableciendo enlaces de hidrógeno y/o fuerzas de van der Waals con las bases nitrogenadas que quedan expuestas en estas regiones de la doble hélice. Moléculas grandes como proteínas y oligonucleótidos pueden interaccionar con el surco mayor, más espacioso [65,66], mientras que moléculas más pequeñas suelen interaccionar con el surco menor [67]. Estas moléculas pequeñas a menudo presentan varios anillos aromáticos y su estructura es alargada y ligeramente curva [68], lo que facilita la interacción con el surco. Generalmente muestran preferencia por secuencias ricas en A–T, debido a que el surco en estas regiones es más estrecho que en secuencias ricas en G–C, favoreciendo las interacciones de van der Waals [69–71]. A diferencia de la intercalación, los enlaces al surco no provocan grandes modificaciones en la estructura de la doble hélice. Algunos ejemplos de los compuestos más conocidos capaces de interaccionar con el surco menor son los antibióticos polipirrólicos distamicina A y netropsina o el marcador nuclear DAPI [67].

- **Enlace externo.**

El enlace externo es de naturaleza electrostática y tiene lugar entre ligandos cargados positivamente y los grupos fosfatos del esqueleto del ADN, cargados negativamente. Por esta razón, es un modo de enlace muy dependiente de la fuerza iónica del medio [72].

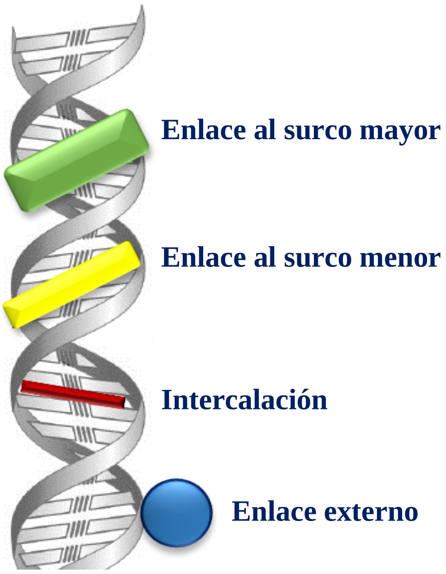

Figura 21. Representación de los tipos de interacción no covalente con ADN.

3.2. Interacción de ligandos con ADN en cuádruple hélice.

La particular geometría de las G-cuádruplex permite su reconocimiento específico por parte de pequeños ligandos a través de distintos modos de enlace, algunos con características comunes a los de la doble hélice [73]. Las interacciones pueden dividirse, de nuevo, en covalentes y no covalentes. Sin embargo, en el caso de las cuádruples hélices, las interacciones no covalentes son más interesantes ya que permiten el diseño de ligandos altamente específicos aprovechando las peculiaridades estructurales de las G-cuádruplex [74–76]. Esta selectividad hacia la G-cuádruplex frente a la doble hélice presenta una gran relevancia, ya que en cualquier sistema biológico la cantidad de ADN en forma de doble hélice será muy superior a la de ADN en forma de G-cuádruplex. Por ello, solo una elevada selectividad puede permitir a un ligando de G-cuádruplex alcanzar su “target” [77]. En la **Figura 22** aparecen representados algunos de los modos de enlace que han sido identificados: las interacciones de stacking con las caras externas de las G-cuádruplex, la intercalación y el enlace al surco [46].

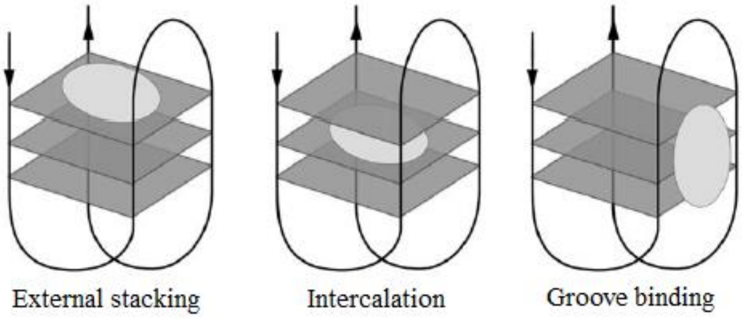

Figura 22. Representación de los modos de interacción ligando – G-cuádruplex más comunes (de ref. [46]).

En general, los ligandos selectivos de G-cuádruplex presentan amplias unidades aromáticas planas en su estructura, lo que favorece las interacciones de π-stacking con las tétradas, que poseen también un elevado carácter aromático [78,79]. Una de las principales consecuencias que este tipo de interacción tiene sobre la G-cuádruplex es la estabilización de su estructura. Existe una amplísima literatura al respecto, abarcando desde moléculas orgánicas a complejos metálicos [80,81]. En la **Figura 23** se recogen algunos de los ejemplos más conocidos de ligandos de G-quadruplex [74,82–85].

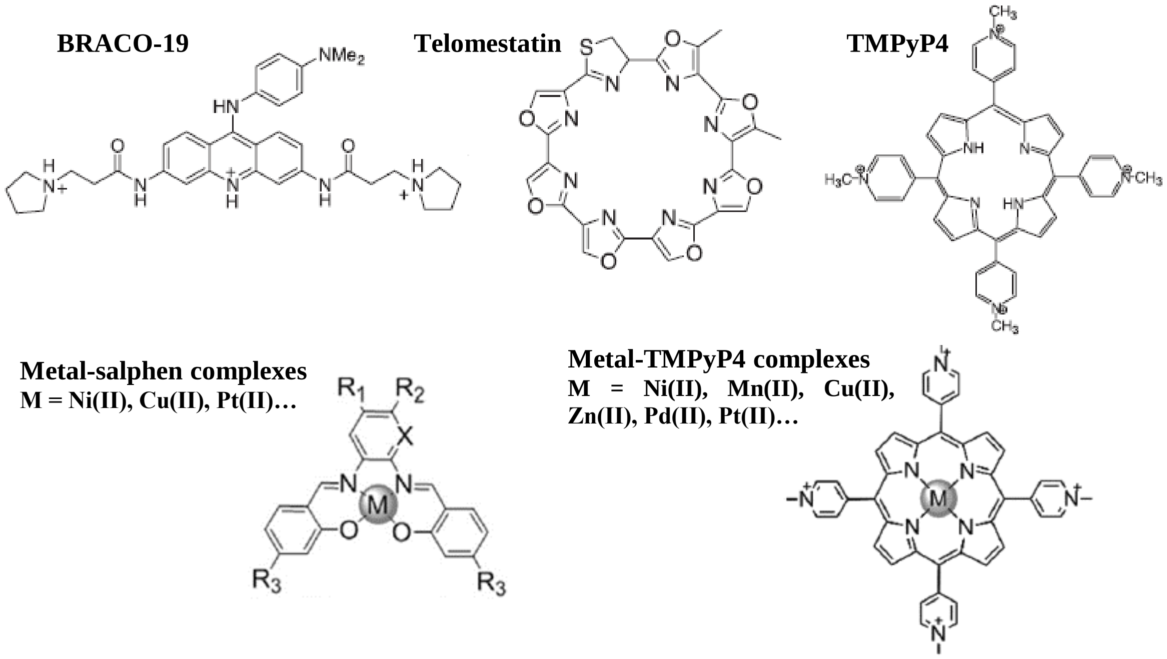
BRACO-19
Telomestatin
TMPyP4
Metal-salphen complexes
M = Ni(II), Cu(II), Pt(II)…
Metal-TMPyP4 complexes
M = Ni(II), Mn(II), Cu(II), Zn(II), Pd(II), Pt(II)…

Figura 23. Ejemplos relevantes de compuestos orgánicos y complejos metálicos capaces de interaccionar y estabilizar estructuras de ADN en cuádruple hélice [74,82–85].

4. Consecuencias biológicas de la interacción droga - ADN.

Una vez descritas las características estructurales de los ácidos nucleicos así como los tipos de interacción que una droga puede establecer con los mismos, es necesario enmarcar estos aspectos en el contexto biológico. ¿Por qué la mayoría de las drogas antitumorales en uso actúan a nivel de ADN?, ¿qué relevancia tiene el estudio de la interacción droga - ADN?; y, en definitiva, ¿cuáles son las consecuencias biológicas de esta interacción? En este punto las fronteras entre las diferentes áreas de la ciencia, establecidas por conveniencia, se difuminan, ya que no podemos enfrentarnos a estas preguntas si no es desde una estrecha colaboración entre los ámbitos de la química, la biología y la medicina.

4.1. El ciclo celular.

Las células se reproducen ejecutando una secuencia ordenada de procesos en los que el contenido celular se duplica y la célula se divide en dos, lo cual se conoce como ciclo celular [51]. Como se representa en la **Figura 24**, el ciclo celular eucariota puede dividirse en cuatro grandes fases secuenciales que involucran diferentes eventos: G1, S, G2 y M.

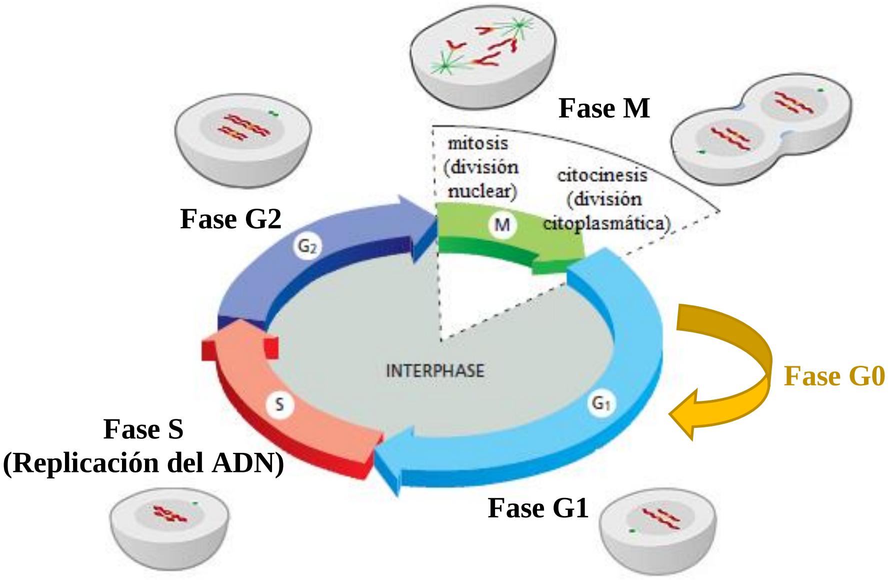
Fase M
mitosis (división nuclear)
citocinesis (división citoplasmática)
M
Fase G2
G2
INTERPHASE
Fase G0
S
G1
Fase S (Replicación del ADN)
Fase G1

Figura 24. Representación esquemática del ciclo celular en células eucariotas (imagen adaptada a partir de imágenes del repositorio WikimediaCommons y de ref. [51])

Una célula que acaba de generarse por división entra en fase G1 ("gap 1"). En esta fase se produce un aumento del volumen celular y la multiplicación de los orgánulos que deberán después repartirse entre las dos células hijas. Si las condiciones externas son desfavorables o este proceso se ve impedido por algún otro motivo, la célula puede detener su proceso proliferativo con el fin de sobrevivir, entrando en un estado de reposo llamado G0, en el que puede permanecer días o incluso años, hasta que las condiciones sean favorables de nuevo y pueda volver a la fase G1 para proseguir con el ciclo celular.

A lo largo del ciclo existen una serie de puntos de control, en los que se chequea que la maquinaria celular haya funcionado correctamente antes de proseguir con las siguientes etapas. Al final de la fase G1 existe un punto de control que da paso a la siguiente fase, la fase **S** o de síntesis, siempre y cuando el entorno sea favorable y la célula haya crecido lo suficiente [86]. Durante esta fase S la célula replica su ADN nuclear, creando una copia completa del mismo. La fase G2 es el segundo "gap" en el ciclo celular y se produce entre la fase S y la fase M (mitosis). En G2 se encuentra el segundo gran punto de control del ciclo, en el cual se verifica que la replicación del ADN haya transcurrido correctamente antes de dar paso a la fase M. Si se detecta que la replicación no se ha completado correctamente, la célula permanecerá en esta transición G2/M hasta que los problemas se hayan solucionado. Finalmente, en la fase M ocurren dos grandes eventos: la división nuclear o mitosis, en la cual los cromosomas que han sido duplicados se distribuyen en dos núcleos para las dos células hijas, y la división citoplasmática o citocinesis, en la que la célula al completo se divide en dos células hijas (**Figura 25**). La mitosis se divide a su vez en cinco etapas que aparecen representadas en la **Figura 25**: profase, prometafase, metafase, anafase, telofase. Es precisamente entre la metafase y la anafase donde se encuentra el tercer gran punto de control.

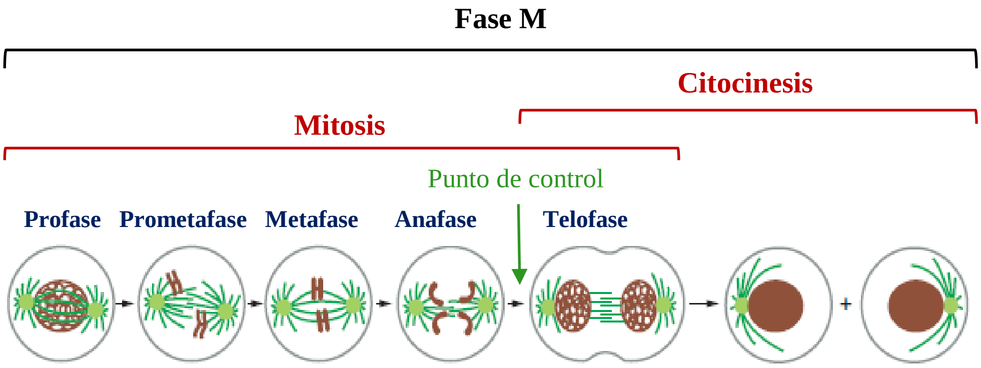

Figura 25. Representación de las etapas de la fase M en una célula eucariota (imagen adaptada a partir de ref. [51]).

Dado nuestro interés en el ADN como diana terapéutica, es importante recalcar que durante la mayor parte de la vida celular el ADN se encuentra en un estado de condensación intermedio en forma de cromatina (ver **apartado 2.2.3, Capítulo I**). Al final de la fase G1 comienza a producirse la descondensación para que puedan separarse las dos hebras de ADN, lo cual es necesario para la replicación del mismo durante la fase S. En la fase G2 el ADN vuelve a condensarse, y es en la fase M donde aparece el máximo grado de compactación: la formación de los cromosomas.

4.2. Efectos biológicos del enlace a ADN en doble hélice.

Como se ha explicado en apartados anteriores, el ADN y los procesos en los que este está involucrado son la principal diana de las drogas antitumorales en uso clínico [21]. En principio, esto convierte a los agentes antitumorales en drogas inespecíficas que afectan tanto a células cancerígenas como a sanas. Cabe preguntarse entonces cuál es la razón de la continuidad del elevado interés científico por este tipo de drogas.

La respuesta a esta pregunta se encuentra en gran medida en las características típicas de las células cancerígenas y su ciclo celular [87,88]. Estas células se dividen sin control y sus mecanismos de senescencia están desactivados, por lo que ejecutan el ciclo celular más veces y de forma más rápida que sus homólogas sanas [88]. La interacción de ligandos con el ADN puede impedir que procesos tan importantes en el ciclo celular como es la replicación del propio ADN (que se produce en la fase S) transcurra de forma correcta. Gracias a esto, muchas de estas drogas consiguen detener el ciclo celular en el punto de control de la fase G2 (ver **apartado 4.1, Capítulo I**), debido a los daños causados en el ADN durante su replicación [89]. Algunos ejemplos relevantes de este modo de acción incluyen el cisplatino o la doxorrubicina [90,91]. En definitiva, la selectividad de este tipo de drogas reside en el hecho de que en un determinado espacio temporal las células cancerígenas ejecutarán más veces el ciclo celular que las células sanas, por lo que estadísticamente afectarán en mayor medida a las cancerígenas.

4.3. Efectos biológicos del enlace a G-cuádruplex.

Existen un gran número de estrategias planteadas para mejorar la selectividad hacia células cancerígenas. Una de ellas consiste en incrementar la selectividad estructural de las drogas, es decir, emplear como diana determinadas estructuras del ADN que pueden jugar papeles importantes en procesos biológicos muy concretos. En el caso de las cuádruples hélices de ADN, el interés a nivel biológico reside en el hecho de que secuencias con la capacidad de plegarse en G-cuádruplex aparecen de forma recurrente en promotores de oncogenes y en los telómeros [80,92]. En el núcleo celular, la formación de G-cuádruplex puede ocurrir cuando el ADN en doble hélice se separa localmente para realizar procesos como la replicación y la transcripción, y también en los telómeros de los cromosomas, que están constituidos por una sola hebra de ADN de secuencia d(TTAGGG)$_n$ y de los que dependen los procesos de senescencia celular (**Figura 26**) [93,94]. Además, el ARN mensajero (mARN) que se encuentra en el citoplasma para realizar la traducción también puede formar G-cuádruplex [27]. Por ello, el diseño drogas que interaccionen y estabilicen específicamente las G-cuádruplex presenta un gran potencial para afectar y modular diferentes procesos celulares de gran importancia, aunque lo cierto es que nos encontramos aún en fases de investigación muy tempranas en lo que se refiere a las consecuencias biológicas de esta interacción [95].

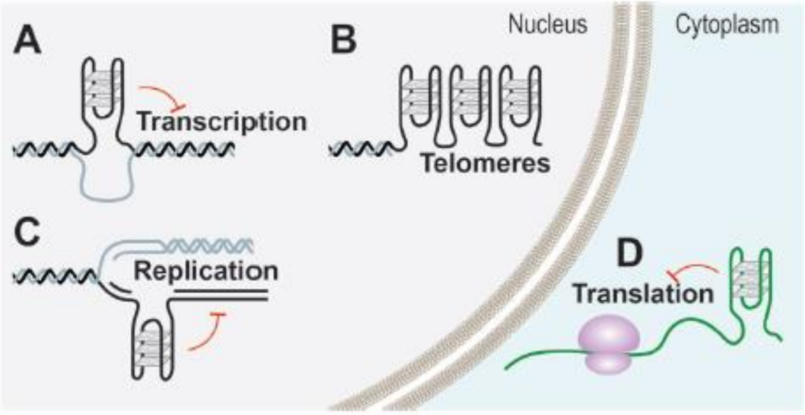

Figura 26. En el núcleo la formación y estabilización de G-cuádruplex puede ocurrir durante la transcripción (**A**) y la replicación (**C**) y en los telómeros (**B**). En el citoplasma pueden formarse G-cuádruplex en el mARN afectando a la traducción (**D**). De ref. [27].

5. Otras dianas contra el cáncer.

A pesar de la gran repercusión de las drogas que actúan a nivel de ADN, en los últimos años se han planteado otras posibles dianas celulares. El objetivo fundamental consiste en disminuir los efectos secundarios perjudiciales de las drogas existentes así como superar la resistencia que puede aparecer después de determinados tratamientos antitumorales. Algunos ejemplos de dianas alternativas investigadas en el ámbito de la quimioterapia incluyen la mitocondria, los microtúbulos o una amplia variedad de proteínas con funciones específicas como los receptores transmembrana, entre otros muchos [96–98].

En la **Parte 3** de esta tesis nos centraremos precisamente en la mitocondria como diana celular de una pequeña familia de complejos metálicos de Iridio y Rodio. Puede decirse que las mitocondrias son orgánulos con roles tanto vitales como letales. Por una parte, son el centro del metabolismo celular, donde a través del proceso de respiración se transforma la energía química de combustibles orgánicos en energía utilizable en todos los procesos celulares necesarios para la vida [51]. Por otra parte, la mitocondria tiene un papel clave en la regulación de la muerte celular vía apoptosis mediante la liberación al citosol de proteínas pro-apoptóticas [99]. Además, es bien conocido que las células cancerígenas presentan diversas alteraciones mitocondriales [100,101]. Como consecuencia, existe un creciente interés en diseñar drogas que presenten como diana alguno de los procesos en los que se involucra la mitocondria, y existe una amplia bibliografía al respecto [102–105]. Una de las ventajas que este tipo de dianas puede suponer consiste en la superación de la resistencia adquirida a tratamientos con agentes antitumotales como el cisplatino, que actúan a nivel de ADN, dado que el mecanismo de acción biológico es totalmente diferente [106].

Capítulo II

Metodología Experimental

1. Metodología Química - Física.

1.1. Reactivos.

1.1.1. Disolvente.

Todas las disoluciones se preparan con agua doblemente desionizada por un sistema Milli-Q® (Millipore, MERCK). Como disolución tampón se emplea en la mayoría de los ensayos cacodilato sódico, NaCaC ($(CH_3)_2AsO_2Na$) o cacodilato de litio, LiCaC ($(CH_3)_2AsO_2Li$), y cloruro sódico (NaCl), cloruro potásico (KCl) o cloruro de litio (LiCl) para ajustar la fuerza iónica (I), salvo en aquellos ensayos en los que se especifique el uso de otra disolución tamponante. Los reactivos para la preparación de las disoluciones se obtuvieron de Sigma Aldrich (MERCK) con grado de pureza > 99 %.

1.1.2. Ligandos comerciales.

1.1.2.1. Doxorrubicina.

El compuesto doxorrubicina (DOX) se adquirió de Sigma Aldrich. Las disoluciones madre se preparan mediante pesada en tampón 2.5 mM NaCaC (pH = 7.0) y se conservan a 4 ^{o}C protegidas de la luz. Las disoluciones de trabajo para realizar los distintos ensayos se preparan a partir de estas en el disolvente tampón especificado en cada caso.

1.1.2.2. TMPyP4

El compuesto TMPyP4 (*meso*-5,10,15,20-Tetrakis-(N-methyl-4-pyridyl)porphine). se adquirió de Sigma Aldrich. Las disoluciones madre se preparan mediante pesada en agua ultrapura y se conservan a 4 ^{o}C protegidas de la luz. A partir de esta disolución madre se preparan las disoluciones de trabajo por dilución en el correspondiente disolvente tampón.

1.1.3. Ligandos no comerciales.

1.1.3.1. Clústeres de plata triatómicos (Ag_3).

Los clústeres de plata triatómicos (Ag_3) estudiados en el **Capítulo IV** fueron suministrados por el Prof. Arturo López Quintela de la empresa NANOGAP (Santiago de Compostela, España) y su síntesis y caracterización se encuentran descritas en la bibliografía [107]. Las muestras se conservan a 4 ^{o}C protegidas de la luz.

1.1.3.2. Complejos metálicos de platino.

Los complejos de platino que se han estudiado en el **Capítulo V** de este trabajo fueron sintetizados y caracterizados por el grupo de los profesores Blanca R. Manzano y Félix A. Jalón, de la Universidad de Ciudad Real (Facultad de Ciencias y Tecnologías

Químicas, España). Las disoluciones madre se preparan por pesada en DMSO, se realizan alícuotas y se conservan a - 20 ºC. Para realizar cada ensayo se descongela una alícuota que es usada una única vez para evitar someter a los complejos en disolución a procesos de congelación – descongelación. Las disoluciones de trabajo se preparan por dilución en la disolución tampón indicada o bien en medio celular para realizar los ensayos biológicos.

1.1.3.3. Complejos metálicos de níquel, cobre y vanadio.

Los complejos metálicos con centros de níquel, cobre y vanadio que aparecen en el **Capítulo VIII** fueron sintetizados y caracterizados por el grupo del profesor Ramón Vilar del Imperial College London (Faculty of Natural Sciences, Reino Unido). Las disoluciones madre se preparan por pesada en DMSO y las alícuotas se conservan a – 20 ºC. Las correspondientes disoluciones de trabajo se preparan por dilución en el tampón especificado en cada caso.

1.1.3.4. Complejos metálicos de iridio y rodio.

Los complejos metálicos con centros de iridio y rodio presentados en el **Capítulo IX** fueron sintetizados y caracterizados por el grupo del profesor Gustavo Espino de la Universidad de Burgos (Facultad de Ciencias, España). Las disoluciones madre se preparan por pesada en DMSO y las alícuotas se conservan a - 20 ºC. Después se diluyen en las correspondientes disoluciones tampón de trabajo o bien en medio celular para realizar los ensayos biológicos.

1.1.4. Polinucleótidos.

1.1.4.1. ADN Calf Thymus.

El ADN Calf Thymus (ctDNA) se adquirió de Sigma Aldrich en forma de sal de sodio liofilizada. Esta sal se disuelve en agua ultrapura, se preparan alícuotas de 10 mL y se someten a un proceso de homogenización ultrasónica con un equipo UP400S equipado con un sonotrodo de titanio de 3 mm de diámetro (Hielscher, Alemania), manteniendo las disoluciones en hielo para evitar efectos térmicos durante la sonicación. Mediante electroforesis en gel de agarosa a 20 V/cm durante 20 min se determina la longitud media de las moléculas de ADN tras la sonicación, siendo aproximadamente de 1000 pares de bases (bp). Para realizar los ensayos, la concentración de ADN expresada en molaridad en pares de bases se determina siempre espectrofotométricamente empleando el coeficiente de extinción molar $\varepsilon = 13200\ M^{-1}\ cm^{-1}$ a $\lambda = 260$ nm, I = 0.1 M y pH = 7.0 [108].

1.1.4.2. Oligonucleótidos para formación de G-cuádruplex.

En este trabajo se han empelado una serie de oligonucleótidos ricos en guanina (G) de secuencias análogas a las encontradas en determinadas regiones del genoma humano que son capaces de formar G-cuádruplex *in vitro*. Además, los mismos oligonucleótidos modificados en sus extremos 5’ y 3’ con los fluoróforos FAM y TAMRA, respectivamente, se usaron para los ensayos de desnaturalización térmica seguida mediante FRET (Transferencia de Energía de Resonancia de Förster).

Todas las secuencias de los oligonucleótidos empleados en este trabajo se encuentran recogidas en la **Tabla 1** junto con sus abreviaturas y bibliografía sobre sus estructuras en G-cuádruplex. Todos estos oligonucleótidos fueron suministrados liofilizados por Eurogentec (Liège, Bélgica) con grado de pureza HPLC. Las disoluciones madre se preparan en agua a una concentración de aproximadamente 100 µM siguiendo las especificaciones del fabricante. La concentración se comprueba mediante espectrofotometría de absorción empleando los coeficientes de extinción molar aportados por el fabricante para cada oligonucleótido. Estas disoluciones madre se conservan a - 20 ºC. Para realizar el templado (annealing) de la G-cuádruplex se preparan las disoluciones de trabajo en el disolvente tampón deseado, típicamente 10 mM LiCaC (pH = 7.4) + 90 mM LiCl + 10 mM KCl, salvo en áquellos casos en los que se indique el uso de otro tampón. Estas disoluciones se mantienen a 95 ºC durante 5 minutos y después se disminuye lentamente la temperatura a lo largo de unas 5 horas hasta alcanzarse la temperatura ambiente. De esta forma se obtienen las estructuras de G-cuádruplex más estables termodinámicamente.

Tabla 1. Secuencias de los oligonucleótidos empleados junto con bibliografía referente a su estructura en G-cuádruplex.

G-cuádruplex de ADN	**Secuencia**	**Bibliografía**
hTelo o Tel22	5’-AGGGTTAGGGTTAGGGTTAGGGTTA-3’	[47,109]
c-Myc	5’-TGAGGGTGGGTAGGGTGGGTAA-3'	[49]
c-kit2	5’-GGGAGGGCGCTGGGAGGAGGG-3'	[110]
22CTA	5’-AGGGCTAGGGCTAGGGCTAGGG-3'	[111]
26CEB	5’-AAGGGTGGGTGTAAGTGTGGGTGGGT-3'	[112]
bcl-2	5’-GGGCGCGGGAGGAAGGGGGCGGG-3'	[113]
G-cuádruplex de ARN		
TERRA	5'-GGGUUAGGGUUAGGGUUAGGG-3'	[114]
Doble hélice de ADN		
ds26	5’-CAATCGGATCGAATTCGATCCGATTG-3'	

1.1.4.3. ADN plasmídico.

Para los ensayos de electroforesis horizontal en gel de agarosa se ha empleado el plásmido artificial pUC18 de 2686 bp. Este se obtiene mediante cultivo y crecimiento de la cepa DH5α de *Escherichia coli* empleando un kit comercial de extracción de ADN plasmídico: “Quiagen Plasmid Purification” (Hilden, Alemania). La concentración de pUC18 de la disolución madre, expresada en molaridad en pares de bases, se determina mediante el kit comercial “Quant-iT^{TM} PicoGreenR dsDNA Assay Kit” de Invitrogen. Las alícuotas de esta disolución madre se mantienen a - 20 ºC hasta su uso.

1.1.5. Proteínas.

1.1.5.1. Seroalbúmina bovina (BSA).

La BSA es una albúmina extraída del suero bovino ampliamente utilizada como modelo sustitutivo de la seroalbúmina humana (HSA) en muchos ensayos bioquímicos, por ser mucho más económica y presentar un comportamiento muy similar a la HSA [115]. Las disoluciones madre de BSA, adquirida liofilizada de Sigma Aldrich, se preparan en la disolución tamponada indicada y la concentración se determina espectrofotométricamente empleando el coeficiente de extinción molar $\varepsilon = 44070\ M^{-1}\ cm^{-1}$ a $\lambda = 278$ nm y pH = 7.0 [116]. Las disoluciones se conservan a 4 ºC protegidas de la luz.

1.2. Técnicas Experimentales.

1.2.1. Medidas de pH.

Las medidas de pH se realizan con un pH-metro Metrohm (Herisau, Suiza) equipado con un microelectrodo de vidrio, un electrodo de referencia y un puente salino de KCl (3 M). Para ajustar el pH se emplean disoluciones de hidróxido sódico (NaOH) o ácido clorhídrico (HCl).

1.2.2. Espectrofotometría de absorción.

1.2.2.1. Fundamento teórico.

Todas las especies moleculares son capaces de absorber radiación de determinadas longitudes de onda (λ). Este proceso de absorción de luz se rige por la ley de Lambert - Beer (ec. 1). Al incidir un haz de luz de una determinada longitud de onda con una intensidad I_0 en una disolución de un cromóforo, una parte de dicha radiación será absorbida, de forma que la parte no absorbida, I, conseguirá atravesar dicha disolución. La transmitancia, T, se define como la relación entre la intensidad transmitida y la incidente (I/I_0). La absorbancia (Abs) se relaciona con la cantidad de luz absorbida por la disolución a una determinada longitud de onda, se define como el logaritmo del inverso de la transmitancia y es directamente proporcional al coeficiente de extinción molar, ε, a la concentración del cromóforo en disolución, C, y al camino óptico recorrido por el haz de luz, l:

$$\text{Abs} = \log\frac{1}{T} = -\log T = -\log\frac{I}{I_0} = \varepsilon \cdot C \cdot l \qquad (1)$$

1.2.2.2. Instrumentación.

Las medidas de absorbancia se han realizado con un espectrofotómetro Agilent 8453 (Agilent Technologies, Palo Alto, California) de haz simple con detección por fotodiodo-array en el rango $\lambda = 190 – 1100$ nm. Para el control de temperatura lleva incorporado un sistema Peltier termostatizador (HP-89090A) con precisión de ± 0.1 ºC. El equipo cuenta con una lámpara de Tungsteno para las mediciones en la región del Visible y una de Xenon para la región UV. Las medidas se realizan en cubetas de cuarzo de alta precisión (Hellma Analytics, Müllheim, Alemania) con 1 cm de camino óptico.

1.2.2.3. Método experimental.

- Procesos de agregación.

Una de las formas para estudiar si una determinada molécula es capaz de formar agregados en disolución es comprobar si cumple la ley de Lambert – Beer (ec. 1) [117]. En la cubeta se parte de la disolución tampón y se realizan adiciones de una disolución del compuesto de interés en el mismo tampón a T = 25 ºC. Tras cada adición, se homogeniza la disolución en cubeta y se recoge el espectro de absorción.

Si ec. 1 se cumple, la representación de la absorbancia a una determinada longitud de onda (preferiblemente en un máximo de absorción) frente a la concentración de compuesto será una recta que pasa por el origen (0,0) y cuya pendiente es el coeficiente de extinción molar del compuesto. La presencia de desviaciones de la linealidad proporcionan información acerca de fenómenos que pueden estar produciéndose en disolución: procesos de dimerización o formación de agregados de orden superior, precipitación, cambios en el índice de refracción de la luz, etc.

- Valoraciones espectrofotométricas.

Las valoraciones se realizan partiendo en la cubeta de un volumen conocido de una disolución de ligando o droga (D) de concentración conocida. El disolvente en ausencia de droga o polinucleótido se emplea para recoger el blanco antes de comenzar la valoración. Se realizan adiciones de una disolución de polinucleótido (P) de concentración conocida (C^0_P), se homogeniza el contenido de la cubeta y se recoge el espectro de absorción a T = 25 ºC. Los espectros son corregidos por el factor de dilución (ec. 2), f_d, que es la relación entre la concentración inicial de D en la cubeta, C^0_D, y la concentración tras cada adición realizada, C_D:

$$f_d = C^0_D / C_D \qquad (2)$$

Para el análisis de los datos experimentales se selecciona una longitud de onda donde los cambios espectrales a lo largo de la valoración sean máximos y se obtiene el valor de la absorbancia en cada punto de la valoración. A continuación se explican los métodos que pueden emplearse para el análisis de estos datos experimentales dependiendo del tipo de sistema estudiado.

Ecuación de Benesi-Hildebrand sencilla.

Entendiendo la interacción entre la droga (D) y el polinucleótido (P) como una reacción en equilibrio en la que se forma un complejo droga/polinucleótido (PD) tenemos que:

$$\mathrm{P} + \mathrm{D} \xrightleftharpoons{\mathrm{K}} \mathrm{PD} \tag{3}$$

siendo K la constante de equilibrio que se define como:

$$\mathrm{K} = \frac{[\mathrm{PD}]}{[\mathrm{P}][\mathrm{D}]} \tag{4}$$

donde [PD], [P] y [D] son las concentraciones en el equilibrio de PD, P y D, respectivamente, con [P] expresada en pares de bases del polinucleótido.

En cada punto de la valoración, la concentración analítica de droga, C_D, es:

$$\mathrm{C_D} = [\mathrm{D}] + [\mathrm{PD}] \tag{5}$$

Por tanto, teniendo en cuenta la ley de Lambert - Beer (ec. 1) para una determinada longitud de onda donde solo absorbe la droga libre y la droga complejada y para un camino óptico de 1 cm, la absorbancia será:

$$\mathrm{Abs} = \varepsilon_{\mathrm{D}}[\mathrm{D}] + \varepsilon_{\mathrm{PD}}[\mathrm{PD}] \tag{6}$$

Introduciendo ec. 5 en ec. 4:

$$\frac{1}{\mathrm{K}} = \frac{(\mathrm{C_D} - [\mathrm{PD}])[\mathrm{P}]}{[\mathrm{PD}]} \tag{7}$$

que puede reescribirse como:

$$\frac{\mathrm{C_D}}{[\mathrm{PD}]} = 1 + \frac{1}{\mathrm{K}[\mathrm{P}]} \tag{8}$$

Por otra parte, sustituyendo ec. 5 en ec. 6 se obtiene:

$$\mathrm{Abs} - \varepsilon_{\mathrm{D}}\mathrm{C_D} = (\varepsilon_{\mathrm{PD}} - \varepsilon_{\mathrm{D}})[\mathrm{PD}] \tag{9}$$

Definiendo:

$$\Delta\mathrm{Abs} = \mathrm{Abs} - \varepsilon_{\mathrm{D}}\mathrm{C_D} \tag{10}$$

$$\Delta\varepsilon = \varepsilon_{\mathrm{PD}} - \varepsilon_{\mathrm{D}} \tag{11}$$

la ec. 9 queda como:

$$[PD] = \frac{\Delta Abs}{\Delta\varepsilon} \qquad (12)$$

Finalmente, introduciendo ec. 12 en ec. 8 se obtiene la ecuación conocida como ecuación de Benesi-Hildebrand sencilla:

$$\frac{C_D}{\Delta Abs} = \frac{1}{\Delta\varepsilon} + \frac{1}{\Delta\varepsilon K}\cdot\frac{1}{[P]} \qquad (13)$$

De la representación de $C_D/\Delta Abs$ frente a $1/[P]$ se obtiene una recta cuya pendiente y ordenada se corresponden con $1/\Delta\varepsilon K$ y $1/\Delta\varepsilon$, respectivamente, por lo que podemos obtener el valor de $\Delta\varepsilon$ de la ordenada y el de K de la pendiente. Dado que [P] depende de la propia constante termodinámica K, es necesario realizar un procedimiento iterativo para el cálculo de K.

Ecuación de Benesi-Hildebrand completa.

La concentración de polinucleótido puede expresarse como:

$$C_P = [P] + [PD] \qquad (14)$$

Teniendo en cuenta ec. 5 y ec. 15 se puede reescribir ec. 4 como:

$$K = \frac{[PD]}{(C_P - [PD])(C_D - [PD])} \qquad (15)$$

Sustituyendo en ec. 15 la ec. 12 se obtiene la ecuación de Benesi-Hildebrand completa:

$$\frac{C_D C_P}{\Delta Abs} + \frac{\Delta Abs}{\Delta\varepsilon^2} = \frac{1}{K\Delta\varepsilon} + \frac{C_P + C_D}{\Delta\varepsilon} \qquad (16)$$

Tomando inicialmente un valor aproximado de $\Delta\varepsilon$, que podemos obtener de la ecuación Benesi-Hildebrand sencilla, se representa $C_D C_P/\Delta Abs + \Delta Abs/\Delta\varepsilon^2$ en función de $C_P + C_D$. De la pendiente y ordenada de la recta se puede calcular $\Delta\varepsilon$ y K. Se sustituye en la ec. 16 el valor de $\Delta\varepsilon$ obtenido y se realiza un procedimiento iterativo hasta alcanzar la convergencia.

Ecuación de McGhee-von Hippel.

La ecuación anterior (ec. 16) es válida para aquellos sistemas en los que el número de bases ocupadas por el ligando o droga, n, sea igual a 1. Podemos entender la interacción como un equilibrio entre el ligando, D, y el número de sitios disponibles en el polinucleótido para ser ocupados por dicho ligando, S. Si n = 1, entonces la concentración de sitios disponibles será igual a la concentración de pares de bases del polinucleótido, es decir, [S] = [P]. Sin embargo, en muchas ocasiones el ligando no ocupa exactamente un par de bases del polinucleótido, por lo que $n \neq 1$ y $[S] \neq [P]$. En estos casos es necesario definir la interacción ligando – polinucleótido como:

$$S + D \overset{K}{\rightleftharpoons} SD \tag{17}$$

La concentración [S] se puede relacionar con C_P a partir de la expresión propuesta por McGhee-von Hippel, en la que se define el parámetro f(r), función de grado de saturación del polinucleótido, r, y del tamaño de sitio, n [118].

$$f(r) = \frac{[1 - nr]^n}{[1 - (n - 1)r]^{n-1}} = \frac{[S]}{C_P} \tag{18}$$

El grado de saturación del polinucleótido dependerá de la concentración total de polinucleótido, C_P, y de la cantidad de complejo formado en el equilibrio [SD], por lo que r se define como:

$$r = \frac{[SD]}{C_P} = \frac{\Delta Abs}{\Delta\varepsilon C_P} \tag{19}$$

Incluyendo esta modificación de la ec. 18 en la ecuación de Benesi-Hildebrand (ec. 13) se obtiene la ecuación de McGhee-von Hippel:

$$\frac{C_D}{\Delta Abs} = \frac{1}{\Delta\varepsilon} + \frac{1}{\Delta\varepsilon K} \cdot \frac{1}{C_P f(r)} \tag{20}$$

Se estima un valor de $\Delta\varepsilon$ a partir de la amplitud de la isoterma de la valoración con el que podemos calcular un valor aproximado de r y de f(r). Representando $C_D/\Delta Abs$ en función de $1/C_P f(r)$ se obtiene una recta de pendiente $1/\Delta\varepsilon K$ y ordenada $1/\Delta\varepsilon$. El nuevo valor de $\Delta\varepsilon$ se emplea para recalcular r y f(r) y se itera tantas veces como sea necesario hasta alcanzar la convergencia para obtener el valor de K.

Ecuación de Scatchard.

En este método también se tiene en cuenta que el número de sitios, n, puede ser distinto de 1. Para ello se introduce un nuevo parámetro, B, que es el número de sitios de enlace por cada par de bases del polinucleótido. La concentración total de sitios se define como:

$$[S]_0 = BC_P \tag{21}$$

Según la hipótesis de Scatchard, los sitios de enlace son independientes entre sí y están saturados, de forma que:

$$[S]_0 = [S] + [SD] \tag{22}$$

Sustituyendo ec. 21 en ec. 22 queda:

$$BC_P = [S] + [SD] \tag{23}$$

e introduciendo en ec. 23 el parámetro r anteriormente definido en ec. 19 queda:

$$BC_P = [S] + rC_P \tag{24}$$

Reordenando ec. 24 obtenemos:

$$[S] = C_P(B - r) \tag{25}$$

Definiendo la constante termodinámica de Scatchard, K_{SC}, como:

$$K_{SC} = \frac{[SD]}{[S][D]} \tag{26}$$

e introduciendo ec. 19 y ec. 25 en ec. 26 se obtiene la ecuación de Scatchard [119]:

$$\frac{r}{[D]} = K_{SC}B - K_{SC}r \tag{27}$$

De la representación de r/[D] en función de r se obtiene una recta cuya pendiente es igual a - K_{SC} y de cuya ordenada podemos obtener el parámetro B, que se relaciona con el tamaño de sitio n mediante la expresión:

$$n = \frac{1 + {}^{1}\!/_{B}}{2} \tag{28}$$

En necesario tener en cuenta que en la mayoría de los casos la ecuación de Scatchard (ec. 27) no se cumple en todo el intervalo de concentraciones de la valoración, ya que la hipótesis inicial de independencia de los sitios no se cumple en todo este rango.

- Seguimiento de cinéticas lentas.

La relación directamente proporcional de la absorbancia con la concentración también nos permite seguir el progreso de reacciones lentas en disolución y obtener mecanismos de reacción. Por ejemplo, la formación de enlaces covalentes entre un ligando y el ADN puede desarrollarse a lo largo de horas o incluso días. Otras reacciones de interés que en ocasiones pueden seguirse de esta forma son las sustituciones de determinados grupos en complejos metálicos, como veremos en el **Capítulo V.** Las cinéticas en absorción se realizaron a T = 25 ^{o}C en la disolución tampón indicada registrando la absorbancia frente al tiempo.

1.2.3. Fluorescencia.

1.2.3.1. Fundamento teórico.

La fluorescencia es una propiedad que presentan ciertas especies extremadamente útil en técnicas asociadas a la química médica y la biología molecular, como veremos a lo largo de este trabajo. Se trata de un fenómeno por el cual una especie, tras recibir y absorber una radiación luminosa, es capaz de emitir una radiación luminosa, siempre a una longitud de onda mayor que la longitud de onda absorbida inicialmente. Esta longitud de onda absorbida se denomina de excitación (λ_{exc}), mientras que la emitida se denomina longitud de onda de emisión (λ_{em}).

En la **Figura 1** se muestra el diagrama de Jablonski, en el que aparecen representadas las posiciones relativas de los niveles de energía electrónicos y vibracionales de una molécula [120]. Un fluoróforo que se encuentra en el estado electrónico singlete fundamental, S_0, puede absorber radiación de determinadas longitudes de onda y pasar a estados electrónicos excitados (S_1, S_2…). En las moléculas, cada uno de estos estados electrónicos presenta a su vez diferentes estados vibracionales, y la excitación puede producirse hasta cualquiera de ellos, razón por la cual existen bandas de absorción que abarcan un rango de longitudes de onda. La vuelta al estado fundamental S_0 puede producirse por distintas vías: radiativas y no radiativas. Por ello, aunque todas las moléculas son susceptibles de absorber radiación y ser excitadas a estados electrónicos superiores, no todas son capaces de emitir radiación al volver al estado fundamental.

Dentro de las vías de relajación no radiativas se encuentra la relajación vibracional y la conversión interna. La primera se produce entre niveles de energía vibracionales y es extremadamente rápida (ver **Tabla 2**). La segunda se produce entre diferentes estados electrónicos de igual multiplicidad gracias a la superposición entre estados vibracionales de los distintos estados electrónicos (por ejemplo, entre S_2 y S_1, y entre S_1 y S_0). Sin embargo, existe la posibilidad de que el retorno a S_0 desde S_1 se produzca de forma radiativa mediante la emisión de un fotón, proceso que se conoce como fluorescencia. La fluorescencia es un proceso relativamente lento, por lo que encuentra mucha competencia con los procesos de relajación no radiativos (**Tabla 2**). Otra posibilidad de relajación al estado fundamental de forma radiativa es la fosforescencia. Para ello primero debe darse un proceso conocido como cruce entre sistemas, en el que se produce un cambio de multiplicidad de spin al pasar del estado singlete S_1 al estado triplete T_1. La fosforescencia se produce por emisión de un fotón al pasar del estado triplete, T_1, al estado singlete fundamental, S_0. Esta transición es prohibida, por lo que es muy lenta y poco probable.

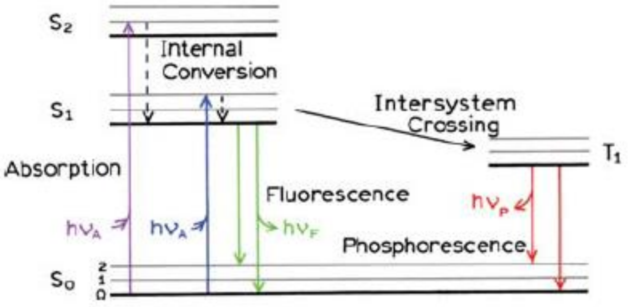

Figura 1. Diagrama de Jablonski (de ref. [120]).

Tabla 2. Escalas de tiempo medios de las transiciones radiativas y no radiativas del diagrama de Jablonski.

Transición	Escala de tiempos (s)	¿Proceso radiativo?
Conversión Interna	10^{-14} - 10^{-11}	no
Relajación Vibracional	10^{-14} - 10^{-11}	no
Absorción	10^{-15}	sí
Fosforescencia	10^{-4} - 10^{-1}	sí
Cruce entre sistemas	10^{-8} - 10^{-3}	no
Fluorescencia	10^{-9} - 10^{-7}	sí

Por tanto, el espectro de fluorescencia de una molécula o fluoróforo es característico de la misma, ya que depende de sus propiedades electrónicas. La espectroscopía de fluorescencia posee muchas ventajas con respecto a otras técnicas como la absorción, ya que presenta una elevada sensibilidad permitiendo trabajar a concentraciones mucho más bajas. Además, otros parámetros relevantes de los fluoróforos son el rendimiento cuántico y el tiempo de vida. El rendimiento cuántico, Φ, es la relación entre el número de fotones absorbidos y el número de fotones emitidos, por lo que su valor puede variar entre 0 y 1, y es una medida de la eficacia del proceso de emisión. El tiempo de vida de un fluoróforo, τ_f, se define como el tiempo promedio que una molécula pasa en el estado excitado antes de retornar al estado fundamental [120].

1.2.3.2. Instrumentación.

Las medidas de fluorescencia de estado estacionario se realizaron en un espectrofluorímetro Shimadzu Corporation RF-5301PC (Duisburg, Alemania) equipado con una lámpara de Xenon (150 W). La temperatura se controla mediante un baño externo Julabo, con una precisión de ± 0.1 ^{o}C. Se emplearon cubetas de cuarzo de fluorescencia de alta precisión de 1 cm de camino óptico (Hellma Analytics, Müllheim, Alemania).

Las medidas de tiempos de vida y de rendimientos cuánticos se realizaron en un espectrómetro modular FLS980 (Edimburgh Instruments, Livingston, Scotland) equipado con detectores fotomultiplicadores de UV-Visible (300 - 900 nm) refrigerado mediante efecto Peltier (**Figura 2**). Como fuentes de excitación dispone de lámpara de Xenon de emisión continua (350 W) y de láseres pulsados de diodo de picosegundos. Los tiempos de vida se midieron con una cubeta de cuarzo de fluorescencia. Para la determinación del rendimiento cuántico se empleó una cubeta de fluorescencia en una esfera integradora junto con el accesorio de ensamblaje de la esfera integradora F-M01 (Edimburgh Instruments, Livingston, Scotland). La esfera integradora consiste en una cavidad esférica de 120 mm de diámetro de un material con una reflectancia > 95 % en el rango λ = 250 - 2500 nm.

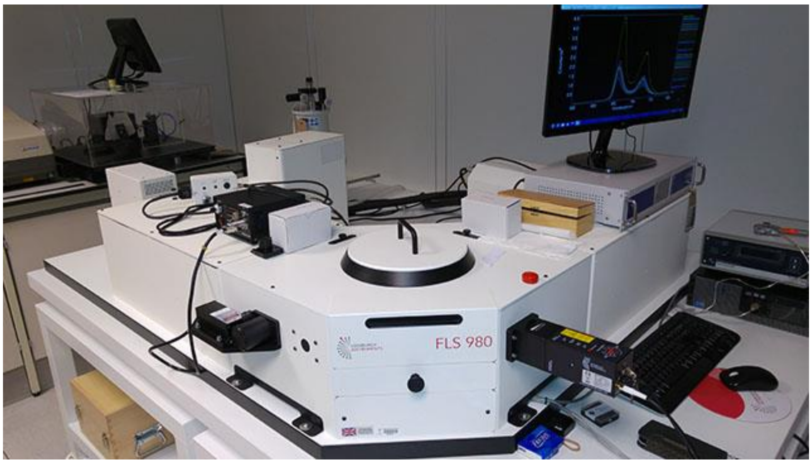

Figura 2. Espectrómetro modular FLS 980 empleado para la determinación de tiempos de vida y rendimientos cuánticos.

1.2.3.3. Método experimental.

- Valoración espectrofluorimétrica.

Las valoraciones se realizaron partiendo de un volumen conocido de disolución de ligando del que conocemos sus características de emisión (longitudes de onda de excitación, λ_{exc}, y de emisión, λ_{em}). Al igual que en las valoraciones en absorción, se procede a realizar adiciones del polinucleótido, homogeneizando la disolución y recogiendo el espectro de fluorescencia tras cada adición a T = 25 ºC. El análisis de los datos se realiza empleando las mismas ecuaciones del **apartado 1.2.2.3** usando el valor de la fluorescencia (F) a una λ_{em} determinada donde los cambios sean máximos, sustituyendo ΔAbs por $\Delta F = F - F_0$.

- Espectroscopía de fluorescencia resuelta en el tiempo.

Para determinar el tiempo de vida medio del estado excitado de las especies fluorescentes es necesario conocer previamente sus características de emisión y seleccionar el láser de diodo óptimo como fuente de excitación pulsada. Los fluoróforos empleados en esta tesis presentaban máximos de excitación por debajo de los 450 nm, por lo que se emplearon láseres pulsados de λ_{exc} = 375 nm o λ_{exc} = 405 nm (50 ps). Las medidas se realizaron en una cubeta de fluorescencia con la disolución del compuesto de interés. Además, se realizaron medidas también en presencia de diferentes concentraciones de polinucleótido, ya que la interacción con el mismo puede modificar los tiempos de vida del fluoróforo. El equipo permite excitar la muestra con un pulso ultrarrápido del orden de los picosegundos y cuantificar los fotones emitidos después del pulso en función del tiempo a una determinada λ_{em}. Esto permite conocer el tiempo de vida medio, τ_f, del estado excitado. El análisis de los datos se realizó con el software FAST 3.4.0.

- Rendimiento cuántico.

Las medidas de rendimiento cuántico se realizaron con el método de la esfera integradora. Para preparar las muestras de ligando, se selecciona la λ_{exc} a la que quiere determinarse el rendimiento cuántico y se prepara una disolución en el disolvente deseado a una concentración tal que la absorbancia del ligando a esa λ sea cercana a 0.1. Se necesitan dos cubetas de fluorescencia idénticas, una conteniendo el disolvente (blanco) y otra la disolución de ligando en dicho disolvente (muestra). Se recoge el espectro de emisión de ambas disoluciones a la λ_{exc} seleccionada, incluido el “scattering” emitido a la misma λ que la excitación, como puede verse en la **Figura 3**.

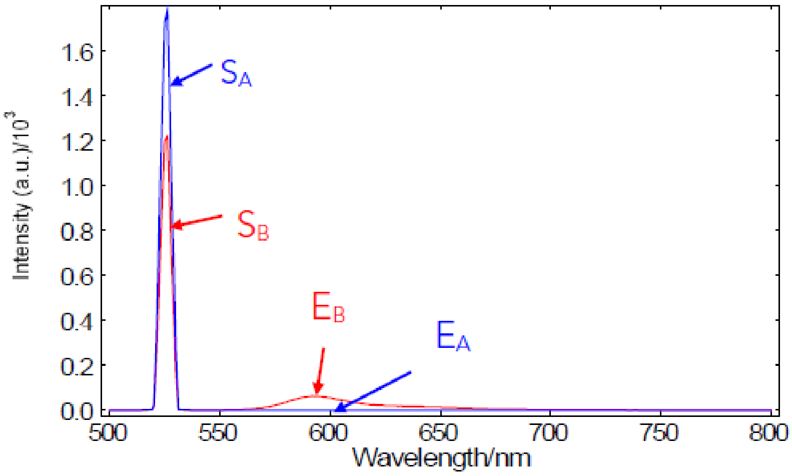

Figura 3. Ejemplo de espectros de emisión recogiendo la región de scattering (S) y la región de emisión (E) de una disolución muestra de ligando (B) y el blanco solo con el disolvente (A) (imagen de Edimburgh Instruments).

El rendimiento cuántico Φ puede obtenerse de forma directa de la siguiente relación:

$$\Phi = \frac{N_{em}}{N_{abs}} = \frac{E_B - E_A}{S_A - S_B} \qquad (29)$$

donde N_{em} y N_{abs} son el número de fotones emitidos y absorbidos por el compuesto, respectivamente, E_B y E_A son las áreas integradas de los picos de emisión del ligando y del blanco y S_B y S_A son las áreas integradas de los picos de scattering del ligando y del blanco, respectivamente.

Este análisis se realizó con el software F980 (Edimburgh Instruments, Livingston, Scotland).

1.2.4. Dicroísmo circular (CD).

1.2.4.1. Fundamento teórico.

El dicroísmo circular es una técnica de espectroscopía de absorción de radiación electromagnética circularmente polarizada. Esta radiación está formada por dos componentes polarizados circularmente, uno a izquierda (L) y otro a derecha (R), que están en fase y tienen la misma amplitud (ver **Figura 4.A**). Cuando una luz circularmente polarizada atraviesa una disolución de una molécula ópticamente activa (con centros quirales), esta puede absorber de forma diferente la luz circularmente polarizada a izquierda y derecha, es decir, $\varepsilon_L \neq \varepsilon_R$. Esta diferencia $\Delta\varepsilon = \varepsilon_L - \varepsilon_R$ se denomina dicroísmo circular e induce un desfase en ambos componentes circularmente polarizados, lo cual genera una rotación del plano de luz polarización de ángulo α (**Figura 4.B**) [121].

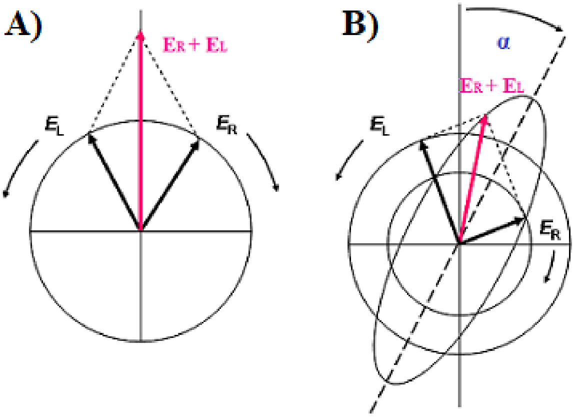

Figura 4. Representación de los componentes de la luz polarizada a izquierda y derecha (E_L y E_R) antes de atravesar la muestra (**A**) y tras atravesar una muestra ópticamente activa que absorbe de distinta manera los componentes E_L y E_R (**B**).

Para definir cuantitativamente el dicroísmo circular recurrimos a la ley de Lambert – Beer – Bouguer [121]. La absorbancia en cada uno de los dos componentes de la radiación será $Abs_L = \log(I_0/I_L)$ y $Abs_R = \log(I_0/I_R)$ y, por tanto, la diferencia en la absorción de ambos componentes al atravesar la muestra será:

$$\Delta Abs = Abs_L - Abs_R = \log\left(\frac{I_0}{I_L}\right) - \log\left(\frac{I_0}{I_R}\right) = \log\frac{I_R}{I_L} \tag{30}$$

y el dicroísmo circular:

$$\Delta\varepsilon = \frac{1}{C \cdot l}\,\Delta Abs \tag{31}$$

Como puede verse en ec. 30, I_0 no aparece en la ecuación, y C y l en ec. 31 son constantes conocidas, por lo que solo es necesario la medición de I_R e I_L por parte del equipo para realizar las medidas de dicroísmo circular. El parámetro físico medido en la técnica de dicroísmo circular es la elipticidad, θ, que se relaciona con Δε de la siguiente forma:

$$\tan\theta = \frac{E_R - E_L}{E_R + E_L} = \Delta\varepsilon \tag{32}$$

En las medidas experimentales el software del instrumento de medición de dicroísmo circular proporciona el valor de θ para cada longitud de onda medida. Los resultados suelen presentarse en forma de elipticidad molar, [θ], en función de la concentración expresada en pares de bases de polinucleótido, o bien en función del número de biomoléculas en el caso de proteínas y oligonucleótidos:

$$[\theta] = \frac{100 \cdot \theta}{C \cdot l} \ (\mathrm{deg} \cdot \mathrm{M}^{-1} \cdot \mathrm{cm}^{-1}) \tag{33}$$

La espectroscopía de dicroísmo circular es extremadamente útil en el estudio de las propiedades conformacionales de biomoléculas como ácidos nucleicos y proteínas. En el caso de los ácidos nucleicos, estos presentan bandas en la región UV, que es donde absorben las bases nitrogenadas [122]. Por ejemplo, el espectro del ctDNA presenta dos bandas características: una negativa en torno a 245 nm, relacionada con la helicidad, y otra positiva a 260 nm, relacionada con las interacciones de stacking entre las bases [123]. La interacción con ligandos puede provocar cambios conformacionales en el ADN que modifican estas bandas aportando información sobre el enlace, o incluso pueden aparecer nuevas bandas en el rango visible debido a la formación de nuevos complejos ligando/ADN en disolución, lo cual se conoce como dicroísmo circular inducido [124,125].

1.2.4.2. Instrumentación.

Para realizar las medidas de dicroísmo circular se empleó un instrumento modular MOS-450 BioLogic (Claix, Francia) con lámpara de arco de Xenon y un modulador electroóptico para obtener la luz circularmente polarizada a izquierda y derecha de forma alterna con una frecuencia de 50 kHz. La detección se realiza mediante un fotomultiplicador, y el software Biokine (versión 3.2) transforma la señal recibida en elipticidad (θ). La temperatura se controla mediante un baño externo Julabo. Para realizar las medidas se emplearon cubetas de cuarzo alta precisión de 1 cm de camino óptico (Hellma Analytics, Müllheim, Alemania). En el caso de los experimentos con oligonucleótidos (G-cuádruplex), debido a su alto coste se emplearon microcubetas de cuarzo de pared negra, que permiten trabajar con volúmenes inferiores a 500 µL.

1.2.4.3. Método experimental.

Para realizar las valoraciones primero se registra un blanco, que consiste en recoger el espectro de CD del disolvente en ausencia de droga y de biomolécula, en las mismas condiciones (rango espectral y velocidad de barrido) que los siguientes espectros. Este blanco se sustrae a los demás espectros para restar la contribución del disolvente al espectro de CD. Se parte de una disolución de polinucleótido o proteína de interés de volumen y concentración conocidos. Se realizan adiciones de ligando de concentración conocida y se registra el espectro (θ frente a λ). Los espectros se corrigen por la concentración de biomolécula según ec. 33 para obtener la elipticidad molar [θ]. En las isotermas se representa [θ] a una determinada longitud de onda donde la variación sea máxima frente a la relación de concentraciones droga/biomolécula (C_D/C_P).

1.2.5. Calorimetría de Valoración Isotérmica (ITC).

1.2.5.1. Fundamento teórico.

La calorimetría de valoración isotérmica o ITC (Isothermal Titration Calorimetry) es una técnica muy potente para el estudio de interacciones droga/biomolécula [126,127], ya que permite medir de forma directa el calor asociado al enlace entre ambos. Se trata de una valoración en la que el ligando se añade progresivamente a una disolución de polinucleótido o proteína, midiendo el calor absorbido o desprendido tras cada adición, lo cual permite determinar los parámetros termodinámicos del enlace [128]. El caso más sencillo se correspondería con un equilibrio del tipo:

$$\mathrm{P + D \xrightleftharpoons{K} PD} \qquad (33)$$

donde P y D son el polinucleótido y el ligando libres, respectivamente, PD el complejo formado y K la constante termodinámica que gobierna el proceso que queda definida como:

$$\mathrm{K} = \frac{[\mathrm{PD}]}{[\mathrm{P}][\mathrm{D}]} \qquad (34)$$

siendo [P], [D] y [PD] las concentraciones en el equilibrio de P, D y PD, respectivamente.

La constante de enlace K determina la diferencia en la energía libre de Gibbs del proceso, ΔG, que se relaciona a su vez con los parámetros termodinámicos de variación de entalpía, ΔH, y entropía, ΔS:

$$\Delta \mathrm{G} = -\mathrm{RTlnK} = \Delta \mathrm{H} - \mathrm{T}\Delta \mathrm{S} \qquad (35)$$

donde R es la constante de los gases y T la temperatura absoluta en grados kelvin.

El equipo de ITC permite obtener de forma directa el valor de K y de ΔH a una temperatura T determinada, con lo que a partir de ec. 35 pueden obtenerse también los valores de ΔG y de ΔS del proceso de enlace [129].

En la **Figura 5** se muestra un diagrama esquemático de un instrumento ITC, el cual presenta dos celdas idénticas, una de referencia y otra de medida, alojadas en un bloque isotérmico aislante que mantiene la temperatura constante a lo largo de la valoración. Estas dos celdas se mantienen en equilibrio térmico durante todo el experimento, de forma que ΔT = 0. En la celda de referencia se introduce agua ultrapura, mientras que en la de medida se encuentra la disolución de polinucleótido o proteína. En esta celda de medida se realizan adiciones de pequeñas alícuotas de disolución de ligando espaciadas en el tiempo, y el equipo mide la energía calorífica por unidad de tiempo (J/s o W) que es necesario aportar a esta celda para mantener ΔT = 0 en todo momento.

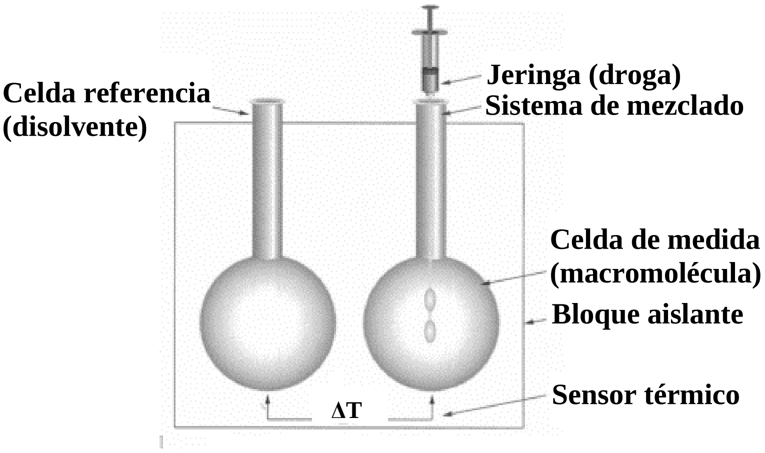
Celda referencia
(disolvente)
Jeringa (droga)
Sistema de mezclado
Celda de medida
(macromolécula)
Bloque aislante
Sensor térmico
ΔT

Figura 5. Diagrama esquemático de un instrumento de ITC (imagen adaptada a partir de ref. [129]).

En la **Figura 6** se muestra un ejemplo de un experimento típico de ITC. Los datos experimentales de la valoración representan potencia (W) frente a tiempo, de forma que se obtienen picos correspondientes a cada una de las adiciones (**Figura 6.A**). El calor absorbido o desprendido tras cada adición de ligando se obtiene del área del pico correspondiente, y puede representarse frente a la relación de concentraciones ligando/macromolécula C_D/C_P (**Figura 6.B**). Mediante el software especializado del equipo se ajustan los modelos de enlace a estos datos experimentales, obteniéndose del área de los picos iniciales el valor de ΔH, y de la pendiente del ajuste la K termodinámica de enlace.

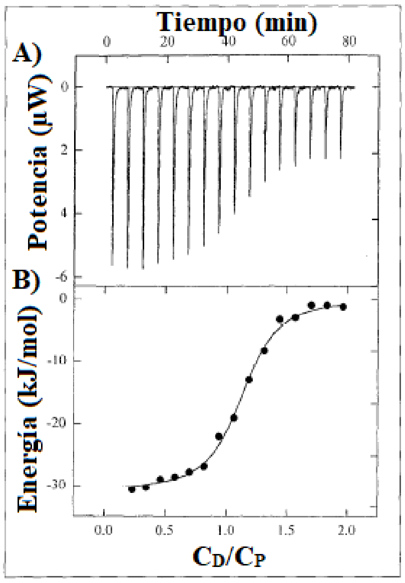

Figura 6. Ejemplo de un experimento típico de ITC obtenido de ref.[129]. **A)** Datos brutos obtenidos para una interacción exotérmica durante la valoración de una macromolécula (P) con un ligando (D). **B)** Isoterma derivada de la integración de los datos brutos a cada relación de concentraciones C_D/C_P.

1.2.5.2. Instrumentación.

Las valoraciones por ITC se realizaron con un Nano ITC (TA Instruments, Newcastle, USA) con celdas de oro de 187 µL. La jeringa de inyección tiene una capacidad de 50 µL y una velocidad de rotación para el mezclado de 250 rpm. Para desgasificar las muestras se emplea una estación de desgasificación (TA Instruments, Newcastle, USA), que también se usa para limpiar el equipo tras cada uso. El software empleado para analizar las valoraciones y obtener los parámetros termodinámicos de enlace es Launch Nanoanalyze 2.0 (TA Instruments, Newcastle, USA).

1.2.5.3. Método Experimental.

Se preparan las disoluciones de polinucleótido y de ligando empleando el mismo disolvente. Este disolvente debe ser una disolución tamponada dado que pequeñas variaciones de pH o fuerza iónica durante la valoración pueden influir notablemente en el calor absorbido o desprendido durante la misma. Tanto la disolución de polinucleótido, que se introduce en la celda de medida con una jeringa Hamilton de 500 µL de volumen, como la de ligando, que se encuentra en la jeringa de inyección de 50 µL, se desgasifican durante 30 min antes de realizar la valoración para evitar la formación de burbujas en las celdas. La celda de referencia se llena con agua ultrapura desgasificada. En un experimento típico, se realizan 50 o 25 inyecciones de 1 o 2 µL del ligando, respectivamente, espaciadas temporalmente entre ellas unos 300 segundos (s). Además, deben realizarse experimentos control en los que se inyecta ligando sobre disolvente, para obtener el calor debido a la dilución del mismo y restarlo al calor de la valoración. Los análisis se realizaron con el software del equipo empleando diferentes modelos de enlace según el sistema estudiado: agregación, un solo modo de enlace o varios modos de enlace. Entre cada experimento se limpia la celda de medida empleando ácido fórmico (10 % v/v), detergente Extran® (MERCK) y finalmente haciendo pasar 2 L de agua ultrapura por la celda.

1.2.6. Calorimetría Diferencial de Barrido (DSC).

1.2.6.1. Fundamento teórico.

La calorimetría diferencial de barrido o DSC (Differential Scanning Calorimetry) es una técnica que permite detectar la cantidad de calor absorbida o liberada por una muestra cuando tiene lugar una transición inducida por una variación de la temperatura. En nuestro caso, esta técnica se ha empleado para estudiar el proceso de desnaturalización térmica del ADN en presencia y ausencia de ligandos que pueden estabilizar o desestabilizar la estructura en doble hélice del mismo, pero es también una técnica muy útil para el estudio de proteínas [130–132].

La desnaturalización térmica del ADN es el proceso por el cual este pierde su estructura secundaria, por ejemplo, la doble o cuádruple hélice de ADN, al producirse un incremento en la temperatura del medio en el que se encuentra. Se trata de un proceso endotérmico en el que los enlaces de hidrógeno establecidos entre las bases nitrogenadas deben romperse. En el caso del ADN en doble hélice, este se desenrolla y separa dando lugar a dos hebras sencillas (**Figura 7**). Se define la temperatura de desnaturalización o de “melting” (T_m) como la temperatura a la cual la fracción entre el ADN nativo y el desnaturalizado es igual a 1. Esta T_m depende de diversos factores, tales como la propia composición del ADN, incrementándose la estabilidad térmica de la doble hélice cuanto mayor es su contenido en pares G-C, debido a la presencia de tres enlaces de hidrógeno que es necesario romper frente a los dos enlaces del par A-T [133,134], o la fuerza iónica del medio [135]. Además, la interacción con ligandos puede afectar sustancialmente a la T_m dependiendo del tipo de interacción establecido, por lo que es un parámetro muy útil en la determinación de la naturaleza del modo de enlace entre un ligando y el ADN. Por ejemplo, los ligandos intercalantes suelen inducir importantes incrementos en la T_m del ADN, debido a la estabilización de la doble hélice por las interacciones de stacking [136].

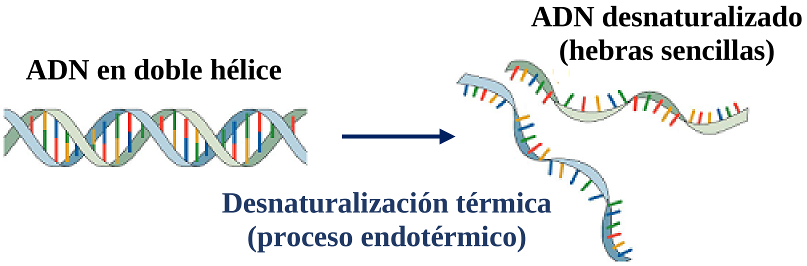

Figura 7. Representación esquemática del proceso de desnaturalización del ADN en doble hélice.

Un calorímetro diferencial de barrido permite medir el intercambio de calor requerido para la desnaturalización del ADN. Para ello, el equipo consta de dos celdas idénticas, una de referencia y otra de medida, integradas en un bloque termostatizado aislante que evita que existan flujos de calor con el exterior (**Figura 8**). En la celda de referencia se encuentra solo el disolvente y en la celda de medida la especie de interés, en nuestro caso ADN, en el mismo disolvente. Entre las dos celdas existe un sensor térmico que determina la diferencia de temperatura entre ambas y cada celda cuenta con un calentador compensatorio. Mediante un sistema termoeléctrico se producen los barridos de temperatura, incrementando o disminuyendo la temperatura dentro del bloque termostatizado a una determinada velocidad (ºC/min). El equipo mide el diferente aporte de calor de los calentadores a la celda de referencia y a la de medida necesario para mantener ambas a la misma temperatura en todo momento. En definitiva, la señal obtenida es un flujo de calor expresado en W (J/s) en función de la temperatura (ºC) a una velocidad de barrido determinada.

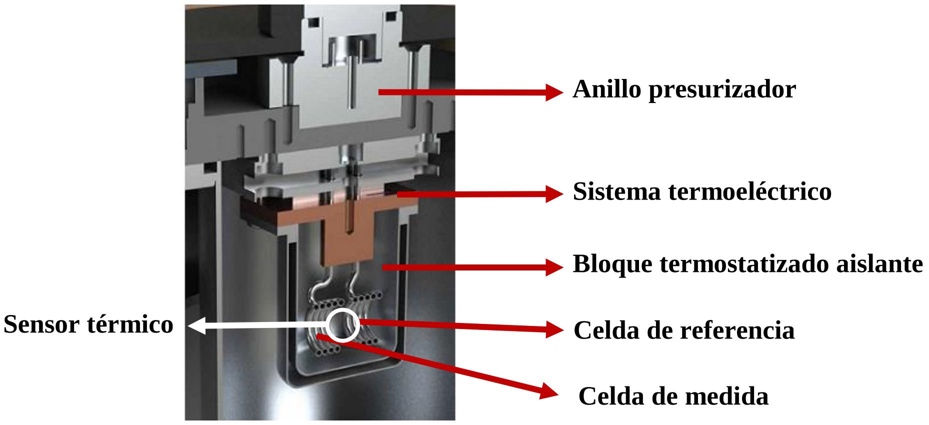
Anillo presurizador
Sistema termoeléctrico
Bloque termostatizado aislante
Sensor térmico
Celda de referencia
Celda de medida

Figura 8. Corte transversal de un equipo Nano DSC para muestras líquidas (imagen original de TA instruments).

Este flujo de calor está directamente relacionado con la capacidad calorífica (C_p) mediante la siguiente expresión [137]:

$$C_p = \text{flujo de calor} \cdot \left(\frac{1}{\text{velocidad de barrido} \cdot C \cdot V} \right) \tag{36}$$

donde C es la concentración molar de biomolécula y V el volumen de disolución en la celda.

A partir de la capacidad calorífica de la transición se pueden determinar otros parámetros termodinámicos como la entalpía, ΔH_{cal}, la entropía, ΔS_{cal}, y la temperatura de desnaturalización, T_m:

$$\Delta H_{cal} = \int_{T_1}^{T_2} C_P \, dT \tag{37}$$

$$\Delta S_{cal} = \int_{T_1}^{T_2} \frac{C_P}{T} \, dT \tag{38}$$

donde T_1 y T_2 son las temperaturas inicial y final de la transición.

Un termograma típico obtenido mediante DSC para una transición como la desnaturalización del ADN se muestra en la **Figura 9**.

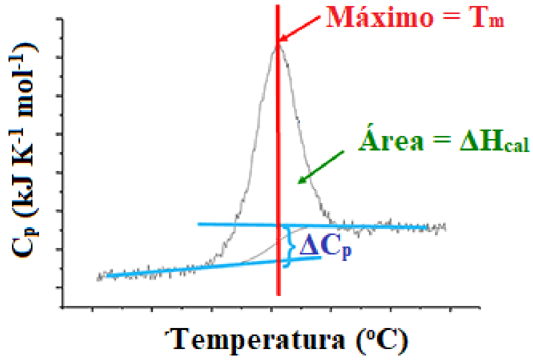

Figura 9. Cálculo de T_m y ΔH_{cal} a partir de un termograma obtenido mediante DSC.

1.2.6.2. Instrumentación.

Las medidas se realizaron en un Nano DSC (TA Instruments, New Castle, USA) diseñado especialmente para el estudio de biomoléculas en disolución. Las celdas capilares de referencia y medida de platino tienen un volumen de 300 µL. El equipo permite trabajar en un rango de temperaturas de entre – 10 y 130 ºC, a velocidades de barrido de entre 0 y 2 ºC/min y presión de entre 0 y 6 atmósferas (atm). La desgasificación de las muestras se realiza en una estación de desgasificación de TA Instruments, que también se emplea para la limpieza del equipo tras cada uso. Para el análisis se empleó el software NanoAnalyze 2.0 (TA Instruments).

1.2.6.3. Método experimental.

Se preparan disoluciones de ctDNA a una concentración determinada solo y en presencia de diferentes concentraciones de ligando. Estas disoluciones de trabajo se introducen en la celda de medida, mientras que en la celda de referencia se introduce el disolvente en el que se hayan preparado dichas disoluciones. Todas las disoluciones se desgasifican previamente durante 30 min para evitar la formación de burbujas en las celdas a lo largo del experimento. En general, los barridos se realizan entre 25 y 110 ºC a P = 3 atm para evitar la ebullición de la muestra y con velocidad de barrido = 1 ºC/min. Es siempre necesario registrar una línea base bajo las mismas condiciones experimentales en la que se introduce solo el disolvente tanto en la celda de referencia como en la de la medida. Esta línea base se resta a los termogramas de las muestras para realizar el análisis de los datos. Tras cada experimento las celdas de medida y de referencia se limpian haciendo pasar 2 L de agua ultrapura por las mismas.

1.2.7. Desnaturalización térmica por FRET.

1.2.7.1. Fundamento teórico.

El fenómeno de transferencia de energía de resonancia de Förster (FRET) puede ser aprovechado para seguir la desnaturalización térmica de distintos tipos de estructuras secundarias de ácidos nucleicos, como veremos a continuación. El proceso FRET consiste en una transferencia de energía entre dos moléculas: una especie dadora y fluorescente (MD) y otra especie aceptora (MA). Este fenómeno puede tener lugar cuando el espectro de emisión de la molécula dadora solapa con el espectro de absorción de la molécula aceptora. Es importante resaltar que el FRET no consiste en la emisión de una radiación por parte de MD que es absorbida por MA (no hay intercambio de fotones), sino que se produce un acoplamiento dipolo-dipolo entre MD y MA gracias al cual se produce la transferencia de energía entre ambos. Este acopamiento es altamente dependiente de la distancia entre MD y MA, requiriéndose generalmente una distancia máxima entre ambos de 50-60 Å [120]. Este es precisamente el factor clave en el que se basa el ensayo de desnaturalización térmica mediante FRET, en el que se emplean oligonucleótidos de determinadas secuencias capaces de formar G-cuádruplex marcados en sus extremos 5’ y 3’ con una molécula MD y una MA, como se representa en la **Figura 10.A**.

Concretamente, la molécula dadora empleada en este trabajo es FAM, un derivado de la fluoresceína, y la aceptora es TAMRA, un derivado de la rodamina [138]. Cuando el oligonucleótido está plegado en forma de G-cuádruplex, sus extremos 5’ y 3’, marcados con FAM y TAMRA, se encuentran próximos entre sí. En estas condiciones, al irradiar la muestra a la λ de excitación del fluoróforo FAM, se produce una transferencia de energía desde FAM a TAMRA, por lo que FAM no presenta emisión. Al incrementarse la temperatura puede producirse la desnaturalización de la G-cuádruplex (**Figura 10.A**), de forma que FAM y TAMRA se alejan entre sí disminuyendo drásticamente el proceso de FRET conforme avanza la desnaturalización. Siguiendo el aumento de la fluorescencia de FAM en función de la temperatura podemos obtener las curvas de desnaturalización térmica o “melting” de la G-cuádruplex, de las que puede obtenerse T_m [139]. Estos ensayos suelen realizarse en Real Time Quantitative PCR (qPCR), que permiten seguir la fluorescencia de 96 disoluciones diferentes simultáneamente empleando pequeñas cantidades de muestra (**Figura 10.B**). Se trata de un método muy útil en el estudio de ligandos de G-cuádruplex, ya que la gran mayoría de ligandos selectivos de estas estructuras inducen un fuerte incremento de su T_m debido a las interacciones de stacking establecidas. Por ello, la diferencia entre la T_m de una G-cuádruplex sola y en presencia de una determinada concentración de ligando (ΔT_m) aporta información sobre la estabilización inducida por dicho ligando [140,141].

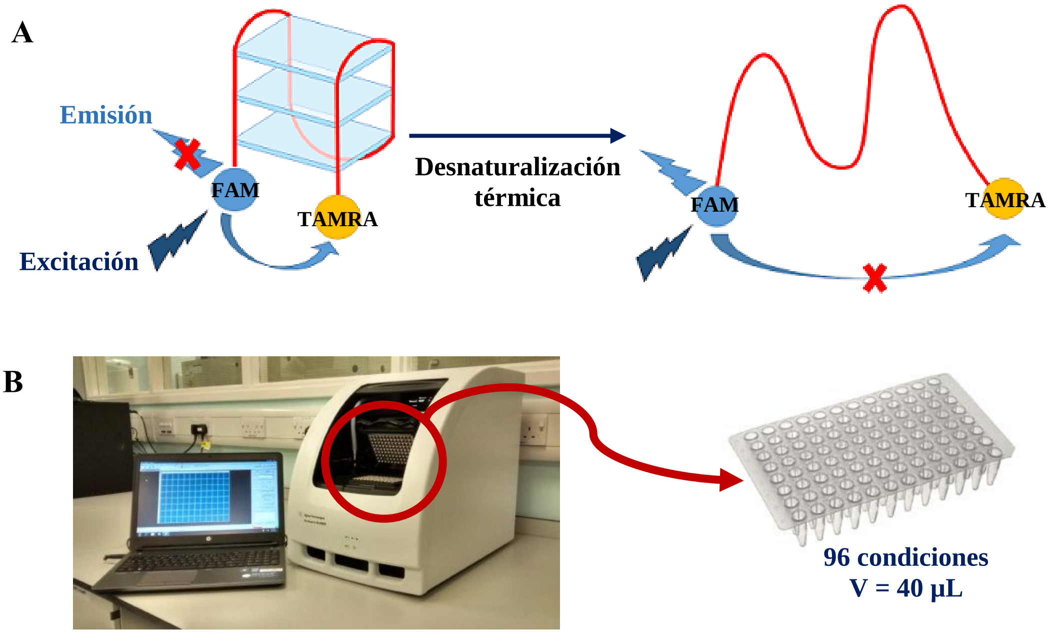

Figura 10. A) Representación esquemática del proceso de desnaturalización de una G-cuádruplex marcada con FAM y TAMRA basada en el fenómeno FRET. **B)** qPCR empleada para realizar los ensayos de desnaturalización por FRET.

1.2.7.2. Instrumentación.

Los ensayos FRET se realizaron en una qPCR Stratagene Mx3005P de Agilent Technologies (**Figura 10.B**) con lámpara halógena de tungsteno como fuente de excitación y tubo fotomultiplicador como detector. La temperatura de la celda se controla mediante un sistema tipo Peltier en un rango que abarca entre 25 y 99 ^{o}C. Para cargar las muestras se emplearon placas de 96 pocillos (30 – 200 µL) aptas para medidas de fluorescencia (Invitrogen Life Science Technologies).

1.2.7.3. Método experimental.

Las disoluciones stock de los oligonucleótidos marcados con FAM y TAMRA en sus extremos 5' y 3' (ver **Tabla 1, Capítulo II**) en agua ultrapura se conservan a - 20 ^{o}C. Entre estos oligonucleótidos se incluye una doble hélice de ADN (ds26) para comprobar la selectividad de los ligandos hacia la G-cuádruplex. Antes de cada ensayo, se preparan disoluciones de concentración 0.4 µM en el disolvente indicado (típicamente 10 mM LiCaC + 90 mM LiCl + 10 mM KCl, pH = 7.4) y se someten a un proceso de templado o "annealing" para que se formen las correspondientes G-cuádruplex. El annealing se realiza en un bloque térmico, manteniendo las disoluciones a 95 ^{o}C durante 5 min y dejando después enfriar lentamente hasta temperatura ambiente a lo largo de 4-5 horas. A continuación se prepararan las disoluciones de trabajo añadiendo el ligando de interés a diferentes concentraciones. Estas disoluciones de trabajo presentan siempre una concentración final de oligonucleótido marcado (G-cuádruplex) de 0.2 µM expresado en moles de moléculas de oligonucleótido, y un volumen de 40 µL. En la qPCR se realiza el barrido de temperatura entre 25 y 95 ^{o}C a una velocidad de barrido de 1 ^{o}C/min recogiendo la fluorescencia de FAM (λ_{exc} = 450 - 495 nm y λ_{em} = 515 - 545 nm) cada 0.5 ^{o}C. Las curvas de desnaturalización, en las que se representa fluorescencia de FAM frente a T, se analizaron con el software Origin 8.5 para obtener T_m a partir del punto de inflexión de la función sigmoide.

1.2.8. Viscosidad.

1.2.8.1. Fundamento teórico.

La medida de la viscosidad de una disolución de ADN es un método hidrodinámico que permite monitorizar cambios en la longitud de la doble hélice de ADN debidos a la interacción con ligandos. De hecho, un parámetro clave de los agentes intercalantes es que provocan el alargamiento de la doble hélice, ya que los pares de bases deben separarse entre sí para alojar la molécula de ligando entre ellos [142]. Este alargamiento de la molécula de ADN provoca un aumento de la viscosidad de la disolución que puede seguirse mediante el uso de un viscosímetro Ubbelodhe (**Figura 11**). La disolución se desplaza por el capilar por gravedad y se mide el tiempo que tarda en pasar desde un punto inicial M_i hasta un punto final M_f.

En el caso de polinucleótidos, los resultados se expresan primero en forma de viscosidad relativa (η/η_0), que se define como:

$$\frac{\eta}{\eta_0} = \frac{t - t_S}{t_0 - t_S} \tag{39}$$

donde t_S es el tiempo de caída del disolvente, t_0 el tiempo de caída del polinucleótido y t el tiempo de caída del polinucleótido con el ligando a una determinada concentración.

Finalmente, la viscosidad relativa se relaciona con la elongación relativa de la molécula de ADN (L/L_0) mediante la siguiente expresión [143]:

$$\frac{L}{L_0} = \sqrt[3]{\frac{\eta}{\eta_0}} \tag{40}$$

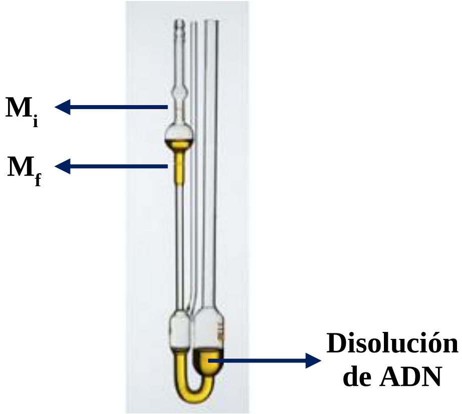

Figura 11. Viscosímetro Ubbelodhe empleado para realizar medidas de viscosidad de disoluciones de ADN en presencia o ausencia del ligando de interés. Para ello se mide el tiempo que la disolución tarda en caer por gravedad desde M_i hasta M_f.

1.2.8.2. Instrumentación.

Se empleó un viscosímetro Ubbelohde (Schott-Instruments, Mainz, Alemania) con una capacidad de volumen entre 2 y 4 mL, inmerso en un baño termostatizado para mantener la temperatura constante a T = 25 ºC. La medida de los tiempos se realiza con un cronómetro manual con precisión de 0.01 s.

1.2.8.3. Método experimental.

Se parte en el viscosímetro de un volumen conocido (en torno a 3 mL) de una disolución de ctDNA de concentración no inferior a 2×10^{-4} M y se mide t_0 por triplicado (ver ec. 39). A continuación se realizan adiciones de una disolución de ligando (el volumen final total no puede sobrepasar los 4 mL), homogeneizando la disolución en cada punto y recogiendo el tiempo t tras cada adición por triplicado. Además, para obtener el valor de t_S, se mide el disolvente en ausencia de polinucleótido y de ligando. Mediante ec. 39 y ec. 40 se calcula la elongación relativa del ADN en cada punto y se representa esta frente a la relación de concentraciones C_D/C_P.

1.2.9. Relajación por salto de temperatura: T-Jump.

1.2.9.1. Fundamento Teórico.

Las técnicas de relajación química fueron implementadas por Manfred Eigen, a quien se concedió el premio Nobel en Química en 1967 por sus estudios de reacciones "extremadamente rápidas" efectuados provocando perturbaciones en el equilibrio por medio de pulsos de energía muy cortos. Estas técnicas se basan en seguir la relajación de un sistema que se encuentra en equilibrio químico tras aplicar una perturbación ejercida por un cambio súbito en alguna de las condiciones claves como la presión (P-Jump), el campo eléctrico (Electric field-Jump) o la temperatura (T-Jump). En este trabajo se ha empleado esta última para estudiar reacciones del orden de microsegundos entre diferentes polinucleótidos (incluyendo doble y cuádruple hélice de ADN) y ligandos. El interés de esta técnica reside en el hecho de que modos de interacción tan relevantes como la intercalación o cambios conformacionales de macromoléculas suelen tener lugar en esta escala de tiempos [144,145].

En la técnica de relajación por salto de temperatura partimos de una disolución de ligando, D, y polinucleótido, P, que en el caso más sencillo se encontrarán en equilibrio con el complejo PD a una temperatura determinada, por ejemplo, T = 22 °C.

$$\mathrm{P + D} \underset{k_d}{\overset{k_f}{\rightleftharpoons}} \mathrm{PD} \tag{41}$$

donde k_f y k_d son las constantes cinéticas de formación y de disociación del complejo PD, respectivamente.

La disolución se encuentra en una celda como la que se muestra en la **Figura 12**. Se realiza una descarga eléctrica de 30 kV entre dos polos de esta celda de forma que, por efecto Joule, se induce en la disolución un incremento de temperatura muy rápido (~ 50 ns), hasta T = 25 °C. El sistema se desplazará hasta alcanzar de nuevo el equilibrio para esta nueva temperatura (siempre y cuando $\Delta H \neq 0$), ya que la constante termodinámica del proceso K depende directamente de la temperatura (ver ec. 35). En definitiva, en disolución se produce una variación de las concentraciones de P, D y PD debido al cambio en el valor de K al haberse modificado la T, y esta variación puede seguirse en el tiempo midiendo parámetros como la absorbancia o la fluorescencia de alguna de estas especies. Así, para unas concentraciones de P y D determinadas, obtendremos una curva cinética en la que se representa Abs a una determinada λ frente al tiempo, de la que puede obtenerse mediante un ajuste por mínimos cuadrados la constante de tiempo $1/\tau$ (s^{-1}). El comportamiento cinético para un mecanismo en una etapa como el representado en ec. 41 se ajusta a la siguiente ecuación:

$$\frac{1}{\tau} = k_d + k_f \cdot \left([P] + [D]\right) \tag{42}$$

De esta forma recogiendo curvas cinéticas a distintas concentraciones de reactivos D y P, podemos representar $1/\tau$ en función de [P] + [D] y obtener los valores de k_f y de k_d de la pendiente y la ordenada, respectivamente. Además, la constante termodinámica del proceso puede calcularse a partir de las constantes cinéticas, ya que $K = k_f/k_d$.

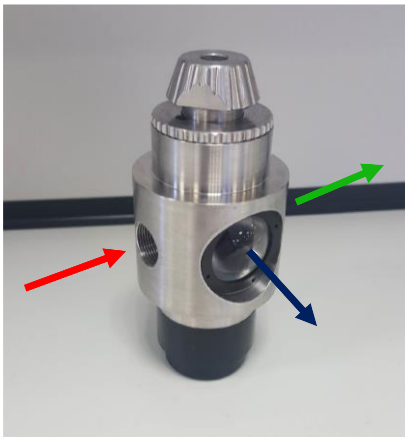

Figura 12. Celda de T-Jump para medidas de absorbancia y de fluorescencia. La luz entra por la ventana pequeña (flecha roja), y se recoge la luz que sale a 90º en el caso de medidas de fluorescencia (flecha azul) y a 180º en el caso de medidas de absorbancia (flecha verde).

1.2.9.2. Instrumentación.

Las medidas cinéticas se llevaron a cabo en un T-Jump construido según el prototipo de Riegler et al [146] y se siguieron siempre por absorción. Como fuente de luz el equipo cuenta con una lámpara de Tungsteno y un detector fotodiodo para las medidas de absorbancia. La celda que contiene la disolución presenta dos electrodos de oro a través de los cuales se transmite la descarga eléctrica, que se realiza con un condensador que genera una descarga de 30 kV elevando la temperatura desde T = 22 ºC a T = 25 ºC. El camino óptico de la misma es de 1 cm. El control de temperatura se lleva a cabo mediante un baño Julabo con precisión ± 0.1 ºC. Los cambios de absorbancia en la disolución se traducen en señales eléctricas que son recogidas por un osciloscopio Agilent 54622A (Santa Clara, CA) y transferidas a un ordenador. El análisis de las curvas cinéticas se realiza con el programa Table Curve del software Jandel Scientific (AISN software, Richmond, CA).

1.2.9.3. Procedimiento experimental.

En la celda se introduce una disolución que contiene concentraciones conocidas del polinucleótido y del ligando. Es muy importante no emplear nunca disolventes con fuerzas iónicas menores a 0.01 M, dado que el paso de la corriente a través de la disolución cuando se produce la descarga eléctrica requiere de la presencia de iones en el medio. Para cada disolución estudiada (que se corresponderán con determinados valores de [P] + [D]) se acumulan entre 6 y 10 curvas de relajación, esperando 10 min entre ellas para dejar que el sistema regrese a la temperatura inicial. Las curvas cinéticas obtenidas se analizaron mediante un ajuste no lineal de mínimos cuadrados para obtener la constante cinética $1/\tau$ en cada punto. A partir de estos datos y mediante ec. 42 se obtienen las constantes cinéticas k_f y k_d y la constante termodinámica K.

2. Metodología Biológica.

2.1. Electroforesis.

La electroforesis es una técnica ampliamente utilizada en el campo de la biología molecular que permite la separación de biomoléculas en función de su tamaño, carga y conformación, al hacerlas atravesar una matriz porosa empleando una corriente eléctrica controlada [147]. Existen distintos tipos de electroforesis, y a continuación se explican las dos modalidades que se han empleado en este trabajo: la electroforesis horizontal de agarosa y la electroforesis vertical de acrilamida.

2.1.1. Electroforesis horizontal de agarosa.

En este trabajo se ha empleado la electroforesis horizontal para la separación y visualización de las bandas de ADN plasmídico (pUC18) en presencia y ausencia de determinados ligandos. La instrumentación requerida para este tipo de electroforesis aparece representada en la **Figura 13.A** y consiste en una cuba electroforética horizontal con un ánodo (polo positivo) en uno de sus extremos y un cátodo (polo negativo) en el otro. En la cuba se sitúa la matriz porosa, en este caso un gel de agarosa, inmersa en tampón electroforético. Mediante una fuente de alimentación externa se aplica una diferencia de potencial entre ambos electrodos de forma que las moléculas negativamente cargadas, como es el caso del ADN a pH ≈ 7, que se encuentren en el gel, migrarán hacia el polo positivo o ánodo. Para una determinada diferencia de potencial aplicada en voltios (V) entre los electrodos separados una determinada distancia (cm), la velocidad de migración de la molécula de ADN dentro de la matriz porosa dependerá de su tamaño, su conformación y su carga neta.

El ADN plasmídico puede existir en tres conformaciones distintas que pueden separarse y visualizarse como bandas aisladas tras la electroforesis (**Figura 13.B**): "supercoiled" (SC), "open-circular" (OC) y "linear" (L) [148]. En ocasiones puede aparecer una cuarta banda cuando la lisis alcalina en el proceso de extracción del plásmido ha durado más tiempo del debido: "circular single-stranded" (CSS). El plásmido en su forma nativa se encuentra mayoritariamente en forma de supercoiled, por lo que es la banda más intensa. En esta conformación el plásmido es una doble cadena circular enrollada sobre sí misma (ver **Figura 13.B**), y migra más rápido que las formas L y OC. En la forma OC se ha producido un corte en una de las hebras de la doble cadena, por lo que aunque el plásmido mantiene la topología circular, pierde el superenrollamiento de la forma SC. Cuando el corte se produce en el mismo punto en las dos hebras de la doble cadena, se pierde la topología circular y el plásmido pasa a ser lineal (L). Las formas OC y L migran más lento que la forma SC.

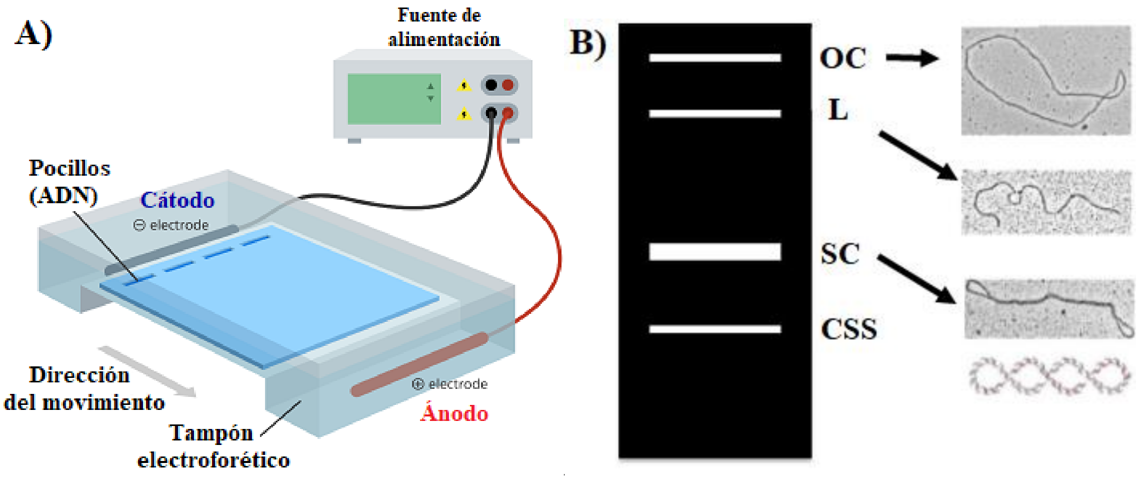

Figura 13. A) Ilustración del equipo de electroforesis horizontal empleado para separación de ADN (imagen adaptada a partir de original de Genome Research Limited). **B)** Representación del orden en el que aparecen las bandas de ADN plasmídico en una electroforesis horizontal (este orden puede variar dependiendo del tampón electroforético empleado) junto con imágenes TEM del plásmido en cada una de las conformaciones descritas.

La interacción de ligandos con el ADN plasmídico puede originar importantes cambios tanto en la movilidad como en la intensidad de las bandas, por lo que es una técnica muy útil para determinar o descartar determinados modos de enlace [123,149]. Por ejemplo, el enlace covalente del cisplatino aumenta la movilidad de la forma OC debido a la compactación inducida por el cross-linking [150].

2.1.1.1.Procedimiento experimental.

El plásmido pUC18 a una concentración de 10-15 µM (expresada en pares de bases) se incuba con diferentes concentraciones de ligando durante un tiempo indicado. Es necesario incluir una muestra control con el plásmido solo y una muestra con el control del vehículo (DMSO) a la máxima concentración empleada en el experimento. El gel de agarosa al 1 % se prepara en el momento de realizar el ensayo añadiendo 1 g de agarosa en 100 mL del tampón electroforético que se vaya a emplear, en nuestro caso TBE x1, y se calienta para facilitar la disolución de la agarosa. Como agente de tinción para revelar las bandas de ADN se emplea bromuro de etidio (EB), que se añade cuando la agarosa está totalmente solubilizada de forma que su concentración final en el gel es 0.05 µg/ml. Este gel se sumerge en TBE en la cuba electroforética y se cargan las muestras (10 µL por pocillo). En un experimento típico se aplica un campo de 5-6 V/cm durante 2 h para una buena separación de las bandas. El gel se visualiza mediante un sistema de imagen Gel Doc XR+ (Bio-Rad Laboratories, Inc., California, USA).

2.1.2. Electroforesis vertical de poliacrilamida (PAGE).

El principio fundamental de la electroforesis vertical es el mismo que el de la horizontal: las macromoléculas cargadas se hacen pasar por una matriz porosa estableciendo una diferencia de potencial entre dos polos. En este caso el gel se sitúa en una cuba vertical como la que se representa en la **Figura 14**. Sin embargo, la principal diferencia entre ambos tipos de electroforesis no reside en la orientación del gel, sino en su composición [151]. En general, para la separación de grandes moléculas de ADN hasta 25 kb (kilobases), como es el caso de plásmidos, se emplea la electroforesis horizontal de agarosa, que presenta un tamaño de poro relativamente grande. Por el contrario, la electroforesis vertical de acrilamida presenta un tamaño de poro mucho menor, por lo que es la técnica óptima cuando necesitamos una mayor resolución con el fin de separar pequeños fragmentos de ADN de hasta 500 bases, como pueden ser oligonucleótidos. Además, es la técnica empleada para la separación de proteínas, ya sea en forma desnaturalizante (SDS-PAGE) o nativa (native-PAGE) [152,153].

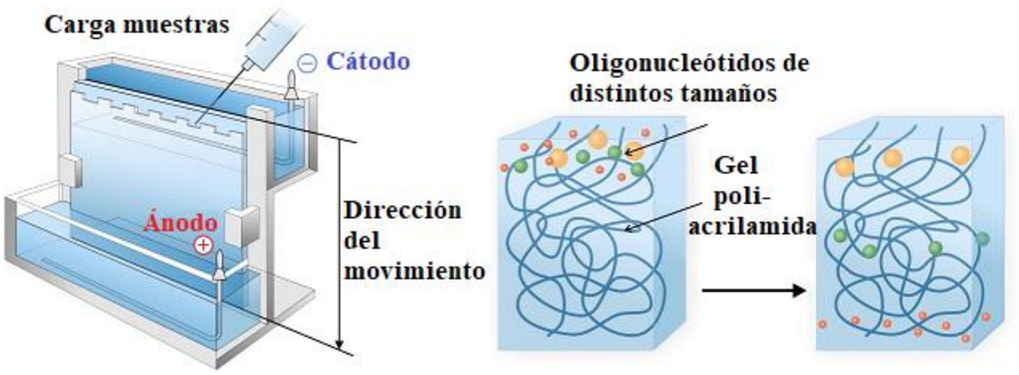

Figura 14. Ilustración del equipo de electroforesis vertical empleado para separar oligonucleótidos de pequeño tamaño (también empleado para separación de proteínas).

A continuación se explican las dos modalidades de electroforesis vertical de acrilamida que se han empleado en este trabajo: electroforesis desnaturalizante para el análisis de oligonucleótidos de ADN y electroforesis nativa para el análisis de la conformación de proteínas.

2.1.2.1. Electroforesis desnaturalizante: separación de oligonucleótidos.

En determinados ensayos no queremos separar macromoléculas en función de su conformación o su carga, sino exclusivamente en función de su tamaño. Por ejemplo, a la hora de determinar la longitud de un oligonucleótido de una sola hebra, es necesario que la única variable que afecte a su movilidad electroforética sea el número de bases nitrogenadas que lo componen, y no las estructuras secundarias que puedan formar [154]. En estos casos se recurre al uso de agentes desnaturalizantes, comúnmente urea o formamida, que impiden la formación de enlaces de hidrógeno entre las bases del ADN y, por tanto, el establecimiento de estructuras secundarias [155].

El porcentaje de acrilamida en los geles determina el tamaño de poro: a mayor concentración de acrilamida menor será el tamaño de poro medio. Teniendo en cuenta el tamaño de los oligonucleótidos a separar en este trabajo, se prepararon geles al 20 % de acrilamida y una concentración 7 M de urea para mantener las condiciones desnaturalizantes. Los geles se preparan el día anterior al ensayo y se conservaban a 4 ºC con alta humedad. Como tampón electroforético se emplea TBE. En este tipo de electroforesis es necesario precorrer el gel durante 30 min (20 V/cm) y después homogeneizar los pocillos con TBE antes de introducir las muestras. Una vez cargadas estas en el gel, se aplica un potencial de 20 V/cm durante 90 min. En nuestro caso, los oligonucleótidos de interés estaban marcados en uno de sus extremos con un fluoróforo (FAM) como se explica en el **apartado 2.2, Capítulo II**, por lo que la visualización de las bandas se realizó de forma directa sin necesidad de tinción en un lector de geles con detección por fluorescencia.

2.1.2.2. Electroforesis nativa de proteínas.

La electroforesis nativa de proteínas emplea condiciones no reductoras y no desnaturalizantes, de forma que se mantiene la estructura secundaria de la proteína y su densidad de carga nativa al pH de trabajo. Muchas de las proteínas empleadas como modelos en biología molecular, como son la seroalbúmina humana (HSA) o bovina (BSA), presentan puntos isoeléctricos (pI) ácidos o ligeramente básicos [156], entre 3 y 8, por lo que al pH de trabajo (pH ~ 8.3) se encuentran negativamente cargadas y migran hacia el ánodo. Si la proteína de interés presentara un pI mayor que el pH de trabajo sería necesario invertir los polos, ya que migraría hacia el cátodo.

Dado que en la electroforesis nativa la movilidad depende no solo del tamaño, sino también de la conformación y carga de la proteína, es necesario encontrar las condiciones experimentales óptimas para cada proteína. En este trabajo se ha empleado la BSA como modelo para estudiar la interacción de seroalbúminas con ligandos [115] y el protocolo empleado es una adaptación de un método que se encuentra en la bibliografía [157]. Tras realizar pruebas a distintas concentraciones de acrilamida y a distintos tiempos y potenciales aplicados, se seleccionaron las siguientes condiciones: los geles se prepararon al 10 % de acrilamida y la electroforesis se realizó con un sistema de refrigeración (~ 4 ºC) para evitar procesos de desnaturalización por calentamiento, aplicando un potencial de 8 V/cm durante 4 h. Después, los geles se tiñeron con Coumassi Brilliant Blue R-250 y se visualizaron con un sistema Gel Doc XR+ Imaging System (Bio-Rad Laboratories, Inc., California, USA).

2.2. Polymerase Stop Assay (PSA).

El ensayo PSA se realizó durante la estancia predoctoral en el Imperial College London para estudiar la capacidad de una familia de complejos metálicos de inhibir la actividad de una enzima polimerasa de ADN mediante la estabilización de una

G-cuádruplex que impidiera dicha actividad. Este nuevo método es una modificación del descrito inicialmente por Salazar et al [158].

Para el ensayo se diseñó un oligonucleótido que llamamos molde o "Template" de 65 deoxinucleótidos (es decir, "65-mer"), que contiene una secuencia de interés capaz de formar una estructura en G-cuádruplex, en nuestro caso c-Myc [159]. En la **Figura 15** se ilustra el diseño y secuencia de este Template. Comenzando desde el extremo 3', primero se introduce una **secuencia complementaria** a otro oligonucleótido llamado "**Primer**" (22-mer) y que está marcado con el fluoróforo FAM. Tras esta secuencia se introduce un "**linker**", cuya función es separar espacialmente la secuencia complementaria al Primer de la secuencia capaz de formar G-cuádruplex: **c-Myc**. Finalmente, tras la secuencia c-Myc se añade una **cola.**

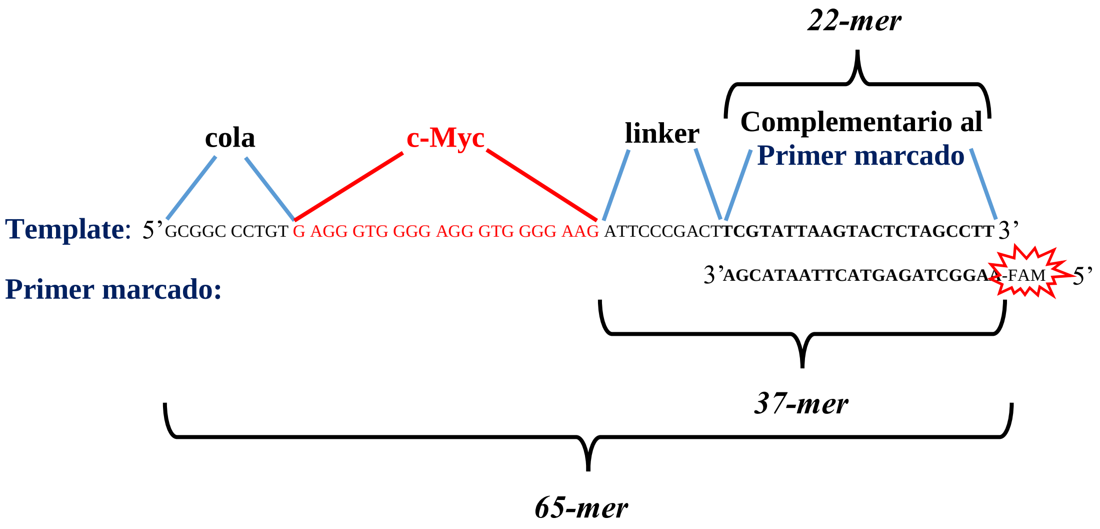
22-mer
cola
c-Myc
linker
Complementario al Primer marcado
Template: 5'GCGGC CCTGT G AGG GTG GGG AGG GTG GGG AAG ATTCCCGACTTCGTATTAAGTACTCTAGCCTT 3'
Primer marcado:
3'AGCATAATTCATGAGATCGGAA-FAM 5'
37-mer
65-mer

Figura 15. Secuencia del Template y del Primer marcado con FAM empleados para el PSA.

En este ensayo se emplea una *Taq* polimerasa de ADN, una enzima capaz de sintetizar ADN en dirección 5' → 3'generando una hebra complementaria a la hebra molde o Template [160]. Fijándonos en la **Figura 15**, el Primer marcado con FAM estará hibridado al Template formando una doble cadena. La *Taq* polimerasa reconocerá esta región de doble cadena y en las condiciones adecuadas (temperatura, disponibilidad de desoxirribonucleótidos, etc.) comenzará a sintetizar ADN complementario al Template en el Primer marcado en dirección 5' → 3'. Si la enzima no encuentra ningún obstáculo, obtendremos una secuencia complementaria al Template completa, es decir, 65-mer, marcada con FAM en su extremo 5'. Sin embargo, si en la región que coincide con la secuencia c-Myc se ha formado una G-cuádruplex estable, debido por ejemplo a la presencia de un ligando que la estabiliza, la enzima no será capaz de seguir avanzando por esta región y la síntesis de ADN se detendrá tras el linker, obteniéndose una secuencia 37-mer.

Para determinar si la *Taq* polimerasa ha conseguido sintetizar el producto 65-mer al completo o, por el contrario, ha habido parada al llegar a la G-cuádruplex obteniéndose el producto de pausa 37-mer, se emplea la electroforesis vertical desnaturalizante (ver

apartado 2.1.2.1, Capítulo II). En la **Figura 16** se muestra un ejemplo de un experimento de PSA realizado en presencia de diferentes concentraciones de uno de los complejos metálicos sintetizados por el grupo del profesor R. Vilar y estudiados en este trabajo, capaz de estabilizar la G-cuádruplex de forma muy efectiva, como veremos en el **Capítulo VIII**. Tras la electroforesis visualizamos el gel por fluorescencia aprovechando que el Primer estaba marcado con FAM, de forma que podemos determinar su longitud. A mayor longitud menor movilidad, por lo que la banda del 65-mer es la que menos avanza y la 22-mer, correspondiente al primer inicial, la que más avanza. Entre ambas aparece el producto 37-mer si ha habido parada y, además, la intensidad de la banda está directamente relacionada con la concentración de producto. Así, en la primera calle se encuentra el control negativo, en el que no hay ningún tipo de especie estabilizante de G-cuádruplex, de forma que se obtienen únicamente las bandas correspondientes al primer inicial 22-mer (se añade en exceso por lo que esta banda aparece en todas las calles) y al producto completo 65-mer. Podemos observar cómo al ir añadiendo concentraciones cada vez mayores de complejo metálico comienza a aparecer la banda del 37-mer, debido a que la enzima no ha podido ejecutar la síntesis de ADN completa al estabilizarse la G-cuádruplex por acción del complejo. Como control positivo, en la última calle se añade una elevada concentración de K^{+}, capaz de estabilizar eficientemente la G-cuádruplex de c-Myc, con lo que también se obtiene el producto de pausa 37-mer. La intensidad de la banda del producto 37-mer se puede representar frente a la concentración de complejo y obtener la concentración a la cual la actividad de la enzima está inhibida al 50 % (EC$_{50}$). De esta forma podemos estudiar la influencia de un ligando en la actividad biológica de una enzima polimerasa de ADN en una secuencia con potencial para formar estructuras en G-cuádruplex.

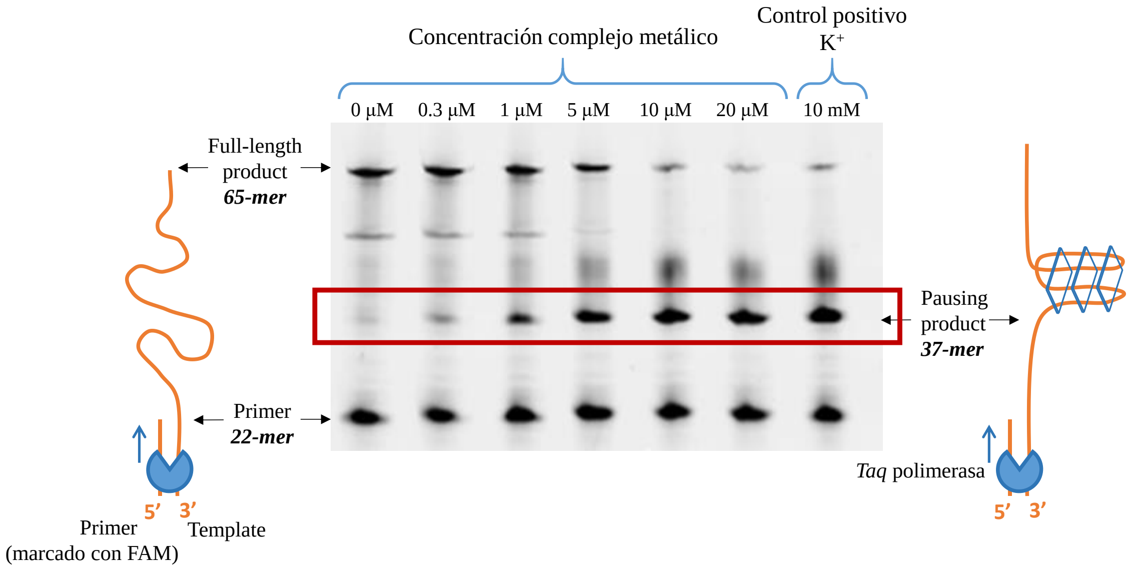

Figura 16. PSA realizado con un complejo metálico capaz de estabilizar estructuras en G-cuádruplex. En el gel se detecta el primer marcado con FAM.

Se realizan además experimentos adicionales para tener la certeza de que la parada de la síntesis de ADN se produce por la presencia de la G-cuádruplex en la secuencia c-Myc, y no debido a otros procesos como puede ser el envenenamiento de la propia enzima al aumentar la concentración de complejo. Para ello se introdujo una mutación en el Template, sustituyendo dos residuos de G de la región c-Myc, necesarios para la formación de la G-cuádruplex, por dos residuos de A. En este caso no se producía parada de la síntesis con ninguna de las concentraciones de complejo testadas, por lo que puede concluirse que la parada se debía exclusivamente a la formación de la G-cuádruplex.

2.2.1. Procedimiento experimental.

Los oligonucleótidos correspondientes al Template y al Primer marcado con FAM se encargaron a Eurogentec (Seraing, Bélgica). Las disoluciones con ambos oligonucleótidos a concentración 1 µM y diferentes concentraciones (0 – 20 µM) de los complejos metálicos se someten a un proceso de annealing a 95 ºC durante 5 min en tampón Tris-HCl (10 mM LiCl, 50 mM Tris-HCl, pH = 7.4). Para el control positivo se sustituye el LiCl del tampón por KCl. Tras dejar enfriar hasta temperatura ambiente las disoluciones, se realizan los ensayos de PSA en *Taq* buffer x1. Las disoluciones de trabajo finales contienen la mezcla de oligonucleótidos anteriormente descrita (0.2 µM), deoxinucleótidos dNTPs (0.2 mM), $MgCl_2$ (1.25 mM) y *Taq* polimerasa (2.5 U). La amplificación se lleva a cabo a 37 ºC durante 30 min, tras lo cual se detiene la reacción mediante la adición de un volumen igual al de la disolución de trabajo de buffer de parada (90 % formamida, 10 mM NaOH). Los productos se analizan por electroforesis vertical desnaturalizante en geles al 20 % de acrilamida en tampón TBE (20 V/cm, 90 min) y se visualizan en un lector de geles de fluorescencia (canal FAM). Para cuantificar la intensidad de las bandas del producto de parada 37-mer se emplea el software GelAnalyzer 2010a.

2.3. Cultivo celular.

En este trabajo se han empleado varias líneas celulares humanas adherentes, entre las que destacan las líneas de adenocarcinoma de pulmón (A549) y colorrectal (SW480). El cultivo se realiza en frascos de cultivo especiales para células adherentes (VWR) y acorde a los estándares de la ATCC (American Type Culture Collection). El medio empleado es DMEM (Dulbecco's Modified Eagle's medium) suplementado con 10 % (v/v) de FBS (Suero Bovino Fetal) y 1 % (v/v) de antibiótico (Penicilina - Estreptomicina), salvo en casos concretos en los que se indique el uso de otro medio. Para subcultivar, se retira el medio de los frascos y se realizan dos lavados con PBS (tampón fosfato salino). Las células se levantan con disolución Tripsina-EDTA (T4174, Sigma Aldrich), se resuspenden en medio de cultivo y se siembran en nuevos frascos con diluciones 1:5 ò 1:10, de forma que se mantiene siempre una confluencia inferior a 80-90 %. Las condiciones de incubación son alta humedad, T = 37 ºC y 5 % CO_2. Todos los componentes del medio mencionados fueron suministrados por Sigma Aldrich.

2.4. Citotoxicidad: ensayo MTT.

La citotoxicidad de un compuesto puede ser determinada mediante el ensayo colorimétrico del MTT, el cual permite estimar la viabilidad celular de forma indirecta mediante medidas espectrofotométricas de absorción [161]. Este ensayo se basa en la reducción de una sal de MTT (methyl-thiazole-tetrazolium) para dar cristales azules de formazan, los cuales son insolubles en el medio de cultivo. Esta reducción se produce debido a la actividad deshidrogenasa en mitocondrias activas y, por tanto, la cantidad de formazan generado es directamente proporcional al número de células vivas metabólicamente activas. Los cristales de formazan generados se disuelven mediante una disolución solubilizadora para poder leer la absorbancia del formazan ($\lambda_{\text{máx}}$ = 590 nm), y la concentración de compuesto que inhibe la proliferación celular al 50 % (IC_{50}) se determina como se explica a continuación.

2.4.1. Procedimiento experimental.

Las células se siembran en placas de 96 pocillos a razón de 5-10 × 10^3 células por pocillo dependiendo del tipo celular y se incuban durante 24 h a 37 ºC y 5 % CO_2. Después se retira el medio, se sustituye por 100 µL de medio fresco con diferentes concentraciones del compuesto a testar y se incuba durante 24 h más. Se retira el tratamiento, se añaden 100 µL de MTT de concentración 0.5 mg/mL y se incuba durante 4 h. Finalmente, se añaden 100 µL de disolución solubilizadora (10 % SDS, 0.01 M HCl) por pocillo y se mantiene a 37 ºC toda la noche para facilitar la solubilización de los cristales de formazan.

La absorbancia de cada pocillo a λ = 590 nm se midió en un lector de placas CLARIOstar® BMG (Labtech) en los ensayos realizados durante la estancia predoctoral en el CiMUS (Santiago de Compostela) y en un Cytation 5 Imaging Reader (BioTEK) en los ensayos realizados en la Universidad de Burgos. La absorbancia se relaciona con la supervivencia celular según la expresión:

$$\%\ \text{supervivencia} = \left(\frac{\text{Abs}_{\text{trat}} - \text{Abs}_{\text{medio}}}{\text{Abs}_{\text{control}} - \text{Abs}_{\text{medio}}} \right) \times 100 \tag{43}$$

donde $\text{Abs}_{\text{medio}}$ es la absorbancia del medio solo, Abs_{trat} la absorbancia a una determinada concentración de compuesto y $\text{Abs}_{\text{control}}$ la absorbancia del control negativo en ausencia de compuesto.

Con estos datos se obtienen las curvas de supervivencia celular (% supervivencia en función de la concentración de compuesto), de las que se calcula el valor de IC_{50} (concentración de compuesto que inhibe la proliferación celular al 50 %) mediante el software GraphPad Prism 6.07. Para obtener los valores del IC_{50} se realizan al menos tres experimentos independientes con cuadriplicados para cada condición testada.

2.5. Captación celular mediante ICP-MS.

Las drogas que actúan como agentes terapéuticos o diagnósticos deben ser capaces de alcanzar su diana en la célula para poder ser efectivas. Estos agentes pueden ser captados por las células a través de diferentes mecanismos, incluyendo difusión pasiva o a través de transportadores de membrana [162]. En el caso de los complejos metálicos, la cuantificación de metal que entra en las células tras un determinado periodo de incubación puede realizarse de forma sencilla mediante ICP-MS (espectrometría masas por plasma acoplado inductivamente) [163,164].

2.5.1. Procedimiento experimental.

Se siembran 1.5×10^5 células por pocillo en 1 mL de medio en placas de 6 pocillos y se incuban durante 24 h a 37 ºC y 5 % CO_2. Después se retira el medio, se añade medio fresco con el complejo metálico a la concentración indicada y se incuba durante un periodo de 4 h. En el ensayo se incluyen controles negativos (células sin tratamiento) y controles positivos (células tratadas con cisplatino). A continuación se retira el tratamiento y las células se lavan dos veces con PBS, tras lo cual se levantan empleando tripsina-EDTA y se recogen en 1 mL de PBS. El número de células recogidas en cada muestra se determina mediante contaje en cámara Neubauer y se realiza una digestión ácida con HNO_3 al 2 % (v/v) para ser analizadas mediante ICP-MS. De este análisis se obtiene la cantidad total de metal presente en cada muestra, y los resultados finales se expresan como cantidad de metal (expresada en gramos o moles) en 1×10^6 células.

2.6. Microscopía Confocal de Fluorescencia.

La microscopía confocal de fluorescencia es una potente técnica de visualización que presenta una serie de ventajas con respecto de la microscopía óptica de fluorescencia (“wide-field”) convencional [165]. En la **Figura 17** aparecen ilustradas las principales diferencias entre un microscopio de fluorescencia “wide-field” y un microscopio confocal. En el primero, una muestra (por ejemplo, una monocapa de células) se ilumina mediante una fuente de luz, típicamente de Xenon, con un sistema de filtros para seleccionar un rango de longitudes de onda de excitación, y se recoge la fluorescencia emitida por la muestra de un plano de la misma relativamente grande (ver **Figura 17.A**). Por el contrario, un microscopio confocal permite visualizar la luz emitida solo de un pequeño plano al introducir un “pin hole” antes del detector, evitando recoger todo el conjunto de la luz emitida por la muestra (**Figura 17.B**). Esto permite obtener imágenes con mucha mayor resolución, como se ejemplifica en la **Figura 18**, donde podemos observar la diferencia entre la resolución de ambos tipos de microscopía. Además, la longitud de onda de excitación en un microscopio confocal se selecciona mediante un monocromador en lugar de mediante un sistema de filtros, lo cual permite evitar fenómenos de solapamiento entre varias sondas fluorescentes.

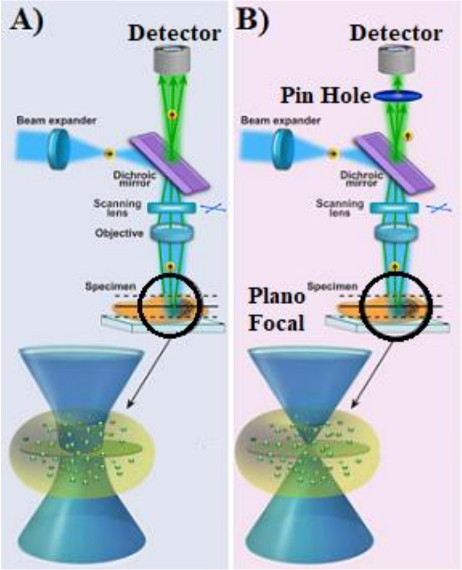
A)
Detector
Beam expander
Dichroic mirror
Scanning lens
Objective
Specimen
B)
Detector
Pin Hole
Beam expander
Dichroic mirror
Scanning lens
Plano Focal
Specimen

Figura 17. Ilustración del funcionamiento de un microscopio óptico de fluorescencia convencional (**A**) y un microscopio confocal (**B**). Adaptado de ref. [165].

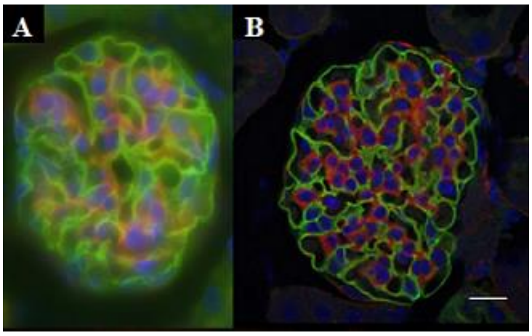

Figura 18. Comparación de la resolución de imágenes tomadas mediante microscopía óptica (**A**) y microscopía confocal (**B**). A y B son imágenes de tejido de riñón de ratón teñidos con DAPI (azul, núcleo), Alexa 488 (verde, membrana) y Alexa 568 (rojo, filamentos de actina). Barra de escala = 20 µM. De ref. [166].

2.6.1. Ensayos de colocalización celular.

La microscopía confocal de fluorescencia se empleó durante la estancia predoctoral en el CiMUS (Santiago de Compostela) para realizar ensayos de colocalización celular. En estos ensayos se emplean sondas fluorescentes comerciales que son capaces de acumularse selectivamente en determinados orgánulos celulares. De esta forma, si un compuesto de interés presenta propiedades de emisión, puede estudiarse su localización celular mediante co-tinción con este tipo de sondas [167,168]. En concreto, se empleó TMRM (Tetrametilrodamina, T668, Thermo Fisher Scientific) para tinción selectiva de mitocondria y LysoTracker™ Red DND-99 (L7528, Thermo Fisher Scientific) para tinción selectiva de lisosomas. Ambas sondas presentan emisión en el rojo (λ_{em} ~ 650 nm).

En cuanto al procedimiento experimental, las células se siembran 24 h antes del tratamiento en placas Petri de 35 mm (1.2×10^5 células por placa) con fondo de vidrio especiales para microscopía (MatTek Corporation, Massachusetts, USA). Después, se incuban durante 30 min con TMRM (100 nM) para colocalización con mitocondria o bien con Lysotracker (75 nM) para colocalización con lisosoma. A continuación se retira el medio con las sondas, se tratan con el compuesto fluorescente de interés y se incuba otros 30 min. Finalmente, se retira el tratamiento, se realizan dos lavados con PBS y se añade medio de cultivo fresco (DMEM) sin rojo de fenol para evitar interferencias en las medidas de fluorescencia. En este trabajo se empleó un microscopio láser confocal (TCS-SP2, Leica, Heidelberg, Alemania) para registrar los diferentes canales de fluorescencia: el complejo metálico estudiado emitía en el verde y las sondas selectivas de mitocondria y lisosoma en el rojo. El grado de colocalización se determina cuantitativamente empleando el software procesador de imágenes Fiji para calcular el factor de correlación de Pearson (PCC) [168]. El valor del PCC puede variar entre 0 y 1, siendo valores cercanos a 1 indicativos de alto grado de colocalización.

2.7. Microscopía Time-Lapse.

La microscopía Time-Lapse permite recoger imágenes de células vivas en cultivo a lo largo de tiempos largos (horas o incluso días) para seguir su evolución frente a determinadas perturbaciones, como puede ser el tratamiento con un compuesto de interés. Un microscopio Time-Lapse, como el que aparece en la **Figura 19**, podría definirse como un microscopio de fluorescencia que lleva acoplado un sistema de incubación, el cual permite mantener condiciones de alta humedad, T = 37 ºC y atmósfera de 5 % CO_2.

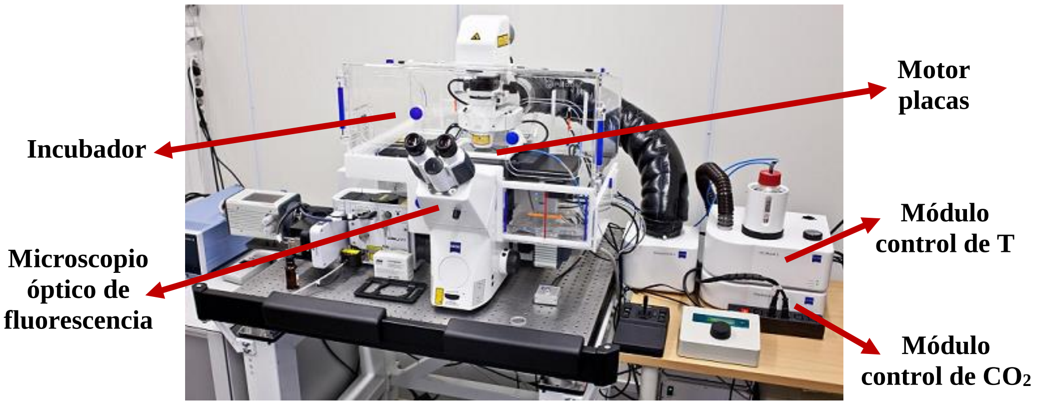

Figura 19. Equipo para microscopía Time-Lapse (imagen original de Zeiss International Corporation).

En el equipo pueden incubarse placas de varios pocillos, y recoger imágenes de todos ellos en un punto determinado gracias al motor que lleva incorporado, junto con un software que permite guardar las coordenadas exactas en los ejes X e Y de todos los campos seleccionados. Así pueden monitorizarse en un mismo ensayo un elevado número de condiciones diferentes (controles, tratamientos, etc.).

2.7.1. Activación de caspasas.

La microscopía de fluorescencia Time-Lapse se empleó durante la estancia en el CiMUS para monitorizar la activación de caspasas, mediadores esenciales en el proceso de apoptosis [169,170], inducida por el tratamiento con determinados compuestos. Para ello se emplea el reactivo comercial CellEvent Caspase-3/7 Green Detection Reagent (C10423, Thermo Fisher Scientific), que es una sonda que contiene el péptido DEVD, el cual impide su enlace al ADN celular. Cuando tiene lugar la activación de caspasa 3 o caspasa 7 en células apoptóticas, el péptido DEVD queda secuestrado y se separa de la sonda. Esta queda libre entonces para unirse al ADN formando un complejo fluorescente que emite en el verde, por lo que detectamos un “flash” de emisión verde desde el núcleo celular tras producirse la activación de caspasa 3 ò 7.

Para realizar estos ensayos se siembran 2×10^4 células por pocillo en placas de 24 pocillos y se dejan incubar 24 h. Las células se tiñen después con el reactivo CellEvent Caspase-3/7 Green Detection Reagent (8 µM) y se tratan con los compuestos a estudiar. Se monitorizan cada una de las condiciones durante 24 h, tomando imágenes en los canales de fluorescencia en el verde y en contraste de fases cada 30 o 45 min, manteniendo siempre T = 37 ºC y 5 % CO_2. El equipo empleado fue un Wide Field Okolab DMI600B, con cámara DFC360FX con un controlador CTR7000HS (Leica Microsystems) y software LAS AF (Leica).

Como ejemplo de estos ensayos, en la **Figura 20** se encuentran códigos QR que dan acceso, mediante cualquier aplicación móvil de lector de códigos QR, a vídeos Time-Lapse obtenidos para un control (células A549 sin tratamiento) y tras aplicar un tratamiento con un compuesto capaz de inducir apoptosis.

A

B

Figura 20. Códigos QR para acceder a los vídeos obtenidos mediante microscopía Time-Lapse durante 24 h de células A549 teñidas con el reactivo CellEvent Caspase-3/7 Green Detection Reagent en ausencia de tratamiento (**A**) y tratadas con 5 µM del compuesto **[Rh-b]Cl** estudiado en el **Capítulo IX** (**B**).

2.8. Citometría de flujo.

La citometría es el proceso en el que se miden determinadas características físicas y/o químicas de células individuales [171]. Un citómetro de flujo es un instrumento que ilumina las células (u otro tipo de partículas de interés) de forma individual con una fuente de luz láser según atraviesan un capilar y recoge la señal lumínica con varios detectores, ya sea luz transmitida, de scattering o de fluorescencia (**Figura 21**). La señal es procesada por un software para obtener información de distintos parámetros simultáneamente:

- De la **luz transmitida** cuando una célula atraviesa el haz de luz se obtiene información sobre el diámetro de la célula y, por consiguiente, de su volumen.
- De la **luz de scattering** que se dispersa al incidir sobre la célula se obtiene información sobre la rugosidad la superficie celular: a mayor rugosidad mayor dispersión.
- De la **fluorescencia** emitida puede obtenerse un amplio abanico de información, ya que las células pueden teñirse con sondas fluorescentes para el seguimiento de muy variados procesos, como veremos a continuación.

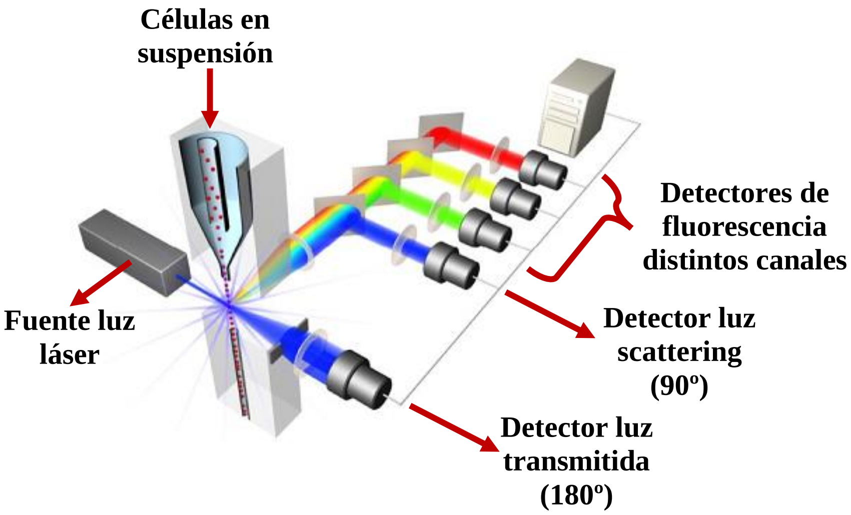
Células en suspensión
Detectores de fluorescencia distintos canales
Fuente luz láser
Detector luz scattering (90º)
Detector luz transmitida (180º)

Figura 21. Esquema de las partes fundamentales de un citómetro de flujo.

2.8.1. Estudio del ciclo celular.

Como se ha explicado en el **Capítulo I**, determinadas drogas pueden provocar alteraciones en el normal transcurso del ciclo celular, deteniendo su avance en determinados puntos del mismo [88]. Una de las formas para analizar la fase del ciclo en la que se encuentra una célula es cuantificar la cantidad de ADN que posee. Durante la fase G1 (o en la fase G0) las células presentan una sola copia de su ADN, hasta que entran en fase S y comienzan a duplicarlo. Finalmente, en la fase G2-M la célula habrá terminado de duplicar su material genético y presentará el doble de ADN que el que tenía en la fase G1 [51].

Empleando una sonda fluorescente específica de ADN como es el yoduro de propidio (PI), que emite en el rojo solo cuando está unido al ADN, podemos cuantificar la cantidad de ADN presente en las células [172]. El citómetro permite analizar la intensidad emitida individualmente por cada célula de una población, y esta intensidad es proporcional a la cantidad de ADN que posee. Los resultados de citometría se presentan en histogramas, en los que se representa el número de células (eje Y) que presentan una determinada intensidad de emisión (eje X). En la **Figura 22** aparece un histograma típico de una población celular teñida con PI analizada mediante citometría. De las áreas de cada una de estas regiones se obtiene el porcentaje de células que se encuentran en cada fase.

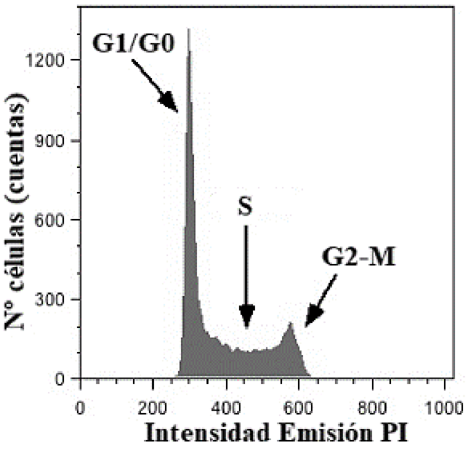

Figura 22. Estudio de ciclo celular mediante determinación del contenido de ADN empleando tinción con PI.

Para realizar estos estudios se siembran 1.5 × 10^5 células por pocillo en placas de 6 pocillos y se dejaron incubar durante 24 h. A continuación se retira el medio y se sustituye por medio fresco con las concentraciones deseadas del compuesto de interés. Los ensayos se realizan aplicando tratamientos de 24 y 48 h, tras lo cual se procede a fijar las células para su posterior análisis mediante citometría de flujo. Para la fijación, las células se levantan con tripsina, se resuspenden en 1 mL de PBS y se fijan con 3 mL de etanol por muestra manteniéndolas durante todo el proceso en hielo. Las células fijadas pueden guardarse a 4 ^{o}C para ser analizadas hasta 3 días después. Para realizar las medidas de citometría las células fijadas se lavan con PBS para retirar el etanol, se resuspenden en 0.5 mL de PBS y se determina el número de células presente en cada muestra mediante un contador automático (TC20™ Automated Cell Counter, Bio-Rad, California, USA). La tinción con PI se realiza con una disolución de 0.1 mg/mL PI, 0.1 mM EDTA, 0.1 % Triton X-100 y 2 mg/mL RNA-sa durante 30 min, teniendo en todas las muestras el mismo número de células para que la tinción sea uniforme. Después se centrifugan las muestras (5 min, 1000 rpm) y se suspenden en 100 µL de PBS para ser analizadas en un citómetro Guava EasyCite (Millipore, MERCK, Madrid, España).

2.8.2. Estudios de viabilidad celular.

A pesar de que el método de rutina más común para determinar la viabilidad celular es el ensayo MTT (**apartado 2.4, Capítulo II**), debe tenerse en cuenta que este método proporciona una medida indirecta de la supervivencia celular, asociada a la actividad mitocondrial. Por esta razón, es conveniente corroborar los datos de viabilidad celular a través de técnicas basadas en procesos alternativos. En este trabajo se empleó la citometría de flujo con el reactivo comercial Guava® ViaCount® Reagent (C4000-0040, Guava Technologies) como técnica complementaria al ensayo MTT para determinar la viabilidad celular a determinadas concentraciones de los complejos estudiados (por ejemplo, en el IC_{50}). Basándose en la distinta permeabilidad celular de dos sondas fluorescentes en células viables y no viables, el ensayo de viabilidad de Guava ViaCount permite cuantificar el número de células vivas y muertas de una muestra de forma directa.

El procedimiento experimental para este ensayo es muy sencillo. Las células se siembran en placas de 12 pocillos a razón de 8×10^4 células por pocillo y se incubaron durante 24 h. A continuación se retira el medio y se añade medio fresco con el tratamiento deseado. Tras incubar durante el tiempo indicado, las células se levantan mediante tripsinización, se lavan con PBS, se centrifugan (5 min, 1.000 rpm) y se resuspenden en 0.5 mL de PBS. A 50 µL de esta suspensión se le añaden 150 µL del reactivo comercial ViaCount y se procede a su análisis mediante citometría. El análisis del número de células viables y no viables en cada muestra se realiza automáticamente con el software CytoSoft de Guava ViaCount (Guava Technologies).

2.8.2.1.Inhibición de caspasas.

El proceso de apoptosis está regulado por una familia de proteasas llamadas caspasas [169]. Estas caspasas se activan a través de la liberación de determinados factores proapoptóticos, como el citocromo-c, como consecuencia de un determinado estímulo y desencadenan el proceso de apoptosis [173]. Para determinar si un compuesto induce muerte por apoptosis puede emplearse un inhibidor de caspasas, de forma que la apoptosis queda impedida, lo que debería traducirse en un incremento de la supervivencia celular. En este trabajo se empleó el inhibidor de caspasas Z-VAD-FMK (tlrl-vad, InvivoGen, San Diego, USA) para comprobar si este promovía un aumento en la supervivencia celular cuando las células eran tratadas con los complejos metálicos estudiados.

Experimentalmente, las células se siembran en placas de 12 pocillos a razón de 8×10^4 células por pocillo y se incuban durante 24 h. A continuación se retira el medio, se añade medio fresco con 20 µM Z-VAD-FMK y medio fresco solo en los controles y se incuba durante 1 h. Después se tratan con el compuesto a estudiar a una determinada concentración y se incuba durante 24 h más. La determinación de la supervivencia celular de cada muestra (controles y tratamientos en presencia y ausencia de Z-VAD-FMK) se realiza mediante el ensayo de viabilidad de Guava ViaCount, explicado en el apartado anterior, en un citómetro Guava EasyCite (Millipore, MERCK).

2.8.3. Acumulación de especies reactivas de oxígeno (ROS).

La citotoxicidad de muchos agentes se debe a la sobreproducción y acumulación de ROS en la célula [174]. En este trabajo se estudió mediante citometría de flujo la capacidad de una serie de compuestos de inducir la generación de determinadas especies ROS. Concretamente, se empleó DHE (dihydroethidium, D1168, Invitrogen™) como sonda específica de anión superóxido y H2DCFDA (2',7'-dichlorodihydro-fluorescein diacetate, D399, Invitrogen™) como sonda para detección de peróxidos y otras especies ROS (**Figura 23**). Estas sondas no son fluorescentes y reaccionan específicamente con las especies ROS indicadas para dar compuestos fluorescentes. La intensidad de esta emisión es proporcional a la cantidad de ROS que se ha generado en la célula durante el tiempo que haya durado el tratamiento.

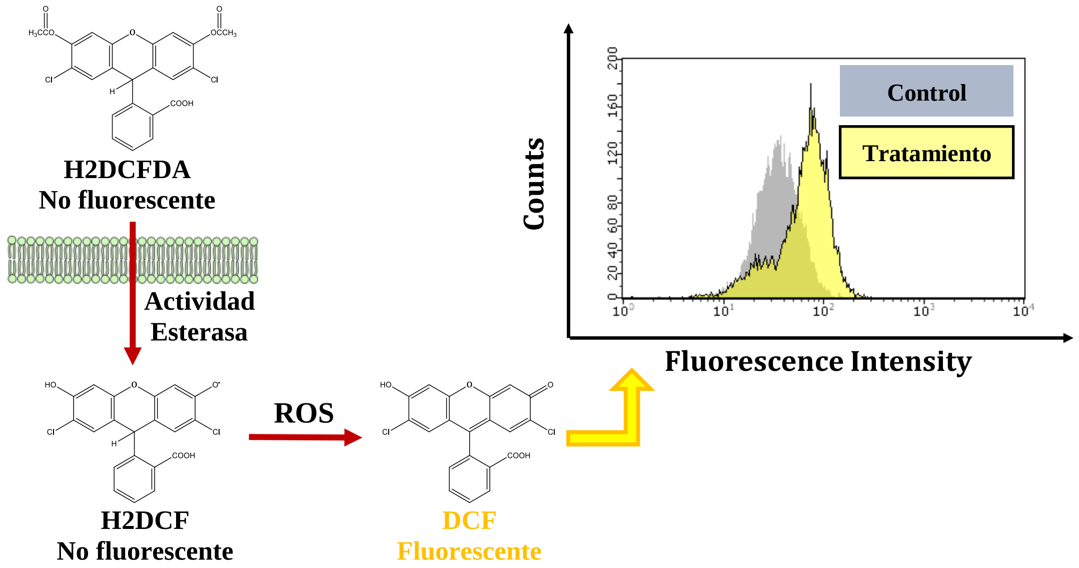

Figura 23. Esquema del proceso de detección de ROS mediante citometría de flujo empleando la sonda H2DCFDA. En el histograma aparecen en amarillo las células que han sido tratadas con un compuesto que incrementa la producción de ROS intracelular y en gris las células control.

Se siembran 4 × 10^4 células por pocillo en placas de 12 pocillos y se incuban durante 24 h. Después, las células se tiñen durante 30 min con 6 µM DHE o bien con 25 µM H2DCFDA en medio Hank´s Balanced Salt Solution (HBSS, H9269, Sigma Aldrich) suplementado con 1% FBS. Se retira este medio, se lava dos veces con PBS, se añade medio fresco completo y se dejan incubar 1 h antes de añadir los tratamientos con los compuestos de interés. Los tratamientos se realizan durante 2 ò 4 h, tras lo cual se levantan las células y se analizan mediante citometría de flujo, en este caso en un citómetro Guava EasyCite (Millipore, MERCK, Madrid, España).

2.8.4. Estudio de la cardiolipina oxidada.

La cardiolipina es un fosfolípido presente en la membrana interna de la mitocondria y su oxidación, por ejemplo producida por ROS, está relacionada con la liberación de citocromo-c al citosol, lo cual desencadena el proceso de apoptosis [99,173]. La oxidación de este fosfolípido como consecuencia del tratamiento con una droga puede detectarse empleando el fluoróforo NAO (Nonyl Acridine Orange), que presenta una elevada afinidad por la forma reducida de la cardiolipina, pero no por su forma oxidada. De esta forma, a mayor cantidad de cardiolipina oxidada se registra una menor intensidad de emisión de la sonda NAO [175,176].

Las células se siembran en placas de 6 pocillos (1.5 × 10^5 células por pocillo). Tras 24 h, las células se tiñen con una disolución 100 nM de NAO (A1372, Thermo Scientific) en HBSS (1 % FBS) durante 15 min. Después se retira la tinción, se lavan dos veces con PBS y se tratan con las concentraciones indicadas de compuesto durante un tiempo determinado (por ejemplo, 4 h). Tras el tratamiento, se levantan las células, se lavan con PBS y se analizan mediante citometría de flujo.

PARTE 1

Interacción de Doxorrubicina, Clústeres Cuánticos Atómicos (AQCs) y Complejos Metálicos de Pt con ADN en Doble Hélice.

CAPÍTULOS III, IV y V

“Conclusion: Big helix in several chains, phosphates on outside, phosphate-phosphate inter-helical bonds disrupted by water. Phosphate links available to proteins.”

Rosalind Franklin, lecture notes, November 1951.

Aim of Part 1

Part 1 of this thesis is divided into three Chapters, namely **Chapters III**, **IV** and **V**, in which we discuss the interaction of different species with double stranded DNA (dsDNA) and the biological consequences of this interaction.

Chapters III and **IV** correspond to already published articles and are both part of a project in collaboration with the groups of Prof. Fernando Domínguez (CiMUS, Santiago de Compostela, Spain) and Prof. Arturo López-Quintela (Universidad de Santiago de Compostela, Spain). The aim of this project was to study the biological consequences of the interaction of silver triatomic quantum clusters (AQCs or Ag_3) with DNA. Their synthesis procedure and characterization, developed by the group of Prof. Arturo López-Quintela, as well as the characteristics of their interaction with dsDNA had been previously studied [107]. In this previous work, it was shown that very low concentrations of ACQs (at AQCs/DNA(BP) concentration ratios below 0.05) induced noticeable changes in the structure of natural DNA, which put forward the question of whether this would have an impact in living organisms. Many vital processes, such as DNA replication or transcription, involves the binding of highly specific proteins to DNA. Certain modifications in the DNA structure can prevent this binding and disrupt the activity of the enzymes with lethal consequences.

Bearing all this in mind, we decided to use a well-known DNA ligand as a model to study how the conformational changes induced in the DNA molecule by very low concentrations of AQCs affected the binding of this ligand. Doxorubicin (DOX), an anticancer agent currently in clinical use that strongly intercalates into DNA, was chosen for this purpose. First, a complete characterization of the interaction of DOX with dsDNA was carried out. This thermodynamic and kinetic characterization is reported in the article named “New Insights into the Mechanism of the DNA/Doxorubicin Interaction” and corresponds to **Chapter III** of this thesis [177].

As explained before, the next step was to study the consequences in the DNA/DOX interaction caused by the conformational changes induced by the AQCs. Indeed, it was observed that the presence of only one Ag_3 cluster every 200 DNA base pairs completely prevented DOX from intercalating into DNA. These observations were in highly good agreement with the biological studies that were carried out by the group of Prof. Fernando Domínguez, which demonstrated the impact of the AQCs on the activity of different DNA-binding enzymes, as well as their bactericidal effect in various species of bacteria isolated from clinical samples. All these results were published in the article named “Interaction of silver atomic quantum clusters with living organisms: bactericidal effect of Ag_3 clusters mediated by disruption of topoisomerase-DNA complexes” that can be found in **Chapter IV** [178].

Chapter V also deals with the interaction of ligands with dsDNA. In this work, we wanted to explore the cytotoxicity as well as the interaction with biomolecules (DNA and seroalbumin) of a family of platinum complexes analogous to cisplatin. This type of compounds usually exert their biological activity through the establishment of covalent bonds with DNA, among other possible mechanisms. The synthesis and the characterization of these metal complexes were carried out by the group of Prof. Blanca R. Manzano and Prof. Félix A. Jalón (Universidad de Ciudad Real, Spain).

Capítulo III

Mecanismo de la Interacción entre el Agente Antitumoral Doxorrubicina y el ADN

Summary

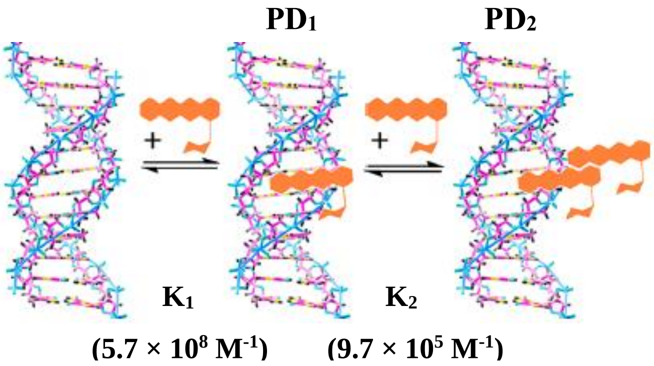

Figure 1. Schematic representation of the DNA/DOX interaction mechanism.

Doxorubicin (DOX) is an anticancer agent of the family of anthracyclines in clinical use since 1974 [24]. Its biological activity as an antitumor drug is related to its binding to DNA (P) that leads to the inhibition of IIA-type human topoisomerase activity [179]. In this respect, the binding features of DOX with nucleic acids have been studied in depth in the literature, and it has been regarded for years as a classical intercalating agent [180].

For convenience, in this work DOX is referred to as “D” and the polinucleotides to as “P”. A set of thermodynamic techniques, including CD, DSC, ITC, viscosity and fluorescence measurements allowed to identify and characterize not one but two distinct DNA/DOX complexes depending on the drug/polynucleotide concentration ratio C_D/C_P: “PD_1” at C_D/C_P ratios below 0.35, and “PD_2” at higher C_D/C_P ratios. In principle, PD_1 exhibited all the typical characteristics of an intercalation complex, as it stabilized the double helix structure increasing its T_m and also induced a marked elongation of the DNA molecule, as evinced from the viscosity measurements. However, the kinetic data obtained for the formation of PD_1 by T-Jump measurements put forward the existence of an intermediate complex, named PD_0, at the expense of which PD_1 gets formed. In order to shed light onto this issue, titrations of synthetic copolymers $[poly(dA-dT)]_2$ and $[poly(dG-dC)]_2$ with DOX were carried out, as intercalating agents often present a marked preference for GC-rich regions, whereas groove binders prefer AT-rich sequences. Interestingly, DOX could bind to both copolymers with significant affinity. These experimental results, along with the bibliographic data regarding the structure and characteristics of the different moieties of the DOX molecule, let us put forward the bifunctional character of PD_1, in which the positively charged amino sugar moiety of DOX interacts with the groove of the DNA molecule, while its planar tetracyclic core intercalates between the DNA base pairs.

As to PD_2, the ability of DOX to form aggregates at high concentrations and the behaviour observed with the different thermodynamic techniques, point to the formation of an external aggregation complex when DOX concentration is raised at C_D/C_P ratios above 0.35.

Reproduced with permission from The Journal of Physical Chemistry B according to ACS's Policy on Theses and Dissertations. Copyright 2014 American Chemical Society.

THE JOURNAL OF PHYSICAL CHEMISTRY B

Article

pubs.acs.org/JPCB

New Insights into the Mechanism of the DNA/Doxorubicin Interaction

Cristina Pérez-Arnaiz, Natalia Busto, José M. Leal, and Begoña García*

Universidad de Burgos, Departamento de Química, 09001 Burgos, Spain

ABSTRACT: Doxorubicin (DOX) is an important anthracycline antibiotic whose intricate features of binding to DNAs, not yet fully understood, have been the object of intense debate. The dimerization equilibrium has been studied at pH = 7.0, I = 2.5 mM, and T = 25 °C. A thermodynamic and kinetic study of the binding of doxorubicin to DNA, carried out by circular dichroism, viscometry, differential scanning calorimetry, fluorescence, isothermal titration calorimetry, and T-jump relaxation measurements, has enabled us to characterize for the first time two different types of calf thymus DNA (ctDNA)/DOX complexes: PD_1 for $C_{DOX}/C_{DNA} < 0.3$, and PD_2 for higher drug content. The nature of the PD_1 complex is described better in light of the affinity of DOX with the synthetic copolymers $[poly(dA\text{-}dT)]_2$ and $[poly(dG\text{-}dC)]_2$. The formation of PD_1 has been categorized kinetically as a two-step mechanism in which the fast step is the groove binding in the AT region, and the slow step is the intercalation into the GC region. This bifunctional nature provides a plausible explanation for the high PD_1 constant obtained ($K_1 = 2.3 \times 10^8$ M^{-1}). Moreover, the formation of an external aggregate complex ctDNA/DOX (PD_2) at the expense of PD_1, with $K_2 = 9.3 \times 10^5$ M^{-1}, has been evinced.

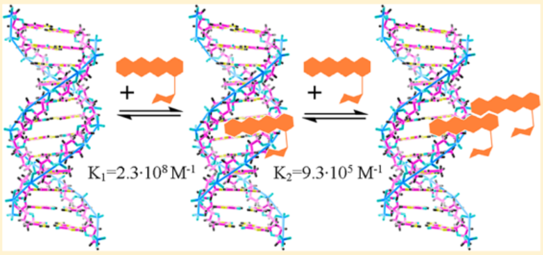

INTRODUCTION

Hydroxydaunorubicin, also known as doxorubicin (DOX), is a prominent family member of anthracycline antibiotics, one of the most effective types of anticancer drugs currently in use.[1] Since this drug was discovered five decades ago, active interest in studies involving DOX continuous to be as vivid as ever; however, despite the intense investigation developed so far, its mechanism of action still remains unclear.[2] The main mode of action appears to be the inhibition of IIA-type human topoisomerase, both by poisoning and by catalytic inhibition.[3] Nowadays, it is recognized that the main features of the binding of DOX to DNA seem to be the origin of its biological action.[4]

Figure 1 shows the various functional moieties of anthracyclines structure;[5] in addition to the amino sugar moiety (positively charged at neutral pH), the b, c, and d rings constitute an intercalative region. The mode of interaction of DOX with double-stranded DNA is determined by the role played by each component.

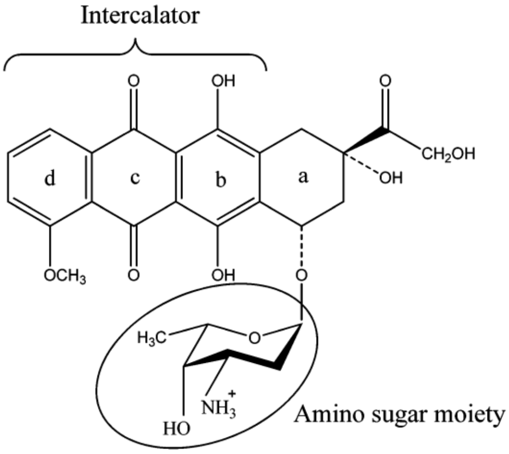

Figure 1. Structure and functional moieties of doxorubicin.

Intercalation of drugs into DNA can distort the polynucleotide structure and result in enzyme inhibition related to the DNA replication and transcription. Due to the insertion of the tetracyclic region into the DNA base pairs, DOX has been regarded for years as a classical intercalating agent.[6] Studies performed with some anthracyclines suggest that the strength of intercalation relies upon the ability to form cleavable topoisomerase II complexes.[7] The kinetics of association and dissociation of the calf thymus DNA (ctDNA)/DOX system was investigated by stopped flow measurements according to a five-step model[8] and by T-jump measurements according to a single association step process,[9] with the mechanism interpreted in terms of site exclusion effects. In both cases the studies were conducted at $I \geq 0.15$ M (NaCl); it is noteworthy to recall that the extracellular medium contains 104 mM Cl^- ion concentration, whereas the intracellular medium has only 4 mM,[10] hence the appropriateness of working at low ionic strength.

Some contributions have emphasized the role played by the amino sugar moiety. Removal or alteration of this unit drastically decreases the binding equilibrium constant of the DNA/DOX system.[11,12] Even though a mixed mode of binding can be put forward,[13] the mechanism of formation of the DNA/

Received: November 20, 2013
Revised: December 24, 2013
Published: January 13, 2014

ACS Publications © 2014 American Chemical Society

DOX complex so far is not well determined. In this work, the thermodynamics of the interaction of DOX with ctDNA and the synthetic copolymers $[\mathrm{poly(dA\text{-}dT)}]_2$ and $[\mathrm{poly(dG\text{-}dC)}]_2$ were studied by viscometry, fluorescence, circular dichroism (CD), differential scanning calorimetry (DSC), and isothermal titration calorimetry (ITC) measurements. As a classical intercalating agent, DOX is expected to interact with $[\mathrm{poly(dG\text{-}dC)}]_2$, but not with $[\mathrm{poly(dA\text{-}dT)}]_2$;[14] in fact, some studies have concluded that DOX displays no traceable binding with $[\mathrm{poly(dA\text{-}dT)}]_2$.[15] By contrast, DOX has been shown here to bind to both $[\mathrm{poly(dA\text{-}dT)}]_2$ and $[\mathrm{poly(dG\text{-}dC)}]_2$. Also, for the first time, two different ctDNA/DOX complexes have been observed and characterized as a function of the drug content.

■ MATERIALS AND METHODS

Materials. Doxorubicin hydrochloride (D), from Sigma Aldrich, was used without further purification. Stock solutions of DOX were prepared by dissolving weighed amounts in 2.5×10^{-3} M sodium cacodylate (NaCaC), $[(CH_3)_2AsO_2Na]$, as a buffer to maintain the pH constant at 7.0. Aqueous solutions were prepared with doubly deionized water from a Millipore Q apparatus (APS; Los Angeles, California). Calf thymus DNA (P), from Sigma Aldrich, was dissolved in water and sonicated using a MSE-Sonyprep sonicator by applying 20 cycles of 10 s to suitable DNA samples (10 mL ctDNA, 2×10^{-3} M) with 20 s pause between cycles, at 98 μm amplitude. The sonicator tip was introduced directly into the solution, kept in an ice bath to minimize thermal sonication effects. Stock solutions of the synthetic copolymers $[\mathrm{poly(dG\text{-}dC)}]_2$ and $[\mathrm{poly(dA\text{-}dT)}]_2$ were prepared by dissolving the solids in water. In all cases, the polynucleotide concentration, C_P, was expressed as molarity of base-pairs (M_{BP}). Stock solutions were stored in the dark at 4 °C.

Methods. Fluorescence titrations were performed on a Shimadzu Corporation RF-5301PC spectrofluorometer (Duisburg, Germany) at $\lambda_{exc} = 490$ nm and $\lambda_{em} = 555$ nm. The titrations were performed by adding increasing amounts of polynucleotide directly into the cell with the dye solution.

The CD spectra were recorded on a MOS-450 Bio-Logic dichrograph (Claix, France). The measurements were performed in 1.0 cm path-length cells at 25 °C. Titrations of the ctDNA/DOX system were carried out by injecting increasing micro amounts of the drug into a known volume of the polymer solution.

The thermal behavior of the ctDNA/DOX system was studied by DSC measurements, using a Nano DSC Instrument (TA, Waters LLC, New Castle, USA). To reduce to a minimum the formation of bubbles upon heating, the reference and the sample solutions were previously degassed in a degassing station (TA, Waters LLC, New Castle, USA). The samples were scanned at 3 atm pressure from 20 to 110 °C at 1 $°C \cdot min^{-1}$ scan rate.

The ITC experiments were performed at 25 °C using a Nano ITC Instrument (TA, Waters LLC, New Castle, USA). To prevent formation of air bubbles, all solutions were degassed in a degassing station (TA, Waters LLC, New Castle, USA). Drug solutions were placed in a 50 μL syringe and continuously stirred. Fifty additions of 1 μL in 400 s intervals were injected into the sample cell containing the buffer or the polymer solution. Control experiments were carried out to determine the contribution of the heat of dilution of both ctDNA and DOX. The integration of these peaks, corrected by the dilution effect, gave the binding isotherms (heat change versus C_D/C_P mole ratio). All the data were analyzed using the NanoAnalyze software.

Viscosity measurements were performed with an Ubbelohde viscometer (Schott, Mainz, Germany) immersed in a water bath at 25 °C. The flow time was measured with a digital stopwatch. The sample viscosity was evaluated as the mean value of at least three replicated measurements. The ctDNA/DOX viscosity readings were reported as $L/L_0 = (\eta/\eta_0)^{1/3}$ versus C_D/C_P ratio,[16] where η and η_0 stand for the polynucleotide viscosity in the presence and in the absence of drug, respectively.

Kinetic measurements were performed with a T-jump apparatus built up according to the Riegler et al. prototype,[17] working in the absorbance mode. The kinetic curves, collected with an Agilent 54622A oscilloscope (Santa Clara, CA), were transferred to a PC and evaluated with the Table Curve program of the Jandel Scientific package (AISN software, Richmond, CA). The time constants were averaged out to 10 repeated kinetic experiments, the observed uncertainty of time constants being 10%.

■ RESULTS AND DISCUSSION

Aggregation Behavior of Doxorubicin. Doxorubicin, a monocation species under physiological conditions, is known to undergo dimerization.[18] This process is influenced by the ionic strength and the buffer used, and must be characterized under the same conditions of the study of the ctDNA/DOX interaction. ITC provides full thermodynamic characterization of the aggregation process. Figure 2 shows an experimental ITC titration curve of DOX in 2.5 mM NaCaC and pH = 7.0. Each

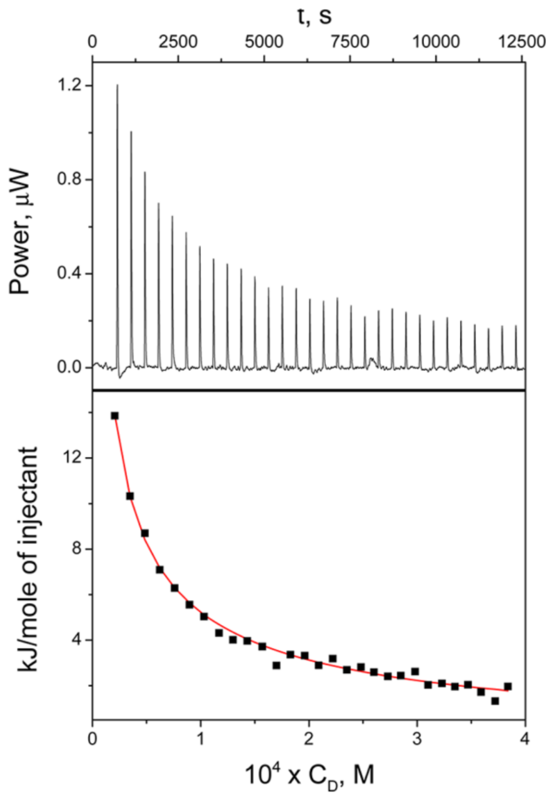

Figure 2. ITC profile of DOX dissociation in buffered solution. C_D^0 = 2.6 mM, I = 2.5 mM, pH = 7.0, and T = 25 °C.

injection produced an endothermic effect due to disaggregation. The binding isotherm was fitted by a dimer dissociation model that allows one to obtain concurrently the thermodynamic parameters of both the dissociation and the aggregation processes.

To reliably tackle the dimerization process without interfering with the study of the ctDNA/DOX system, the conditions in which the dimer content was negligible had to be carefully selected. The thermodynamic dimerization constant (K_d) obtained by ITC was quite close to that obtained by fitting to the spectrophotometric data-pairs a model that only considers monomer and dimer species in solution.[19] It can then be concluded that under these conditions, the formation of higher order aggregation species can be disregarded. Table 1 lists the data collected for the dimerization reaction 1:

$$2\mathrm{D} \overset{K_d}{\rightleftharpoons} \mathrm{D}_2 \qquad (1)$$

Table 1. Best-Fit Thermodynamic Parameters Obtained by ITC Measurements from a Dimer Dissociation Model[a]

10^{-4} K_d (M^{-1})	ΔH_d (kJ mol^{-1})	ΔS_d, (J mol^{-1} K^{-1})
1.4 (±0.3)	−52 (±5)	−95 (±17)

[a] K_d is the aggregation equilibrium constant, ΔH_d the enthalpy, and ΔS_d the dimerization entropy (eq 1).

Thermodynamic and Kinetic Features of the ctDNA/DOX Binding. *Circular Dichroism.* CD titrations were performed by adding increasing amounts of DOX to a ctDNA solution. The CD spectra collected are shown in Figure 3A. Different trends can be differentiated in the intricate 325−600 nm spectral region. For instance, a new 480 nm band was formed upon raising the DOX content. Moreover, the isoelliptic point at λ = 293 nm reveals the formation of new species in solution (Figure 3A, inset); this isoelliptic point appeared only for very low drug contents ($0 < C_D/C_P < 0.1$) and vanished when the C_D/C_P ratio was raised. The assumption of different types of complexes is also reinforced by the changes observed in the overall spectra. The characteristic negative band centered at 300 nm experienced a hypsochromic shift, which became more intense when the C_D/C_P ratio was raised.

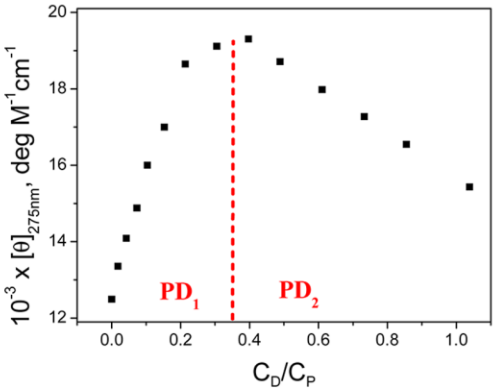

Figure 4. Molar ellipticity at 275 nm of the ctDNA/DOX system versus C_D/C_P ratio. C_P^0 = 1.02 × 10^{-4} M, I = 2.5 mM, pH = 7.0, and T = 25 °C.

Doxorubicin is a quiral molecule in nature, and its CD contribution should be taken into account (Figure 3B). At 275 nm, DOX displayed no dichroic effect, and hence it is an appropriate point to study the behavior displayed in Figure 3A. Figure 4 shows that the intensity of the 275 nm band increased when the C_D/C_P ratio was raised. At C_D/C_P = 0.35, the trend changed drastically, suggesting a critical transition in the binding features, most likely reflecting the appearance of a different mode of binding when the drug content was raised. As an implication, two different complexes (PD_1 and PD_2) can be presumed in solution. The different binding features are even more clear in Figure 3B, in which two spectra were recorded at C_D/C_P = 0.2 and C_D/C_P = 0.6 to compare the change in intensity and location of the bands. At C_D/C_P = 0.2, none of the typical DOX bands were evinced, suggesting that the content of free drug in solution was negligible when PD_1 is the prevailing form. By contrast, for the C_D/C_P = 0.6 limit, in which the PD_2 species is present, the trend changed and the positive band at 250 nm sharply rose.

Viscosity. The viscosity measurements revealed two different effects (Figure 5), in fairly good agreement with the CD experiments. The first effect, for C_D/C_P ratio between 0 and 0.35, consists of a sharp increase in the relative contour length

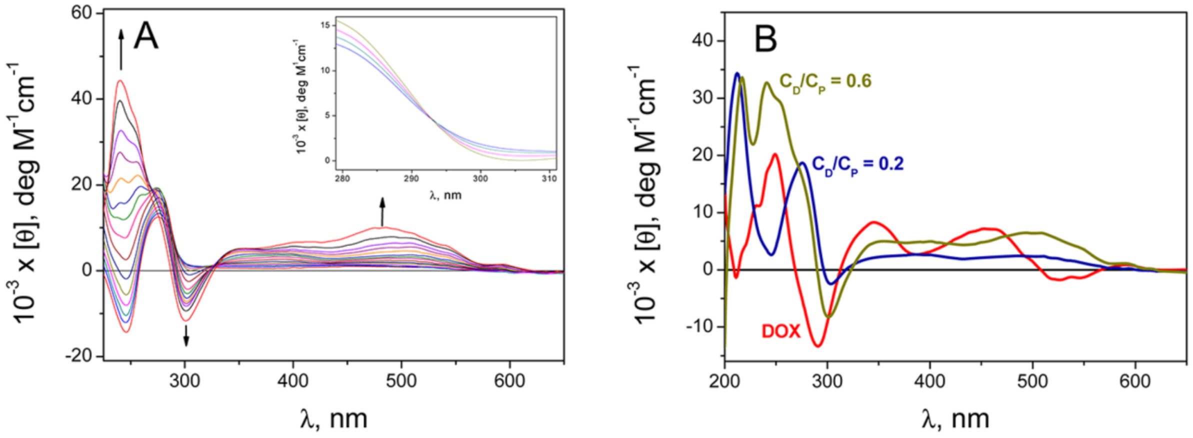

Figure 3. (A) CD spectra recorded for the ctDNA/DOX system between $0 < C_D/C_P < 1.0$. Inset: isoelliptic point (λ = 293 nm) displayed by ctDNA/DOX between $0 < C_D/C_P < 0.1$. (B) CD spectra recorded for free DOX (red line) and C_D/C_P = 0.2 (blue line) and C_D/C_P = 0.6 (green line) ratio. C_P^0 = 1.02 × 10^{-4} M, I = 2.5 mM, pH = 7.0, and T = 25 °C.

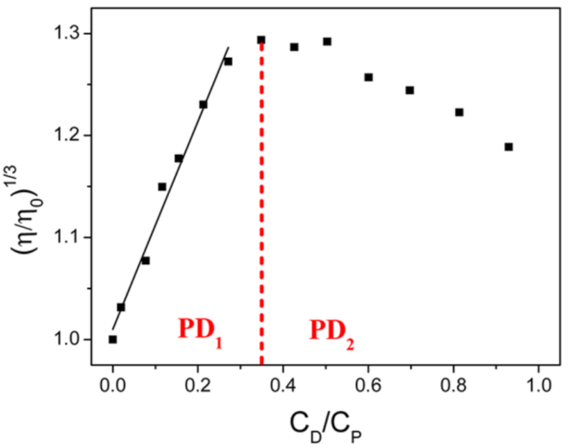

Figure 5. Relative viscosity of the ctDNA/DOX system. $C_P^0 = 2.03 \times 10^{-4}$ M, $I = 2.5$ mM, pH = 7.0, and $T = 25$ °C.

when the drug content was raised. The projected slope (1.02 ± 0.06) is consistent with formation of an intercalative complex (PD_1).[16] At $C_D/C_P \sim 0.35$, a maximum was reached followed by a drop in the relative viscosity, revealing the formation of a second type of ctDNA/DOX complex (PD_2). This diminution in the polymer contour length points to partial loss of the intercalative nature of DOX in the PD_1 complex; that is, PD_2 is formed at the expense of PD_1. Therefore, DOX is partially intercalated and serves as a scaffold to form the aggregated complex, PD_2.

Thermal Stability. The melting process of the ctDNA/DOX system was studied by DSC, monitoring the endothermic transition peaks in the $C_D/C_P = 0{-}0.7$ range. Figure 6A shows two DSC curves at $C_D/C_P = 0.0$ and 0.3, observing only a single transition. The maximum temperature corresponded to the melting temperature (T_m). To ensure that possible disaggregation upon increasing the temperature does not interfere with the melting temperature, the free drug was analyzed also by DSC. Indeed, no disaggregation peaks were observed (data not shown), hence the endothermic peaks recorded can be put down to denaturation of the ctDNA/DOX complexes. Figure 6B shows the T_m values obtained as a function of the C_D/C_P ratio.

Up to $C_D/C_P = 0.2$, the ctDNA/DOX system underwent a 38 °C increase in the melting temperature relative to ctDNA in the absence of drug. As expected for intercalating agents, the formation of PD_1 lends a marked thermal stabilization to the double helix. It is noteworthy that this significant increase in the melting temperature is much higher than that caused by most classical intercalators (as an example, proflavine causes $\Delta T_m = 3$ °C at $C_D/C_P = 0.3$[20] and ethidium bromide $\Delta T_m = 13$ °C at $C_D/C_P = 0.1$[21]). Above the $C_D/C_P = 0.3$ ratio, the melting temperature remained nearly constant. Therefore, from Figure 6B one can conclude that the second complex (PD_2) detected at higher drug content displays different thermal features, as it does not stabilize the DNA double helix structure. These results concur with those obtained from CD and viscosity experiments, bearing out the existence of two complexes with different features.

Kinetic Study. The kinetic study of the ctDNA/DOX interaction was undertaken with the T-jump relaxation technique at $I = 0.1$ M. To determine the mechanism of formation of PD_1, the experiments were carried out in excess of DNA ($C_D/C_P \leq 0.1$). The kinetic curves recorded displayed monophasic behavior (Figure 7A). Analyses of the effect of the reactants concentration on the reciprocal relaxation time (Figure 7B) suggests a two-step mechanism according to eq 2:

$$P + D \overset{K_0}{\rightleftharpoons} PD_0 \underset{k_{-1}}{\overset{k_1}{\rightleftharpoons}} PD_1 \tag{2}$$

fitting eq 3 to the kinetic data:

$$\frac{1}{\tau} = \frac{K_0 k_1([P] + [D])}{1 + K_0([P] + [D])} + k_{-1} \tag{3}$$

The formation of PD_1 is preceded by a fast step that leads to formation of PD_0, with K_0 being the equilibrium constant, and k_1 and k_{-1} the rate constants of formation of PD_1 from PD_0 in the forward and reverse direction, respectively, being $K_1' = k_1/k_{-1}$. The overall apparent equilibrium constant, K_1, can be obtained from eq 4:

$$K_1 = K_0(1 + K_1') \tag{4}$$

Table 2 lists the values of equilibrium and kinetic constants obtained. The high value of K_0 (1.0×10^4 M^{-1}) points up an interaction stronger than that stemming from an ion-pair drug/

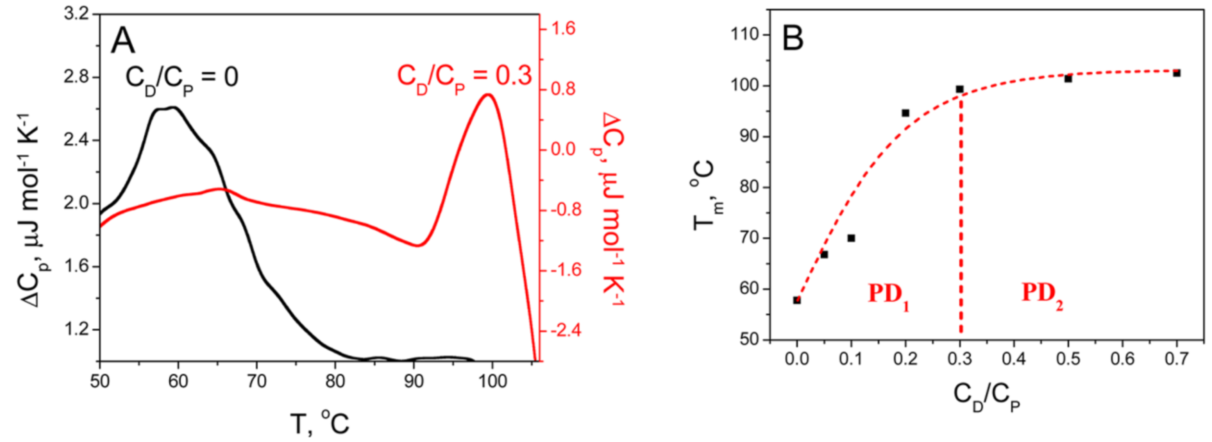

Figure 6. (A) DSC curves recorded for the melting process of ctDNA/DOX system: $C_D/C_P = 0$ (black line) and $C_D/C_P = 0.3$ (red line). $C_P = 5 \times 10^{-4}$ M, $I = 2.5$ mM, pH = 7, scan rate 1 °C/min and $P = 3$ atm. (B) Melting temperature as a function of the C_D/C_P ratio.

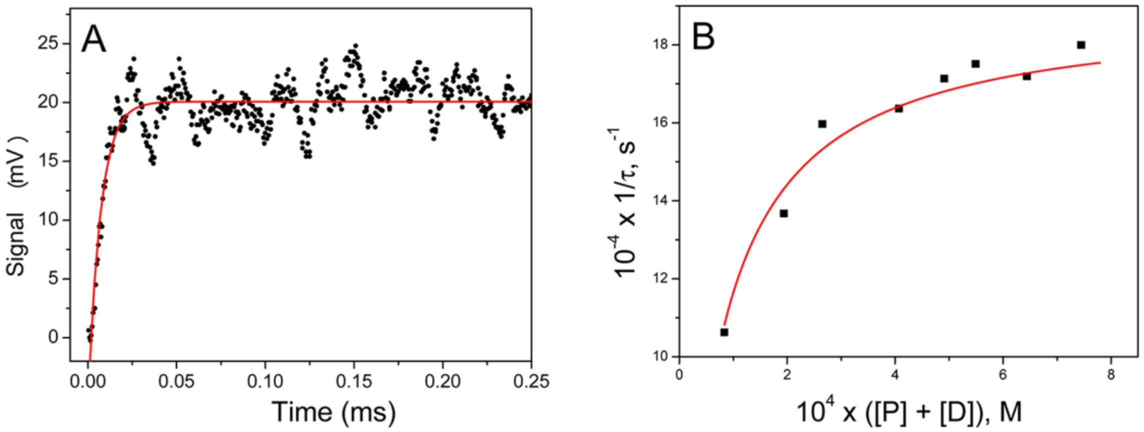

Figure 7. (A) Kinetic curve for the ctDNA/DOX system, $C_D = 1.8 \times 10^{-5}$ M, $C_P = 5.7 \times 10^{-4}$ M, $\lambda = 510$ nm, $I = 0.1$ M, pH = 7.0 and $T = 25$ °C. (B) $1/\tau$ versus ([P] + [D]) plot for ctDNA/DOX system and data fitting using eq 3.

Table 2. Rate (k_1, k_{-1}) and Equilibrium (K_0, K'_1, and K_1) Constants for the ctDNA/DOX System According to Eqs 3 and 4[a]

10^{-5} k_1 (s^{-1})	10^{-2} k_{-1} (s^{-1})	10^{-4} K_0 (M^{-1})	10^{-3} K_1'	10^{-7} K_1 (M^{-1})
1.9	1.8	1.6	1	1.6 57[b]

[a] $I = 0.1$ M, pH = 7, and $T = 25$°C. [b] $I = 2.5$ mM, corrected with eq 5.

DNA complex formed "outside", whose K_0 value lies below 100.[22] Additionally, a groove complex is formed faster and more stable than an intercalative one.[23] Therefore, it can be surmised reasonably that the fast step corresponds to formation of PD_0, a groove binding complex markedly electrostatic in nature, as suggested earlier.[8] This binding should correspond to the interaction at the sugar site, in which the electrostatic charge of DOX is located in the phosphate groups. The binding to the groove is also favored by formation of H bonds between the OH substituent of the amino sugar and the nucleobase oxygen (or nitrogen) site; this set of interactions may justify the rather high K_0 value deduced. At this point, the slow process corresponding to intercalation of the tetracyclic core would afford the PD_1 complex. A five-step mechanism has been claimed by stopped flow measurements, obtaining the dissociation constants in the presence of SDS.[8] For convenience, the five steps are rearranged in an association mechanism with two branches, although other mechanisms should not be ruled out. Chaires has suggested other mechanisms valid for antracyclines different from DOX.[24] The model put forward here for the ctDNA/DOX binding is closer to the single-step mechanism by Föster et al.,[9] even though their T-jump kinetic studies were carried out under excess of DOX, conditions for which we have verified the formation of the PD_2 species; the kinetic equilibrium constant (8×10^5 M^{-1}) concurs well with what we report here for PD_2 obtained by ITC, as shown below.

According to our results, the values $k_1 = 1.9 \times 10^5$ s^{-1} and $k_{-1} = 180$ s^{-1} match fairly well the dissociation and formation rate

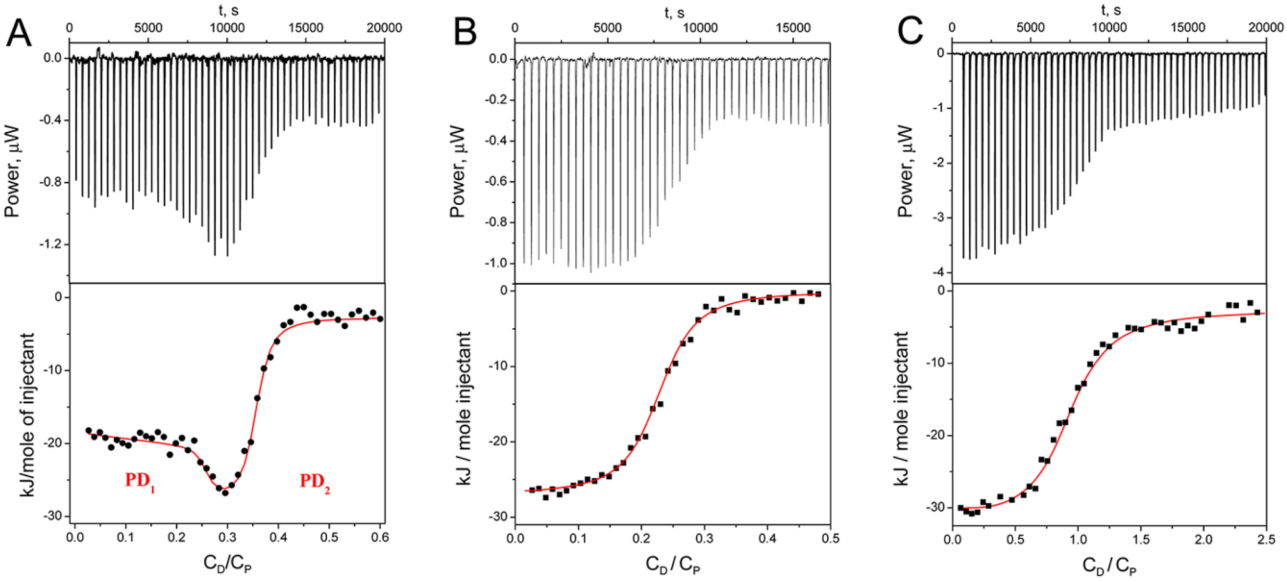

Figure 8. ITC titrations of DOX with (A) ctDNA, (B) $[poly(dG\text{-}dC)]_2$, and (C) $[poly(dA\text{-}dT)]_2$. $C_P^0 = 4 \times 10^{-4}$ M, $I = 2.5$ mM, pH = 7.0 and T = 25 °C.

Table 3. Thermodynamic Parameters Determined for the Binding of DOX to ctDNA Using a Two-Site Model (PD_1 and PD_2 Complexes) and to $[poly(dG\text{-}dC)]_2$ and $[poly(dA\text{-}dT)]_2$ Using a One-Site Model[a]

polymer	10^{-5} K (M^{-1})	ΔG (kJ mol^{-1})	ΔH (kJ mol^{-1})	ΔS (J mol^{-1} K^{-1})
ctDNA (PD_1)	2300 ± 800	−47.7 ± 0.7	−4.8 ± 0.3	144 ± 3
ctDNA (PD_2)	9.3 ± 0.7	−34.1 ± 0.2	−2.69 ± 0.02	105.2 ± 0.7
$[poly(dG\text{-}dC)]_2$	6.3 ± 0.7	−33.1 ± 0.3	−22.8 ± 0.3	34 ± 2
$[poly(dA\text{-}dT)]_2$	0.78 ± 0.03	−27.9 ± 0.1	−24.8 ± 0.1	10.1 ± 0.7

[a] I = 2.5 mM, pH = 7.0, and T = 25 °C.

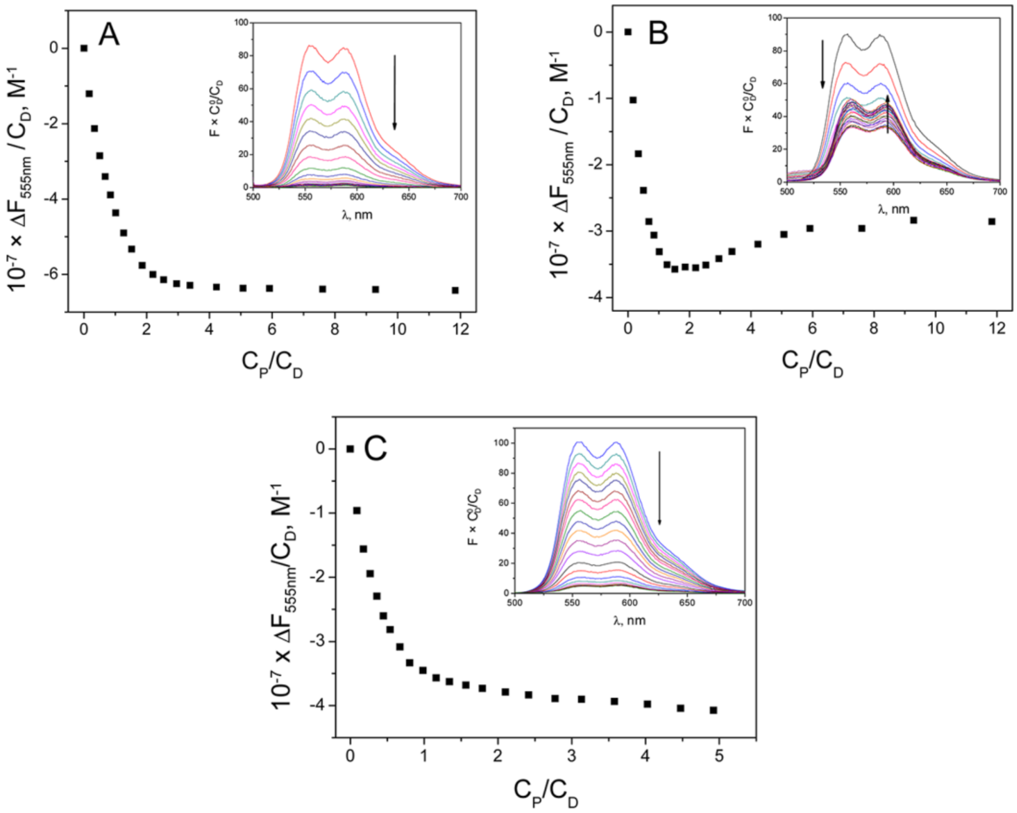

Figure 9. (A) Binding isotherm for the $[poly(dG\text{-}dC)]_2$/DOX system. Inset: Spectrofluorometric titration of the $[poly(dG\text{-}dC)]_2$/DOX system. (B) Binding isotherm for the $[poly(dA\text{-}dT)]_2$/DOX system. Inset: Spectrofluorometric titration of the $[poly(dA\text{-}dT)]_2$/DOX system. (C) Binding isotherm for the ctDNA/DOX system. Inset: Spectrofluorometric titration of the ctDNA/DOX system. $C_D^0 = 1.62 \times 10^{-6}$ M, λ_{exc} = 490 nm, λ_{em} = 555 nm, I = 2.5 mM, pH = 7.0, T = 25 °C.

constants of PD_1 from PD_0. The equilibrium constant $K_1' = 1 \times 10^3$ is at least one order higher than the binding constant expected for the formation of an intercalative complex from a pure electrostatic complex.[25] That is, PD_0 helps to form PD_1, a bifunctional complex in which the chromophore intercalates into the DNA base-pairs and the amino sugar spreads along the minor groove. This mechanism, much simpler than that by Rizzo et al,[8] is in fairly good agreement with the structural data of the DNA/DOX interaction.[13] To hold fair comparison of the T-jump equilibrium constant with that from ITC measurements (under considerably smaller ionic strength, I = 2.5 mM), K_1 had to be corrected considering the ionic strength effect according to the Manning and Record equation:[26]

$$\frac{\Delta \log K}{\Delta(-\log \mathrm{Na}^+)} = m'\Psi \tag{5}$$

where m' stands for the number of phosphodiester residues occupied by one drug unit, and Ψ is the DNA charge counteracted by the external ions. The value reported for $m'\Psi$ equals 0.97;[11] thus, the thermodynamic constant for formation of PD_1 (under 2.5 mM ionic strength) was $K_1 = 5.7 \times 10^8$ M^{-1} (Table 2).

Isothermal Titration Calorimetry. ITC measurements may provide full thermodynamic characterization of the equilibrium interactions of DOX with ctDNA, $[poly(dA\text{-}dT)]_2$ and $[poly(dG\text{-}dC)]_2$. Solutions containing the polynucleotide were titrated with increasing amounts of DOX. For the ctDNA/DOX system, a "two-site" model has served to fit the binding isotherm (Figure 8A), corroborating two different modes of binding that depend on the drug/polynucleotide concentration ratio. The titration data for ctDNA/DOX displayed a minimum for C_D/C_P = 0.3, borne out by the CD and viscosity experiments. Table 3 lists the thermodynamic constants, K, and enthalpy and entropy parameters, ΔH and ΔS, corresponding to formation of PD_1 and PD_2. The thermodynamic constant obtained by ITC (2.3×10^8 M^{-1}) agrees well with that obtained from T-jump measurements at low drug content, once corrected for I = 2.5 mM (K_1 = 5.7 × 10^8 M^{-1}) (Table 2). This figure, corresponding to formation of PD_1, is twice and three times, respectively, that for classical intercalators such as proflavine or ethidium bromide,[20,27] revealing a more complex interaction. Table 3 also shows that formation of PD_1 is exothermic and highly entropic, whereas intercalative complexes are known to display rather moderate entropic contribution.[28] These results support that, under these conditions, PD_1 does not behave as a classical intercalator, consistent with its groove binder nature, as inferred from the two-step mechanism observed by T-jump.

Groove binders quite often show preference for AT-rich sequences, whereas intercalating agents prefer GC-rich sequences.[14] With this in mind, the affinity of DOX with the synthetic copolymers $[poly(dA\text{-}dT)]_2$ and $[poly(dG\text{-}dC)]_2$ was studied to draw information on the nature of the respective interactions. Figure 8B,C shows the ITC experiments corresponding to $[poly(dG\text{-}dC)]_2$/DOX and $[poly(dA\text{-}dT)]_2$/DOX, respectively. The binding isotherms obtained in both cases suggest that at least two different types of interactions between DOX and DNA are at work, depending on the nucleotide sequence. A "one-site" model was used to fit the ITC data for $[poly(dG\text{-}dC)]_2$/DOX and $[poly(dA\text{-}dT)]_2$/DOX systems. As to the equilibrium constants obtained (K_{GC} and K_{AT}), K_{GC} was one order higher than K_{AT}. In contrast to the data previously published at I = 0.1 M,[15] the ITC profile makes clear that DOX does bind to $[poly(dA\text{-}dT)]_2$. Therefore, formation of the bifuncional PD_1 complex requires the presence of GC and AT regions.

The high values of the affinity constants (Table 3) relative to K_d (Table 2), enables one to hypothesize that the dimer concentration present in the solution containing DNA is negligible; however, the heat of dilution of D_2 has been considered in the calculations, as explained in the Methods subsection.

Spectrofluorometric Titrations. Fluorescence experiments have served to verify the different nature of the interaction of DOX toward the synthetic copolymers $[poly(dA\text{-}dT)]_2$ and $[poly(dG\text{-}dC)]_2$. The fluorescence behavior of these systems considerably differ from one another (Figure 9), corroborating the different binding nature observed by ITC. It also suggests intercalation process with the GC-rich sequence and a different type of interaction toward the AT-rich sequence. Figure 9A shows that the fluorescence dropped to nearly zero when the reaction between $[poly(dG\text{-}dC)]_2$ and DOX was to completion. An analysis of the isotherm as reported earlier[29] yields the value K_{GC} = (5.0 ± 0.2) × 10^5 M^{-1}, in good agreement with the ITC result (Table 3), bearing out the nonfluorescent nature of the intercalated complex.

The $[poly(dA\text{-}dT)]_2$/DOX interaction meets fully different features. Inspection of Figure 9B unveils two different processes. First, the fluorescence diminishes upon addition of $[poly(dA\text{-}dT)]_2$ to the cell containing the DOX solution, that is, at high D content. From $C_P/C_D > 1$ (or $C_D/C_P < 1$), the fluorescence increased gently, giving way to the binding isotherm. It should be noticed that the binding observed by ITC (Figure 8C) occurs in the same range of concentration ratio as that of the isotherm corresponding to the second process (Figure 9B). In other words, the DOX binding to the $[poly(dA\text{-}dT)]_2$ groove yielded a fluorescent complex whose equilibrium constant evaluated by ITC (Table 3) could not be obtained accurately from the fluorescence data.

Therefore, from Figure 9A,B it seems clear that the quenching effect due to intercalation exceeds the fluorescence increase due to the binding to the groove; because of this, the overall observable effect in the ctDNA/DOX system was the quenching (Figure 9C). This behavior resembles that of the $[poly(dG\text{-}dC)]_2$/DOX system; the amplitude of the isotherm in the former was less, as expected from the influence of the binding to the groove which, combined with intercalation, yields PD_1. Unlike with ITC, for ctDNA/DOX two types of binding were not observed from fluorescence measurements, indicating that both PD_1 and PD_2 are nonfluorescent species. An analysis in light of the Scatchard plot[30] yielded K = (1.16 ± 0.04) × 10^7, a value intermediate between the formation constants of PD_1 and PD_2 deduced from ITC measurements (Table 3).

Bearing all this in mind, the kinetic mechanism proposed in eq 2 finds now convincing explanation. The PD_0 species is formed when the charged amino sugar moiety interacts with the AT region. The value K_0 =1.0 × 10^4 M^{-1} obtained by T-jump measurements at I = 0.1 M (Table 2) compares fairly well with the constant K_{AT} = 7.8 × 10^4 M^{-1} obtained at I = 2.5 mM (Table 3). Taking for granted the electrostatic nature of PD_0, the ionic strength effect on the binding constant was corrected according to the Güntelberg equation,[31,32] $\log K = \log K^0 + 1.01 Z_AZ_BI^{1/2}/(1 + I^{1/2})$, Z_AZ_B being −1. However, the value obtained for K_0, once corrected, lies below K_{AT}. This feature points to the non-fully electrostatic nature of the interaction to the groove; instead, it would include also H-bonding through the OH of the sugar moiety; such interactions were not considered in the above equation. In addition, PD_1 is finally formed when the planar core of the drug intercalates into the GC base-pairs. In conclusion, the above sets of results have enabled us not only to describe but also to quantify the kinetic and thermodynamic parameters of the ctDNA/DOX system, in good agreement with those drawn from the structural data.[13]

As for the second complex, PD_2, with K_2 = 9.7 × 10^5 M^{-1}, it could be the outcome of an external aggregation complex from PD_1. The formation of PD_2 requires large entropic contribution, consistent with the release of water molecules from the complex interface.[33] The partial release in PD_1 of intercalated drug molecules from the base-pairs, observed with viscosity measurements, favors the formation of PD_2. Lastly, a reaction mechanism consistent with eq 2 can be put forward in the form:

$$P + D \overset{K_0}{\rightleftharpoons} PD_0 \underset{k_{-1}}{\overset{k_1}{\rightleftharpoons}} PD_1 \overset{+D}{\rightleftharpoons} PD_2 \qquad (6)$$

CONCLUSIONS

The formation of two nonfluorescent complexes (PD_1 and PD_2) between DOX and ctDNA, depending on the C_D/C_P ratio, has been reported for the first time from thermodynamic and kinetic measurements. For $C_D/C_P < 0.3$, the PD_1 complex prevails, a bifunctional mode of binding formed by a two-step mechanism. The first (fast) step involves groove binding to the AT sequence, in which the DOX amino sugar moiety spreads, giving way to a gently fluorescent complex. This AT-DOX interaction has not been reported hitherto. The second (slow) step consists of the intercalation of the aromatic DOX core to the GC sequence, giving way to a nonfluorescent complex. In addition, the appearance of a second complex, PD_2, with rather different binding features is evinced at higher drug content. The

PD_2 species, formed at the expense of PD_1 when all the intercalative sites are occupied, could be an external complex that partially overhangs from the intercalated core in PD_1, thus serving as a scaffold to form the aggregate.

■ AUTHOR INFORMATION

Notes

The authors declare no competing financial interest.

■ ACKNOWLEDGMENTS

The financial support by Ministerio de Educación y Ciencia, Project CTQ2009-13051/BQU, supported by FEDER, Junta de Castilla y León (Fondo Social Europeo, project BU-299A12-1), and Obra Social "la Caixa" project OSLC-2012-007, Spain, are gratefully acknowledged.

■ REFERENCES

(1) Carvalho, C.; Santos, R. X.; Cardoso, S.; Correia, S.; Oliveira, P. J.; Santos, M. S.; Moreira, P. I. Doxorubicin: The good, the bad and the ugly effect. *Curr. Med. Chem.* **2009**, *16*, 3267−3285.

(2) Gewirtz, D. A. A critical evaluation of the mechanisms of action proposed for the antitumor effects of the anthracycline antibiotics Adriamycin and Daunorubicin. *Biochem. Pharmacol.* **1999**, *57*, 727−741.

(3) Pommier, Y.; Leo, E.; Zhang, H.-L.; Marchand, C. DNA Topoisomerases and Their Poisoning by Anticancer and Antibacterial Drugs. *Chem. Biol.* **2010**, *17*, 421−433.

(4) Minotti, G.; Menna, P.; Salvatorelli, E.; Cairo, G.; Gianni, L. Anthracyclines: Molecular advances and pharmacologic developments in antitumor activity and cardiotoxicity. *Pharmacol. Rev.* **2004**, *56*, 185−229.

(5) Yang, X. L.; Wang, A. H. J. Structural studies of atom-specific anticancer drugs acting on DNA. *Pharmacol. Ther.* **1999**, *83*, 181−215.

(6) Aubel-Sadron, G.; Londos-Gagliardi, D. Daunorubicin and doxorubicin, anthracycline antibiotics, a physicochemical and biological review. *Biochimie* **1984**, *66*, 333−52.

(7) Bodley, A.; Liu, L. F.; Israel, M.; Seshadri, R.; Koseki, Y.; Ciuliani, F. C.; Kirschenbaum, S.; Silber, R.; Potmesil, M. DNA topoisomerase II-mediated interaction of doxorubicin and daunorubicin congeners with DNA. *Cancer Res.* **1989**, *49*, 5969−78.

(8) Rizzo, V.; Sacchi, N.; Menozzi, M. Kinetic studies of anthracycline−DNA interaction by fluorescence stopped flow confirm a complex association mechanism. *Biochemistry* **1989**, *28*, 274−82.

(9) Förster, W.; Stutter, E. Interaction of anthracycline antibiotics with biopolymers: 9. Comparative study of the interaction kinetics of daunomycin, adriamycin and iremycin with DNA. *Int. J. Biol. Macromol.* **1984**, *6*, 114−24.

(10) Bogojeski, J.; Bugarcic, Z. D.; Puchta, R.; van, E. R. Kinetic studies on the reactions of different bifunctional platinum(II) complexes with selected nucleophiles. *Eur. J. Inorg. Chem.* **2010**, 5439−5445.

(11) Chaires, J. B.; Satyanarayana, S.; Suh, D.; Fokt, I.; Przewloka, T.; Priebe, W. Parsing the free energy of anthracycline antibiotic binding to DNA. *Biochemistry* **1996**, *35*, 2047−2053.

(12) Zunino, F.; Gambetta, R.; Di, M. A.; Velcich, A.; Zaccara, A.; Quadrifoglio, F.; Crescenzi, V. The interaction of adriamycin and its β anomer with DNA. *Biochim. Biophys. Acta, Nucleic Acids Protein Synth.* **1977**, *476*, 38−46.

(13) Frederick, C. A.; Williams, L. D.; Ughetto, G.; Van, d. M. G. A.; Van, B. J. H.; Rich, A.; Wang, A. H. J. Structural comparison of anticancer drug−DNA complexes: adriamycin and daunomycin. *Biochemistry* **1990**, *29*, 2538−49.

(14) Ren, J. S.; Chaires, J. B. Sequence and structural selectivity of nucleic acid binding ligands. *Biochemistry* **1999**, *38*, 16067−16075.

(15) DuVernay, V. H., Jr.; Pachter, J. A.; Crooke, S. T. Deoxyribonucleic acid binding studies on several new anthracycline antitumor antibiotics. Sequence preference and structure−activity relationships of marcellomycin and its analogues as compared to adriamycin. *Biochemistry* **1979**, *18*, 4024−30.

(16) Cohen, G.; Eisenberg, H. Viscosity and sedimentation study of sonicated DNA-proflavine complexes. *Biopolymers* **1969**, *8*, 45−55.

(17) Rigler, R.; Rabl, C. R.; Jovin, T. M. Temperature-jump apparatus for fluorescence measurements. *Rev. Sci. Instrum.* **1974**, *45*, 580−8.

(18) Di, M. A.; Casazza, A. M.; Dasdia, T.; Necco, A.; Pratesi, G.; Rivolta, P.; Velcich, A.; Zaccara, A.; Zunino, F. Changes of activity of daunorubicin, adriamycin and stereoisomers following the introduction or removal of hydroxyl groups in the amino sugar moiety. *Chem.−Biol. Interact.* **1977**, *19*, 291−302.

(19) Menozzi, M.; Valentini, L.; Vannini, E.; Arcamone, F. Self-association of doxorubicin and related compounds in aqueous solution. *J. Pharm. Sci.* **1984**, *73*, 766−70.

(20) Garcia, B.; Leal, J. M.; Ruiz, R.; Biver, T.; Secco, F.; Venturini, M. Change of the Binding Mode of the DNA/Proflavine System Induced by Ethanol. *J. Phys. Chem. B* **2010**, *114*, 8555−8564.

(21) Cory, M.; McKee, D. D.; Kagan, J.; Henry, D. W.; Miller, J. A. Design, synthesis, and DNA binding properties of bifunctional intercalators. Comparison of polymethylene and diphenyl ether chains connecting phenanthridine. *J. Am. Chem. Soc.* **1985**, *107*, 2528−36.

(22) Biver, T.; Boggioni, A.; Secco, F.; Turriani, E.; Venturini, M.; Yarmoluk, S. Influence of cyanine dye structure on self-aggregation and interaction with nucleic acids: A kinetic approach to TO and BO binding. *Arch. Biochem. Biophys.* **2007**, *465*, 90−100.

(23) Busto, N.; Garcia, B.; Leal, J. M.; Secco, F.; Venturini, M. The mode of binding ACMA-DNA relies on the base-pair nature. *Org. Biomol. Chem.* **2012**, *10*, 2594−2602.

(24) Chaires, J. B.; Dattagupta, N.; Crothers, D. M. Kinetics of the daunomycin-DNA interaction. *Biochemistry* **1985**, *24*, 260−267.

(25) Biver, T.; De, B. A.; Secco, F.; Venturini, M.; Yarmoluk, S. Cyanine dyes as intercalating agents: Kinetic and thermodynamic studies on the DNA/Cyan40 and DNA/CCyan2 systems. *Biophys. J.* **2005**, *89*, 374−383.

(26) Record, M. T., Jr.; Lohman, T. M.; De, H. P. Ion effects on ligand-nucleic acid interactions. *J. Mol. Biol.* **1976**, *107*, 145−58.

(27) Baguley, B. C.; Falkenhaug, E. M. The interaction of ethidium with synthetic double-stranded polynucleotides at low ionic strength. *Nucleic Acids Res.* **1978**, *5*, 161−71.

(28) Chaires, J. B. Calorimetry and thermodynamics in drug design. *Annu. Rev. Biophys.* **2008**, *37*, 135−151.

(29) Lozano, H. J.; Garcia, B.; Busto, N.; Leal, J. M. Interaction of Thionine with Triple-, Double-, and Single-Stranded RNAs. *J. Phys. Chem. B* **2013**, *117*, 38−48.

(30) Scatchard, G. The attraction of proteins for small molecules and ions. *Ann. N.Y. Acad. Sci.* **1949**, *51*, 660−72.

(31) Prue, J. E. *Ionic Equilibria. The International Encyclopedia of Physical Chemistry and Chemical Physics, Topic 15: Equilibrium Properties of Electrolyte Solutions*; Pergamon Press: Oxford, U.K., 1966; Vol. 3.

(32) Guntelberg, E. Interaction of ions. *Z. Phys. Chem.* **1926**, *123*, 199−247.

(33) Jelesarov, I.; Bosshard, H. R. Isothermal titration calorimetry and differential scanning calorimetry as complementary tools to investigate the energetics of biomolecular recognition. *J. Mol. Recognit.* **1999**, *12*, 3−18.

Capítulo IV

Efectos de la Interacción de Clústeres Atómicos de Plata con el ADN

Summary

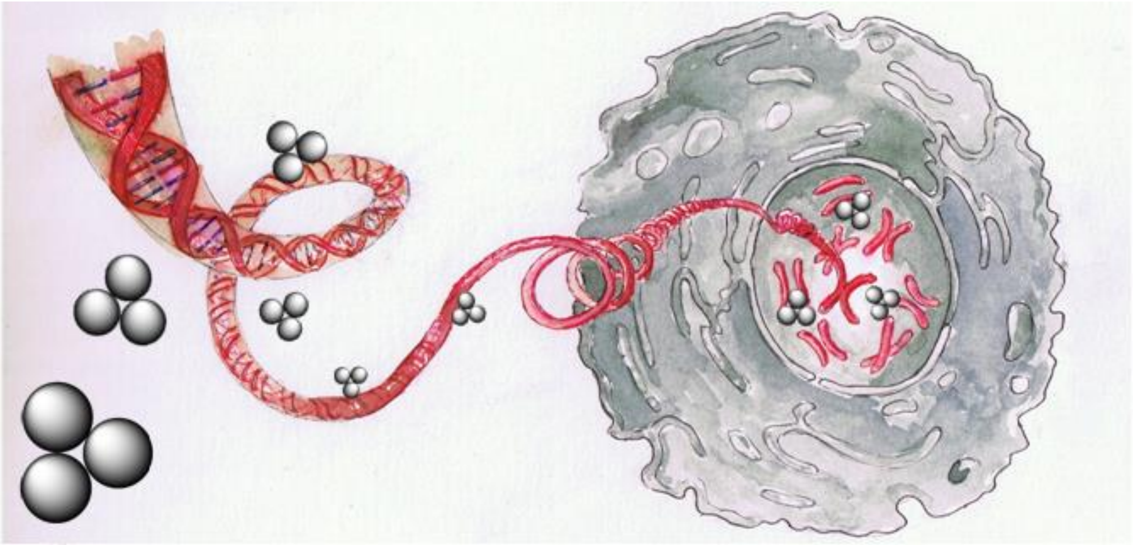

The bactericidal effect of silver has been known for many centuries, although the exact mechanism (or mechanisms) of action still remains unclear. Silver ions (Ag^+) or silver nanoparticles (NPs) have been proposed to be responsible for this effect [181,182]. It is worth noting that the cytosol of the cells is a very reducing environment in order to keep reactive oxygen species (ROS) at very low levels [183], so Ag^+ could be reduced to Ag^0. For this reason, we explore in this work the biological effect of small neutral triatomic silver clusters (Ag_3), which could get form in bacteria exposed to silver.

These Ag_3 clusters had been shown to intercalate into DNA inducing some changes in the dsDNA molecule at very low concentrations [107]. Many vital biological processes, such as replication and transcription, take place through the formation of specific protein-DNA complexes, in which the enzymes need to recognize their DNA binding site by either recognition of specific sequences or recognition of DNA geometry. Changes in the DNA structure could impede this recognition disrupting the enzyme activity.

On one hand, using DOX as a model DNA ligand, we assessed whether the modifications induced by very low concentrations of Ag_3 in the DNA structure could modify or even prevent the DNA/DOX interaction. ITC, fluorescence and circular dichroism titrations demonstrated that the formation of the intercalated complex PD_1, previously characterized in **Chapter III** of this thesis, could not get formed when DNA had been incubated overnight with only one Ag_3 cluster for every 200 BP of DNA. As a negative control, the same experiments were carried out incubating DNA overnight with Ag^+ ions instead of with Ag_3, and the formation of PD_1 was not inhibited.

On the other hand, the effect of Ag_3 on the biological activity of DNA-binding enzymes was studied by the group of Prof. Fernando Domínguez (CiMUS, Santiago de Compostela, Spain). In particular, they tested the effect exerted on proteins that bind to DNA in a sequence-dependent mode, such as the restriction enzyme HindIII, and proteins that recognize DNA geometry, such as type II topoisomerases. They found that the activity of these enzymes was inhibited at nanomolar concentration levels of Ag_3. In addition, they studied the bactericidal activity against various species of bacteria isolated from clinical samples, finding that Gram-positive bacteria were more resistant to the Ag_3 treatment than Gram-negative bacteria, probably due to the action of the peptidoglycan layer in the cell wall present in Gram-positive bacteria. In any case, Ag_3 displayed great bactericidal activity against some of the Gram-negative isolates.

Resistance to antibiotics is one of the biggest threats to global health, so there is a major interest in the developing of new antibiotics that could help overcome this problem. In this work, we described for the first time the bactericidal activity of AQCs (**Figure 1**), which are currently being studied in depth not only as potential antibiotics, but also as enhancers of the anticancer activity of certain drugs.

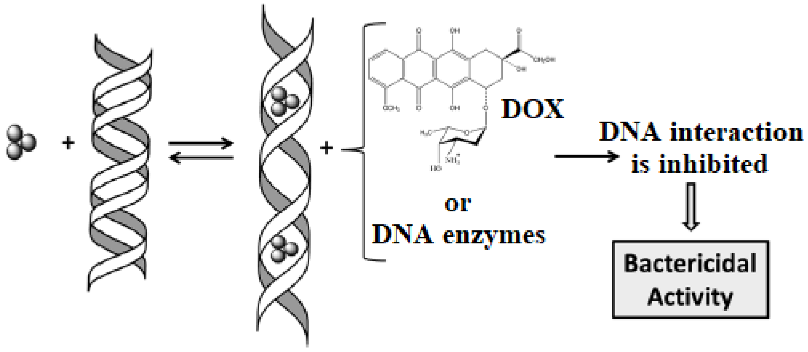

Figure 1. Schematic representation of the bactericidal activity of Ag_3.

Volume 6 | Number 12 | December 2015 | Pages 6681–7356

Chemical Science

www.rsc.org/chemicalscience

ISSN 2041-6539

ROYAL SOCIETY OF CHEMISTRY

EDGE ARTICLE

B. García, F. Dominguez *et al.*

Interaction of silver atomic quantum clusters with living organisms: bactericidal effect of Ag_3 clusters mediated by disruption of topoisomerase–DNA complexes

Chemical Science

ROYAL SOCIETY OF CHEMISTRY

EDGE ARTICLE

View Article Online
View Journal | View Issue

Cite this: *Chem. Sci.*, 2015, **6**, 6717

Interaction of silver atomic quantum clusters with living organisms: bactericidal effect of Ag_3 clusters mediated by disruption of topoisomerase–DNA complexes[†]

J. Neissa,[‡a] C. Pérez-Arnaiz,[‡b] V. Porto,[a] N. Busto,[b] E. Borrajo,[a] J. M. Leal,[b]
M. A. López-Quintela,[c] B. García*[b] and F. Dominguez*[a]

Essential processes for living cells such as transcription and replication depend on the formation of specific protein–DNA recognition complexes. Proper formation of such complexes requires suitable fitting between the protein surface and the DNA surface. By adopting doxorubicin (DOX) as a model probe, we report here that Ag_3 atomic quantum clusters (Ag-AQCs) inhibit the intercalation of DOX into DNA and have considerable influence on the interaction of DNA-binding proteins such as topoisomerase IV, *Escherichia coli* DNA gyrase and the restriction enzyme HindIII. Ag-AQCs at nanomolar concentrations inhibit enzyme activity. The inhibitory effect of Ag-AQCs is dose-dependent and occurs by intercalation into DNA. All these effects, not observed in the presence of Ag^+ ions, can explain the powerful bactericidal activity of Ag-AQCs, extending the knowledge of silver bactericidal properties. Lastly, we highlight the interest of the interaction of Ag clusters with living organisms, an area that should be further explored due to the potential consequences that it might have, both beneficial and harmful.

Received 5th June 2015
Accepted 13th July 2015

DOI: 10.1039/c5sc02022k

www.rsc.org/chemicalscience

Introduction

The bactericidal properties of silver have been known since ancient times; however, nowadays the underlying mechanisms are only poorly understood. Whether silver nanoparticles (NPs),[1] silver ions (Ag^+)[2] or both are responsible for the cytotoxicity of silver is open to discussion,[2–4] largely because of their relative bioavailability.[5] Cells can reduce Ag^+ to the metallic form, which constitutes a well-known biosynthetic method to prepare NPs.[6] On the other hand, NPs taken up into eukaryotic cells dissolve quickly and chemical species of silver change over time from Ag^0 to Ag–O– to Ag–S– forms.[7] NPs are unstable in the presence of excess of S-containing chemicals such as glutathione, present in cells at millimolar levels,[8] which can etch NPs to produce Ag clusters.[9] At the same time, in the course of the formation of NPs by reduction of Ag^+, stable Ag clusters can also be formed.[10] Therefore, the possibility that Ag clusters are present in bacteria exposed to silver should not be excluded.

Earlier, we have reported that Ag_3 clusters (denoted here as Ag-AQCs) interact with DNA through intercalation.[11] The effect exerted by Ag-AQCs on the DNA conformation is stronger than by classical intercalators such as acridines or ethidium bromide, mainly for two reasons: (a) Ag atoms have larger radii than C atoms and the unwinding and subsequent lengthening of the double helix induced by Ag-AQCs is in consequence larger than that occasioned by polycyclic aromatic ligands;[11] and (b) the dissociation rate constant for the Ag-AQCs/DNA complex is several orders of magnitude lower than those with classical intercalators,[11] thus prolonging the residence time in the intercalated position. In a topologically closed DNA domain, changes in the secondary structure are immediately reflected by a change in the overall shape, helping to disrupt the protein binding. This outcome raises naturally the question of whether Ag-AQCs can inhibit the binding of DNA-ligands. To shed some light on this issue, we firstly address the effect of Ag-AQCs, incubated in DNA, on the DOX–DNA binding. Likewise, for comparison purposes, a parallel study replacing Ag-AQCs by Ag^+ ions was carried out. DOX is a renowned member of the anthracycline family, a very effective type of anticancer drugs currently in use.[12–14] Recently, we have studied the interaction of DOX with calf thymus DNA (ct-DNA), reporting that this system is able to form a strong intercalated-groove DOX–DNA complex.

---

[a] *Department of Physiology and Centro de Investigaciones en Medicina Molecular y Enfermedades Crónicas (CIMUS), University of Santiago de Compostela, E-15782 Santiago de Compostela, Spain. E-mail: fernando.dominguez@usc.es*

[b] *Department of Chemistry, University of Burgos, E-9001 Burgos, Spain. E-mail: begar@ubu.es*

[c] *Department of Physical Chemistry, Fac. Chemistry and Nanomag Laboratory, IIT. University of Santiago de Compostela, E-15782 Santiago de Compostela, Spain*

[†] Electronic supplementary information (ESI) available: Fig. 1SI and 2SI and fitting procedure of eqn (1SI). See DOI: 10.1039/c5sc02022k

[‡] JN and CP-A equally contributed to this paper.

This journal is © The Royal Society of Chemistry 2015

The formation of this complex is categorized kinetically as a two-step mechanism in which the fast step is the groove binding of the amino sugar moiety and the slow step is the intercalation of the anthracycline group.[15] We hypothesize that the distortion of the DNA groove as a consequence of the intercalation of Ag-AQC reported earlier[11] is responsible for the inhibition of the binding of DOX to DNA.

We then study the effect of the Ag-AQCs incubated in DNA on major groove binding proteins such as topoisomerase IV, *E. coli* DNA gyrase and the restriction enzyme HindIII. Lastly, the effects of Ag-AQCs in living organisms were assessed by evaluation of their antibacterial activity. A schematic diagram of the research performed is outlined in Fig. 1.

Results and discussion

Influence of Ag-AQCs and Ag^+ ions on the DNA–DOX interaction

The study of ternary systems containing DOX, DNA and Ag-AQCs (or silver ions, used for comparison purposes) was conducted by isothermal titration calorimetry (ITC) and circular dichroism (CD) measurements. This physicochemical study will allow us to learn the effect caused by the cluster, once intercalated into the DNA, on different types of groove-binders. The study is composed of two types of experiments: (1) titration with DOX of a DNA sample previously incubated overnight with submicromolar amounts of Ag^+ ($C_{DNA} : C_{Ag^+} = 200$), and (2) identical conditions, replacing Ag^+ by Ag-AQCs.

The ITC profile was generated by adding micromolar amounts of DOX (C_D, molar concentration) to: (a) ct-DNA + Ag^+ (Fig. 2A), and (b) ct-DNA + Ag-AQCs (Fig. 2B), (C_P stands for the DNA concentration expressed as molar base pairs). Table 1 collects the thermodynamic binding constants, K_1 and K_2, obtained for DOX/(ct-DNA + Ag^+) using a two-sites model; for comparison, the same data for the DOX/ct-DNA system is also included. The small diminution of the K_1 and K_2 values for DOX/(ct-DNA + Ag^+) relative to DOX/ct-DNA indicates that the Ag^+ ions exert only a small effect on the binding of DOX to ct-DNA. In contrast, a substantially different behavior was observed in the presence of Ag-AQCs (Fig. 2B); Ag-AQCs species are responsible for the observed full inhibition of the intercalation of DOX into ct-DNA, even for very small $C_{DNA}/C_{Ag\text{-}AQCs}$ ratios.

Fig. 2 also shows the CD spectra recorded upon addition of micromolar amounts of DOX to (ct-DNA + Ag^+) and to (ct-DNA + Ag-AQCs). The set of CD spectra and the molar ellipticity *versus* C_D/C_P plot recorded for DOX/(ct-DNA + Ag^+) at $\lambda = 275$ nm (Fig. 2C, inset) and those for DOX/ct-DNA[15] are very similar, meaning that the effect of the Ag^+ ions on the CD spectra is trivial. In contrast, the pattern obtained with Ag-AQCs differs noticeably; disappearance of the positive bands at 240 and 500 nm, and the observed increase of the negative band at 540 nm both denote heavy structural distortion of the DNA. The molar ellipticity profile at $\lambda = 275$ nm (Fig. 2D, inset) reveals that, in the presence of Ag-AQC, the strong intercalated-groove complex is not formed for both DOX–DNA and DOX/(DNA + Ag^+) systems, as stacking interactions are characterized by positive variation around 275 nm.[15] However, the observed diminution of $[\theta]$ for $C_D/C_P > 0.4$ indicates that an external complex could be formed.

Likewise, formation of the non-fluorescent complex DOX/Ag-AQCs has been studied in the absence of DNA. Fig. 1SIA† shows the isotherm plot; fitting of the data pairs (see ESI†) yielded the value $K = (2.9 \pm 0.1) \times 10^8\ M^{-1}$. Regarding absorption measurements, the isosbestic points at 300 and 350 nm in the set of spectral curves of Fig. 1SIB† support interaction between DOX and Ag-AQCs; by contrast, lack of spectral changes in the titration of DOX with Ag^+ reveals that no reaction is at work.

The ITC results have shown that the interaction with DNA of the species resulting from DOX + Ag-AQCs differs only slightly from the interaction of DOX with DNA (Fig. 2SI†); the constants obtained for DOX–DNA were only an order of magnitude greater than those obtained for (DOX + Ag-AQCs)/DNA (see Table 1).

In summary, so far we can conclude that Ag-AQCs intercalated into DNA are responsible for the observed non-intercalation of DOX into DNA and also that Ag-AQCs strongly interact with DOX in the absence of DNA. This study affords useful information to understand the mechanisms of inhibition of biological groove-binding agents, such as proteins, by Ag-AQCs.

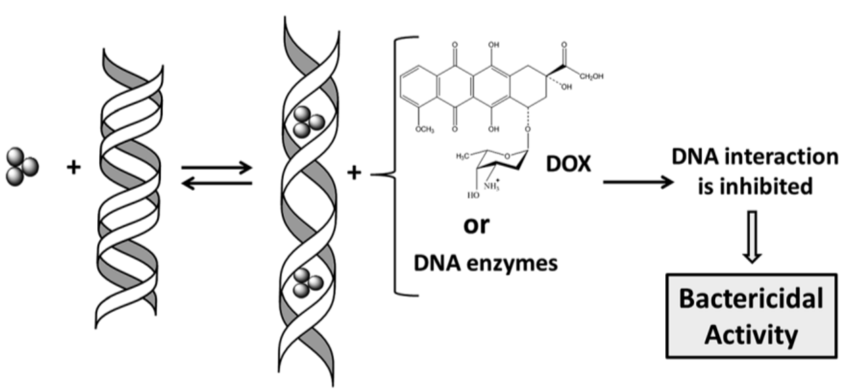

Fig. 1 Schematic representation of the bactericidal activity of Ag-AQC. The inhibiting action of different types of groove-binders is due to the enlargement and subsequent distortion of DNA caused by intercalation of the cluster.

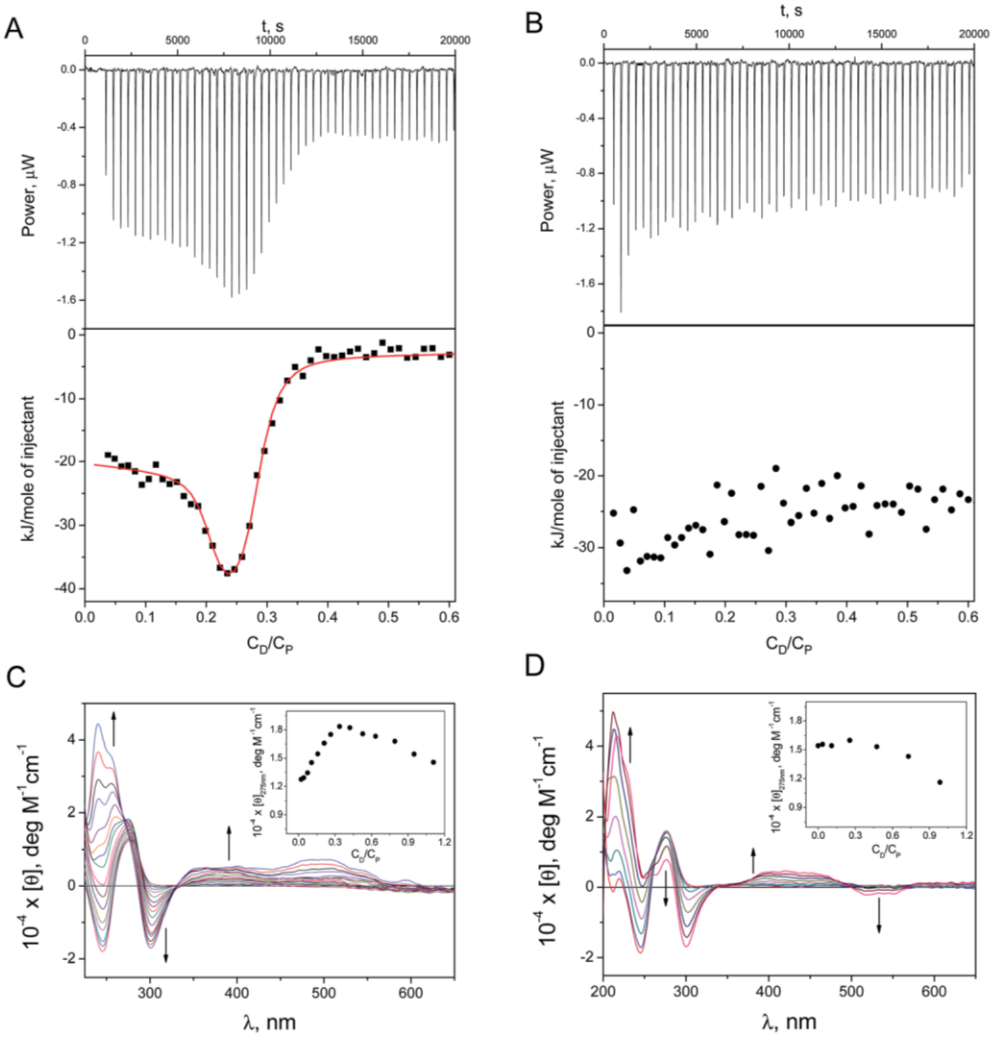

Fig. 2 Ag-AQCs clusters prevent the binding of DOX to ct-DNA. ITC profile obtained for (A) DOX/(ct-DNA + Ag^+) system, and (B) DOX/(ct-DNA + Ag-AQCs) system, $C_P = 400$ μM. CD spectra recorded for (C) DOX/(ct-DNA + Ag^+) system, and (D) DOX/(ct-DNA + Ag-AQCs) system. Inset: molar ellipticity *versus* C_D/C_P ratio at $\lambda = 275$ nm, $C_P = 50$ μM. Ionic strength = 2.5 mM, pH = 7 and $T = 25$ °C.

Ag-AQCs affect the biological activity of DNA-binding proteins

We also looked into the influence of Ag-AQCs on groove-binding agents such as DNA-binding proteins, for Ag-AQCs inhibit the binding of DOX to DNA. Initially, we focused on proteins that can bind to DNA in a dependent sequence mode, such as restriction enzymes; these enzymes recognize DNA with pronounced selectivity, as this is the basis to provide defense mechanism against invading foreign DNA. HindIII is a restriction enzyme that cuts pTG7 (4892 bp plasmid DNA), releasing two fragments of 3757 and 1135 bp (Fig. 3A, lane 3). Ag-AQCs at nanomolar levels inhibited HindIII restriction activity (Fig. 3A, lanes 4–12). On the other hand, Ag^+ at 6 μM concentration,

Table 1 Thermodynamic constants obtained for binding of DOX/ctDNA, DOX/(1Ag^+ + 200 base pair ct-DNA) and (DOX + Ag-AQCs)/ct-DNA using a two-sites model. K_1 corresponds to the bifunctional (intercalative–groove binding) complex and K_2 to the external complex. K calculated from fluorescence experiments. Ionic strength = 2.5 mM, pH = 7 and $T = 25$ °C

	$K_1{}^a$ (M^{-1})	$K_2{}^a$ (M^{-1})	K^b (M^{-1})
DOX/ctDNA	$(2.3 \pm 0.8) \times 10^8$	$(9.3 \pm 0.7) \times 10^5$	
DOX/(ctDNA + Ag^+)	$(4 \pm 2) \times 10^7$	$(7 \pm 1) \times 10^5$	
DOX/(ctDNA + Ag-AQCs)	—	—	
(DOX + Ag-AQCs)/ctDNA	$(1.0 \pm 0.4) \times 10^7$	$(6 \pm 1) \times 10^4$	
DOX/Ag-AQC			$(2.9 \pm 0.1) \times 10^8$

[a] From ITC experiments; K_1 and K_2 for DOX–DNA taken from ref. 15. [b] From fluorescence experiments.

higher than any dose of Ag-AQCs used, produced no effect (Fig. 3A, lane 13). Thus, as occurs with DOX intercalation, the inhibitory action of the enzymatic cleavage is characteristic of Ag-AQCs, but not of Ag^+ ions.

DNA binding proteins can recognize DNA binding sites by two types of mechanisms: recognition of specific DNA sequence[16] and recognition of DNA geometry such as type II topoisomerases.[17] Bacteria require topoisomerases, that is, proteins that specifically alter the DNA topology to enable DNA replication. Therefore, we also studied the effects of Ag-AQCs on two members of bacterial type II topoisomerases, topoisomerase IV (Topo IV) and DNA gyrase.

The decatenation activity assay for Topo IV utilizes the kinetoplast DNA (kDNA), a large network of interlocked (catenated) circles, which cannot enter the agarose gel.[18] *E. coli* Topo IV decatenates the circles from the network (Fig. 3B, lane 1); the free circles are detected upon decatenation as discrete bands on the gel (Fig. 3B), nicked open-circular, and covalently closed-circular DNA (NOC and CCC, respectively). Ag-AQCs at nanomolar concentration levels inhibited the Topo IV activity (Fig. 3B, lanes 3–14) with an IC_{50} value of (roughly) 16 nM.

Topo IV, a type II enzyme with remarkable similarity in sequence to DNA gyrase, can relax but not introduce negative supercoils into DNA.[19] The activity of *E. coli* gyrase can be assessed by a supercoiling based assay in which a relaxed plasmid DNA, pBR322, is treated with *E. coli* DNA gyrase. This enzyme converts the relaxed topoisomers to the SC form of the plasmid, which migrates faster on agarose gel. Also an upper band corresponding to the nicked OC DNA is visible, which was also present in the relaxed substrate, but co-migrates with some of the relaxed topoisomers (Fig. 3C, lane 1). Ag-AQCs at nanomolar levels inhibited the activity of *E. coli* gyrase (Fig. 3C, lanes 2–11). Notably, we found that SC DNA had less mobility in the presence of increasing Ag-AQCs concentrations (Fig. 3C, lanes 4–11, dotted red line) concurrent with the observation that the negative SC DNA may have slightly less mobility than normal, depending on the amount of intercalant bound to DNA.[20] The different mobility of SC DNA clearly indicates that the Ag-AQCs

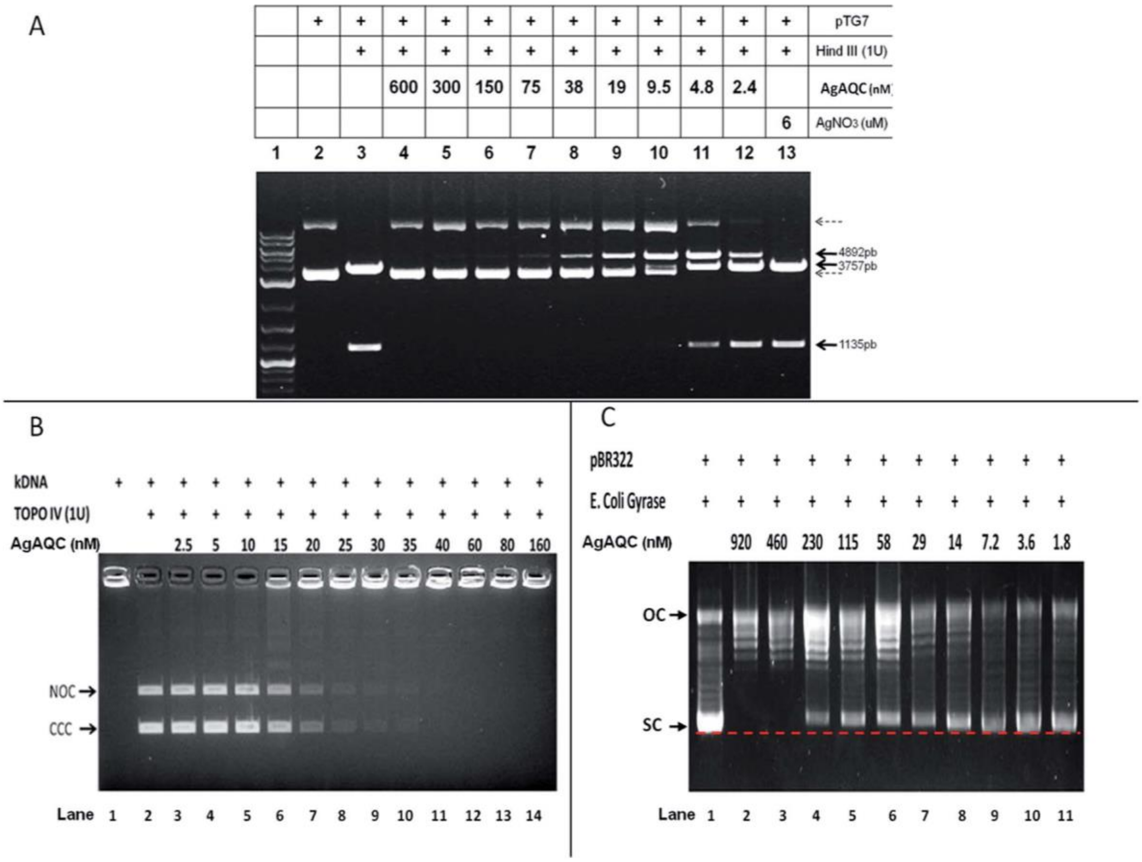

Fig. 3 Agarose gel electrophoresis showing the inhibition by Ag-AQCs of (A) restriction enzyme HindIII activity. The pTG7 plasmid (lane 2) was incubated for 30 min at 37 °C with one HindIII unit (lane 3) in the presence of nanomolar concentration of Ag-AQCs (lanes 4–12), or $AgNO_3$ (6 μM, lane 13), the reaction products were run on agarose gel. Continuous arrows indicate the theoretical products obtained after cut of the plasmid. Dotted arrows indicate the location of the plasmid with different supercoiling conformations. Lane 1, molecular weight markers. (B) *E. coli* topoisomerase IV decatenation activity. This gel contains ethidium bromide, which allows one to clearly resolve topoisomerase IV generated nicked (NOC) and covalently closed circular (CCC) DNA. The kDNA networks are too large to enter the gel; (C) *E. coli* DNA gyrase activity. The open-circular (OC) and supercoiled (SC) DNA are resolved and the relaxed DNA species are present as a Gaussian distribution of topoisomers, SC DNA has less mobility with increasing Ag-AQCs concentrations (dotted red line, lanes 4–9). The images are representative of at least three independent experiments.

inhibitory effect occurs by intercalation into DNA in a dose-dependent manner, the inhibition being greater the larger the number of Ag-AQCs intercalated into DNA.

Ag-AQCs bactericidal activity

The topological consequences of intercalation are even more evident in bacteria, whose circular genomes exist in a tightly regulated topological state.[21] Actually, DNA gyrase is affected *in vitro* by the presence of Ag-AQCs, therefore we explored whether it could also be affected *in vivo*. Fig. 4A shows that Ag-AQCs at low concentration display antimicrobial activity against *E. coli*. It has been reported that gyrase inhibitors induce oxidative damage cellular death in *E. coli*;[22] hence, the effect of Ag-AQCs on the bacterial ROS levels was investigated. As shown in Fig. 4B, addition of Ag-AQCs to bacteria increases the superoxide levels over the controls, indicating that the bactericidal activity of Ag-AQCs could be partially mediated by oxidative damage.

Ag-AQCs have a prominent inhibitory effect on bacterial DNA topoisomerases, that is, mediated by the distortion of the DNA topology. The DNA structure is evolutionarily well preserved, suggesting that any change affecting it could also affect multiple bacteria species. To probe this argument, we tested the activity of Ag-AQCs against randomly selected bacteria isolated from clinical samples representing various species. Interestingly, not all of the isolates were equally susceptible to the Ag-AQCs bactericidal action (Fig. 4C). After treatment with Ag-AQCs, five isolates showed strongest resistance to 50% viability. So far it is unknown whether this differential susceptibility is an outcome of the particular isolates or it is common to the species they belong to. However, our data point to

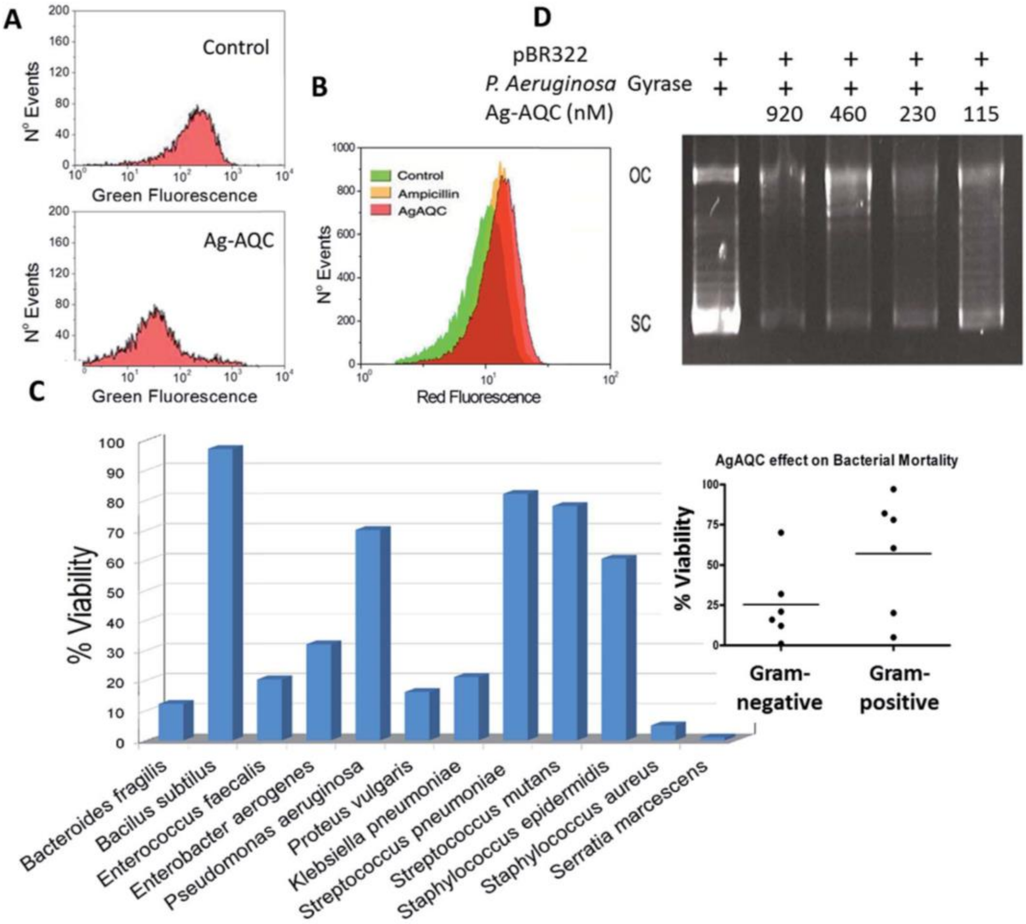

Fig. 4 (A) Bacterial survival. *E. coli* were treated for 3 h with vehicle (control) or with Ag-AQCs (83 ng ml^{-1}) and stained with the green fluorescent vital dye Syto 9; the number of green cells (viable bacteria) was assessed with flow cytometer. The image is representative of at least three independent experiments. (B) ROS generation. *E. coli* was treated for 3 h with Ag-AQCs (83 ng ml^{-1}) (red), ampicillin (5 μg ml^{-1}) (yellow) and vehicle (green). At the end of the incubation dihydroethidium was added to detect the presence of ROS, superoxide, and the fluorescence was assessed with flow cytometer. The image is representative of at least three independent experiments. (C) Bacteria isolated from clinical samples were treated for 1 h with Ag-AQC (83 ng ml^{-1}) and grown for 20 h. At the end of the incubation, the absorbance at 600 nm was read, percentage viability is assessed as the percentage of absorbance of the Ag-AQCs treated bacteria *versus* control (vehicle). Inset: percentage viability of bacteria from different species grouped according to Gram-staining (horizontal lines, mean values of the group). Mean values of two independent experiments. (D) *P. aeruginosa* DNA gyrase activity. The OC and SC DNA are resolved and the relaxed DNA species are present as a Gaussian distribution of topoisomers. SC DNA has less mobility with increasing Ag-AQCs concentration. The images are representative of at least two independent experiments.

bacterial species as the key factor in Ag-AQCs resistance. In fact, Gram-positive bacteria seem to be more resistant than Gram-negative (Fig. 4C, inset); actually, four out of five resistant strains were Gram-positive. The difference among Gram-positive and Gram-negative species is the presence of a thick peptidoglycan layer in the bacterial cell wall. The interaction of Ag-AQCs with DOX shown here (Fig. 1SI†) is an example of a more general interaction of Ag-AQCs with aromatic and cyclic compounds (unpublished results). Therefore, one can speculate that the increased resistance of Gram-positive bacteria could be explained by the action of the peptidoglycan of the wall cell that prevents Ag-AQCs from entering the bacteria. The only Gram-negative isolate displaying above 50% survival was *Pseudomonas aeruginosa*. This observation led us to consider whether *P. aeruginosa* gyrase could be less sensitive than *E. coli* gyrase to the action of Ag-AQCs, which could explain the increased resistance of *P. aeruginosa*. We assessed the activity of *P. aeruginosa* DNA gyrase in the presence of Ag-AQCs and found it as sensitive to the Ag-AQCs action as *E. coli* DNA gyrase (Fig. 4D and 3C, respectively). Therefore, we are inclined to believe that the resistance should be due to insufficient Ag-AQCs concentration inside the bacteria to kill them. Supporting this view, it has been described that most strains of *P. aeruginosa* produce diffusible cyclic pigments[23] that may interact with Ag-AQCs, restraining its entry into the bacteria.

Human resistance to antibiotics is a worldwide problem.[24] Use of antibiotics is the most important single event leading to resistance.[25] Ag-AQCs is a new material whose beneficial and useful bactericidal action could provide an alternative to antibiotics that manifest resistance. Our preliminary results point in that direction and deserve further study. Finally, the interest of Ag-AQCs, which are able to interact with living organisms, should be highlighted, as this is an area that should be explored due to the potential consequences it may have, both beneficial and harmful. In a previous work[11] we calculated theoretically that Ag_3 intercalates, whereas Ag_2 binds covalently to the DNA. However, so far obtaining sufficiently pure samples of Ag_2 for biological assays has not been feasible. In view of the interesting biological activities showed by Ag_3 it should be of interest to undertake a systematic study of the chemical and biological effects of silver clusters of different sizes. Such study will depend on future developments of synthetic strategies for the preparation of monodisperse cluster samples without strong binding ligands, which may affect their biological activities. This is currently a main challenge.

In summary, we have described for the first time that Ag-AQCs display bactericidal activity. These findings give way to new promising avenues to extend the understanding of the silver microbicidal properties, an important topic that has been discussed for centuries without having yet been resolved.

Experimental

Unless otherwise stated, all chemicals were obtained from Sigma-Aldrich. Stock solutions of DOX were prepared by dissolving weighed amounts at pH = 7.0 in a buffer containing 2.5×10^{-3} M sodium cacodylate (NaCaC), $[(CH_3)_2AsO_2Na]$. ct-DNA was dissolved in water and sonicated employing a MSE-Sonyprep sonicator (20 cycles of 10 s each, with 20 s pause between cycles, 96 μm amplitude). The sonicator tip was introduced directly into the solution, which was kept in an ice bath to minimize thermal effects. Agarose gel electrophoresis tests showed that the polymer length was reduced to approximately 1000 base pair fragments. Aqueous solutions were prepared with doubly deionized water from a Puranity TU System with UV lamp and ultrafilter (VWR). Stock solutions were standardized spectrophotometrically using $\varepsilon = 13\,200$ M^{-1} cm^{-1} at $\lambda = 260$ nm, ionic strength = 0.1 M (0.975 M NaCl + 0.025 M NaCaC) and pH = 7.0.

Ag_3 clusters were obtained by an electrochemical procedure, as previously described.[11] In a typical synthesis, a three-electrode chemical cell was used with two foil electrodes, Ag (working) and Pt (counter) electrodes, and a hydrogen reference electrode. 2 V constant voltage was applied for 1200 s in nitrogen deaerated MiliQ water at 25 °C. Prior to synthesis, the silver electrode was polished with sand paper (600 grid, Wolfcraft) followed by alumina (≈50 nm, Buehler), washed thoroughly with MiliQ water and sonicated. The platinum electrode was cleaned electrochemically by cyclic voltammetry in 1 M MeOH/1 M NaOH solution followed by cyclic voltammetry in 1 M H_2SO_4. After the synthesis, the remaining Ag^+ ions were removed by addition of NaCl and subsequent precipitation and filtration. Purified samples (Ag-AQCs) were then concentrated at 35 °C using a rotary evaporator. Sample characterization was carried out by UV-Vis and fluorescence spectrometry, cyclic voltammetry, ESI-TOF mass spectrometry, X-ray absorption near edge structure (XANES) and atomic force microscopy, as previously described.[11]

Isothermal titration calorimetry

The ITC experiments were performed at 25 °C using a Nano ITC Instrument (TA, Waters LLC, New Castle, USA). To prevent formation of air bubbles, all of the solutions were degassed in a degassing station (TA, Waters LLC, New Castle, USA). DOX solutions were placed in a 50 μL syringe continuously stirred and 50 additions of 1 μL in 400 s intervals were injected into the sample cell containing the buffer or the ct-DNA solution previously incubated with Ag^+ or Ag-AQCs. Control experiments were carried out to determine the contribution of the heat of dilution of both ct-DNA and DOX. The integration of the peaks, corrected by the dilution effect, yielded the binding isotherms (heat change *versus* C_D/C_P mole ratio). All of the data were analyzed using the NanoAnalyze software.

Circular dichroism titration

The CD titrations were recorded on a MOS-450 Bio-Logic dichrograph (Claix, France) using 1.0 cm path-length cells. The titrations were carried out by injecting increasing DOX micro amounts into a known volume of the ct-DNA solution previously incubated with Ag^+ or Ag-AQCs.

Fluorescence titration

Fluorescence titrations were performed on a Shimadzu Corporation RF-5301PC spectrofluorometer (Duisburg, Germany) at

$\lambda_{exc} = 490$ nm and $\lambda_{em} = 555$ nm by adding increasing amounts of Ag-AQC directly into the cell with the DOX solution.

Topoisomerase IV decatenation assay

E. coli topoisomerase IV activity was assessed using a commercial kit (Inspiralis, UK). Briefly, 200 ng of kDNA were preincubated for 5 min at room temperature with Ag-AQCs at various concentrations in 40 mM HEPES–KOH (pH 7.6), 100 mM potassium glutamate, 10 mM magnesium acetate, 10 mM DTT, 1 mM ATP and 50 μg ml ^{1} albumin, in 30 μl total reaction volume. After that, 1U of Topo IV was added and incubation was continued for 30 min at 37 °C. The reaction was stopped by addition of 30 μl chloroform/iso-amyl alcohol and 6 μL of loading buffer 6×, vortexed and centrifuged briefly (5–10 seconds each) before being loaded on an agarose gel (1%: w/v) in TAE (40 mM Tris–acetate, 2 mM EDTA) buffer with ethidium bromide (0.5 μg ml ^{1}). The IC_{50} for inhibition of decatenation was assessed using gel documentation software and statistical analysis of 3 independent experiments.

Gyrase supercoiling assay

The activity of gyrase from *E. coli* and *P. Aeruginosa* were assessed using the gyrase supercoiling kit according to the manufacturer (Inspiralis, UK). Briefly, 0.5 μg of relaxed pBR322 DNA were preincubated for 30 min at room temperature with Ag-AQCs in 30 μl reaction under the following conditions: 35 mM Tris–HCl (pH 7.5), 24 mM KCl, 4 mM $MgCl_2$, 2 mM DTT, 1.8 mM spermidine, 1 mM ATP, 6.5% (w/v) glycerol and 0.1 mg ml ^{1} BSA. After that, 1U of gyrase was added and incubation was continued for 30 min at 37 °C. The reaction was stopped by addition of 30 μl chloroform/iso-amyl alcohol and 6 μL of loading buffer 6× before being loaded on an agarose gel (1%: w/v) in TAE (40 mM Tris–acetate, 2 mM EDTA) buffer without ethidium bromide. At least three independent experiments were conducted for each gyrase.

Assay of HindIII activity

pTG7, a 4892 base pairs plasmid, is cut by HindIII in two sites releasing a 1135 bp fragment. 300 ng of pTG7 was cut with 1 enzyme Hind III unit (New England Biolabs), 10 mM Tris–HCl, 50 mM NaCl, 10 mM $MgCl_2$, 1 mM DTT at pH 7.9 in 25 μl final volume for 30 min at 37 °C. When required, Ag-AQCs were added at the beginning of the incubation at different concentrations. The reaction products were run in 1% agarose gel. At the end of the running the gel was stained in TAE buffer with 0.5 μg ml ^{1} ethidium bromide.

Bactericidal assay

Briefly, *E. coli* (ATCC 25922) were picked from an agar plate and grown in Luria Bertani medium (LB) at 37 °C with 225 rpm constant agitation. Growth was monitored turbidimetrically and adjusted to achieve the standard McFarland 0.5 (OD 620 nm between 0.08 and 0.13), about 1×10^8 cfu ml ^{1}. Bacteria (5×10^5 cfu ml ^{1}) were incubated for 1/2 h at 37 °C in 60 μl final volume of PBS in the presence of different doses of Ag-AQCs, after which they were centrifuged and resuspended in LB medium and grown for 3 h. At the end of the incubation 50 μl of bacteria were mixed with 25 μl Syto 9 (Life Technologies) and green fluorescence was assessed by flow cytometry (Guava, EasyCyte, Merk-Millipore). Bacteria isolated from clinical samples were kindly provided by the Department of Microbiology, Faculty of Medicine, University of Santiago de Compostela, Spain. Briefly, bacteria were selected from an agar culture and grown in Mueller-Hinton broth (MHB) at 37 °C with 225 rpm constant shaking. Growth was monitored by turbidimetry and adjusted to the McFarland Standard no. 0.5 (OD 620 nm between 0.08 and 0.13), approximately 1 × 108 cfu ml ^{1}. A bacterial inoculum of approximately 5 × 105 cfu ml ^{1} was incubated with different Ag-AQCs doses for 1 h at 37 °C in 60 μL final volume PBS. At the end of the incubation, bacteria were centrifuged and resuspended in MHB and grown for 20 h. Turbidity was observed by reading the absorbance at 600 nm on a plate reader. Additionally, we determined whether the treatment with the maximum concentration of Ag-AQCs could inhibit colony formation on agar plates.

Detection of reactive oxygen species (ROS)

Dihydroethidium (DHE) (Life Technologies), by virtue of its ability to freely permeate cell membranes, is extensively used to monitor superoxide production. DHE essentially detects superoxide radicals. *E. coli* were grown in LB to a density equivalent to McFarland standard 0.5 (OD 620 nm between 0.08 and 0.13) and then diluted 10-fold to obtain an inoculum of approximately 1×10^7 cfu ml ^{1}. Ag-AQCs, diluted in medium, were added and incubated for 3 h at 37 °C under 225 rpm constant stirring. To equalize the number of bacteria in all of the samples, at the end of the incubation the absorbance was read at 620 nm and adjusted to be the same in all samples before addition of DHE (5 μm/100 μl). After 20 min, samples were extensively washed with PBS and the fluorescence present in the bacteria was assessed by flow cytometry (Guava, EasyCyte, Merk-Millipore). A minimum of 20 000 events were captured on the region of interest.

Acknowledgements

This work was supported by Obra Social"la Caixa" (OSLC-2012-007), European Commission through FEDER program (0681 InveNNta 1 E); Ministerio de Ciencia e Innovación, Spain (MAT2010-20442, MAT2011-28673-C02-01); MINECO, Spain (MAT2012-36754-C02-01 and CTQ2014-58812-C2-2-R), Xunta de Galicia, Spain (GRC2013-044, FEDER Funds). C. P.-A. is grateful for the FPU grant from Ministry of Education, Culture and Sports, Madrid, Spain (FPU13/00180).

Notes and references

1 J. R. Morones, J. L. Elechiguerra, A. Camacho, K. Holt, J. B. Kouri, J. T. Ramirez and M. J. Yacaman, *Nanotechnology*, 2005, **16**, 2346–2353.

2 M. I. Setyawati, X. Yuan, J. Xie and D. T. Leong, *Biomaterials*, 2014, **35**, 6707–6715.

3 X. Yuan, M. I. Setyawati, D. T. Leong and J. Xie, *Nano Res.*, 2014, **7**, 301–307.

4 X. Yuan, M. I. Setyawati, A. S. Tan, C. N. Ong, D. T. Leong and J. Xie, *NPG Asia Mater.*, 2013, **5**, e39.

5 J. Y. Maillard and P. Hartemann, *Crit. Rev. Microbiol.*, 2013, **39**, 373–383.

6 D. Mandal, M. E. Bolander, D. Mukhopadhyay, G. Sarkar and P. Mukherjee, *Appl. Microbiol. Biotechnol.*, 2006, **69**, 485–492.

7 X. Jiang, T. Miclăuş, L. Wang, R. Foldbjerg, D. S. Sutherland, H. Autrup, C. Chen and C. Beer, *Nanotoxicology*, 2015, **9**, 81–89.

8 D. Nies, S. Silver and D. Nies, in *Molecular Microbiology of Heavy Metals*, Springer Berlin Heidelberg, 2007, vol. 6, pp. 117–142.

9 B. S. Gonzalez and M. A. Lopez-Quintela, in *Functional Nanometer-Sized Clusters of Transition Metals: Synthesis, Properties and Applications*, The Royal Society of Chemistry, 2014, pp. 25–50.

10 Y. A. Attia, D. Buceta, C. Blanco-Varela, M. B. Mohamed, G. Barone and M. A. López-Quintela, *J. Am. Chem. Soc.*, 2014, **136**, 1182–1185.

11 D. Buceta, N. Busto, G. Barone, J. M. Leal, F. Domínguez, L. J. Giovanetti, F. G. Requejo, B. García and M. A. López-Quintela, *Angew. Chem., Int. Ed.*, 2015, **54**, 7612–7616.

12 C. Carvalho, R. X. Santos, S. Cardoso, S. Correia, P. J. Oliveira, M. S. Santos and P. I. Moreira, *Curr. Med. Chem.*, 2009, **16**, 3267–3285.

13 G. Minotti, P. Menna, E. Salvatorelli, G. Cairo and L. Gianni, *Pharmacol. Rev.*, 2004, **56**, 185–229.

14 Y. Pommier, E. Leo, H. L. Zhang and C. Marchand, *Chem. Biol.*, 2010, **17**, 421–433.

15 C. Pérez-Arnaiz, N. Busto, J. M. Leal and B. García, *J. Phys. Chem. B*, 2014, **118**, 1288–1295.

16 D. Suman and G. S. Kumar, *J. Mol. Struct.*, 2008, **872**, 56–63.

17 R. Rohs, S. M. West, A. Sosinsky, P. Liu, R. S. Mann and B. Honig, *Nature*, 2009, **461**, 1248–1253.

18 A. K. McClendon, A. C. Gentry, J. S. Dickey, M. Brinch, S. Bendsen, A. H. Andersen and N. Osheroff, *Biochemistry*, 2008, **47**, 13169–13178.

19 J. L. Nitiss, E. Soans, A. Rogojina, A. Seth and M. Mishina, *Current Protocols in Pharmacology*, 2012, unit 3.3.

20 A. D. Bates and A. Maxwell, *DNA Topology*, Oxford University Press, 2005.

21 Inspiralis,technical information, http://www.inspiralis.com/go/gyrase_supercoiling.php.

22 F. Yang, S. S. Teves, C. J. Kemp and S. Henikoff, *Biochim. Biophys. Acta*, 2014, **1845**, 84–89.

23 D. J. Dwyer, M. A. Kohanski, B. Hayete and J. J. Collins, *Mol. Syst. Biol.*, 2007, **3**(91), 1–15.

24 D. Greenwood, M. Barer, R. Slack and W. Irving, *Medical Microbiology*, Churchill Livingstone, 18th edn, 2012.

25 WHO Antimicrobial resistance, Fact sheet No. 194, Updated April 2015, Centers for Disease Control and Prevention, Antibiotic resistance threats in the United States, 2013, http://www.cdc.gov/drugresistance/threat-report-2013/index.html.

This journal is © The Royal Society of Chemistry 2015

Electronic Supplementary Information

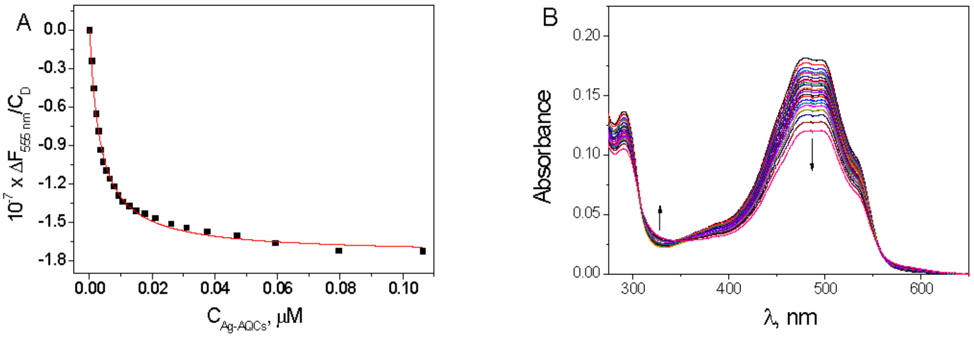

Fig. 1SI A) Fluorescence binding isotherm for DOX/Ag-AQCs system; the continuous line is obtained by fitting of eq (1) to the data pairs. B) Variation of the absorbance spectra during the titration of DOX with Ag-AQC. $0 < C_{Ag\text{-}AQC}/C_D < 0.01$ in the arrows sense, $C^0_D = 5 \times 10^{-5}$ M, I = 2.5 mM, pH = 7 and T = 25 °C.

The fitting of eq (1) to the $\Delta F/C_D$ data pairs versus the equilibrium concentration [Ag-AQCs] has enabled us to obtain by iteration the value $K = (2.9 \pm 0.1) \times 10^8\ M^{-1}$ $\Delta\phi$ being the change in the fluorescence optical variable; only few iterations sufficed to attain the convergence.

$$\frac{\Delta F}{C_D} = \frac{K \cdot \Delta\phi \cdot [Ag - AQCs]}{1 + K \cdot [Ag - AQCs]} \qquad (1SI)$$

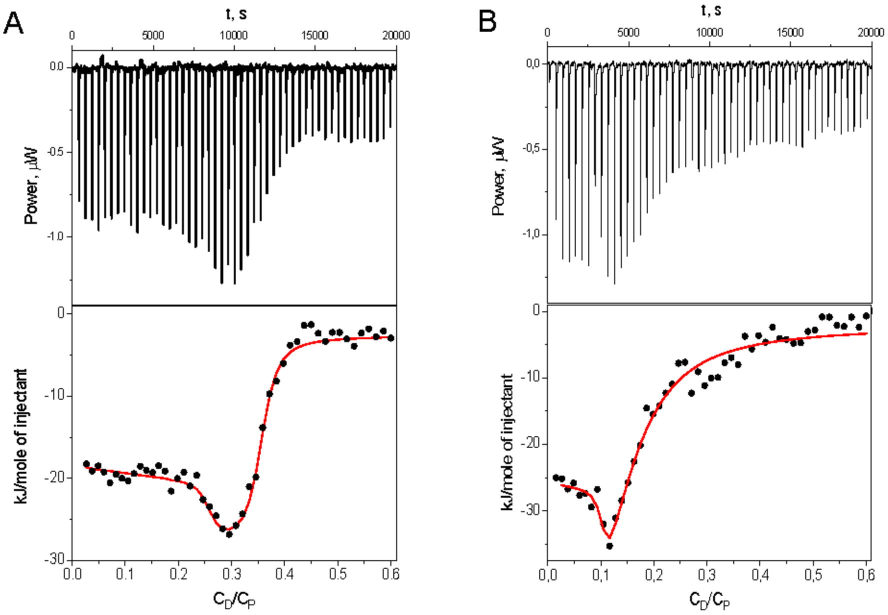

Fig. 2SI ITC profile obtained for the DNA/DOX system (**A**) (taken from ref. 12), and (Ag-AQCs + DOX)/DNA system (**B**). $C_D = 0.8$ mM, $C_{DNA} = 0.4$ mM, pH = 7, I = 2.5 mM, T = 25 °C.

Capítulo V

Interacción con ADN y Proteínas de Complejos de Platino con Ligandos N^N Dadores. Consecuencias en su Citotoxicidad.

Summary

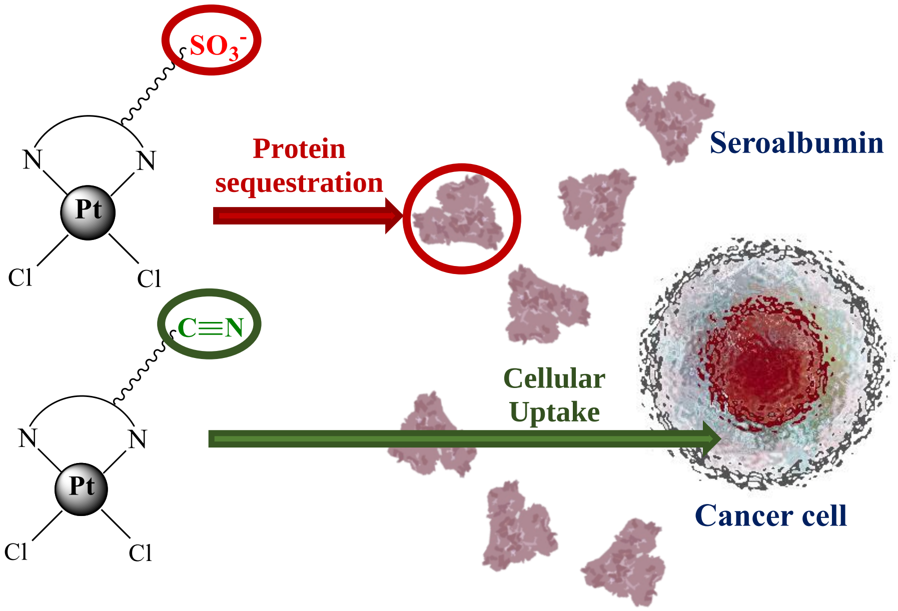

Figure 1. The role of seroalbumin in the cytotoxicity of four new cis-dichloro Pt(II) complexes with (N^N)-donor ligands bearing functionalized tails has been explored. These four Pt complexes can bind to DNA. However, the nature of their functionalized tails is a key factor that determines their ability to interact with seroalbumin proteins present in the extracellular medium, which prevents them from reaching their target.

Given the potent anticancer properties of the metal complex cisplatin and knowing its mode of action [58], we have explored the cytotoxicity and the binding to DNA and proteins of four new cis-[$PtCl_2$(N^N)] complexes bearing different functionalized tails. Two of them (**1** and **2**) present N-substituted pbi ligands (pbiR = 1-R-2-(2-pyridyl)benzimidazole) and the other two complexes (**3** and **4**) present 4,4'-disubstituted bpy ligands (bpy = 2,2'-bipyridine). These complexes were synthesized and characterized by the group of Prof. Blanca R. Manzano and Prof. Félix A. Jalón (Universidad de Ciudad Real, Spain).

First, the substitution of the chlorido ligands of the complexes for other solvent molecules (DMSO and H_2O) was studied by means of UV-Visible spectroscopy, as the biological activity of cisplatin derivatives is often related to the substitution of their chlorido ligands for other solvent molecules such as H_2O, and the following covalent binding to DNA [57]. The next step was to study their interaction with dsDNA by means of DSC, CD, viscosity measurements and agarose gel electrophoresis, in order to determine whether these complexes were capable of interacting with DNA. The set of results pointed to the formation of covalent bonds between DNA and complexes **1**, **2** and **3**; and of a non-covalent interaction in the case of complex **4**. These conclusions also concurred well with ^1H NMR measurements carried out with the platinum complexes in the presence of deoxyguanosine monophosphate (dGMP) by Dr. Mónica Vaquero (data not shown in this thesis). However, despite their ability to interact with DNA, they all were found to be non-toxic against human lung adenocarcinoma A549 cell line using the standard cell culture conditions.

It was therefore reasonable to think that these complexes were incapable of reaching their target in the cell, which would prevent them from displaying a cytotoxic effect. In order to study if some component present in the cell culture medium was responsible for this setback, additional experiments were carried out varying certain characteristics of the medium. In particular, it was found that the decrease in the fetal bovine serum (FBS) concentration in the culture medium from 10 % to 1 % (v/v) induced a marked increase in the cytotoxic activity of the platinum complexes. Cisplatin was included as a control, and its cytotoxicity was nearly the same in the presence of 10 % or 1 % FBS.

FBS contains a large amount of proteins. In particular, bovine serum albumin (BSA) is one of its major components. Considering this, CD measurements and native acrylamide electrophoresis were performed to evaluate whether the interaction of the platinum complexes with BSA could be the reason for their low cytotoxicity. Indeed, the results point to the sequestration of the complexes in the extracellular medium by proteins such as BSA as the key factor responsible for the lack of cytotoxic activity (**Figure 1**). In fact, uptake experiments demonstrated that complexes **2** and **3**, the ones that caused the strongest effect on the BSA conformation, were incapable of entering the cell. This sequestration seems to be related to the nature of the functionalized tails of these complexes, which could be useful in the future rational design of new platinum complexes with improved biological properties.

1. Introduction.

Despite the notable advances in the discovery of new anticancer drugs that could become an alternative to cisplatin, some of the disadvantages of this compound remain unsolved satisfactorily in our days [57,184]. It is therefore necessary to continue designing new active structural fragments and to modify those that have proved to be ineffective, probably because they present limitations in reaching their target. For example, certain factors such as protein binding or lipophilicity have a determinant impact on the absorption, distribution, metabolism and excretion processes of many anticancer drugs [185].

There is a wide variety of Pt complexes analogous to cisplatin that can be found in the literature. Among them, [$PtCl_2$(bpy)] (bpy = 2,2'-bipyridine) and other complexes with bpy bisubstituted in the 4,4' positions and rollover cyclometalated Pt compounds based in the same backbone exhibit much lower cytotoxic activity than cisplatin [186,187]. Comparable lack of activity has been found for the [$PtCl_2$(Hpbi)] (Hpbi = 2-(2'-pyridyl) benzimidazole) counterparts [188,189]. These results are surprising taking into account the high cytotoxicity of many compounds with the cis-$PtCl_2$ unit and may indicate the existence of limitations in the arrival of these molecules to their targets. In contrast, the also neutral organometallic derivative [PtMe(DMSO)(pbi)] (pbi = deprotonated form of Hpbi) shows a notable cytotoxic activity against A2780 and A2780R cancer cell lines [190], which indicates that minor changes in their structure can induce pronounced differences in the biological activity.

In this work the effect of different side lateral functionalized chains in both pbi and bpy ligands of cis-$PtCl_2$ derivatives (**Chart 1**) on their cytotoxicity and their ability to bind to DNA and protein models are explored. According to the literature, the side-chains and functional groups present in these Pt complexes exert a favorable action in the effect of different drugs. The cyano-ethyl fragment, present in complex **1**, improved the cell permeability of drugs such as various JAK (Janus protein tyrosine kinases) inhibitors [191]. The biological activity of gold and silver N-heterocyclic carbenes bearing alkyl-sulfonate groups, as that included in complex **2**, has been studied both in bacteria [192] and in cancer cells [193]. Moreover, the propylsulfonate chain present in complex **2** forms part of merocyanine 540, a popular probe used as a model to study the permeation of cell membranes [194], and an important active molecule capable of distinguishing between the subtle differences in the plasma membranes of very similar cells such as leukemic and non-leukemic lymphocytes [195]. The 5-diethylamino-2-pentylamino group, present in ligand bpyam (see **Chart 1**) and in complex **3**, is a fragment widely used in drugs. Particularly relevant is its role in the formulation of the antimalarial drugs, chloroquine (CQ) and quinacrine (QC), in which the stated aminated tail of the drug is responsible for the accumulation of the drug in the digestive vacuole of the pathogen, the site of the drug action [196]. In addition, both of them are strong DNA intercalating agents with cytotoxic activity [197] that display a synergic effect in tumour cells treated with cisplatin [198]. Finally, the plane architecture of complex **4** makes it an interesting compound to be analyzed as a drug that could target DNA.

In summary, the biological properties of these four Pt complexes as well as their binding to relevant biomolecules such as DNA and serum proteins have been studied in order to identify the determinant factors of their cytotoxicity. For convenience, the Pt complexes are referred to as D and their concentrations to as C_D, and the biomolecules (DNA or proteins) to as P and their concentration to as C_P.

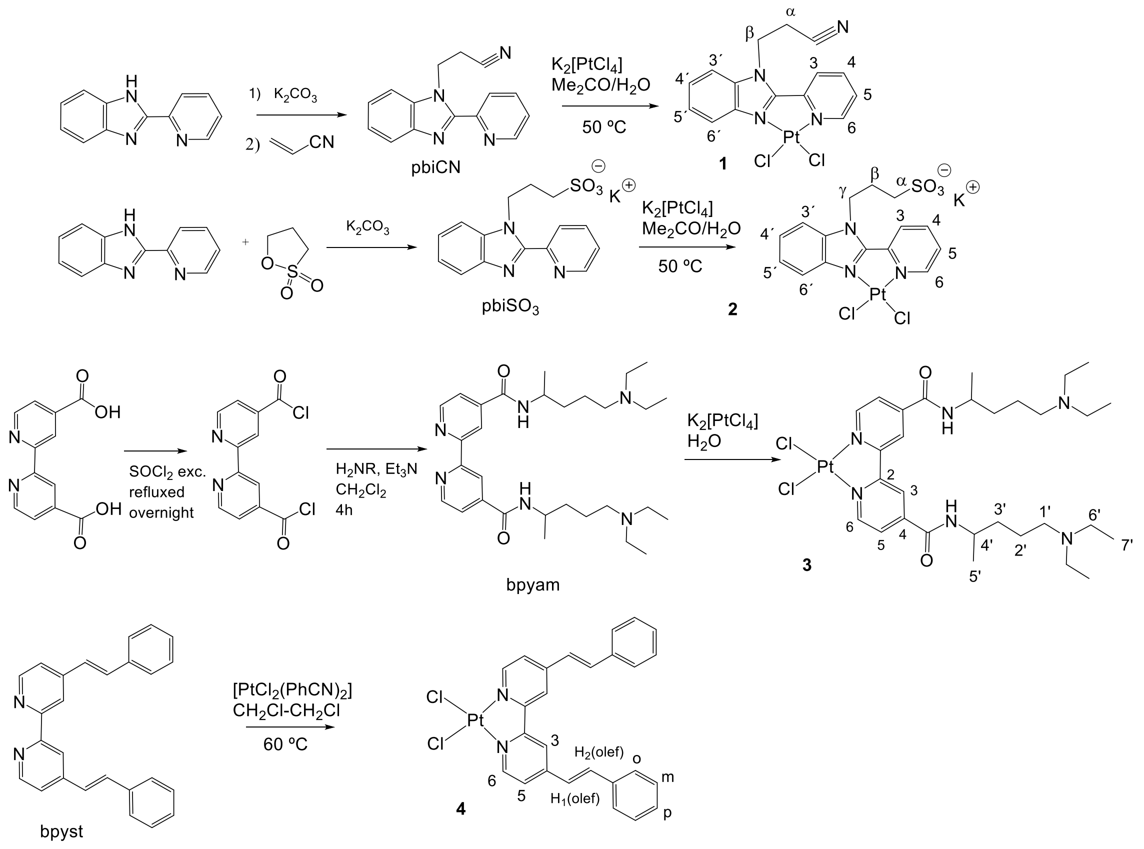
1) K_2CO_3
2) CN
pbiCN
$K_2[PtCl_4]$
Me_2CO/H_2O
50 ºC
1
K_2CO_3
pbiSO$_3$
2
$SOCl_2$ exc.
refluxed
overnight
H_2NR, Et_3N
CH_2Cl_2
4h
bpyam
$K_2[PtCl_4]$
H_2O
3
bpyst
$[PtCl_2(PhCN)_2]$
CH_2Cl-CH_2Cl
60 ºC
4
H_2(olef)
H_1(olef)

Chart 1. Structures and synthesis of ligands and complexes **1**–**4** kindly provided by the group of Prof. Blanca R. Manzano and Prof. Félix A. Jalón (Universidad de Ciudad Real, Spain).

2. Results and discussion.

2.1. Stability in DMSO and aqueous solution.

The biological activity of cisplatin and its derivatives is known to be related to the substitution of the chlorido ligands for other molecules such as H_2O, which then leads to the covalent binding with DNA [199]. As complexes **1-4** are soluble in DMSO, the concentrated stock solutions (20 mM) were prepared in this solvent and then diluted solutions in aqueous buffer medium were prepared prior to carrying out the experiments. Because of this, the stability of the complexes, both in DMSO and in aqueous buffer solution (2.5 mM NaCaC, pH = 7.4), was studied by means of spectrophotometric measurements. As to the chlorido substitution, monoexponential or biexponential kinetic processes were observed for complexes **1**, **3** and **4**, indicating that the substitution for DMSO takes place for one or both chlorido ligands. This substitution was not observed for complex **2**. As an example, **Figure 2** shows the biexponential behavior of complex **1** after being dissolved in DMSO. Once the DMSO substitution had finished, the complexes in DMSO were dissolved in water, and no spectral changes with time were observed for complexes **1**, **2** and **4**, which could indicate that once the DMSO-complexes are formed, the aquation does not take place. However, UV-Vis measurements provide kinetic evidence of the processes taking place in solution, but not structural information about the products that are being formed. For this reason, ^{1}H NMR measurements in DMSO and D_2O were carried out by Dr. Mónica Vaquero (Universidad de Burgos, Spain) to confirm all the spectroscopic observations, and the results about the DMSO and H_2O substitution for the four Pt complexes are summarized in **Table 1**.

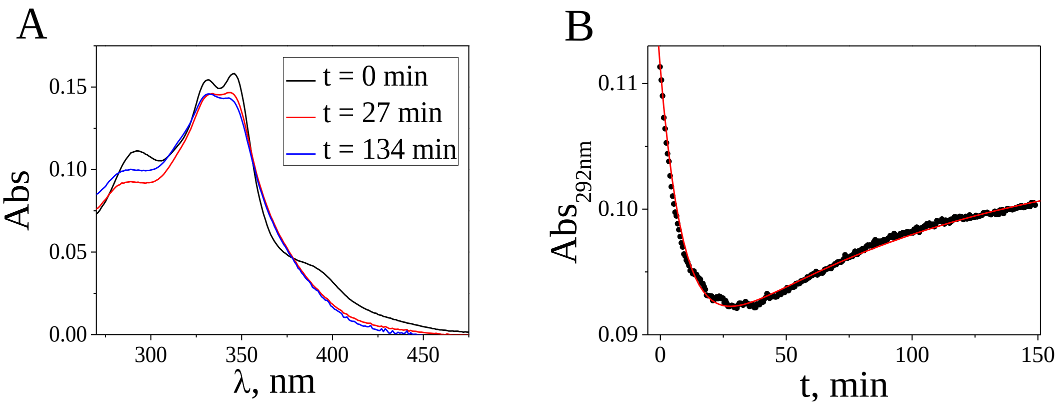

Figure 2. A) Representative absorbance spectra of complex **1** dissolved in DMSO at t = 0 min, 27 min and 134 min. **B)** Absorbance of complex **1** at λ = 292 nm *vs* time after being dissolved in DMSO and fitting of a biexponential equation ($k_1 = 0.0017\ s^{-1}$ and $k_2 = 0.0002\ s^{-1}$) to the experimental data (red line). C_D = 10 µM, DMSO, T = 25 °C.

2.2. DNA binding.

As mentioned before, the biological activity of cisplatin analogous is usually related to the establishment of covalent bonds with DNA. In particular, cisplatin is itself an inert compound that is activated by a series of aquation reactions in which one or both chlorido ligands are substituted by H_2O molecules [199]. These mono- and bi-aquated cisplatin forms are highly reactive and are prone to interact with different substrates, including DNA [200].

CD measurements of ctDNA with the four Pt complexes were carried out at different times, as certain modes of interaction such as covalent binding usually need hours or even days to be completed. Indeed, only complex **4** induced instant modifications in the CD spectra, which points towards the establishment of a rapid non-covalent interaction between **4** and DNA. **Figure 3** shows the CD and the viscosity titrations of ctDNA with increasing amounts of **4** carried out without a previous incubation period. In addition, agarose gel electrophoresis of pUC18 plasmid using cisplatin as a positive control was performed in order to completely rule out the presence of covalent binding with DNA. As can be seen in **Figure 4**, complex **4** did not cause changes in the migration of the characteristic plasmid DNA bands, whereas cisplatin induced remarkable differences.

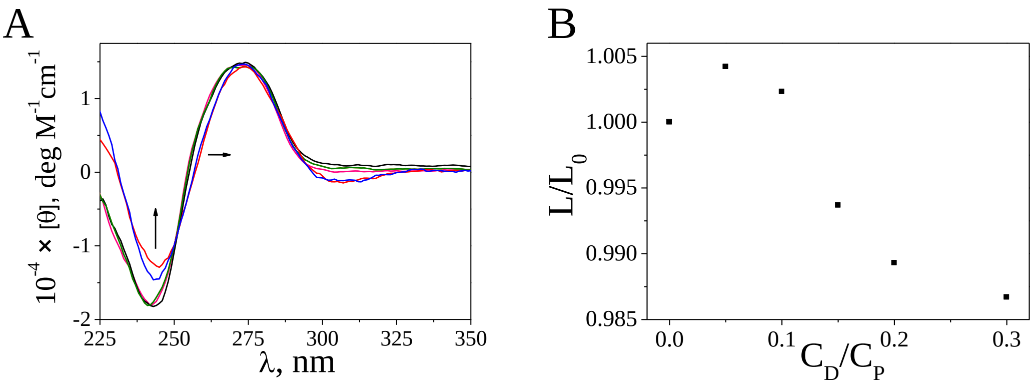

Figure 3. A) CD spectra of ctDNA in the presence of different concentrations of complex **4** (C_D/C_P = 0 - 1.2) without previous incubation period, $C_P = 8 \times 10^{-5}$ M. **B)** Relative elongation (L/L_0) of ctDNA treated with different concentrations of complex **4** (C_D/C_P = 0 - 0.3), $C_P = 2 \times 10^{-4}$ M. I = 2.5 mM (NaCaC, pH = 7.4), T = 25 ºC.

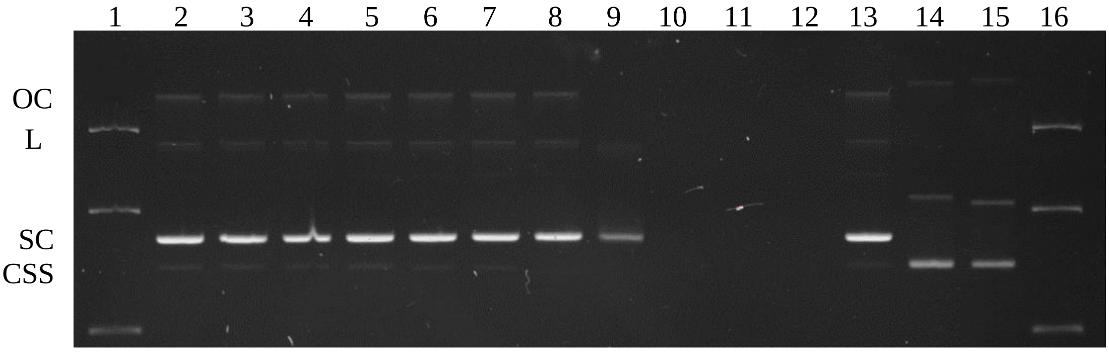

Figure 4. Agarose gel electrophoresis of plasmid pUC18 incubated overnight with different concentrations of complex **4** and with cisplatin as a positive control for covalent binding. Lanes 1 and 16: DNA ladder; lane 2 and 13: pUC18 alone; lane 3: pUC18 + DMSO; lanes 4-12: pUC18 + complex **4** at C_D/C_P concentration ratios = 0.1, 0.2, 0.5, 1, 2, 5, 10, 20 and 50; lanes 14 and 15: pUC18 + cisplatin at C_D/C_P concentration ratios = 1 and 10, respectively. Labelling: OC (nicked, open circular), L (linear), SC (supercoiled) and C, SS (circular, single-stranded).

On the contrary, there were remarkable changes in the DNA CD spectra with the time for complexes **1-3**. For example, in the case of complex **3**, the binding process took 72 h to be completed. **Figure 5.A** shows the final CD spectra of ctDNA incubated with complexes **1-4** for 72 h at a C_D/C_P ratio of 1, in order to compare their ability to modify the DNA structure under the same experimental conditions. Intense changes were induced upon binding of complexes **1-3**, whereas **4** exhibited the same slight modifications than those shown in **Figure 3.A**, that is, no changes were observed with the time with **4**.

DSC experiments were also carried out to provide additional information about the characteristics of the binding. **Figure 5.B** shows the thermograms obtained for ctDNA incubated alone or in the presence of complexes **1-4** at a C_D/C_P ratio of 0.5 for 72 h at 25 ºC (higher concentration ratios could not be studied due to precipitation phenomena).

Complex **4** induces a slight increase in T_m of 4.7 °C, which confirms once more the presence of interaction between complex **4** and DNA. In the cases of complexes **1, 2** and **3**, the increase in the T_m values were 32.5 °C, 9.7 °C and 25.3 °C, respectively. The largest ΔT_m values were induced by **1** and **3**, and could be related to the formation of interstrand cross-linkings, which stabilize the double stranded DNA structure [201].

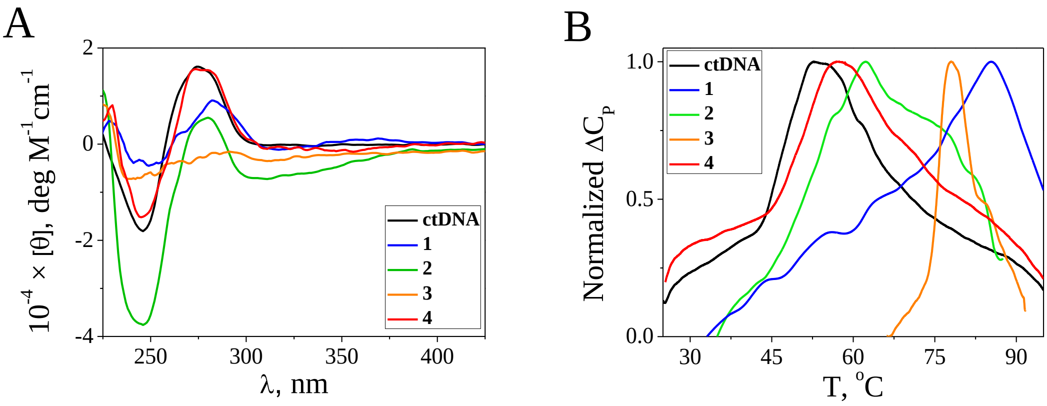

Figure 5. A) CD spectra of ctDNA incubated for 72 h with complexes **1-4** at a concentration ratio $C_D/C_P = 1$ ($C_P = 8 \times 10^{-5}$ M) at T = 25 °C, $C_{DMSO} = 0.4$ %. **B)** DSC thermograms of ctDNA incubated for 72 h with complexes **1-4** at a concentration ratio $C_D/C_P = 0.5$ ($C_P = 4 \times 10^{-4}$ M) at a scan rate = 1 °C/min, $C_{DMSO} = 1$ %. I = 2.5 mM (NaCaC, pH = 7.4).

^{1}H NMR experiments with deoxyguanosine monophosphate (dGMP) were also performed by Dr Mónica Vaquero with complexes **2** and **3** and confirmed the slow formation of covalent bonds (data not shown in this work). Complexes **1** and **4** could not be tested by means of this technique as they precipitated out at the concentrations required for the NMR experiments.

The summary of the results obtained for the substitution of the chlorido groups as well as for the covalent binding to dGMP and DNA is shown in **Table 1**. It is worth noting that, unlike cisplatin, it seems not to exist a clear correlation between the chlorido substitution by DMSO and H_2O and the covalent binding with DNA for complexes **1-3**.

Table 1. Summary of the results collected for the substitution of the chlorido ligands by DMSO and H_2O, the covalent binding with dGMP and ctDNA and the binding to BSA for **1-4**.

Complex	DMSO substitution	H_2O substitution	Covalent binding to *d*GMP^a	Covalent binding to DNA	BSA binding^b
1	✓	×	n.o.	✓	×
2	×	×	✓	✓	✓
3	✓	✓	✓	✓	✓
4	✓	×	n.o.	×	×

$^{a)}$ **1** and **4** could not be studied due to precipitation phenomena under the ^{1}H NMR experimental conditions. n.o.: not observed. $^{b)}$ For complex **4**, the interaction is only observed at high concentrations of complex ($C_D/C_P = 20$).

2.3. Cytotoxicity studies.

Once the characteristics of the binding with DNA had been studied, their cytotoxic activity against human lung carcinoma A549 cell line was evaluated by the MTT assay after an incubation period of 72 h. For comparison purposes, the cytotoxicity of cisplatin was also tested. The half-maximal inhibitory concentration (IC_{50}) values are summarized in **Table 2**. Although the four Pt complexes were capable of interacting with DNA either by covalent or non-covalent modes of binding, none of them displayed remarkable cytotoxicity compared to that of cisplatin. This set of results raises the question of which the determinant factors for their lack of cytotoxic activity are.

Many new metal complexes with novel modes of action, such as selective protein interaction that may lead to improved accumulation in the tumor and enhanced antiproliferative efficacy, have been reported [202]. However, it has also been reported that the binding of metal complexes to certain proteins present in the cell culture medium can affect negatively their uptake due to protein sequestration of the drug, which in turn affects their biological activity [185,203].

In order to shed light onto this issue, the cytotoxic activity of the complexes was tested against A549 cells in a comparative manner, using not only the standard serum supplemented (10 % FBS, Fetal Bovine Serum) but also a serum-deprived (1 % FBS) cell culture medium, including cisplatin in the study as a control. FBS contains a large amount of proteins that can interact irreversibly with certain drugs and drastically decrease their bioavailability. Indeed, the cytotoxicity of complexes **1**, **2** and **4** notably increased in serum-deprived medium following the trend **1** > **4** > **2** (see **Table 2**), in which the protein concentration was much lower. On the other hand, cisplatin is known to interact rather weakly with serum albumins such as HSA ($K = 8.52 \times 10^{2}\ M^{-1}$) [204], which explains why its cytotoxicity was nearly the same in the presence of 10 % or 1 % FBS. As to complex **3**, its cytotoxicity was very low even at 1 % FBS.

Table 2. Cytotoxic activity of complexes **1-4** and cisplatin after 72 h of treatment expressed as IC_{50} values (μM).

	IC_{50}, μM	
	A549[a]	A549[b]
1	> 100	39.7 ± 0.7
2	> 100	65 ± 3
3	> 100	> 100
4	> 100	41.9 ± 0.9
cisplatin	17 ± 1	14 ± 1

[a]Serum supplemented medium (10% FBS)

[b]Serum-deprived medium (1% FBS)

2.4. Protein binding.

Serum albumin plays a key role in the drug delivery process due to its binding properties and its abundance in blood plasma. Bovine serum albumin (BSA) is a suitable model for protein binding studies because of its resemblance with human serum albumin (HSA) [115]. Thus, considering the effect of the FBS concentration in the cytotoxicity of the Pt complexes, native acrylamide electrophoresis of BSA was performed to further examine whether protein binding could be a determinant factor in their cytotoxic activity. BSA was incubated with complexes **1-4** for 72 h in the dark at 25 ºC at C_D/C_P concentration ratios of 10 and 20 (**Figure 6**). Lanes 1 and 2 correspond to BSA alone and in the presence of the maximum concentration of DMSO used in the experiment (0.3 %). Complexes **2** and **3** affected in a deep manner the protein conformation (lanes 5-6 and 9-10). Complex **4** also interacted in some extent with BSA, but higher concentrations were needed to affect the BSA conformation, as at $C_D/C_P = 10$ there was still no noticeable effect on the migration of the protein band (lane 3). Complex **1** did not affect the migration of the BSA band even at high C_D/C_P ratios (lanes 7-8). Noteworthy, complexes **1** and **4** displayed the lower IC_{50} values against A549 cells when low FBS concentrations (1 %) were used (**Table 2**).

Lane	1	2	3	4	5	6	7	8	9	10
BSA (P)	+	+	+	+	+	+	+	+	+	+
Complex (D)	-	DMSO	**4**	**4**	**2**	**2**	**1**	**1**	**3**	**3**
C_D/C_P	-	-	10	20	10	20	10	20	10	20

Figure 6. Native acrylamide electrophoresis of BSA incubated with complexes **1-4** for 72 h at C_D/C_P concentration ratios of 10 and 20. $C_P = 1.5$ µM, $C_{DMSO} = 0.3$ %.

CD experiments (**Figure 7**) confirmed the native protein electrophoresis results. Complexes **2** and **3** induced a marked change in the characteristic negative band of BSA at $\lambda = 220$ nm. On the other hand, complex **4** modified only slightly this band, whereas complex **1** had almost no effect on the shape and intensity of the protein CD band, confirming that no interaction was established between **1** and BSA. Cellular uptake experiments were performed to check is these behaviors had an impact on the cell internalization of the metal complexes.

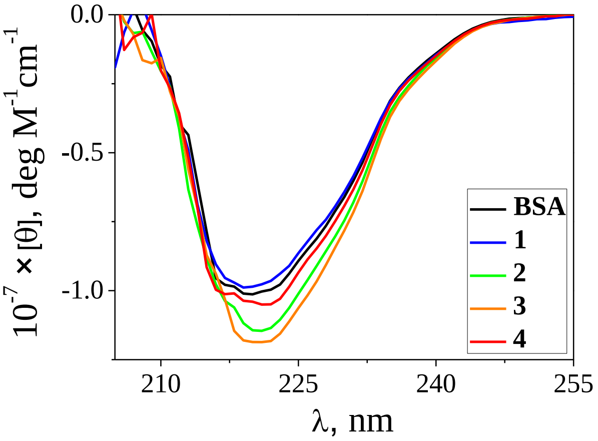

Figure 7. CD spectra of BSA incubated for 72 h in the absence and in the presence of complexes **1-4** at a C_D/C_P concentration ratio of 5. C_{BSA} = 0.5 µM, C_{DMSO} = 0.002 %, I = 2.5 mM (NaCaC, pH = 7.4), T = 25 ºC.

2.5. Cellular uptake.

The platinum accumulation in A549 cells after 4 h of treatment with complexes **1-4** at C_D = 10 µM was evaluated by ICP-MS measurements in order to verify if the interaction with the BSA present in the medium influenced their cell internalization. The results are summarized in **Figure 8**. Cisplatin was included as a positive control and its uptake concurred well with previously reported studies [205].

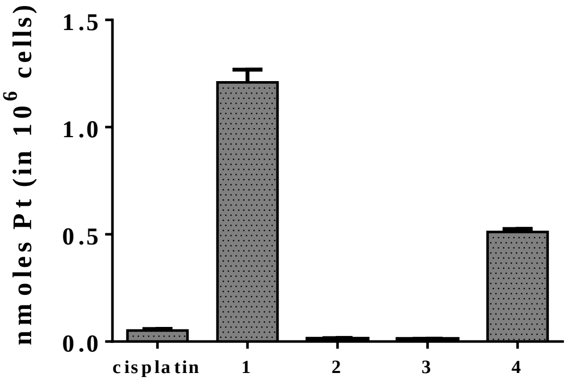

Figure 8. Platinum accumulation in A549 cells treated with complexes **1-4** and cisplatin at C_D = 10 µM for 4 h. Data were obtained from duplicates of two independent experiments and expressed as mean values (bars) ± SD.

Complex **1**, which did not interact with BSA, presents the highest metal accumulation in A549 cells. Complex **4** induced changes in the BSA conformation only at high C_D/C_P ratios (**Figure 6**), and also presents a higher uptake rate than cisplatin, although not as high as complex **1**. On the contrary, complexes **2** and **3**, the ones that induced drastic changes in the BSA conformation even at low C_D/C_P ratios, are incapable of entering the cell and reaching their target.

3. Conclusions.

On one hand, although there has been an active interest in finding new antitumor Pt complexes with behaviours similar to that of cisplatin, we have shown here that aquation is not a necessary step to bind to DNA covalently (see **Table 1**).

On the other hand, the distinct characteristics of the interaction of complexes **1-4** with BSA can be explained taking into account bibliographic available data. The binding of Merocyanine 540 to erytroid cells is hindered by the presence of serum proteins in the media, probably due to the presence of a propylsulfonate chain in its structure [195]. Thus, this moiety could be the determining factor for the interaction of complex **2** with BSA. As to complex **3**, it was published only very recently that chloroquine (that contains the lateral chain located on the backbone of complex **3**) can bind to HSA [206]. These type of complexes are prone to be sequestered by extracellular proteins, which can prevent them from entering the cell and reaching their target, as verified here by cellular uptake measurements. Indeed, complexes **2** and **3** displayed the highest IC_{50} values against A549 cell line (see **Table 2**). The set of results gathered in this work let us suggest that it is possible to perform a rational design of new functionalized Pt complexes avoiding structures that have been shown to bind to protein models such as BSA or HSA in order to improve their availability and, consequently, their cytotoxic activity.

PARTE 2

Interacción de TMPyP4 y de Complejos Metálicos de Ni, Cu y V con G-cuádruplex.

CAPÍTULOS VI, VII y VIII

“If G-quadruplexes form so readily *in vitro*,
Nature will have found a way of using them *in vivo*’”

Statement by Aaron Klug (Nobel Prize in Chemistry) over
30 years ago.

Aim of Part 2

Part 2 of this thesis is also divided into three Chapters, namely **Chapters VI**, **VII** and **VIII**. All of them deal with the study of G-quadruplexes.

Chapters VI and **VII** are focused on the study of human telomeric DNA, which consists of TTAGGG repeats, capable of forming G-quadruplex structures in solution [207]. Telomeres are located at the end of eukaryotic chromosomes and have vital roles in chromosome stability and the regulation of cell senescence [94]. One of the characteristics of telomeric G-quadruplex DNA is its high degree of polymorphism, as different G-quadruplex conformations have been determined for a given sequence [208]. In fact, its structure depends on factors such as the nature of the ions present in the medium (Na^+, K^+...), the flanking nucleotides of the oligonucleotide sequence or the presence of cosolvents [47,113,209,210]. For this reason, the first step was to characterize the behaviour of the specific sequence used in this work, which can be referred to as "Tel22" or "hTelo" (d[AGGG(TTAGGG)$_3$]), under our experimental conditions. **Chapter VI** corresponds to an already published short communication and presents the intramolecular processes of Tel22 that were observed in the microsecond timescale by T-Jump measurements [211]. After having characterized the kinetic behaviour of the Tel22 G-quadruplex both in Na^+ and K^+-containing solutions, we decided to use a well-known ligand to explore the kinetic behaviour of G-quadruplex binders also in the microsecond time-scale. Unlike with dsDNA, for which the kinetics and mechanisms of the different modes of interaction have been widely reported in the literature, this field was virtually unexplored for G-quadruplex structures. The organic molecule TMPyP4 was chosen to carry out this study that is also already published (**Chapter VII**) [212].

Chapter VIII of this thesis presents the results gathered during the predoctoral stay at Imperial College London (London, UK) under the supervision of Prof. Ramón Vilar (Faculty of Natural Sciences). This project aimed at studying and comparing a family of metal complexes bearing Ni, Cu and V metal centres that provided their structure with different degrees of planarity, in order to determine the consequences on their binding to various types of G-quadruplexes. The synthesis of the new complexes present in this work had been carried out by Dr Anna Łeczkowska and the project was being developed by Dr Jorge González.

Capítulo VI

Procesos Intramoleculares de la G-cuádruplex de ADN Telomérico

Summary

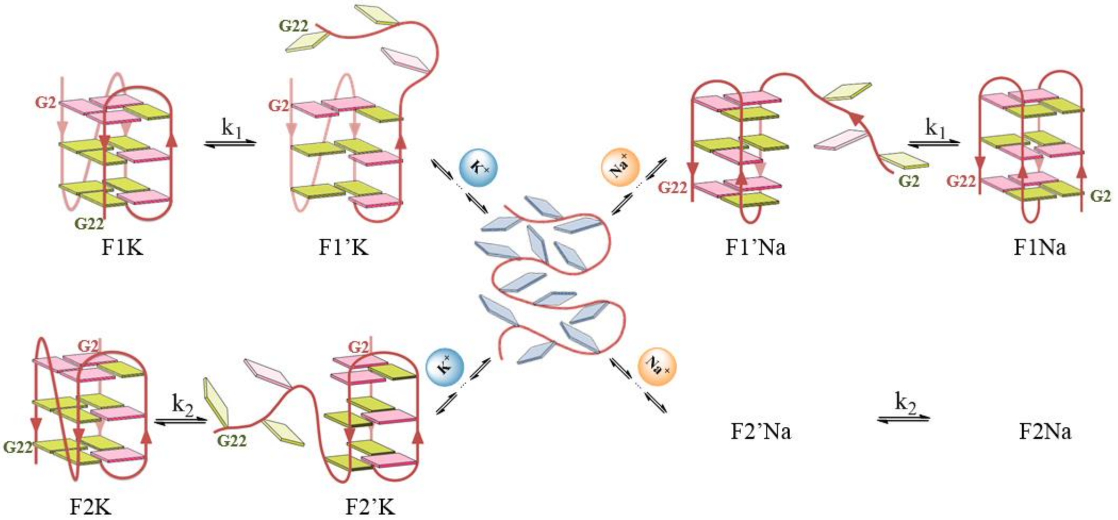

Figure 1. Schematic intramolecular reaction mechanism proposed to explain the kinetic behaviour of Tel22 G-quadruplex in the presence of K^+ or Na^+.

Human telomeric DNA consists of thousands of tandem repeats of the sequence $(TTAGGG)_n$ ending with a single-stranded DNA of 100-200 nucleotides. The shortening of telomeres to a critical length is a signal for cellular senescence [213], but this shortening is prevented by the activity of enzyme telomerase, which is upregulated in ≥ 85 % of human tumours [214]. This provides cancer cells with a telomere maintenance mechanism that contributes to cellular immortalization and tumour progression [215]. G-quadruplex formation in telomeric DNA has been shown to inhibit the activity of the enzyme telomerase, which is the reason for the high interest on the study of the G-quadruplex structures in this region.

In this communication, the results obtained from T-Jump relaxation kinetic experiments in the microsecond time-scale for the human telomeric G-quadruplex sequence Tel22 in solution are reported. First, we determined that all the kinetic curves belonged to intramolecular processes, as the kinetic constants did not depend on the G-quadruplex concentration. On the other hand, these curves had a biexponential character, giving way to two kinetic constants, k_1 and k_2, that had very close values but opposite amplitude sign. Interestingly, this behaviour was observed in the presence of both K^+ and Na^+ ions. The explanation can be found in the previously reported structural characteristics of telomeric G-quadruplex DNA, as two different G-quadruplex conformations are known to coexist in K^+ or Na^+ solutions. The two distinct intramolecular effects, corresponding to k_1 and k_2, should therefore belong to intramolecular processes of these two different conformations present in solution.

The next step was to elucidate the nature of these processes. Taking into account the kinetic constants reported for the different types of possible interactions, and the previously reported timescale estimated for the G-triplex – G-quadruplex conversion by computational calculations [216], we put forward the reaction mechanism shown in **Figure 1**, that concurred well both with our experimental data and with the results reported in the literature. It has been proposed very recently that G-triplex structures as those represented in **Figure 1** could represent a new approach to target G-rich sequences despite their transient state, and new ligands are being design with this aim [217].

RSC Advances

COMMUNICATION

View Article Online
View Journal | View Issue

Cite this: *RSC Adv.*, 2016, **6**, 39204

Received 16th February 2016
Accepted 7th April 2016

DOI: 10.1039/c6ra04203a

www.rsc.org/advances

New microsecond intramolecular reactions of human telomeric DNA in solution

Cristina Pérez-Arnáiz, Natalia Busto, José M. Leal and Begoña García*

Careful T-jump relaxation kinetic experiments in the microsecond timescale conducted in dilute solutions of human telomeric DNA at pH = 7.5 and 25 °C, have evinced for the first time two different equilibria. The sets of data recorded concur with two G-quadruplex ↔ G-triplex equilibria coexisting in the presence of both Na^+ and K^+-buffer ions.

Nucleic acids with four-stranded architectures, also known as G-quadruplexes, are endowed with technological applications and potentially impact biological regulation mechanisms and define a new area of research.[1–3] The possibility of building different conformations from the same sequence is a complex issue that confers G-quadruplexes with very interesting physical chemistry features. On the other hand, the obtaining of reliable kinetic data constitutes quite an adequate tool to determine reaction mechanisms between conformations in equilibrium. However, despite the number of articles published on G-quadruplex structures and related properties, equilibrium studies on fast intramolecular rearrangement remain virtually unexplored, whereas kinetic studies on irreversible folding–unfolding in solution abound in the literature.[4–10] The steps involved in such processes display a variety of rates. The fastest folding of G-quadruplexes involving four-stranded structures evolve between 40 and 80 ms in K^+ buffer,[6] and between 20 and 60 ms in Na^+ buffer, depending on the particular sequence.[10] In this work, we report on faster reactions between different structures in equilibrium in these buffers, once the G-quadruplexes are formed at 25 °C and pH = 7.5.

Telomeres, the ends of eukaryotic chromosomes, play an important role in cellular senescence and are central to the chromosome stability.[11] The human telomere presents single stranded overhanging at the 3′ end, which consist of repeats of the TTAGGG sequence that can fold into intramolecular G-quadruplexes. Thus, the representative d(AGGG(TTAGGG)$_3$) sequence of the human telomeric DNA, also known as 'Tel22', has been used to conduct this study. The T-jump relaxation technique is ideally suited to observe reactions in equilibrium capable of evolving in milliseconds to microseconds, provided that the reaction enthalpy differs from zero. To the best of our knowledge, this type of study has not been reported hitherto.

The type of G-quadruplex folding is determined by the type of ions in the medium, K^+ or Na^+,[5,12,13] whereas the DNA concentration,[14] the cosolvent used,[15] or even the sequence inversion in G-rich DNA from 5′ → 3′ to 3′ → 5′,[13] exert a substantial effect on the number of structures formed.

The circular dichroism (CD) spectra of Tel22 recorded in aqueous solution containing either 0.15 M NaCl or 0.15 M KCl (Fig. 1A) support G-quadruplex structures. In 0.15 M NaCl medium, the observed CD bands, positive at ~295 nm and negative at ~260 nm, reveal the presence of the basket-type G-quadruplex structure. Likewise, in 0.15 M KCl medium, the strong positive peak at ~290 nm, with a weak shoulder at ~250 nm, and the weak negative band at ~235 nm, primarily denote mixed parallel/antiparallel hybrid-type G-quadruplex structure.[16] Nevertheless, also is true that, despite these findings, different G-quadruplex polymorphic forms in solution

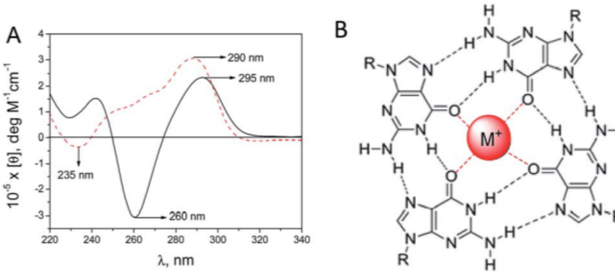

Fig. 1 CD spectra of Tel22 G-quadruplexes formed in the presence of 0.15 M NaCl (–) and 0.15 M KCl (- -). $C_P = 5\ \mu M$, pH = 7.5 (10 mM Tris–HCl, 1 mM EDTA) and $T = 25$ °C (A). G-Quartet structure stabilized by Hoogsteen H-bonding and a monovalent ion resided in the central channel (B).

Departamento de Química, Universidad de Burgos, E-9001, Burgos, Spain. E-mail: begar@ubu.es

This journal is © The Royal Society of Chemistry 2016

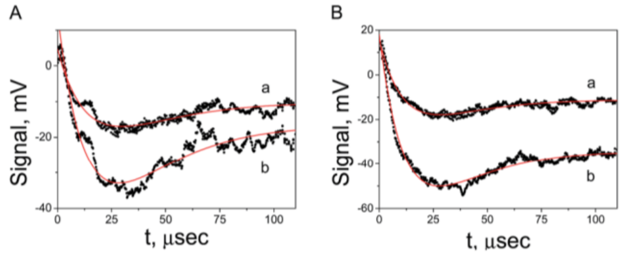

Fig. 2 T-Jump millivolts (mV)–time (t) relaxation curves recorded for Tel22 G-quadruplex (P) at C_P concentration, (a) $C_P = 5$ μM and (b) $C_P = 15$ μM in the presence of (A) 0.15 M NaCl and (B) 0.15 M KCl. $\lambda = 260$ nm, pH = 7.5 (10 mM Tris–HCl, 1 mM EDTA), $T = 25$ °C, $\Delta T = 2.5$ °C, rise time = 5 μs. Continuous red lines were obtained from biexponential fitting of eqn (1) to the data pairs.

should not be excluded, because the CD technique is useful to differentiate single conformations but not to distinguish between different polymorphisms of same conformation.[17]

Fig. 2 shows two examples of T-jump kinetic curves recorded at 25 °C and pH = 7.5 in 0.15 M NaCl and 0.15 M KCl solutions for two different Tel22 concentrations. The kinetic traces obtained in the presence of Na^+ (Fig. 2A) and K^+ (Fig. 2B) are very similar. The data treatment of equilibrium reactions monitored by T-jump relaxation measurements is compatible with exponential functions only, regardless of the number and concentration of reactants and products involved. Thus, the kinetic constants were obtained by fitting the biexponential kinetic eqn (1) to the relaxation curves:

$$A = A_1 e^{-k_1 t} + A_2 e^{-k_2 t} \tag{1}$$

where k_1 and k_2 are the kinetic constants (s^{-1}) that govern the two fast reactions.

The values obtained for k_1 and k_2 are independent of the Tel22 concentration (Fig. 3), revealing unimolecular mechanism in both Na^+ and K^+ buffering ions. Moreover, the average values for k_1 and k_2 were close to each other (Table 1), suggesting the occurrence of two concurrent reactions.

At the same time, the difference in intensity and sign of the reaction amplitudes A_1 and A_2 (Fig. 2), reveal different spectroscopic or thermodynamic features and confirm that the two reactions involve different Tel22 structural forms in Na^+ and K^+ buffers. On the basis of these observations, the scheme proposed includes two folded G-quadruplex forms in both Na^+ and K^+ ions, hereinafter referred to as FiM in equilibrium with triplex forms (see below), denoted as Fi′M ($i = 1, 2$ and $M = Na^+$ or K^+) (Fig. 4).

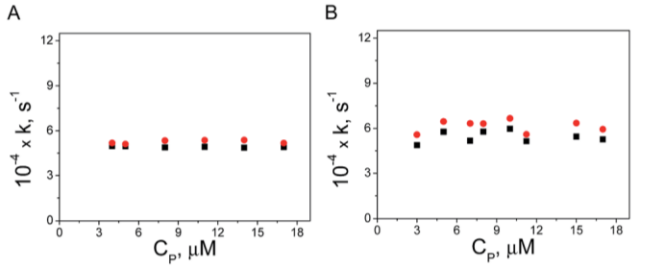

Fig. 3 k_1 (s^{-1}) (●) and k_2 (s^{-1}) (■) *versus* Tel22 concentration (C_P) plots in the presence of (A) 0.15 M NaCl and (B) 0.15 M KCl. pH = 7.5 (10 mM Tris–HCl, 1 mM EDTA) and $T = 25$ °C.

Table 1 Average rate constants, k_1 (s^{-1}) and k_2 (s^{-1}) and thermodynamic constant, K_F = [F1M]/[F2M] (M = Na^+ or K^+), obtained for the Tel22 G-quadruplex in 0.15 M NaCl and 0.15 M KCl, pH = 7.5 (10 mM Tris–HCl, 1 mM EDTA) and $T = 25$ °C

	10^{-4} k_1 (s^{-1})	10^{-4} k_2 (s^{-1})	K_F
Tel22 (NaCl)	5.2 ± 0.1	4.92 ± 0.04	0.39 ± 0.02
Tel22 (KCl)	5.8 ± 0.2	5.4 ± 0.4	0.23 ± 0.02

In K^+ solutions, the main conformation of human telomeric DNA is a G-quadruplex hybrid-type fold with (3 + 1) G-tetrad core containing three tetrads, one double-chain-reversal loop and two edgewise loops. Two structures containing this core with the same type and number of loops but differing by their loop arrangement have been identified. This feature reveals the existence of different hybrid G-quadruplex forms for Tel22 under physiological conditions (F1K and F2K, Fig. 4, left).[18] In Na^+ diluted solutions, the antiparallel basket-type structure was found for the Tel22 sequence (F1Na, Fig. 4, right).[19] Although the basket form has been acknowledged openly as the only folded conformation, recent studies have provided convincing evidence for the polymorphism of telomeric sequences in Na^+, with possible interconversion between various structural forms.[20] Noer *et al.*, using single molecule FRET microscopy, have identified at least four different G-quadruplex states in Na^+, an unfolded state and three G-quadruplex related states that can convert into each other.[21] These states are dynamically populated with times around 10 s. It seems clear that these states do not correspond with those we have observed, because the difference in reaction rates is too large.

In this work, we provide kinetic evidence for at least four species (F1Na, F2Na, F1′Na and F2′Na) in equilibrium in solution of Na^+, in a similar way as in the presence of K^+ ions. Considering that the F1M ↔ F2M interconversion is rather slow,[7,22] we propose that k_1 and k_2 correspond to the much faster reactions F1K $\overset{k_1}{\leftrightarrow}$ F1′K, F2K $\overset{k_2}{\leftrightarrow}$ F2′K, F1Na $\overset{k_1}{\leftrightarrow}$ F1′Na and F2Na $\overset{k_2}{\leftrightarrow}$ F2′Na (microsecond time scale). Being monomolecular reactions in nature, k_1 and k_2 are the overall {forward (k_{fi}) + backward (k_{di})} kinetic constants and therefore the equilibrium constants, $K = k_{fi}/k_{di}$, of the FiM ↔ Fi′M reactions cannot be determined.

Thus, the point is how to explain the similar rates of the FiM ↔ Fi′M equilibrium for different G-quadruplex structures in different buffer ions.

Hydrophobic interactions determine the fast reaction rates FiM ↔ Fi′M

To determine the type of interaction that governs the FiM ↔ Fi′M conversion, we can compare the main features of our reactions (microsecond time scale and buffer ion) with the processes involved in the formation of G-quartets (H-bonding

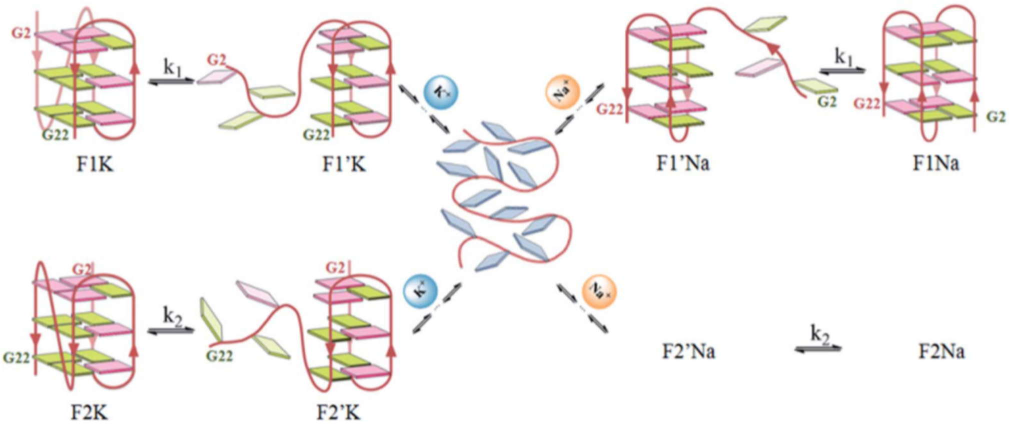

Fig. 4 Representation of Tel22 G-quadruplex with two major folded conformations F1M and F2M (M representing K^+ and Na^+ ions), in equilibrium with the G-triplex structures F1′M and F2′M, respectively. Loops are coloured red; *anti* and *syn* guanines are coloured green and pink, respectively. The F1M ↔ F2M equilibria between G-quadruplexes occur through the random coil. Other long-live intermediates should not be ruled out.

and specific ionic interactions $M^+\cdots O$, see Fig. 1B) and of G-quadruplex structures (stacking of successive planes of four guanine residues arranged as a square planar G-quartet).

Regarding G-quartets, the rates of H-bonding formation and dissociation fall into picoseconds.[23] An important issue is that hydrogen bonds are weak enough so as to continuously dissociate and reform at room temperature. Some of the most significant biological processes, such as DNA replication and protein folding, are feasible due to the reversible nature of hydrogen-bond formation.[24] According to Eigen, coordination of Na^+ and K^+ ions to the O atoms, similar to G-quartets interactions, occurs in nanoseconds.[25,26] This outcome has enabled us to exclude H-bonding and $M^+\cdots O$ interactions as the effects observed by T-jump.

As for G-quadruplexes, channel, loop and phosphates are main regions where the ion binding may occur. Ida and Wu have reported that the residence time of Na^+ ions inside the channel of the antiparallel bimolecular G-quadruplex ($G_4T_4G_4$) is 20 ms, whereas the residence time of Na^+ ions in the loop is 220 μs, the latter value being comparable with our results.[27] However, the slower mobility of K^+ ions relative to Na^+ ions[28] together with the difference in the loops of the Na^+ and K^+ conformations and the topologically more complex Na^+-stabilized fold[5] should yield different k_1 and k_2 constants in Na^+ and K^+ media, contrary to our observations. Actually, the kinetics and thermodynamics of formation of quadruplexes have been found cation-dependent.[5,12] Lastly, the electrostatic binding cation/DNA phosphate, which leads to a mobile cloud, yields rate constants close to diffusion-controlled.[29] In conclusion, according to literature data, none of the interactions that govern the formation of G-quartets or the release of ions from G-quadruplex described so far, evolve in the microsecond timescale and are independent of the type of ion, as occurs in our case.

Although the type of ion, Na^+ or K^+, affects the conformational equilibria of G-quadruplex (F1M ↔ F2M) and facilitates the FiM ↔ Fi′M equilibria due to the decrease in electrostatic repulsion, the monocation species is not involved in the rate-determining step and has no influence on the reaction rates. According to Record[30] and Kool,[31] the observation that the k_1 and k_2 constants are the same order in Na^+ and K^+ solutions confirms that the hydrophobic effects are larger than other stabilizing stacking effects, such as electrostatic and dispersion effects. Therefore, we can conclude that hydrophobic stacking interactions are key to these reactions.

G-Triplex structures in equilibrium with G-quadruplexes

A particular type of reaction governed by hydrophobic interactions occurs in the microsecond time scale and can be studied by T-jump, namely, on-slot ↔ off-slot equilibrium reactions of intercalation (on) and dissociation (off) of an aromatic ligand between the DNA base-pairs.[32–34] These features have enabled us to establish parallelism between the observed mechanism of Tel22 in solution and the intercalation reaction. According to Fig. 4, three guanines linked to the terminal strand in the G-quadruplexes are prone to dissociate (off) and link (on) to the G-quartet by fast on-G ↔ off-G equilibria determined by stacking interactions between each guanine and the adjacent G-leaflets. These interactions are responsible for the k_1 and k_2 constants in the presence of K^+ and Na^+ ions. This type of reaction is common to all conformations and could justify the non-dependence of the reaction rate on both the conformation, structural form and type of buffer cation.

Hydrophobic stacking interactions can also be present in another type of intermediates, such as quadruplex dimers or hairpins. For dimerization, such reaction would be bimolecular, $2\text{Fi} \leftrightarrow (\text{Fi})_2$, and the rate constants k_1 and k_2 would depend on the oligonucleotide concentration, in contrast to our results.

Hairpin-like structures have been suggested as intermediates in folding processes from single-stranded guanine (G)-rich DNA.[18,29] Chang *et al.* have identified two Watson–Crick base-pairing topologies of hairpin structure as well as the Hoogsteen H-bonding patterns of the WT22 G4 structure induced by addition of K$^+$ ions.[22] The kinetics associated with the potassium ion-induced hairpin-to-G4 transition are very slow, and fall into the 4800 s time scale, the unfolding of the hairpin structure being the rate-determining step for formation of WT22 G4. Therefore, folding and unfolding of single-stranded guanine (G)-rich DNA to form hairpin structures in microseconds should be discarded.

On the other side, also Sponer *et al.* have simulated the theoretical interconversion between hairpins involved in folding of human telomeric sequence quadruplexes with sub-μs scale rearrangement between them.[35] We have excluded the reactions observed in this work to occur between hairpins in equilibrium, mainly because interconversion between hairpins implies rearrangement of H-bonding, whose lifetime is of some picoseconds.[23] Moreover, to be able to record appreciable T-jump kinetic traces, the absorbances of the reactant and the reaction product must differ appreciably at the particular wavelength used; we believe that the absorbance of the simulated hairpins will be very similar and therefore the amplitude of the kinetic traces would be negligible or even vanish.

Therefore, equilibria of G-quadruplex ↔ G-triplex type, such as those proposed in Fig. 4, could be consistent with the type of interaction and the experimental observations.

As reported in the Introduction section, the FiM G-quadruplex structures in K$^+$ and Na$^+$ buffers are supported by literature data.[17,18] Additionally, recent computational studies support the triplex structures proposed for Fi′M. Molecular dynamics calculations by Sugiyama *et al.* have suggested that, in potassium media, folded human telomeric F1K and F2K structures are formed through intermediate species.[36] Random coils may form to a first stage hairpins and triplexes, and afterwards the latter can form type-1 and type-2 G-quadruplex structures (similar to F1K and F2K). All of the intermediates would be in equilibrium in a way such that F1K and F2K can interconvert to each other only through the random coil form, which entails slow interconversion. The G-triplex structures suggested by these authors are similar to F1′K and F2′K (Fig. 4, left). That is, F1′K and F2′K could be intermediate species in the F1K ↔ F2K equilibria.

Moreover, Sponer *et al.*, based on molecular dynamics simulations, have reported that several triplexes (such as F1′K) remain stable in the microsecond time scale.[37] Our experimental observations concur with this time scale and with the existence of short-lived intermediate G-triplex species, not only in the presence of K$^+$ ions, but also in the presence of Na$^+$ ions. This way, F1′Na and F2′Na would be intermediate G-triplexes also in the equilibrium F1Na ↔ F2Na (Fig. 4, right). Fig. 4 outlines schematically a parallel behaviour as a function of the type of salt employed with the different structural forms.

In addition to k_1 and k_2, the equilibrium constant between the folded conformations, K_F = [F2M]/[F1M], can also be assessed. Fig. 2 shows that, even though the amplitudes A_1 and A_2 vary with the Tel22 concentration, the A_2/A_1 ratio remains constant and is reproducible for each buffer and Tel22 concentration. Since the k_1 and k_2 constants are close to each other, the A_2/A_1 ratio provides at 25 °C the K_F values 0.23 and 0.39, respectively, for the equilibrium constants, F1K ↔ F2K in 0.15 M KCl and F1Na ↔ F2Na in 0.15 M NaCl (Table 1). Very close K_F values have been reported for interconversion between two stable folding conformations with similar sequence and under close conditions.[4] Burrows *et al.* have demonstrated that in KCl solution the hybrid-1 dominates over hybrid-2 for the human telomeric sequence 5′-TAGGG(TTAGGG)$_3$TT-3′, being K_F = 0.45 at 37 °C, pH 7.9 in 50 mM KCl.[38] Likewise, these authors have suggested the formation of triplex structures.

Conclusions

The T-jump technique has allowed us to characterise kinetically and thermodynamically the processes that occur in dilute aqueous solutions of human telomeric DNA containing both Na$^+$ and K$^+$ ions in near physiological conditions. We have shown that this is a very complex system, in which at least four different forms, two G-quadruplexes and two G-triplexes, coexist in equilibrium in both Na$^+$ and K$^+$ buffers. The reaction is governed by hydrophobic guanine–guanine interactions, regardless of the type of buffering ion and Tel22 conformation.

Experimental

Sample preparation. Dried d[AGGG(TTAGGG)$_3$] DNA oligonucleotide, labeled "Tel22", was purchased from Thermo Fisher Scientific Inc. Stock solutions were prepared with nuclease-free water in buffers containing 10 mM Tris–HCl, 1 mM EDTA at pH = 7.5 and 0.15 M of either NaCl or KCl. The formation of the G-quadruplex was carried out by heating oligonucleotide solutions up to 90 °C for 6 min and slowly cooling down to room temperature. The solutions were then incubated overnight at 4 °C. The concentration of the single stranded oligonucleotide was determined by measuring at 90 °C the absorbance at 260 nm using the absorptivity value 228 500 M ^{1} cm ^{1}. To ensure the formation of the G-quadruplex from the d(AGGG(TTAGGG)$_3$) sequence and that the equilibrium between all of the possible species in solution was reached, the study of these processes was conducted after overnight incubation of the Tel22 sequence.

CD spectra were recorded on a MOS-450 spectrophotometer (Bio-Logic SAS, Claix, France) over the 220–340 nm range at 25 °C, using 1 cm path-length cells with black quartz sides to mask the light beam. The buffer baseline was collected and subtracted from the sample spectra.

Fast kinetic measurements were performed with a Dialog T-jump instrument built according to the Rigler *et al.* prototype, in 1.0 cm path-length cells, working in the absorbance mode.[39] The system is perturbed in microseconds with a sudden 20 kV discharge. The cell was thermostatted at 22.5 °C and, following the discharge, a sudden 2.5 °C increase in temperature occurs in 2.5 μs for [NaCl] = 0.15 M in a standard cell, R = 100 ohm. The relaxation occurs at the final temperature 25 °C, for which the kinetic parameters are calculated. The changes were monitored in the microsecond timescale at 260 nm, where Tel22 displays maximum absorption.

The kinetic curves, collected with an Agilent 54622A oscilloscope (Santa Clara, CA, USA), were transferred to a PC and were evaluated with the Table Curve program of the Jandel Scientific package (AISN software, Richmond, CA, USA). To corroborate the k_1 and k_2 values obtained, the mV *versus* time data pairs were also analysed using two fitting programs: Origin and Bio-Kinet 32 software (Bio-Logic Science Instruments). In all three cases, the k_1 and k_2 values were obtained by iteration until convergence was attained. The k_1 and k_2 values obtained were reproducible regardless of the program used. In view of the high reproducibility for all of the concentrations and programs, we came to the conclusion that the difference obtained between the k_1 and k_2 values, though not very large, suffices to be fitted by a biexponential function and the values obtained are reliable. Moreover, the time constants were averaged out from 6–10 repeated kinetic experiments.

Acknowledgements

This work was supported by Obra Social “la Caixa” (project OSLC-2012-007) and MINECO, Spain (CTQ2014-58812-C2-2-R, FEDER Funds). C. P.-A. is grateful for the FPU grant from Ministry of Education, Culture and Sports, Madrid, Spain (FPU13/00180).

Notes and references

1 P. Murat and S. Balasubramanian, *Curr. Opin. Genet. Dev.*, 2014, **25**, 22–29.

2 S. Dhakal, Y. Cui, D. Koirala, C. Ghimire, S. Kushwaha, Z. Yu, P. M. Yangyuoru and H. Mao, *Nucleic Acids Res.*, 2013, **41**, 3915–3923.

3 G. Biffi, D. Tannahill, J. McCafferty and S. Balasubramanian, *Nat. Chem.*, 2013, **5**, 182–186.

4 L. Ying, J. J. Green, H. Li, D. Klenerman and S. Balasubramanian, *Proc. Natl. Acad. Sci. U. S. A.*, 2003, **100**, 14629–14634.

5 A. N. Lane, J. B. Chaires, R. D. Gray and J. O. Trent, *Nucleic Acids Res.*, 2008, **36**, 5482–5515.

6 A. Y. Q. Zhang and S. Balasubramanian, *J. Am. Chem. Soc.*, 2012, **134**, 19297–19308.

7 R. D. Gray, J. O. Trent and J. B. Chaires, *J. Mol. Biol.*, 2014, **426**, 1629–1650.

8 N. M. Brown, P. A. Rachwal, T. Brown and K. R. Fox, *Org. Biomol. Chem.*, 2005, **3**, 4153–4157.

9 I. Bessi, H. R. A. Jonker, C. Richter and H. Schwalbe, *Angew. Chem., Int. Ed.*, 2015, **54**, 8444–8448.

10 R. D. Gray and J. B. Chaires, *Nucleic Acids Res.*, 2008, **36**, 4191–4203.

11 R. J. O'Sullivan and J. Karlseder, *Nat. Rev. Mol. Cell Biol.*, 2010, **11**, 171–181.

12 E. Largy, A. Marchand, S. Amrane, V. Gabelica and J.-L. Mergny, *J. Am. Chem. Soc.*, 2016, **138**, 2780–2792.

13 M. Marusic and J. Plavec, *Angew. Chem., Int. Ed.*, 2015, **54**, 11716–11719.

14 J. Palacky, M. Vorlickova, I. Kejnovska and P. Mojzes, *Nucleic Acids Res.*, 2013, **41**, 1005–1016.

15 R. Buscaglia, M. C. Miller, W. L. Dean, R. D. Gray, A. N. Lane, J. O. Trent and J. B. Chaires, *Nucleic Acids Res.*, 2013, **41**, 7934–7946.

16 A. Ambrus, D. Chen, J. Dai, T. Bialis, R. A. Jones and D. Yang, *Nucleic Acids Res.*, 2006, **34**, 2723–2735.

17 A. I. Karsisiotis, N. M. A. Hessari, E. Novellino, G. P. Spada, A. Randazzo and D. S. M. Webba, *Angew. Chem., Int. Ed.*, 2011, **50**, 10645–10648.

18 A. T. Phan, K. N. Luu and D. J. Patel, *Nucleic Acids Res.*, 2006, **34**, 5715–5719.

19 Y. Wang and D. J. Patel, *Structure*, 1993, **1**, 263–282.

20 K. W. Lim, V. C. M. Ng, N. Martin-Pintado, B. Heddi and A. T. Phan, *Nucleic Acids Res.*, 2013, **41**, 10556–10562.

21 S. L. Noer, S. Preus, D. Gudnason, M. Aznauryan, V. Birkedal and J.-L. Mergny, *Nucleic Acids Res.*, 2016, **44**, 464–471.

22 M. H.-J. Kuo, Z.-F. Wang, T.-Y. Tseng, M.-H. Li, S.-T. D. Hsu, J.-J. Lin and T.-C. Chang, *J. Am. Chem. Soc.*, 2015, **137**, 210–218.

23 J. Zheng and M. D. Fayer, *J. Am. Chem. Soc.*, 2007, **129**, 4328–4335.

24 G. R. Desiraju and T. Steiner, *The Weak Hydrogen Bond: In Structural Chemistry and Biology*, Oxford University Press, 1999.

25 M. Eigen and K. Tamm, *Z. Elektrochem. Angew. Phys. Chem.*, 1962, **66**, 107–121.

26 M. Eigen, *Pure Appl. Chem.*, 1963, **6**, 97–115.

27 R. Ida and G. Wu, *J. Am. Chem. Soc.*, 2008, **130**, 3590–3602.

28 J. Toehl and W. Eimer, *J. Mol. Model.*, 1996, **2**, 327–329.

29 H. Diebler, F. Secco and M. Venturini, *Biophys. Chem.*, 1987, **26**, 193–205.

30 M. T. Record Jr, C. F. Anderson and T. M. Lohman, *Q. Rev. Biophys.*, 1978, **11**, 103–178.

31 K. M. Guckian, B. A. Schweitzer, R. X. F. Ren, C. J. Sheils, D. C. Tahmassebi and E. T. Kool, *J. Am. Chem. Soc.*, 2000, **122**, 2213–2222.

32 F. J. Meyer-Almes and D. Porschke, *Biochemistry*, 1993, **32**, 4246–4253.

33 N. Busto, B. Garcia, J. M. Leal, F. Secco and M. Venturini, *Org. Biomol. Chem.*, 2012, **10**, 2594–2602.

34 J. Valladolid, C. Hortigueela, N. Busto, G. Espino, A. M. Rodriguez, J. M. Leal, F. A. Jalon, B. R. Manzano, A. Carbayo and B. Garcia, *Dalton Trans.*, 2014, **43**, 2629–2645.

35 P. Stadlbauer, P. Kuhrova, P. Banas, M. Otyepka, J. Koca, G. Bussi, L. Trantirek and J. Sponer, *Nucleic Acids Res.*, 2015, **43**, 9626–9644.

36 T. Mashimo, H. Yagi, Y. Sannohe, A. Rajendran and H. Sugiyama, *J. Am. Chem. Soc.*, 2010, **132**, 14910–14918.

37 P. Stadlbauer, L. Trantirek, T. E. Cheatham III, J. Koca and J. Sponer, *Biochimie*, 2014, **105**, 22–35.

38 N. An, A. M. Fleming and C. J. Burrows, *J. Am. Chem. Soc.*, 2013, **135**, 8562–8570.

39 R. Rigler, C. R. Rabl and T. M. Jovin, *Rev. Sci. Instrum.*, 1974, **45**, 580–588.

This journal is © The Royal Society of Chemistry 2016

Capítulo VII

Interacción de la G-cuádruplex de ADN Telomérico con el Ligando TMPyP4

Summary

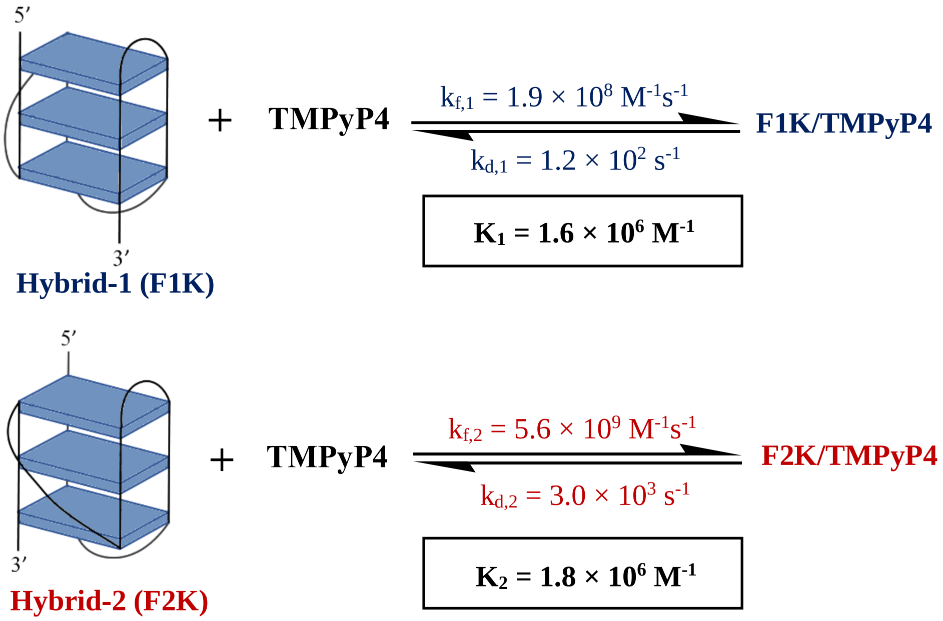
5′
3′
Hybrid-1 (F1K)
+ TMPyP4
$k_{f,1} = 1.9 \times 10^8\ M^{-1}s^{-1}$
$k_{d,1} = 1.2 \times 10^2\ s^{-1}$
F1K/TMPyP4
$K_1 = 1.6 \times 10^6\ M^{-1}$
5′
3′
Hybrid-2 (F2K)
+ TMPyP4
$k_{f,2} = 5.6 \times 10^9\ M^{-1}s^{-1}$
$k_{d,2} = 3.0 \times 10^3\ s^{-1}$
F2K/TMPyP4
$K_2 = 1.8 \times 10^6\ M^{-1}$

Figure 1. Schematic representation of the kinetic behaviour of the TMPyP4/Tel22 system in the presence of K^+.

The development of small ligands capable of stabilizing G-quadruplex structures attracts a great deal of attention, as this may have remarkable biological consequences on different processes such as the inhibition of telomerase, among others. Thermodynamic studies on ligand/G-quadruplex interactions abound in the literature, but the kinetics of these interactions remain less explored. In this work, TMPyP4 was used as a model G-quadruplex binder to study the kinetic mechanisms of its interaction, as this study could provide information about the processes taking place in solution between ligands and G-quadruplexes.

The human telomeric sequence Tel22, studied in **Chapter VI**, was chosen because of its biological relevance and its characteristic polymorphism, forming two different conformations in solution. In K^+ solutions, these two conformations are known as “hybrid-1” and “hybrid-2”, and they present the same core and number and type of loops, but different loop arrangement (see **Figure 1**). It had been suggested before that these very similar characteristics could make them thermodynamically indistinguishable [218].

Indeed, the thermodynamic techniques used in this work, including ITC, fluorescence lifetime measurements and FRET melting experiments, only allowed to observe one global interaction process between TMPyP4 and Tel22 at low C_D/C_P ratios. On the contrary, the kinetic measurements performed by the T-Jump technique under the same experimental conditions, provided evidence of two reactions taking place in solution with the same thermodynamic constant, K, but with different formation and dissociation constants, k_f and k_d, as represented in **Figure 1**. This let us hypothesize that TMPyP4 could interact with the two distinct Tel22 hybrid forms present in solution at a different rate but equal thermodynamic constant, which would make these distinct interactions indistinguishable by thermodynamic techniques.

In order to confirm this hypothesis, the group of Prof. Giampaolo Barone carried out the molecular dynamic simulations that are present in this article. They analysed the theoretical time it would take to the TMPyP4 molecule to reach the equilibrium with hybrid-1 and hybrid-2 forms of Tel22. The final complexes reached in the simulation were thermodynamically similar, but the time needed to get formed were different, in highly good agreement with our experimental data.

BBA - General Subjects 1862 (2018) 522–531

Contents lists available at ScienceDirect

BBA - General Subjects

journal homepage: www.elsevier.com/locate/bbagen

Kinetic evidence for interaction of TMPyP4 with two different G-quadruplex conformations of human telomeric DNA

Cristina Pérez-Arnaiz[a], Natalia Busto[a], Javier Santolaya[a,b], José M. Leal[a], Giampaolo Barone[b,*], Begoña García[a,*]

[a] Department of Chemistry, University of Burgos, 09001 Burgos, Spain
[b] Dipartimento di Scienze e Tecnologie Biologiche, Chimiche e Farmaceutiche (STEBICEF), Università degli Studi di Palermo, Viale delle Scienze Ed. 17, 90128 Palermo, Italy

ARTICLE INFO

Keywords:
Tel22 conformations
TMPyP4
Fast reactions
Molecular dynamics

ABSTRACT

Background: Stabilization of G-quadruplex helices by small ligands has attracted growing attention because they inhibit the activity of the enzyme telomerase, which is overexpressed in > 80% cancer cells. TMPyP4, one of the most studied G-quadruplex ligands, is used as a model to show that the ligands can exhibit different binding features with different conformations of a human telomeric specific sequence.
Methods: UV–Vis, FRET melting Assay, Isothermal Titration Calorimetry, Time-resolved Fluorescence lifetime, T-Jump and Molecular Dynamics.
Results: TMPyP4 yields two different complexes with two Tel22 telomeric conformations in the presence of Na^+ or K^+. T-Jump kinetic experiments show that the rates of formation and dissociation of these complexes in the ms time scale differ by one order of magnitude. MD simulations reveal that, in K^+ buffer, "hybrid 1" conformation yields kinetic constants on interaction with TMPyP4 one order lower than "hybrid 2". The binding involves π–π stacking with external loop bases.
Conclusions: For the first time we show that for a particular buffer TMPyP4 interacts in a kinetically different way with the two Tel22 conformations even if the complexes formed are thermodynamically indistinguishable.
General significance: G-quadruplexes, endowed with technological applications and potential impact on regulation mechanisms, define a new research field. The possibility of building different conformations from same sequence is a complex issue that confers G-quadruplexes very interesting features. The obtaining of reliable kinetic data constitutes an efficient tool to determine reaction mechanisms between conformations and small molecules.

1. Introduction

The study and advancement of small molecules capable of binding and stabilizing higher-order DNA structures, such as G-quadruplexes, has attracted growing interest [1]. G-quadruplexes can be formed in guanine-rich DNA stretches in the presence of stabilizing ions such as Na^+ or K^+. Although the *in vivo* existence of such structures is still a matter of debate [2], under physiological conditions the human genome contains a large number of potential quadruplex-forming sequences [3,4]. Human telomeric DNA consisting of TTAGGG repeats is an interesting instance of such sequences. Stabilization of telomeric G-quadruplex helices by small ligands is known to inhibit the activity of the enzyme telomerase, which is overexpressed in > 80% of cancer cells and acts as tumour promoter [5].

In intracellular media, potassium ions abound more than sodium ions, giving way to extensive research of G-quadruplex conformations stabilized by K^+ [6]. The main conformation reported for the human telomeric sequence in K^+ solutions "Tel22" (d[AGGG(TTAGGG)$_3$]) consists of a G-quadruplex fold with (3 + 1) G-tetrad core containing three tetrads, one side-chain reversal loop and two lateral loops [7]. Two distinguishable conformations (known as hybrid-1 and hybrid-2) have been identified containing this core with the same number and type of loops but different loop arrangement [8]. On the other hand, in Na^+ solutions the antiparallel basket-type structure was found for human telomeric DNA. Although this basket form is the only folded conformation fully characterized under these conditions [9], subsequent studies provide evidence for the polymorphism of telomeric sequences in Na^+ solutions, with possible interconversion between various structural forms [10].

In line with these observations, we have reported recently the fast

---

[*] Corresponding authors.
E-mail addresses: giampaolo.barone@unipa.it (G. Barone), begar@ubu.es (B. García).

https://doi.org/10.1016/j.bbagen.2017.10.020
Received 16 May 2017; Received in revised form 13 October 2017; Accepted 27 October 2017
Available online 31 October 2017
0304-4165/ © 2017 Elsevier B.V. All rights reserved.

processes that govern different Tel22 structures in equilibrium at 25 °C. Kinetic T-jump measurements provide evidence for the presence of two G-quadruplex conformations, F1M and F2M, in equilibrium with G-triplex structures, F1'M and F2'M, with M = Na^+ or K^+ [11]. These results, along with other studies, evince the complexity of this system [12–15], thus posing the question of whether small molecules can differentiate between different specific sequence conformations coexisting in solution, a striking feature not reported hitherto. To this aim, we have studied the interaction of Tel22 with the cationic *meso*-tetrakis(*N*-methyl-4-pyridyl)porphyrin (TMPyP4), capable of stabilizing quadruplex structures and inhibiting the telomerase activity [16]. In spite of being nonselective for quadruplex helices over duplex DNA [17], TMPyP4 is one of the most studied G-quadruplex ligands ever and its structure has inspired the development of other porphyrin derivatives [18,19]. Nevertheless, certain controversy over the nature of the G-quadruplex/TMPyP4 interactions still remains, and intercalation between adjacent G-tetrads or end-stacking onto the external faces of the G-quadruplex have been proposed [20–22].

Due to its demonstrated affinity with G-quadruplex structures, TMPyP4 has been used in this work as a model molecule to show that certain ligands can exhibit different binding features towards different conformations of a specific sequence. Even though these features can be thermodynamically indistinguishable, they take place at different rates, as suggested recently by J. Lah et al. [23] and shown here by T-jump measurements and MD calculations. The F1M/TMPyP4 and F2M/TMPyP4 complexes get formed at low TMPyP4/Tel22 concentration ratio and have very close binding constants ($K_1 = k_f/k_d$), whereas the formation, k_f, and dissociation, k_d, kinetic constants differ considerably. At higher TMPyP4/Tel22 concentration ratio, another type of complex with binding constant K_2 gets formed. This complex has been reported before and is assumed to involve an external mode of binding [24]. This work is a starting point; actually, the interactions of other types of ligands biologically more relevant than TMPyP4 with different oligonucleotides are to be explored in future studies.

2. Materials and methods

2.1. Sample preparation

The DNA oligonucleotide d[AGGG(TTAGGG)$_3$], known as "Tel22", was purchased from Thermo Fisher Scientific Inc. as dried samples. Stock solutions were prepared with nuclease free water in buffers containing 10 mM Tris-HCl, 1 mM EDTA and 0.15 M of either NaCl or KCl at pH = 7.5 unless otherwise specified. The formation of the G-quadruplex was carried out by incubating for 6 min the oligonucleotide solution at 90 °C and slowly cooling down (~ 5 h) to room temperature in order to obtain the thermodynamically equilibrated G-quadruplex structures [13]. Solutions were then stored at 4 °C overnight to avoid degradation processes and afterwards allow reaching room temperature prior to carry out the measurements. The concentration of the single stranded oligonucleotide was determined by measuring at 90 °C the absorbance at 260 nm using the absorptivity value of 228,500 M^{-1} cm^{-1} provided by the supplier. The double-labeled oligonucleotide FAM-Tel22-TAMRA (F-Tel22-T) was purchased from Thermo Fisher Scientific Inc. TMPyP4 was supplied by Sigma Aldrich. Stock aliquots of TMPyP4 were prepared in water and stored in the dark at − 20 °C.

2.2. UV spectroscopy

Spectrophotometric measurements were performed with a HP 8453A photodiode array spectrophotometer (Agilent Technologies, Palo Alto, CA) endowed with a temperature control Peltier system. Titrations were carried out by adding increasing amounts of Tel22 solutions to the TMPyP4 solution in 1 cm path-length cells with black quartz sides at 25 °C. The data were corrected by the dilution factor C_D^0/C_D.

2.3. ITC titrations

Isothermal titration calorimetry (ITC) experiments were performed at 25 °C using a Nano ITC (TA Instruments, Newcastle, USA). The stirring speed was maintained constant at 250 rpm. The TMPyP4 solution was injected into the calorimetric cell containing the Tel22 solution. Prior to use, all solutions were degassed to reduce to a minimum the formation of bubbles during the experiments. Control experiments were carried out to determine the contribution of the heat of dilution of TMPyP4 and rule out the presence of aggregation processes of the drug that would interfere with the analysis of the ITC data to obtain the TMPyP4/Tel22 thermodynamic parameters. The thermograms (integrated area of the peak/mole of injectant *versus* C_D/C_P ratio) obtained in the titrations were fitted by a "two-site model", as simpler models including the "one-site model" were insufficient to fit the data suitably.

2.4. FRET melting assay

F-Tel22-T was dissolved in water as 100 μM stock solutions and then annealed for 5 min at 0.4 μM concentration at $T = 90$ °C in a buffer containing 0.15 M KCl or NaCl, 10 mM Tris-HCl and 1 mM EDTA at pH = 7.5. Each well of a 96-well plate contained 0.2 μM of F-Tel22-T and different concentrations of TMPyP4. Measurements were performed in a 7500 Real-Time PCR (Applied Biosystems). Readings were performed with excitation at 450–495 nm and detection at 515–545 nm from 25 to 95 °C at a scan rate of 0.5 °C/min.

2.5. Time-resolved fluorescence lifetime

Fluorescence lifetime measurements of TMPyP4 were performed both in the absence and in the presence of different amounts of Tel22 in Na^+ or K^+ buffer using FLS980 equipment (Edinburg Instruments). The excitation was accomplished at 405 nm using an EPL 405 pulsed diode laser and the emission was collected at 705 nm. Data were analyzed by FAST 3.4.0 software.

2.6. T-Jump measurements

The fast kinetic measurements were performed with a Dialog T-jump instrument built up according to the Riegler et al. prototype [25] in 1.0 cm path-length cells, working in the absorbance mode. The kinetic curves, collected with an Agilent 54622A oscilloscope (Santa Clara, CA, USA), were transferred to a PC and evaluated with the Table Curve program of the Jandel Scientific package (AISN software, Richmond, CA, USA). The time constants were averaged out from 6-fold repeated kinetic experiments.

2.7. Molecular dynamics

The structures of the Tel22 G-quadruplex in K^+ solution were taken from the *Protein Data Bank*, with PDB id "*2HY9*" for hybrid-1, F1K, and PDB id "*2JPZ*" for hybrid-2, F2K [26]. In detail, the first and last two nucleotides of the G-quadruplex chain of the two PDB id files, both 26-mer hybrids, have been removed to generate the same Tel22 sequence of the experimental studies. The starting molecular structure of TMPyP4 was obtained by full geometry optimization, firstly through semiempirical PM6 calculations [27] and, subsequently, through DFT calculations, using the M06-2X functional [28] in the presence of water as implicit solvent, mimicked by the "conductor-like polarized continuum model" implicit method [29,30]. Atomic partial charges of TMPyP4 were obtained by DFT calculations and force field parameters of TMPyP4 and DNA models were generated with the ACPYPE software (AnteChamber Python Parser interfacE) [31,32]. The Amber99SB force field ParmBSC0 nucleic acid torsion parameters were used for the DNA models [33]. A triclinic box of TIP3P water was generated around the G-quadruplex/TMPyP4 system, to a 0.8 nm depth on each side of the solutes, for a total of about 5500 solvent molecules; 39 K^+ ions and 17 Cl^- ions were added to neutralize the DNA negative charge of the sugar- phosphate backbone and to set the solution ionic strength to about 0.15 M.

Explicit solvent molecular dynamics (MD) simulations for F1K/TMPyP4 and F2K/TMPyP4 systems were performed using the Gromacs 5.0.4 software package, [34,35] in the canonical NPT ensemble (for which number of particles, N, pressure, P, and temperature, T, are constant), at 300 K, under control of a velocity-rescaling thermostat [36]. The mesh particle Ewald method was used to describe long-range interactions [37]. Preliminary energy minimizations were run for 5000 steps with the steepest descent algorithm, during which the equilibration of the G-quadruplex/TMPyP4 systems were harmonically restrained with a force constant of 1000 kJ mol^{-1} nm^{-2}, gradually relaxed in five consecutive steps of 100 ps each, to 500, 200, 100 and 50 kJ mol^{-1} nm^{-2}. Four MD simulations with different initial poses of TMPyP4 (see Figure 4SI) were initially conducted for 100 ns for the binding of TMPyP4 with each DNA hybrid. The starting structures were obtained by the Maestro software [Maestro, version 10.2, Schrödinger, LLC, New York, NY, 2015]. Two final MD simulations were conducted for 300 ns and 200 ns, for the TMPyP4/F1K and TMPyP4/F2K systems, respectively.

3. Results and discussion

UV–vis and ITC measurements were carried out to set the most adequate concentration range to conduct the kinetic study. Same experiments were performed in Na^+ and K^+ media to gather information about the similarities and differences of the studied system in the presence of these representative ions.

3.1. Isothermal titration calorimetry

ITC titrations of Tel22 (P) with increasing amounts of TMPyP4 (D) in 0.15 M NaCl and 0.15 M KCl were carried out. The profile of the titration isotherms (Fig. 1) shows two well differentiated steps. A general mechanism for this behaviour is represented in Eqs. (1) and (2). For low C_D/C_P concentration ratios, the complex PD_1 gets formed (Eq. (1)). As to the second process, PD_2 gets formed from PD_1 when the C_D/C_P ratio increases (Eq. (2)), and is probably related to formation of external aggregates when the TMPyP4 concentration is raised.

$$P + D \overset{K_1}{\rightleftharpoons} PD_1 \tag{1}$$

$$PD_1 + D \overset{K_2}{\rightleftharpoons} PD_2 \tag{2}$$

The "two-site model" best fitted the experimental data, and the thermodynamic parameters obtained are listed in Table 1. The thermodynamic constant, K_1, for formation of PD_1 in the presence of K^+ was one order higher compared to Na^+, whereas with K_2 the opposite effect occurs. The reaction enthalpies were always negative. ΔH_1 varied with the type of buffer used, ΔH_1 (Na^+) < ΔH_1 (K^+), whereas ΔS_1 (Na^+) < 0 and ΔS_1 (K^+) > 0, indicating different hydration extent of the Tel22 conformations in Na^+ and K^+ buffers [38]. The ΔH_2 values remained nearly constant, whereas for the reaction entropy ΔS_2 (Na^+) > ΔS_2 (K^+) > 0, an effect attributed to dehydration of PD_1 to yield PD_2, in good agreement with formation of an external complex. The K_1 and K_2 values concur with those reported before in KCl buffer for the interaction of TMPyP4 and different types of human telomeric G-quadruplexes [24,39].

3.2. Spectrophotometric titration

The two differentiated processes observed with ITC measurements were also observed by spectrophotometric titrations of the Tel22/TMPyP4 system in 0.15 M NaCl (Fig. 2A) and 0.15 M KCl (Fig. 1SIA). The spectral curves recorded upon addition of increasing amounts of Tel22 to a TMPyP4 solution displayed a biphasic isotherm at λ = 433 nm with minimum at $C_P/C_D = 0.5$ (Fig. 2A, inset). An isosbestic point at λ = 429 nm with pronounced bathochromic shift of the maximum is observed for low TMPyP4 concentration ($C_D/C_P < 2$) (Fig. 2B), whereas for $C_D/C_P > 2$ a new isosbestic point at λ = 437 nm appears and the location of the maximum remains unaltered (Fig. 2C). This behaviour points to the existence of different types of Tel22/TMPyP4 complexes depending on the C_D/C_P concentration ratio, concurrent with the ITC results and with the scheme shown in Eqs. (1) and (2).

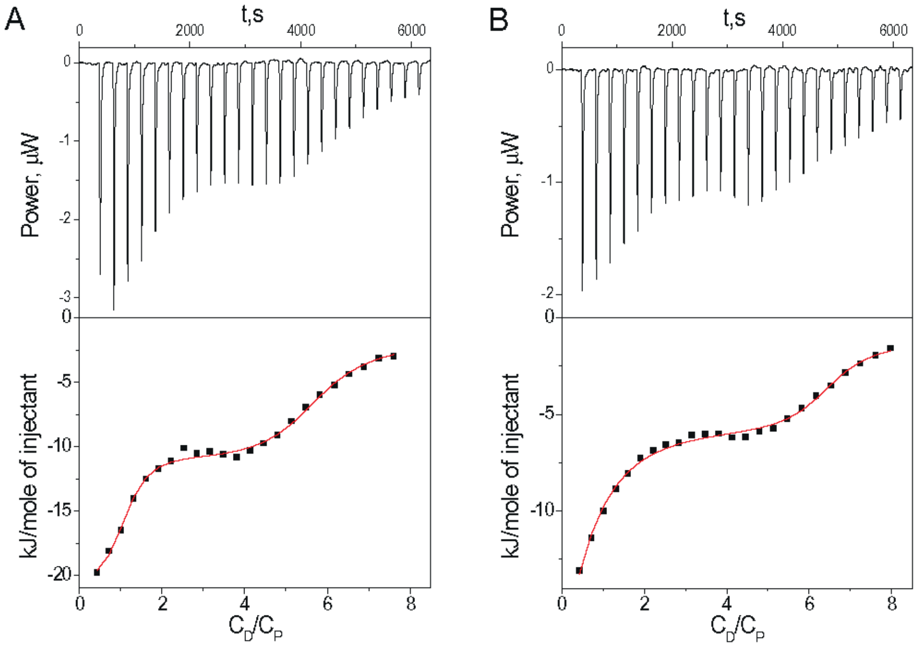

Fig. 1. ITC titrations of Tel22 with TMPyP4 in 0.15 M NaCl (A) and 0.15 M KCl (B). C_P^0 = 0.065 mM, C_D^0 = 1.7 mM, pH = 7.5 (10 mM Tris-HCl, 1 mM EDTA), T = 25 °C.

Table 1
Thermodynamic parameters determined for the binding of TMPyP4 to Tel22 using a “two-site model”. K_1 and K_2 are the thermodynamic constants and ΔH_1 and ΔH_2 the enthalpy change for the processes in Eqs. (1) and (2).

	10^{-5} K_1, M^{-1}	ΔH_1, kJ mol^{-1}	10^{-5} K_2, M^{-1}	ΔH_2, kJ mol^{-1}
Tel22/TMPyP4[a]	1.6 ± 0.6	− 45 ± 2	70 ± 30	− 21 ± 2
Tel22/TMPyP4[b]	25 ± 7	− 15 ± 1	3.5 ± 0.9	− 27 ± 1

[a] 0.15 M NaCl.
[b] 0.15 M KCl.

3.3. *FRET melting measurements*

A number of secondary structures, such as different G-quadruplex conformations, i-motifs and triplexes, can be present in solution for Tel22 and other important G-quadruplex sequences [11,40]. TMPyP4 promotes a notable increase in the melting temperature of G-quadruplex DNA structures [41]. Förster resonance energy transfer (FRET) melting experiments were carried out to obtain information about the main features of the Tel22/TMPyP4 interaction. Tel22 become stabilized upon binding with TMPyP4 both in Na^+ and K^+ buffers. Fig. 3A and B show the normalized FRET melting curves, whereas Fig. 3C and D show the T_m values determined in the mid-transition ($T_{1/2}$) for each C_D/C_P ratio. In the presence of TMPyP4, the ΔT_m value obtained for the dual fluorescently labeled (FAM and TAMRA) Tel22 oligonucleotide in the presence of Na^+ is equal to or greater than in the presence of K^+ for the same $\Delta(C_D/C_P)$, which reveals the influence of the ligand on the stabilization of different G-quadruplex Tel22 structures.

3.4. *Time-resolved fluorescence lifetime measurements*

Fluorescence lifetime measurements have been widely used to study the existence and main features of ligand/G-quadruplex complexes [42]. The emission properties of the Tel22/TMPyP4 system were determined at different C_D/C_P ratios (Fig. 2SI). A monoexponential decay fitting was applied for free TMPyP4, whereas a biexponential fitting was needed to obtain acceptable χ^2 values when Tel22 is present. The τ_1 values were quite close to those of TMPyP4 alone, whereas the τ_2 values correspond to PD_1 (Table SI1). By means of this technique it was unfeasible to differentiate between different hybrid/TMPyP4 complexes, probably due to the close fluorescence lifetime values ascribable to their similar structure.

3.5. *Kinetic T-Jump measurements*

Thermodynamic data is valuable material to assess the final state of interacting systems, even though they cannot provide detailed mechanistic information. We studied the kinetic features of the Tel22/TMPyP4 interaction with the T-Jump technique in the microsecond time scale to verify if the presence of the two different G-quadruplex conformations, F1M and F2M, entail any significance on the way the ligands do interact with Tel22 in the presence of Na^+ and K^+. To this aim, T-Jump measurements were performed for C_D/C_P ratio < 2, where PD_1 (Eq. (1)) prevails. Kinetic measurements monitoring the absorbance were carried out at two different wavelengths, one at each

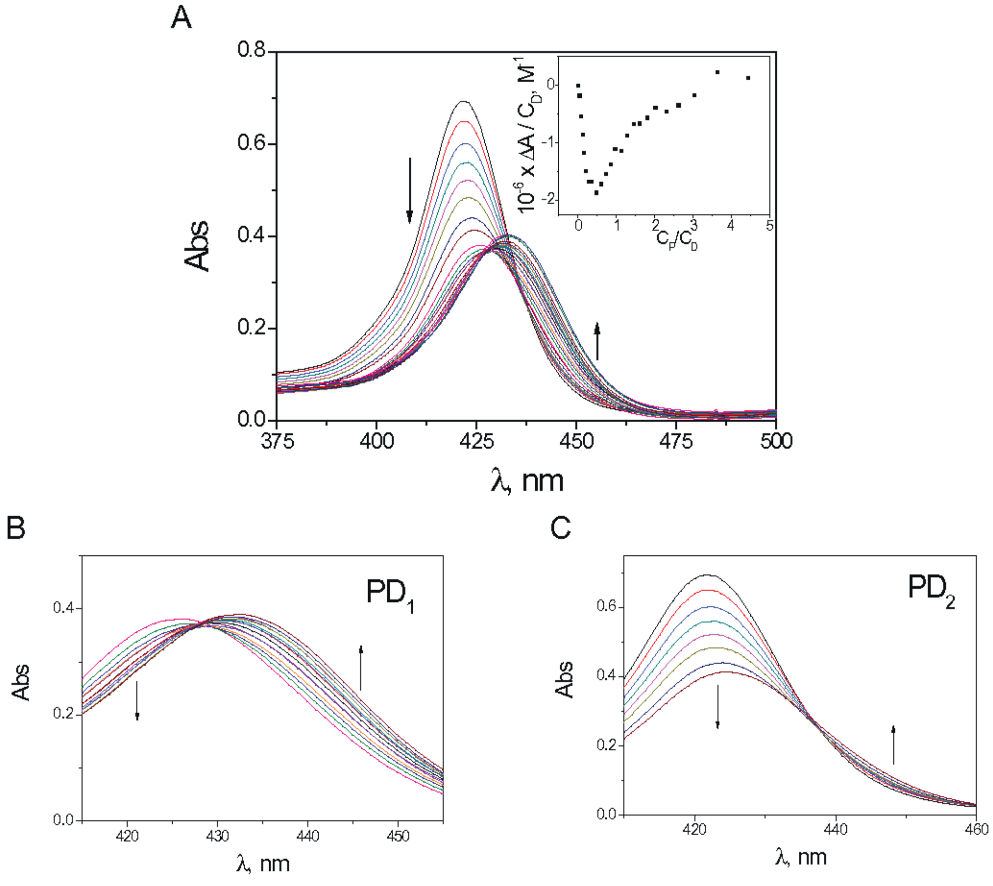

Fig. 2. Absorption spectra obtained from the titration of the TMPyP4/Tel22 system in 0.15 M NaCl. Inset: Binding isotherm at 433 nm (A). The spectral curves of Fig. 2A show two differentiated behaviours with two different isosbestic points at C_D/C_P < 2 (B) and at C_D/C_P > 2 (C). C_D^0 = 3.5 μM, pH = 7.5 (10 mM Tris-HCl, 1 mM EDTA), T = 25 °C.

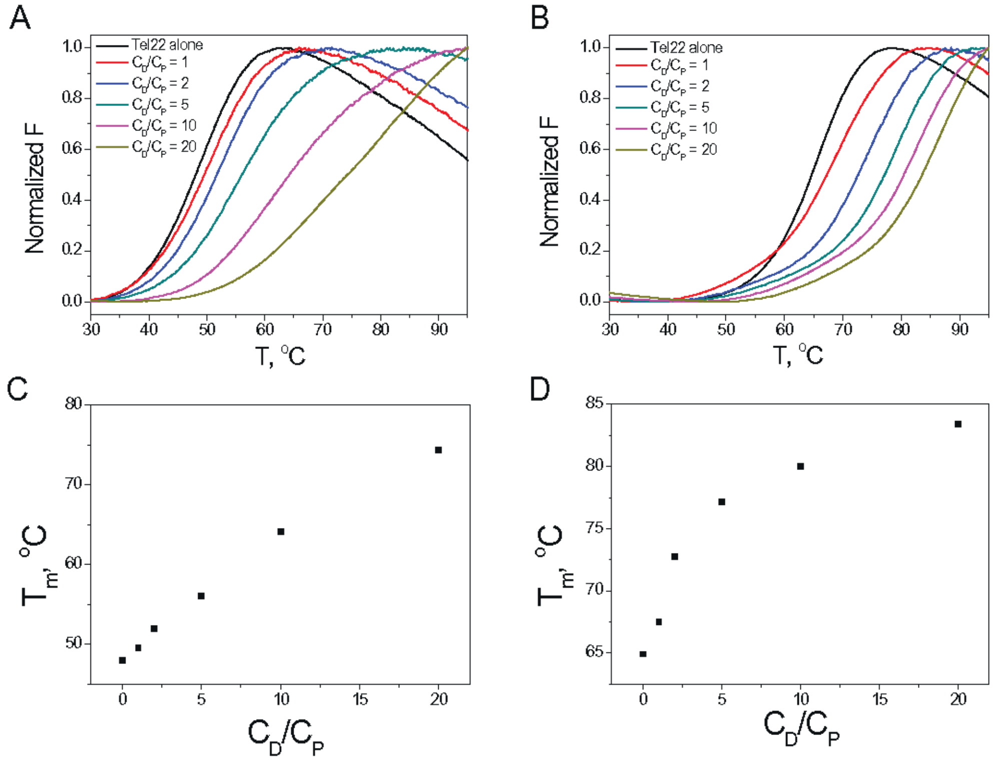

Fig. 3. FRET melting curves obtained for the TMPyP4/Tel22 system in 0.15 M NaCl (A) and in 0.15 M KCl (B) at different C_D/C_P ratios. Representation of the melting temperature (T_m) *versus* the C_D/C_P ratio in NaCl (C) and in KCl (D). C_P = 0.2 µM, pH = 7.5 (10 mM Tris-HCl, 1 mM EDTA).

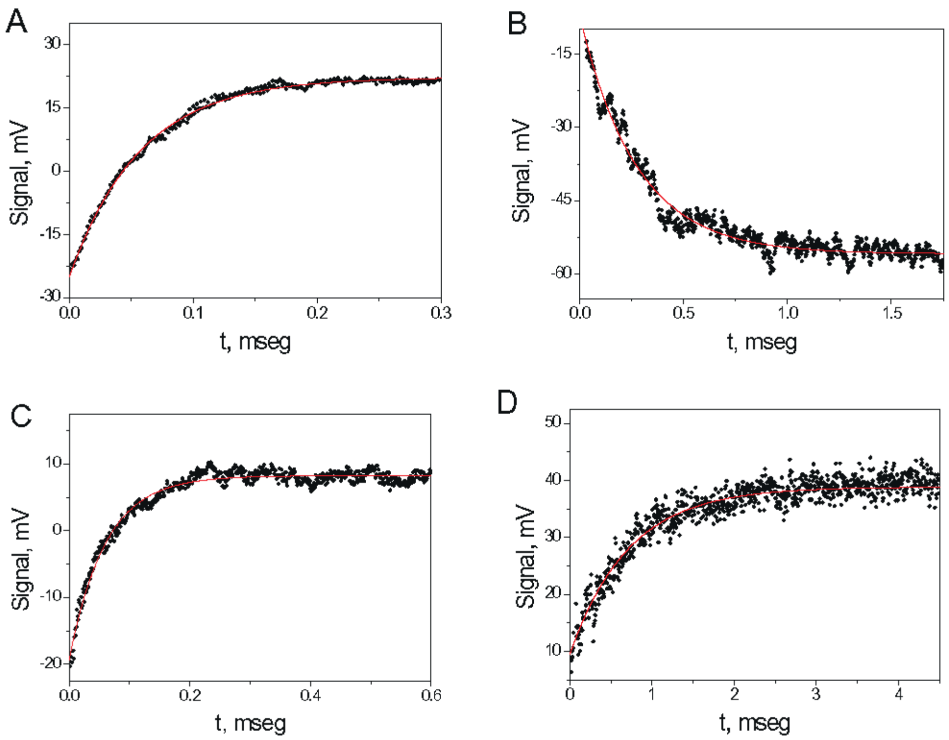

Fig. 4. Examples of kinetic curves obtained for the Tel22/TMPyP4 system in 0.15 M NaCl at λ = 437 nm (A) and λ = 422 nm (B) and in 0.15 M KCl at λ = 437 nm (C) and λ = 422 nm (D). C_D = 3.5–15 µM, C_P = 6–20 µM. pH = 7.5 (10 mM Tris-HCl, 1 mM EDTA), *T* = 25 °C.

side of the 429 nm isosbestic point. Fig. 4 collects examples of kinetic curves for the Tel22/TMPyP4 system in Na^+ and in K^+, recorded at 422 nm and 437 nm (see Figs. 2B and 1SIB). Single exponential functions were fitted to the experimental data (red line), from which the reciprocal relaxation time $1/\tau$ was obtained. Interestingly, the kinetics observed with equal concentration of Tel22 and TMPyP4 and same type of ion, showed that two reactions with quite different kinetic behaviour are at work. The faster reaction, which lasts < 1 ms, could be observed at λ = 437 nm for both Na^+ and K^+ buffers (Fig. 4A and C, respectively), whereas the slower reaction can be followed at λ = 422 nm (Fig. 4B and D).

To obtain the forward and reverse kinetic constants of the four processes, plots of the reciprocal relaxation time ($1/\tau$) *versus* the equilibrium concentration function ([P] + [D]) (Fig. 5) were fitted according to Eq. (3):

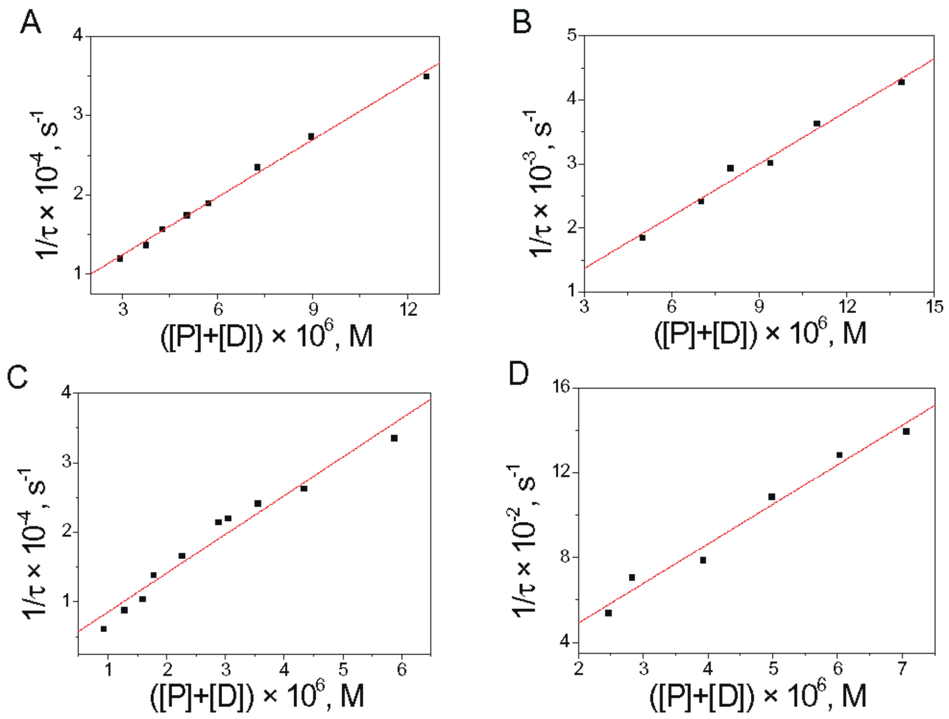

Fig. 5. ($1/\tau$) *versus* ([P] + [D]) plot and fitting of Eq. (3) to the data obtained for the Tel22/TMPyP4 system in 0.15 M NaCl at (A) λ = 437 nm, and (B) λ = 422 nm and in 0.15 M KCl at (C) λ = 437 nm and (D) λ = 422 nm.

$$\frac{1}{\tau} = k_f \cdot ([P] + [D]) + k_d \tag{3}$$

where k_f and k_d represent the formation and dissociation rate constants between Tel22 and TMPyP4 obtained at a specific wavelength.

Table 2 lists the rate constants together with the kinetic equilibrium constant, K_1, obtained from the ratio of the forward over the reverse kinetic constant ($k_{f,i}/k_{d,i}$). The kinetic constants $k_{f,2}$ and $k_{d,2}$ obtained at 437 nm were one order higher than $k_{f,1}$ and $k_{d,1}$ obtained at 422 nm both in NaCl and KCl, whereas the thermodynamic value K_1 obtained at the two wavelengths are quite close for a particular buffer, being $K_1 \sim 4 \times 10^5\ M^{-1}$ and $2 \times 10^6\ M^{-1}$ in the presence of Na^+ and K^+ ions, respectively. This means that, although the two processes observed in the presence of each of the ions display well-differentiated kinetic behaviour, the overall thermodynamic equilibrium constant remains virtually unaffected. The binding constants concur fairly well with the K_1 value obtained from the ITC measurements in Table 1 for formation of PD_1 (Eq. (1)).

In conclusion, P in Eq. (1) is the sum (F1M + F2M) and PD_1 is the sum (F1M/TMPyP4 + F2M/TMPyP4) in the presence of each M = Na^+ or K^+ ions. Therefore, the equilibrium in Eq. (1) can be split into Eq. (4) and Eq. (5), $k_{f,i}$ and $k_{d,i}$ being the kinetic constants (Table 1)

Table 2
Kinetic ($k_{f,i}$ and $k_{d,i}$) and thermodynamic ($K_1 = k_{f,i}/k_{d,i}$) constants of the equilibrium represented in Eqs. (4) and (5) for the Tel22/TMPyP4 system at low TMPyP4 concentration (C_D/C_P < 2).

	$10^{-8}\ k_{f,i}$, $M^{-1}\ s^{-1}$	$10^{-2}\ k_{d,i}$, s^{-1}	$10^{-5}\ K_1$, M^{-1}
F1Na/TMPyP4 (0.15 M NaCl)[a]	2.5 ± 0.2	5.5 ± 0.2	4.5 ± 0.2
F2Na/TMPyP4 (0.15 M NaCl)[b]	24.2 ± 0.6	52 ± 4	4.7 ± 2
F1K/TMPyP4 (0.15 M KCl)[a]	1.9 ± 0.1	1.2 ± 0.7	16 ± 1
F2K/TMPyP4 (0.15 M KCl)[b]	56 ± 4	30 ± 10	19 ± 7

[a] λ = 422 nm.
[b] λ = 437 nm.

corresponding to two different conformations. However, so far the experimental results are insufficient to unambiguously assign the Tel22 conformation and the kinetic constants. This difficulty will be overcome below by means of the MD simulations.

$$F1M + TMPyP4 \underset{k_{d,1}}{\overset{k_{f,1}}{\rightleftharpoons}} F1M/TMPyP4 \tag{4}$$

$$F2M + TMPyP4 \underset{k_{d,2}}{\overset{k_{f,2}}{\rightleftharpoons}} F2M/TMPyP4 \tag{5}$$

Several other possible mechanisms could describe the kinetic data in terms of induced-fit and/or conformational selection pathways. However, on one side the existence of two hybrid forms in K^+ buffer (F1K and F2K) has been described amply (See, for instance, refs [10] and [11] and references therein), providing useful hints about the types of processes observed. On the other hand, if, together with the formation of the TMPyP4/Tel22 complexes, there would exist other T-jump processes, then some other complex reactions should be observed, prone to fitting with multiexponential functions. However, as a matter of fact single exponential functions sufficed to fit absolutely all the T-jump kinetic curves, which indicate that, under the different conditions studied, only a single kinetic process in the T-Jump time scale is at work. Likewise, the good linearity fulfilled by the different instances shown in Fig. 5 reveals independent reactions from one another in every case.

To analyze the formation of PD_2 (Eq. (2)), a number of T-Jump experiments were conducted in the concentrated region, $C_D/C_P \geq 2$, at different wavelengths around 422 nm, but no signals could be recorded, probably because the reaction is too fast to be observed by T-jump, which is compatible with the binding of additional TMPyP4 molecules to PD_1 to build the external complex PD_2.

As to the type of interaction of TMPyP4 with G quadruplex, different modes of binding have been proposed, including intercalation of the ligand between adjacent G-quartets, end-stacking on the external G-tetrads and groove-binding with external loops [20,22,43]. On one hand, the rather high k_d values obtained by T-jump measurements (Table 2) appear to be incompatible with intercalation of TMPyP4 into the G-tetrads, as the residence time is too short compared to other processes involving this mode of binding [44]. On the other hand, the pronounced red shift observed (Figs. 2B and 1SIB) indicates that PD$_1$ involves stacking between TMPyP4 and Tel22. This shift has been attributed to end-stacking of TMPyP4 on the external G-tetrads of the G-quadruplex [22,39]. However, the X-ray structure reported by Neidle et al. for human telomeric G-quadruplex/TMPyP4 complex has shown that TMPyP4 failed to directly interact with the external G-tetrad due to steric clashes between the G-tetrad edges and the *N*-methylpyridyl groups of TMPyP4 [21]. Instead, TMPyP4 established π-π interactions with external bases and electrostatic interactions between the cationic *N*-methylpyridyl groups and the phosphate ions of the telomeric DNA. Hence, MD simulations were carried out to shed light both on i) the distinct experimental kinetic behaviour observed as a consequence of the interaction of TMPyP4 with the two G-quadruplex conformations of Tel22, and ii) on the nature of its mode of binding.

3.6. MD simulations

The T-jump technique demonstrated quantitatively that the rates of formation of F1M/TMPyP4 and F2M/TMPyP4 were different, but it is unable to differentiate which of the two complexes gets formed faster. Moreover, the structural difference between F1M and F2M provides a convincing explanation for the different reaction rates which, notwithstanding, does not alter the affinity for TMPyP4, thus presenting very similar values of the affinity constants K$_1$. To discern this issue, explain the reasons for such a difference and shed some light into the binding features of the Tel22/TMPyP4 system, MD simulations were carried out using the well-characterized hybrid Tel22 conformations in K$^+$. These two conformations display quite similar structure containing the same type and number of loops (one reversal and two lateral loops), but their arrangement is actually different. In the hybrid-1 (F1K), the 5′ loop is in the reversed configuration, whereas in the hybrid-2 (F2K) the 3′ loop is the one in the reversed configuration, as represented in Scheme 1 [40]. Fig. 3SI shows the optimized structure of TMPyP4, where the central aromatic moiety remains planar, while the methylpyridine groups can rotate nearly perpendicular to the molecular plane. The Root-Mean-Square Deviation (RMSD) plot, red line in Fig. 6, and the atom-atom distance between TMPyP4 and a selected nucleotide, blue line in Fig. 6, both enable one to follow the host-guest binding process occurring along the MD trajectory, where important conformational changes occur before and at the equilibrium phase. Different intermediate structures of the F1K/TMPyP4 and F2K/TMPyP4 complexes, occurring along the MD simulation are also shown (Fig. 6A and B), and describe the molecular recognition process until the equilibrium (plateau) is reached. In particular, the distance between one of the four pyrrole nitrogen atoms of TMPyP4 and one atom of the external bases, thymine O1 for F1K and adenine N1 for F2K, reveals that the final stacking distance between TMPyP4 and both DNA hybrids oscillates around 4 Å when the equilibrium phase has been reached. The initial and final position of TMPyP4 (gray) is shown in Fig. 7 (see also Fig. 4SI for all considered starting positions). It can be observed that TMPyP4 binds to the nucleic acid through π-π stacking interactions with a nitrogen base in the groove (thymine in F1K and adenine in F2K). In addition, the methylpyridyl groups, positively charged, remain oriented towards the negatively charged phosphate groups of the G-quadruplex chain.

The analysis of the experimental data demonstrates that the thermodynamics of the binding of TMPyP4 to F1K and F2K are similar, as indicated by the very close values of the thermodynamic constant, $K_1 = k_f/k_d$, of the equilibria represented in Eqs. (4) and (5). The results of the MD simulations provide a plausible explanation for such phenomena, as the binding mode and the final structure of the F1K/TMPyP4 complex and those of the F2K/TMPyP4 complex are closely akin (Fig. 7), which render them thermodynamically indistinguishable.

On the other hand, the values of the kinetic constants k_f and k_d indicate that one of the two binding processes is faster by one order of magnitude than the other (Table 2). Interestingly, remarkable differences were found in the molecular recognition process along the MD trajectory. In fact, Fig. 8 reveals that TMPyP4 binds rapidly to an adenine residue (highlighted green) in both hybrids, F1K and F2K, at roughly 2.5 ns. However, in the F2K/TMPyP4 system the binding to the adenine base persists up to the end of the simulation (Fig. 8A), so the equilibrium is attained faster. By contrast, an important change in the position of the ligand is observed at 101 ns for the F1K/TMPyP4 system (Fig. 8B). In particular, it is released from the binding site at the adenine base and binds to a thymine residue (highlighted yellow), finally reaching an equilibrium state. In our opinion, this difference can be related to the slower kinetics of binding experimentally observed by T-jump for one of the two hybrids.

In summary, the pathway observed during the molecular recognition process points to a difference in the time needed to reach the equilibrium structure for the F1K/TMPyP4 and F2K/TMPyP4 complexes. As k_f and k_d are directly related to the reciprocal time of formation and dissociation of the F1K/TMPyP4 and F2K/TMPyP4 complexes, the MD simulation results are in fairly good agreement with the two different experimental values observed for $k_{f,i}$ and $k_{d,i}$.

It also allows one to assess that, in the case of Tel22 in K$^+$, the faster

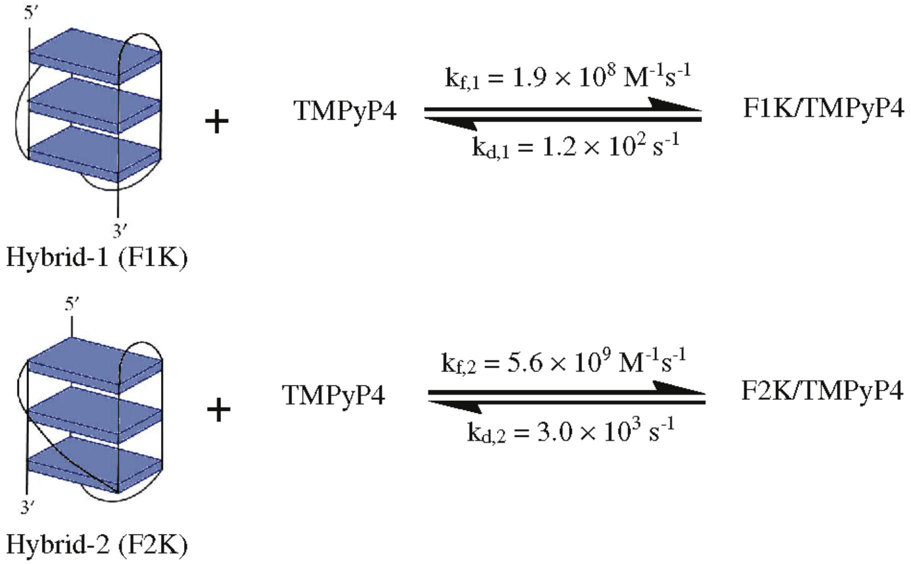
5′
3′
Hybrid-1 (F1K)
+
TMPyP4
$k_{f,1} = 1.9 \times 10^8\ M^{-1}s^{-1}$
$k_{d,1} = 1.2 \times 10^2\ s^{-1}$
F1K/TMPyP4
5′
3′
Hybrid-2 (F2K)
+
TMPyP4
$k_{f,2} = 5.6 \times 10^9\ M^{-1}s^{-1}$
$k_{d,2} = 3.0 \times 10^3\ s^{-1}$
F2K/TMPyP4

Scheme 1. Schematic representation of the kinetic behaviour of the Tel22/TMPyP4 system in K$^+$.

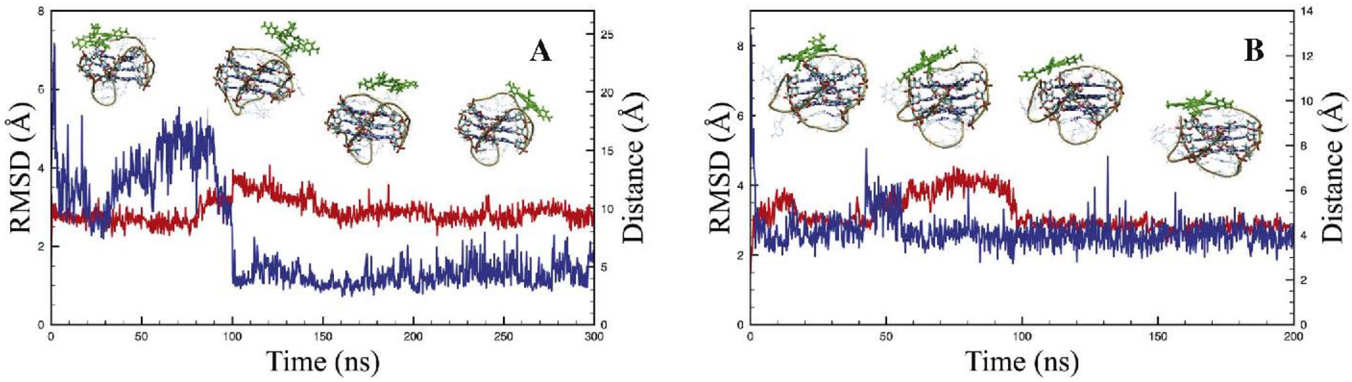

Fig. 6. RMSD plot (red) and specific distance between one of the four pyrrole nitrogen atoms of TMPyP4 and one atom of the binding base (blue) for the F1K/TMPyP4 (A) and the F2K/TMPyP4 system (B).

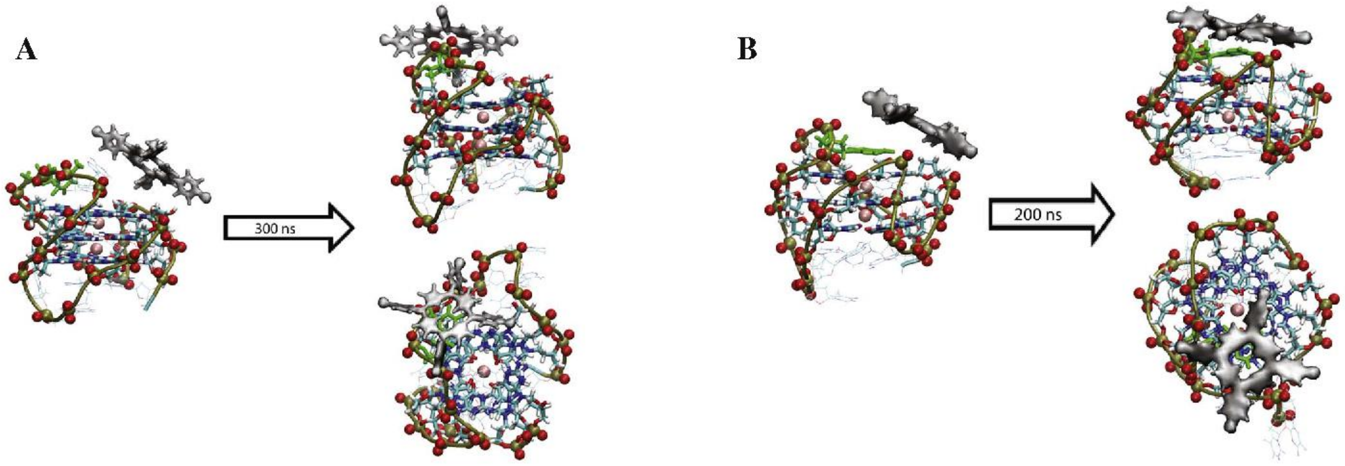

Fig. 7. Initial and final (top and side views) relative positions in the MD simulation of TMPyP4 (gray) and Tel22. Oxygen atoms in phosphate groups are represented as red balls; water and counterions have been removed. (A) Hybrid-1 F1K; the thymine base interacting with TMPyP4 is highlighted in green. (B) Hybrid-2 F2K; the adenine base interacting with TMPyP4 is highlighted in green.

kinetics involves the binding of TMPyP4 to the hybrid-2 form, F2K, whereas the slower kinetics is related to the binding of TMPyP4 to the hybrid-1 form, F1K. The $k_{f,i}$ and $k_{d,i}$ values of reactions 4 and 5 are defined and assigned in Scheme 1 for K^+ buffer.

The possibility of building different conformations from the same sequence is a complex issue that confers G-quadruplexes very interesting physical chemistry features. When the biological relevance of these conformations becomes well-known, we shall be aware of the importance conveyed by the fact that a ligand may stay more or less time bound to a particular G4 conformation. For example, in ligand/

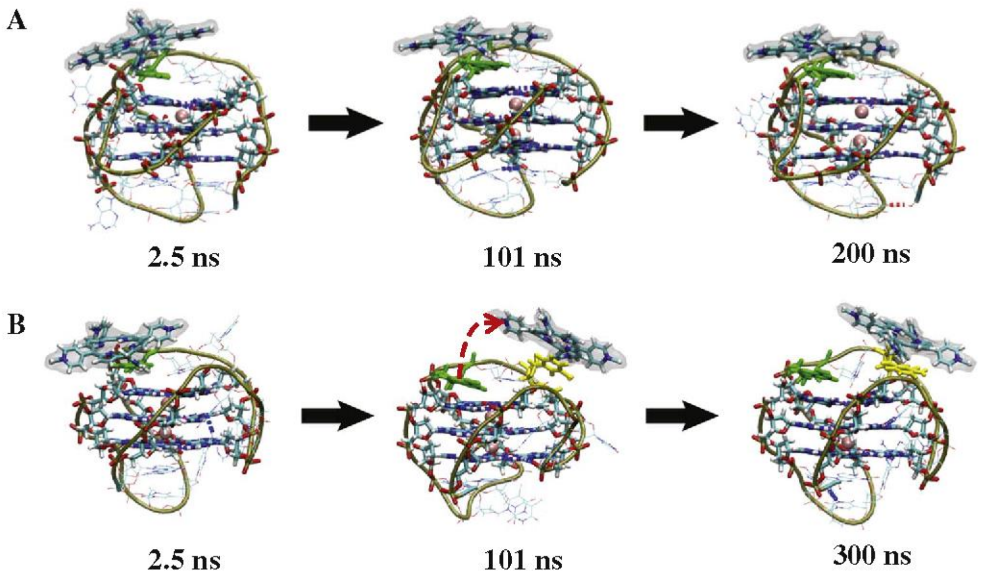

Fig. 8. Molecular recognition scheme during the MD simulation of the F2K/TMPyP4 system (A) and the F1K/TMPyP4 system (B).

DNA intercalation reactions, slow dissociation rates are viewed as an important criterion regarding their efficiency as cancer therapeutics, because such drugs remain longer in the intercalation position and are assumed to alter the DNA transcription [45].

4. Conclusions

We have shown for the first time by experimental measurements and molecular modeling that a small ligand such as the cationic porphyrin TMPyP4 interacts in a distinct way with the two forms of G-quadruplex present in solution for the human telomeric sequence Tel22, both in Na^+ and K^+ buffers. In fact, for a particular buffer, under the same experimental conditions, two different sets of rate constants (k_f and k_d) differing by one order of magnitude but yielding the same affinity constant $K_1 = k_f/k_d$ were observed. MD simulations performed with the Tel22 structures in the presence of K^+ ions suggest that the hybrid-2 reaches the equilibrium with TMPyP4 faster than with hybrid-1. However, the structural difference between the two final equilibrium complexes is small, rendering the two types of Tel22/TMPyP4 complex thermodynamically indistinguishable and accounting for the only thermodynamic constant value obtained for K_1. Moreover, it provides convincing explanation for the observation that, although the coexistence of different conformations in solution has been probed for several G-quadruplex sequences, only kinetic techniques can fully characterize the binding mechanism of small ligands to the different structures when the final equilibrium states are nearly equivalent.

Conflict of interest

The authors have no conflict of interest to declare.

Transparency document

The Transparency document associated with this article can be found, in online version.

Acknowledgements

The research leading to these results has received funding from “la Caixa” Foundation (project OSLC-2012-007), MINECO, (CTQ2014-58812-C2-2-R) and Junta de Castilla y León, (BU042U16), FEDER Funds Spain, are gratefully acknowledged. C.P-A. is grateful for the FPU grant from Ministry of Education, Culture and Sports, Spain (FPU13/00180).

Appendix A. Supplementary data

Supplementary data to this article can be found online at https://doi.org/10.1016/j.bbagen.2017.10.020.

References

[1] D. Monchaud, M.-P. Teulade-Fichou, A hitchhiker's guide to G-quadruplex ligands, Org. Biomol. Chem. 6 (2008) 627–636.

[2] P. Murat, S. Balasubramanian, Existence and consequences of G-quadruplex structures in DNA, Curr. Opin. Genet. Dev. 25 (2014) 22–29.

[3] V.S. Chambers, G. Marsico, J.M. Boutell, M. Di Antonio, G.P. Smith, S. Balasubramanian, High-throughput sequencing of DNA G-quadruplex structures in the human genome, Nat. Biotechnol. 33 (2015) 877–881.

[4] A. Bedrat, J.-L. Mergny, L. Lacroix, Re-evaluation of G-quadruplex propensity with G4Hunter, Nucleic Acids Res. 44 (2016) 1746–1759.

[5] S. Neidle, Human telomeric G-quadruplex: the current status of telomeric G-quadruplexes as therapeutic targets in human cancer, FEBS J. 277 (2010) 1118–1125.

[6] H. Lodish, A. Berk, C.A. Kaiser, M. Krieger, M.P. Scott, A. Bretscher, H. Ploegh, P. Matsudaira, Intracellular ion environment and membrane electric potential, in: N.Y.W.H. Freeman (Ed.), 4th ed, Mol. Cell Biol. 2000.

[7] A. Ambrus, D. Chen, J. Dai, T. Bialis, R.A. Jones, D. Yang, Human telomeric sequence forms a hybrid-type intramolecular G-quadruplex structure with mixed parallel/antiparallel strands in potassium solution, Nucleic Acids Res. 34 (2006) 2723–2735.

[8] A.T. Phan, K.N. Luu, D.J. Patel, Different loop arrangements of intramolecular human telomeric (3 + 1) G-quadruplexes in K^+ solution, Nucleic Acids Res. 34 (2006) 5715–5719.

[9] Y. Wang, D.J. Patel, Solution structure of the human telomeric repeat d [AG3(T2AG3)3]G-tetraplex, Structure 1 (1993) 263–282.

[10] K.W. Lim, V.C.M. Ng, N. Martin-Pintado, B. Heddi, A.T. Phan, Structure of the human telomere in Na + solution: an antiparallel (2 + 2) G-quadruplex scaffold reveals additional diversity, Nucleic Acids Res. 41 (2013) 10556–10562.

[11] C. Perez-Arnaiz, N. Busto, J.M. Leal, B. Garcia, New microsecond intramolecular reactions of human telomeric DNA in solution, RSC Adv. 6 (2016) 39204–39208.

[12] M. Aznauryan, S. Sondergaard, S.L. Noer, B. Schiott, V. Birkedal, A direct view of the complex multi-pathway folding of telomeric G-quadruplexes, Nucleic Acids Res. 44 (2016) 11024–11032.

[13] J. Palacky, M. Vorlickova, I. Kejnovska, P. Mojzes, Polymorphism of human telomeric quadruplex structure controlled by DNA concentration: a Raman study, Nucleic Acids Res. 41 (2013) 1005–1016.

[14] J. Sponer, G. Bussi, P. Stadlbauer, P. Kuhrova, P. Banas, B. Islam, S. Haider, S. Neidle, M. Otyepka, Folding of guanine quadruplex molecules-funnel-like mechanism or kinetic partitioning? An overview from MD simulation studies, Biochim. Biophys. Acta, Gen. Subj. 1861 (2017) 1246–1263.

[15] M. Boncina, G. Vesnaver, J.B. Chaires, J. Lah, Unraveling the thermodynamics of the folding and interconversion of human telomere G-quadruplexes, Angew. Chem. Int. Ed. 55 (2016) 10340–10344.

[16] R.T. Wheelhouse, D. Sun, H. Han, F.X. Han, L.H. Hurley, Cationic porphyrins as telomerase inhibitors: the interaction of tetra(*N*-methyl-4-pyridyl)porphine with Quadruplex DNA, J. Am. Chem. Soc. 120 (1998) 3261–3262.

[17] T.L. Ruan, S.J. Davis, B.M. Powell, C.P. Harbeck, J. Habdas, P. Habdas, L.A. Yatsunyk, Lowering the overall charge on TMPyP4 improves its selectivity for G-quadruplex DNA, Biochimie 132 (2017) 121–130.

[18] A.J. Gaier, D.R. McMillin, Binding studies of G-Quadruplex DNA and porphyrins: Cu (T4) vs sterically friendly Cu(tD4), Inorg. Chem. 54 (2015) 4504–4511.

[19] J.I. DuPont, K.L. Henderson, A. Metz, V.H. Le, J.P. Emerson, E.A. Lewis, Calorimetric and spectroscopic investigations of the binding of metallated porphyrins to G-quadruplex DNA, Biochim. Biophys. Acta, Gen. Subj. 1860 (2016) 902–909.

[20] I. Haq, J.O. Trent, B.Z. Chowdhry, T.C. Jenkins, Intercalative G-Tetraplex stabilization of telomeric DNA by a cationic porphyrin, J. Am. Chem. Soc. 121 (1999) 1768–1779.

[21] G.N. Parkinson, R. Ghosh, S. Neidle, Structural basis for binding of porphyrin to human telomeres, Biochemistry 46 (2007) 2390–2397.

[22] C. Wei, G. Jia, J. Zhou, G. Han, C. Li, Evidence for the binding mode of porphyrins to G-quadruplex DNA, Phys. Chem. Chem. Phys. 11 (2009) 4025–4032.

[23] M. Boncina, C. Podlipnik, I. Piantanida, J. Eilmes, M.-P. Teulade-Fichou, G. Vesnaver, J. Lah, Thermodynamic fingerprints of ligand binding to human telomeric G-quadruplexes, Nucleic Acids Res. 43 (2015) 10376–10386.

[24] L. Martino, B. Pagano, I. Fotticchia, S. Neidle, C. Giancola, Shedding light on the interaction between TMPyP4 and human telomeric quadruplexes, J. Phys. Chem. B 113 (2009) 14779–14786.

[25] R. Rigler, C.R. Rabl, T.M. Jovin, Temperature-jump apparatus for fluorescence measurements, Rev. Sci. Instrum. 45 (1974) 580–588.

[26] J. Dai, C. Punchihewa, A. Ambrus, D. Chen, R.A. Jones, D. Yang, Structure of the intramolecular human telomeric G-quadruplex in potassium solution: a novel adenine triple formation, Nucleic Acids Res. 35 (2007) 2440–2450.

[27] J.J.P. Stewart, Optimization of parameters for semiempirical methods V: modification of NDDO approximations and application to 70 elements, J. Mol. Model. 13 (2007) 1173–1213.

[28] Y. Zhao, D.G. Truhlar, The M06 suite of density functionals for main group thermochemistry, thermochemical kinetics, noncovalent interactions, excited states, and transition elements: two new functionals and systematic testing of four M06-class functionals and 12 other function, Theor. Chem. Accounts 120 (2008) 215–241.

[29] V. Barone, M. Cossi, Quantum calculation of molecular energies and energy gradients in solution by a conductor solvent model, J. Phys. Chem. A 102 (1998) 1995–2001.

[30] M. Cossi, N. Rega, G. Scalmani, V. Barone, Energies, structures, and electronic properties of molecules in solution with the C-PCM solvation model, J. Comput. Chem. 24 (2003) 669–681.

[31] J. Wang, R.M. Wolf, J.W. Caldwell, P.A. Kollman, D.A. Case, Development and testing of a general Amber force field, J. Comput. Chem. 25 (2004) 1157–1174.

[32] J. Wang, W. Wang, P.A. Kollman, D.A. Case, Automatic atom type and bond type perception in molecular mechanical calculations, J. Mol. Graph. Model. 25 (2006) 247–260.

[33] A.T. Guy, T.J. Piggot, S. Khalid, Single-stranded DNA within nanopores: conformational dynamics and implications for sequencing; a molecular dynamics simulation study, Biophys. J. 103 (2012) 1028–1036.

[34] D. Van Der Spoel, E. Lindahl, B. Hess, G. Groenhof, A.E. Mark, H.J.C. Berendsen, GROMACS: fast, flexible, and free, J. Comput. Chem. 26 (2005) 1701–1718.

[35] B. Hess, C. Kutzner, D. van der Spoel, E. Lindahl, GROMACS 4: algorithms for highly efficient, load-balanced, and scalable molecular simulation, J. Chem. Theory Comput. 4 (2008) 435–447.

[36] G. Bussi, D. Donadio, M. Parrinello, Canonical sampling through velocity rescaling, J. Chem. Phys. 126 (2007) 014101/1–014101/7.

[37] T. Darden, D. York, L. Pedersen, Particle mesh Ewald: an N·log(N) method for Ewald sums in large systems, J. Chem. Phys. 98 (1993) 10089–10092.

[38] I. Jelesarov, H.R. Bosshard, Isothermal titration calorimetry and differential scanning calorimetry as complementary tools to investigate the energetics of

biomolecular recognition, J. Mol. Recognit. 12 (1999) 3–18.

[39] A. Arora, S. Maiti, Effect of loop orientation on quadruplex-TMPyP4 interaction, J. Phys. Chem. B 112 (2008) 8151–8159.

[40] R.D. Gray, J.O. Trent, J.B. Chaires, Folding and unfolding pathways of the human telomeric G-quadruplex, J. Mol. Biol. 426 (2014) 1629–1650.

[41] A. De Rache, J.-L. Mergny, Assessment of selectivity of G-quadruplex ligands via an optimised FRET melting assay, Biochimie 115 (2015) 194–202.

[42] A. Spinello, G. Barone, J. Grunenberg, Molecular recognition of naphthalene diimide ligands by telomeric quadruplex-DNA: the importance of the protonation state and mediated hydrogen bonds, Phys. Chem. Chem. Phys. 18 (2016) 2871–2877.

[43] C. Wei, G. Jia, J. Yuan, Z. Feng, C. Li, A spectroscopic study on the interactions of porphyrin with G-Quadruplex DNAs, Biochemistry 45 (2006) 6681–6691.

[44] W.D. Wilson, C.R. Krishnamoorthy, Y.H. Wang, J.C. Smith, Mechanism of intercalation: ion effects on the equilibrium and kinetic constants for the interaction of propidium and ethidium with DNA, Biopolymers 24 (1985) 1941–1961.

[45] A. Rhoden Smith, B.L. Iverson, Threading polyintercalators with extremely slow dissociation rates and extended DNA binding sites, J. Am. Chem. Soc. 135 (2013) 12783–12789.

Kinetic evidence for interaction of TMPyP4 with two different G-quadruplex conformations of human telomeric DNA

Cristina Pérez-Arnaiz,[a] Natalia Busto,[a] Javier Santolaya,[a,b] José M. Leal,[a] Giampaolo Barone[b*] and Begoña García[a*]

SUPPORTING INFORMATION

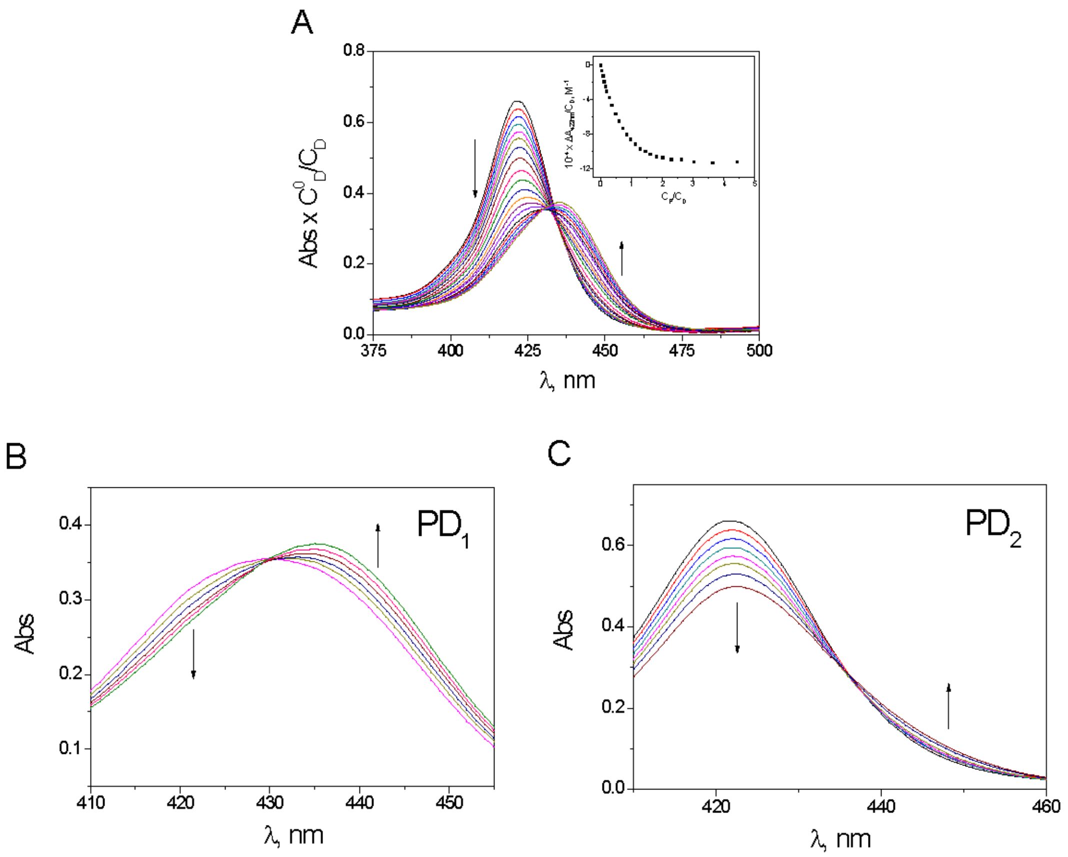

Fig. 1SI. Absorption spectra obtained from the titration of the TMPyP4/Tel22 system in 0.15 M KCl. Inset: Binding isotherm at 422 nm (**A**). The spectral curves of **Fig. 1SI.A** show two different behaviours in diluted solution, $C_D/C_P < 2$ (**B**) and in concentrated solution $C_D/C_P > 2$ (**C**). $C^0_D = 3.5$ μM, pH = 7.5 (10 mM Tris-HCl, 1 mM EDTA), T = 25 °C.

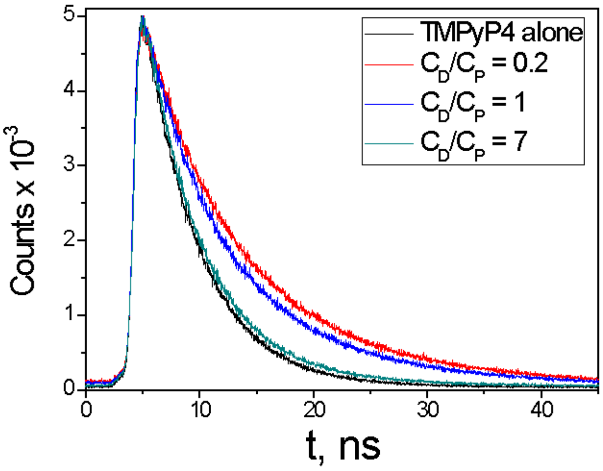

Fig. 2SI. Fluorescence lifetime decay for TMPyP4 (C_D = 3 μM) in the presence of different concentrations of Tel22 in 0.15 M KCl using excitation at λ_{exc} = 405 nm and emission at λ_{em} = 712 nm. pH = 7.5 (10 mM Tris-HCl, 1 mM EDTA) and T = 25 °C.

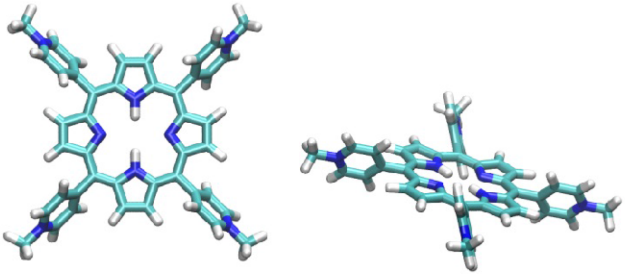

Fig. 3SI. Optimized structure of TMPyP4.

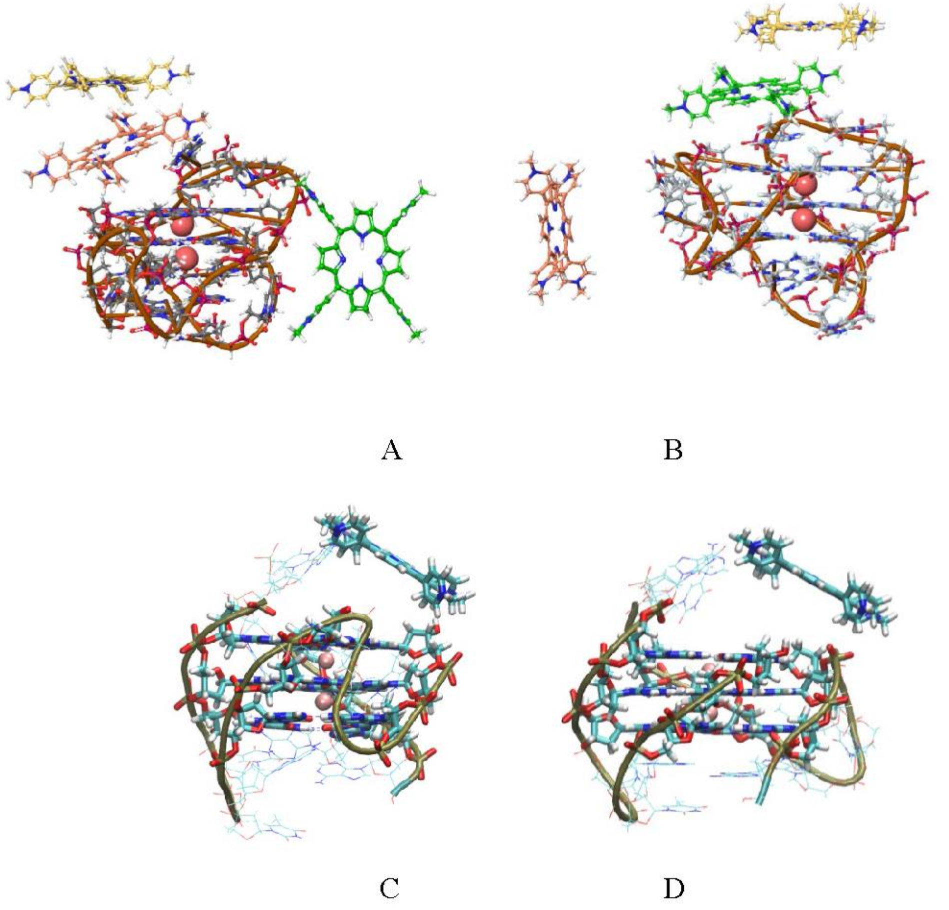

Figure 4SI. Initial relative positions for TMPyP4 and 2HY9 (F1K A) and 2JPZ (F2K B), opened F1K (C) and opened F2K (D)

Table 1SI. Fluorescence lifetime obtained for the Tel22/TMPyP4 system at different C_D/C_P ratios using λ_{exc} = 405 nm and λ_{em} = 712 nm. τ_1 and τ_2 stand for the lifetime of TMPyP4 and the Tel22/TMPyP4 complex (PD_1), respectively. f_1 and f_2 stand for the fractional amplitudes.

	Na^+					**K^+**				
C_D/C_P ratio	τ_1 (ns)	τ_2 (ns)	f_1 (%)	f_2 (%)	χ^2	τ_1 (ns)	τ_2 (ns)	f_1 (%)	f_2 (%)	χ^2
0	4.79	-	100	-	1.06	4.77	-	100	-	1.08
0.2	5.11	10.06	15.2	84.8	1.06	5.02	11.01	12.8	88.2	1.04
1	5.13	10.57	40.6	59.4	1.02	4.75	10.73	34.2	65.8	0.99
7	4.71	10.55	85.8	14.2	0.93	4.72	10.73	81.6	18.4	1.01

Capítulo VIII

Interacción de Complejos de Ni, Cu y V con Diferentes Secuencias de G-cuádruplex

Summary

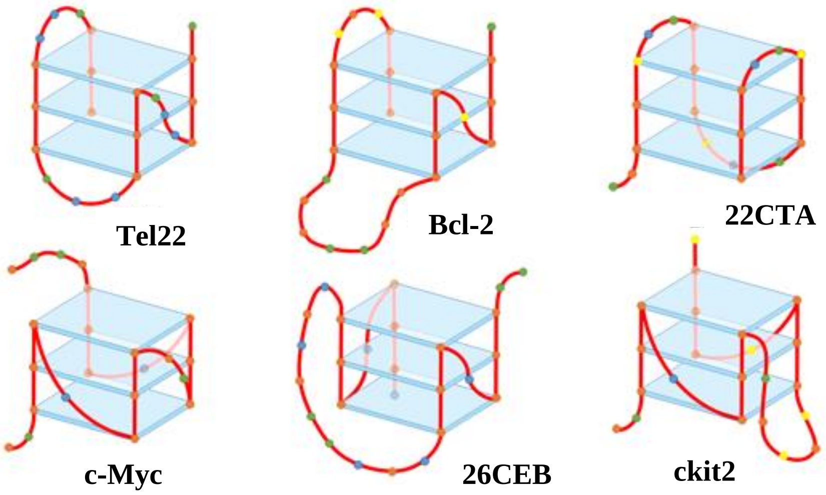

Figure 1. Schematic representation of the DNA G-quadruplex structures used in this work.

The interaction of four metal complexes, based on salphen or bipyridine scaffolds, with different G-quadruplexes (**Figure 1**) has been explored to gain insight into their structural selectivity. Most of the results presented in this Chapter were obtained during the predoctoral stay at Imperial College (London, UK) under the supervision of Prof. Ramón Vilar, except for the UV-Vis and ITC titrations that were carried out after returning to University of Burgos. The three salphen complexes bearing nickel(II), copper(II) and oxovanadium(IV) centres, named here as **1**, **2** and **3**, respectively, had been previously reported by Ramón Vilar et al [219,220]. They present different degrees of planarity, which determines their ability to stabilize the folded G-quadruplex structures through stacking interactions with the external G-quartets. The new nickel(II)-bipyridine complex, named as **4**, which presents a larger aromatic core compared to the salphen complexes, was synthesized and characterized by Dr Anna Łeczkowska

In this project, which was being developed by Prof. Ramón Vilar and Dr Jorge González, we aimed at determining if there were significant differences in the stabilizing ability of the metal complexes towards different quadruple-stranded structures. This would imply that besides presenting selectivity towards G-quadruplex over duplex DNA, there could exist selectivity towards specific G-quadruplex sequences of interest thanks to their particular structural features.

First, the stabilizing effect of the four metal complexes was tested against the different G-quadruplexes and also against a double-stranded oligonucleotide by FRET melting measurements. Then, ITC was used to obtain the thermodynamic binding parameters with human telomeric G-quadruplex DNA (Tel22). The polymerase stop assay (PSA) was also performed to evaluate if the stabilization of the G-quadruplex structure induced by these complexes had an impact on a biologically relevant event such as the inhibition of DNA replication by a DNA polymerase enzyme. As the PSA could not be performed with Tel22 due to experimental problems, the well-known c-Myc sequence was chosen for this assay.

Altogether, we can conclude that the new bipyridine complex represents a remarkable improvement over the previous salphen scaffold, probably due to the larger planar aromatic surface that enhances the stacking interactions with the external G-quartets. On the other hand, these metal complexes were capable of inhibiting the activity of a DNA polymerase enzyme, as demonstrated here by the PSA results, which implies that this stabilization could have important biological consequences.

1. Introduction.

The majority of anticancer chemotherapeutic drugs target DNA, which is a relatively indiscriminate manner to treat cancer that brings about issues such as high toxicity and generation of resistance mechanisms. Because of this, there has been a high interest in the development of new approaches to make DNA a more selective target. One interesting approach is to design DNA sequence-specific drugs that could inhibit the transcription of particular genes. However, this type of compounds need to recognize sequences of 16 to 20 nucleotides to be selective, making it difficult to obtain effective therapeutic agents [80]. Another approach involves the structural selectivity, in which smaller molecules can target specific sequences taking advantage of their potential to form four-stranded DNA structures with very particular features: the G-quadruplexes [95].

G-quadruplex structures are formed in guanine-rich sequences. Their basic structural unit is the G-quartet, a planar motif generated from four guanine residues that are held together by Hoogsteen hydrogen bonds [43]. The core of a G-quadruplex is formed by two or more stacked G-quartets, stabilized by cations such as Na^+ or K^+ coordinated to the guanine oxygen atoms pointing towards the inner channel, and connected by the intervening sequences termed “loops”. G-quadruplexes are highly polymorphic, as their structure depends on factors such as their nucleotide sequence and the composition of the medium (see **section 2.2.2, Chapter I**).

Recently, more than 700.000 sequences with the potential to form G-quadruplexes have been identified in the human genome, and it was found that they are significantly associated with sequences present in oncogenes and tumor suppressor genes [29]. Although their biological role is not completely understood, they are thought to be related with processes such as telomere maintenance, gene regulation or replication [92], and recent studies also provide evidence for their formation in live cells [221]. Thus, these regions may represent promising targets for cancer intervention [26]. Moreover, their polymorphism could be useful for the selective targeting of specific G-quadruplex sequences of interest by small molecules. For this reason, the selectivity of a family of metal complexes (**Figure 2.A**) towards a set of DNA G-quadruplex sequences, including the human telomeric region (Tel22) and the promoter regions of several oncogenes such as c-Myc or Bcl-2, and one RNA G-quadruplex sequence, TERRA, has been explored in this work. The sequences of all the G-quadruplexes used in this study and the literature describing their structural characteristics can be found in **section 1.1.4.2, Chapter II**. In order to better visualize these structures, a schematic representation of the main conformations of the DNA G-quadruplexes derived from the data available in the literature is shown in **Figure 2.B**.

The G-quadruplex stabilization occurs, in most cases, via π-stacking and electrostatic interactions between the ligand, usually a flat molecule, and the external G-quartet of the G-quadruplex. Because of this, the rational design of new selective G-quadruplex binders is based on molecules that feature a large planar aromatic surface to enhance the stacking interactions with the external G-quartets [78].

The ligands studied in this work are four metal complexes with either a salphen or a bipyridine scaffold (**Figure 2.A**). The synthesis and characterization of the nickel(II), copper(II) and vanadyl-salphen complexes (**1-3**) and their binding characteristics towards telomeric DNA G-quadruplex had been previously reported [219,220]. The geometry around the Ni(II) and Cu(II) centres is square-planar, whereas the vanadyl complex presents a square-based pyramidal geometry. The new Ni(II)-bipyiridine complex (**4**) presents a larger planar aromatic surface in its core. For convenience, the metal complexes can be referred to as "D" and the polinucleotide species to as "P" in the text.

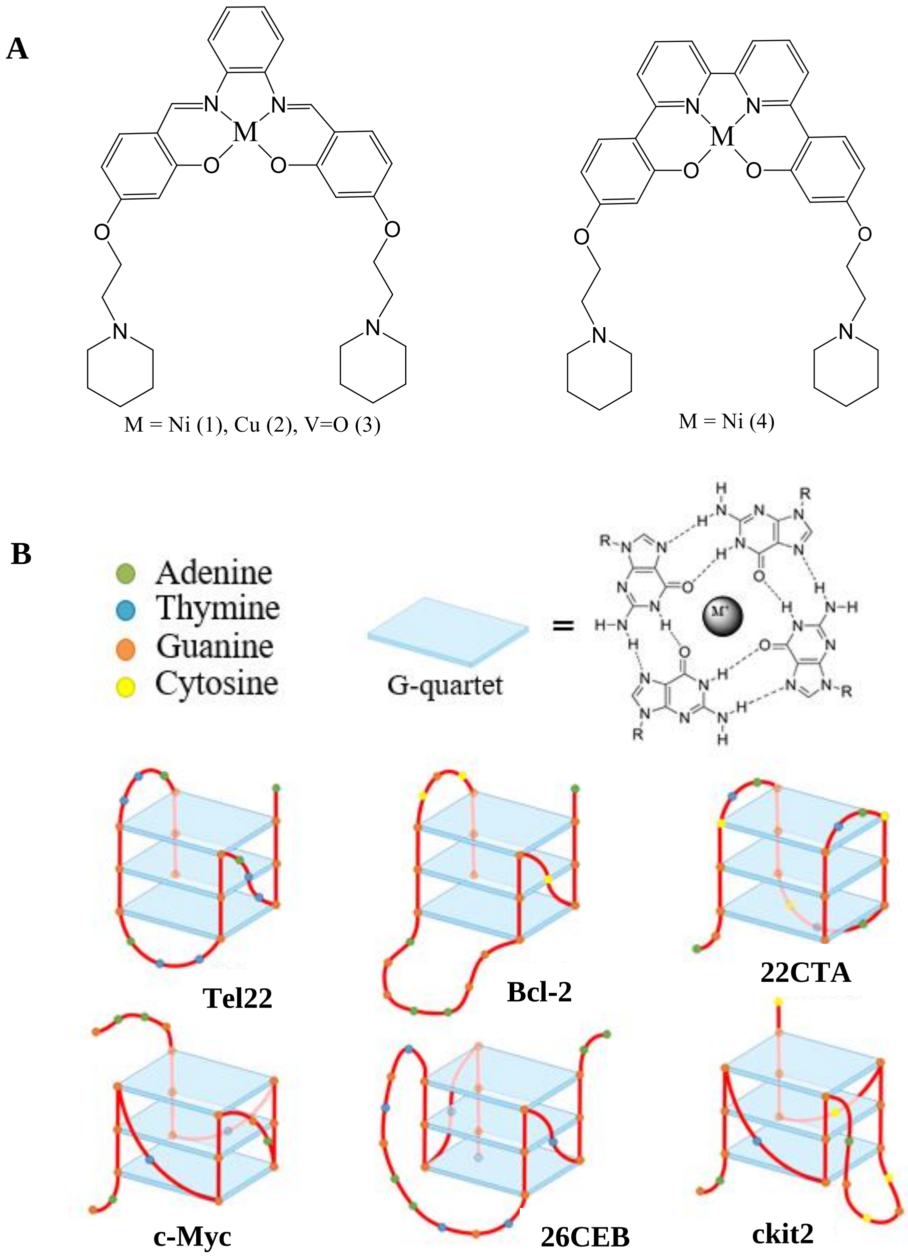
A
M = Ni (1), Cu (2), V=O (3)
M = Ni (4)
B
Adenine
Thymine
Guanine
Cytosine
G-quartet
=
Tel22
Bcl-2
22CTA
c-Myc
26CEB
ckit2

Figure 2. A) Chemical structures of the salphen and bipyridine complexes. **B**) Representation of the main conformations of the DNA G-quadruplex structures derived from the literature shown in **section 1.1.4.2, Chapter II.**

This study intended to reach the following objectives: (a) to check whether the rational modification introduced in the new complex, **4**, results in a higher affinity towards G-quadruplex structures; (b) to explore the stabilization effect of the four metal complexes towards different G-quadruplexes, including parallel and antiparallel conformations, and different size and arrangement of loops, as shown in **Figure 2.B**; and (c) to determine if the stabilization induced by the complexes had an impact on the activity of a DNA polymerase enzyme.

2. Results and discussion.

2.1. pK$_a$ studies.

The acid dissociation constants, K$_a$, of the four metal complexes were obtained to determine the nature of the species present in solution in the experimental conditions used in this work. In all cases, the existance of two isosbestic points unveils the existence of three different species depending on the pH, which is in good agreement with the deprotonation of the two amine groups in the ethyl piperidine units of the four metal complexes. **Figures 3-6** show the spectra recorded for complexes **1-4** in the pH range = 4.5 – 9.5. The pK$_{a1}$ and pK$_{a2}$ values can be obtained by plotting the absorbance at the wavelengths corresponding to each of the two isosbestic points against the pH, as shown in **Figures 3-6**, according to **eq 1**:

$$A = \frac{A_B - A_{HB^+}}{1 + 10^{(pK_a - pH)}} + A_{HB^+} \qquad (1)$$

where A_{HB+} and A_B stand for the absorbance of the protonated and the deprotonated forms, respectively, and A stands for the total absorbance at each point.

Table 1 lists the two pK$_a$ values obtained for each complex. All of them present pK$_a$ values above the working pH, so they are protonated and positively charged in aqueous solution under physiological conditions. Cationic G-quadruplex binders present several advantages, as they can establish electrostatic interactions with the negatively charged inner channel of the G-quadruplex and/or with the phosphate groups of the loops.

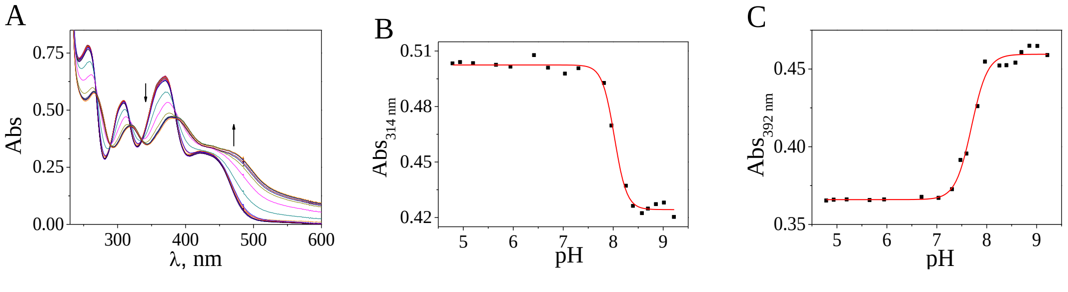

Figure 3. A) Absorbance spectra of **1** recorded with increasing pH (arrow sense) from pH = 4.5 to pH = 9.5. **B)** Absorbance *vs* pH plot of **1** at λ = 314 nm and **C)** at λ = 392 nm and fitting of **eq 1** to the absorbance data (red line).

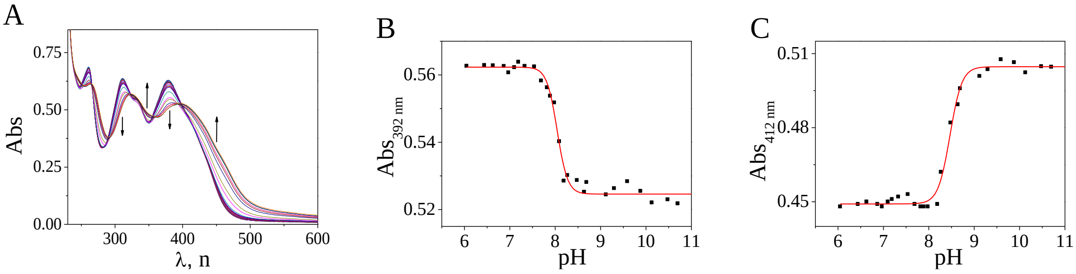

Figure 4. A) Absorbance spectra of **2** recorded with increasing pH (arrow sense) from pH = 4.5 to pH = 11. **B)** Absorbance *vs* pH plot of **2** at λ = 392 nm and **C)** at λ = 412 nm and fitting of **eq 1** to the absorbance data (red line).

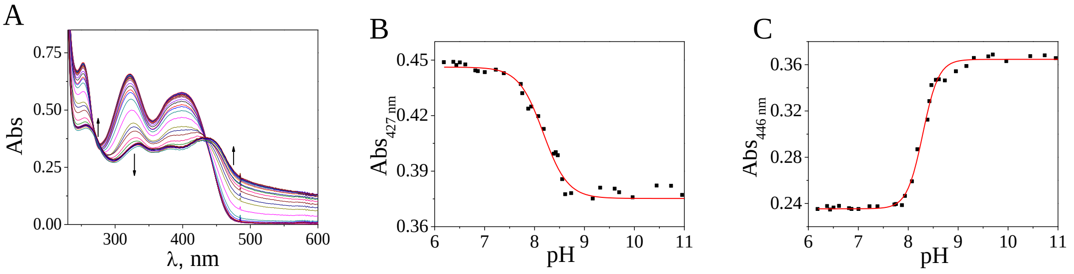

Figure 5. A) Absorbance spectra of **3** recorded with increasing pH (arrow sense) from pH = 4.5 to pH = 11. **B)** Absorbance *vs* pH plot of **3** at λ = 427 nm and **C)** at λ = 446 nm and fitting of **eq 1** to the absorbance data (red line).

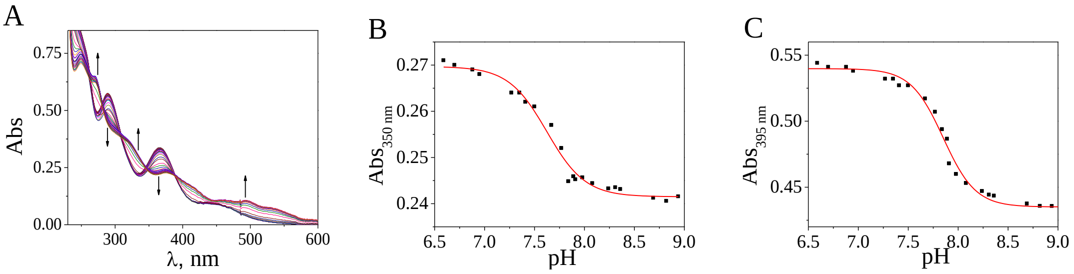

Figure 6. A) Absorbance spectra of **4** recorded with increasing pH (arrow sense) from pH = 4.5 to pH = 11. **B)** Absorbance *vs* pH plot of **4** at λ = 350 nm and **C)** at λ = 395 nm and fitting of **eq 1** to the absorbance data (red line).

Table 1. pK_{a1} and pK_{a2} values obtained for complexes **1-4**.

Complex	pK_{a1}	pK_{a2}
1	7.69 ± 0.02	8.02 ± 0.01
2	8.04 ± 0.02	8.47 ± 0.02
3	8.17 ± 0.03	8.30 ± 0.01
4	7.62 ± 0.02	7.85 ± 0.01

2.2. Aggregation studies.

The formation of aggregates in solution can be studied by following the absorbance of the metal complexes at different concentrations. If only the monomer species is present in solution, the absorbance - concentration data pairs will obey the Lambert-Beer law [222]. **Figure 7** gathers the spectra of the complexes at pH = 7.0 and **Figure 8** the fitting of the Lambert-Beer equation to the experimental data for complexes **1-4** at the different absorbance maxima, so we can conclude that only the monomer species is present in solution in the studied concentration range.

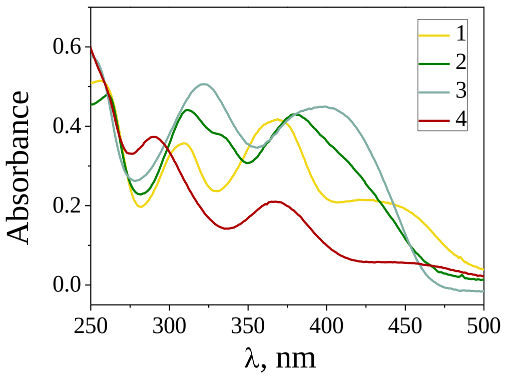

Figure 7. Absorbance spectra of complexes **1-4** at C_D = 20 µM. 50 mM Tris-HCl (pH = 7.0), 10 mM KCl, T = 25 ºC.

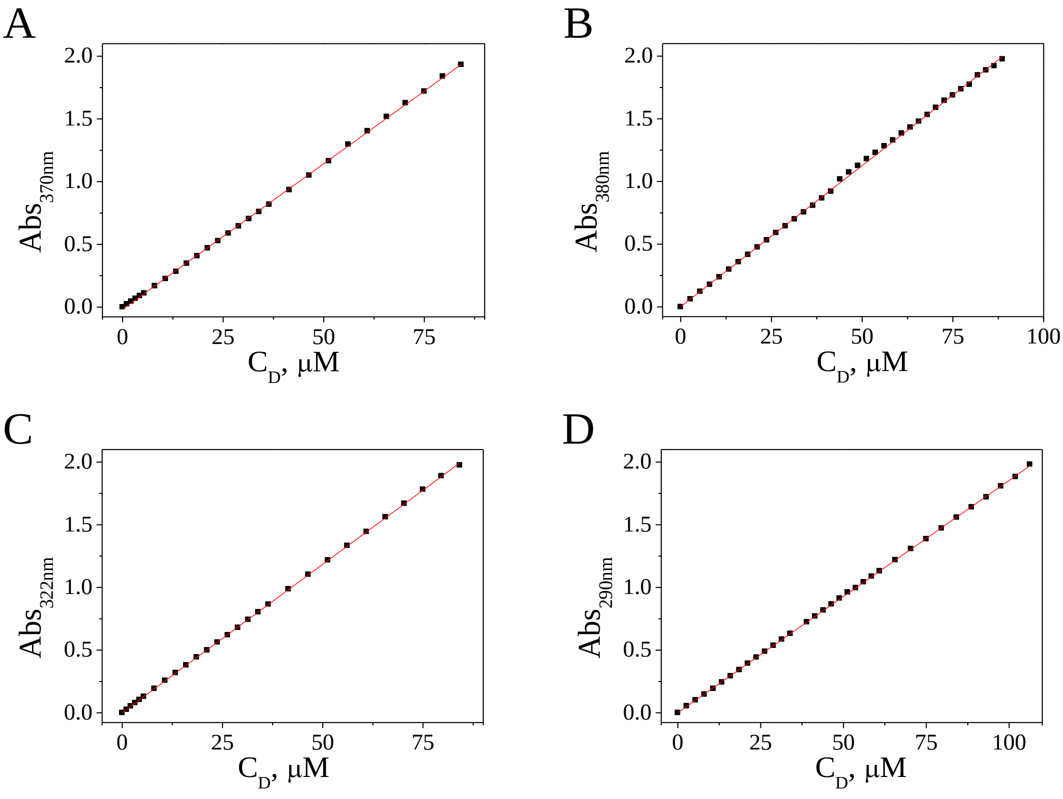

Figure 8. Fitting of the Lambert-Beer equation for complexes **1** (**A**), **2** (**B**), **3** (**C**) and **4** (**D**) complexes at λ = 370 nm (**A**), λ = 380 nm (**B**), λ = 322 nm (**C**) and λ = 290 nm (**D**). 50 mM Tris-HCl (pH = 7.0), 10 mM KCl, T = 25 ºC.

2.3. FRET melting assay.

The ability of complexes **1-4** to stabilize G-quadruplexes with antiparallel (22CTA), mixed parallel/antiparallel or hybrid (Tel22 and Bcl-2) and parallel (26CEB, c-kit2, c-Myc and TERRA) conformations was tested by FRET melting measurements [223]. A duplex DNA (ds26) was also included to investigate their selectivity for G-quadruplex over duplex DNA (see **section 1.1.4.2, Chapter II** for details of all sequences). As an example, the melting curves obtained for the antiparallel G-quadruplex 22CTA with varying concentrations of the two Ni(II) complexes (**1** and **4**) are shown in **Figure 9**.

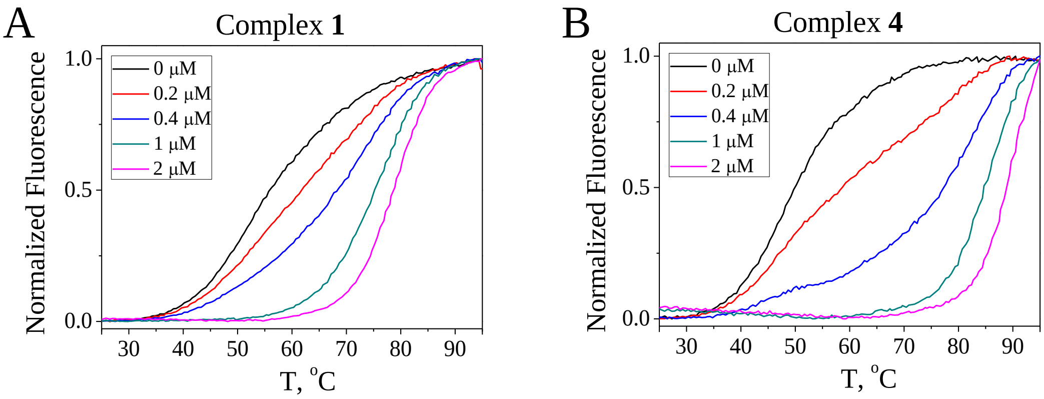

Figure 9. FRET melting curves obtained for the 22CTA G-quadruplex with increasing concentrations (C_D = 0 – 2 μM) of complex **1** (**A**) and **4** (**B**). C_P = 0.2 μM (expressed as a function of G-quadruplex molecules). 10 mM LiCaC (pH = 7.4), 90 mM LiCl, 10 mM KCl, scan rate = 1 °C/min.

Figure 10 summarizes the results of the ΔT_m (T_m in the presence of ligand - T_m in the absence of ligand) values obtained for the G-quadruplexes and the dsDNA (ds26) at a complex/polynucleotide molar ratio of C_D/C_P = 5. The new Ni(II)-bipyridine complex, **4**, exhibited the greatest thermal stabilization of all, which implies that the rational development of a larger aromatic surface compared to the salphen complexes results in a significant improvement in its G-quadruplex stabilization properties. However, it should also be noticed that this modification brings about an undesirable effect: the partial stabilization of the dsDNA (ds26). This could be related to a partial intercalation of complex **4** into the double stranded DNA. Another interesting point is that complexes **1**, **2** and **4** seem to exhibit a greater stabilization effect on antiparallel and hybrid conformations over parallel ones. Actually, no stabilization effect was observed for the parallel ARN G-quadruplex TERRA.

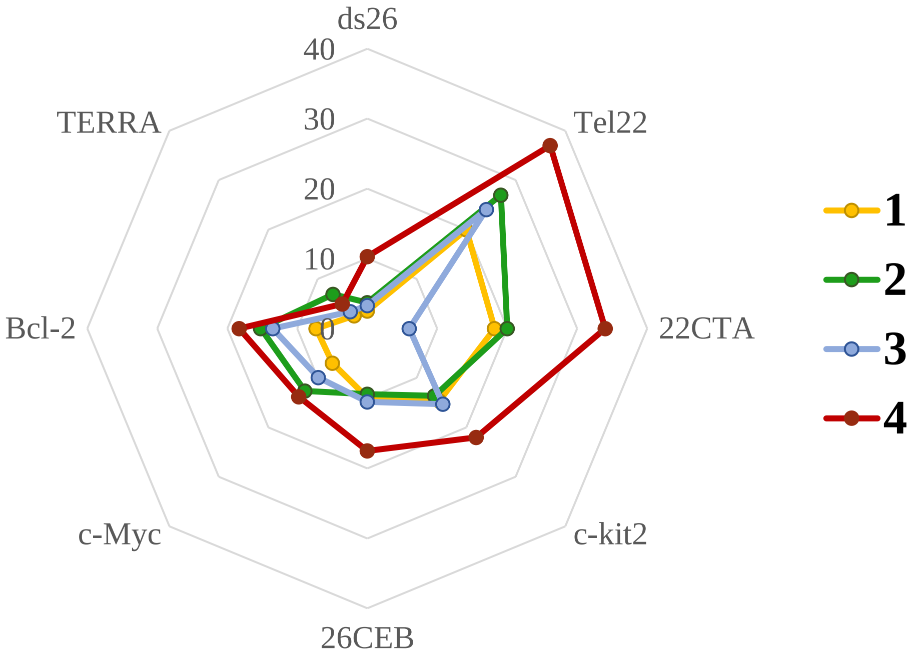

Figure 10. Spider plot of the ΔT_m (ºC) values ranging from 0 to 40 ºC obtained in the FRET melting assay at a molar ratio $C_D/C_P = 5$, $C_P = 0.2$ µM (expressed as a function of oligonucleotide molecules). Results were obtained from triplicates of three independent experiments.

2.4. Spectrophotometric titrations.

The most stabilized G-quadruplex by complexes **1-4** was Tel22, as shown before in **Figure 10**. It is worth noting that a high thermal stabilization does not necessarily imply a high thermodynamic constant for the ligand/G-quadruplex interaction, as the former strongly depends on the mode of binding [72,224]. Because of this, the binding of Tel22 to complexes **1-4** was first studied by spectrophotometric titrations.

Figure 11 shows the example of the titration of complex **4** with increasing amounts of Tel22 G-quadruplex. Three different trends can be clearly distinguished depending on the C_P/C_D molar ratio, which evinces the presence of three different modes of binding in the case of complex **4**. The isotherms obtained for the titrations of the four metal complexes can be seen in **Figure 12** in order to compare their binding characteristics. Interestingly, the isotherms of the titration of the salphen complexes **1** and **2** corresponds to the presence of two different modes of binding, whereas for the vanadyl-salphen complex **3** only one mode of binding is observed. The equations described in **section 1.2.2.3, Chapter II** cannot be used to obtain the thermodynamic constant of a process in which more than one polynucleotide/drug complex is formed, as there are more than two species that absorb at the studied wavelength. ITC titrations were carried out to overcome this problem and obtain the thermodynamic parameters of the bindings of the four metal complexes with Tel22.

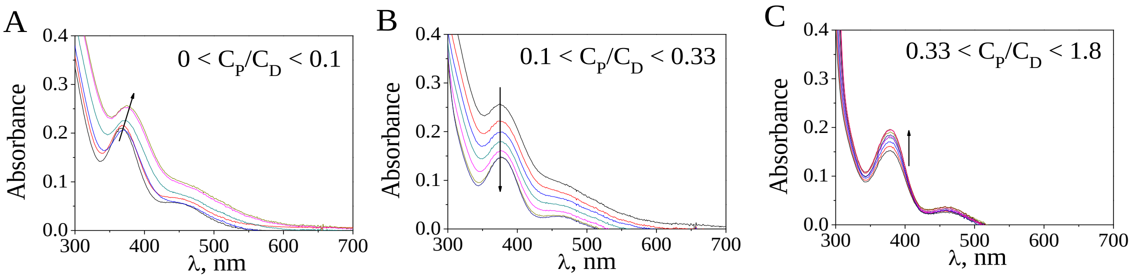

Figure 11. Absorbance spectra recorded during the titration of complex **4** with Tel22 at $0 \leq C_P/C_D \leq 0.1$ (**A**), $0.1 \leq C_P/C_D \leq 0.33$ (**B**) and $0.33 \leq C_P/C_D \leq 1.8$ (**C**). C^0_D = 20 µM, 50 mM Tris-HCl (pH = 7.0), 10 mM KCl, T = 25 ºC.

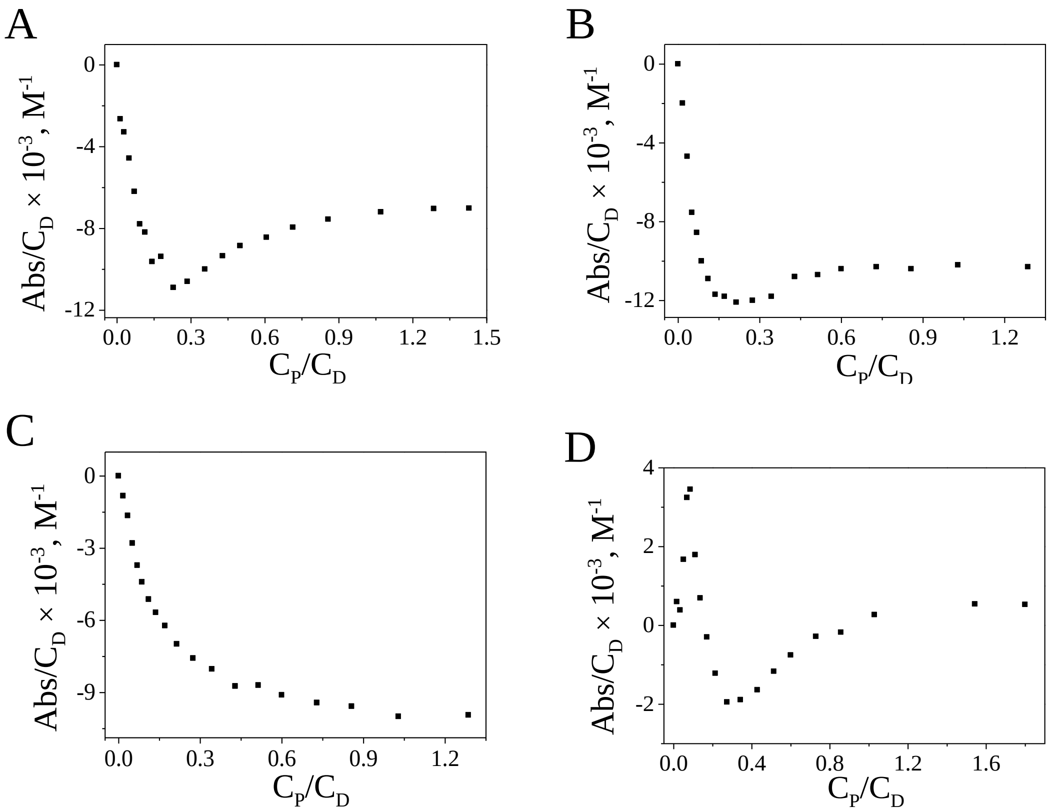

Figure 12. Absorbance binding isotherms of **1** (**A**), **2** (**B**), **3** (**C**) and **4** (**D**) with increasing concentrations of Tel22 at λ = 370 nm (**A**), λ = 380 nm (**B**), λ = 322 nm (**C**) and λ = 380 nm (**D**). C^0_D = 20 µM, 50 mM Tris-HCl (pH = 7.0), 10 mM KCl, T = 25 ºC.

2.5. ITC measurements.

ITC was performed to obtain the thermodynamic parameters of the binding of complexes **1-4** with Tel22. The ITC experiments and their binding isotherms are shown in **Figure 13** and, in highly good agreement with the spectrophotometric titrations, they correspond to one single binding process in the case of complex **3**, two binding processes for **1** and **2** and three distinct binding processes for complex **4**.

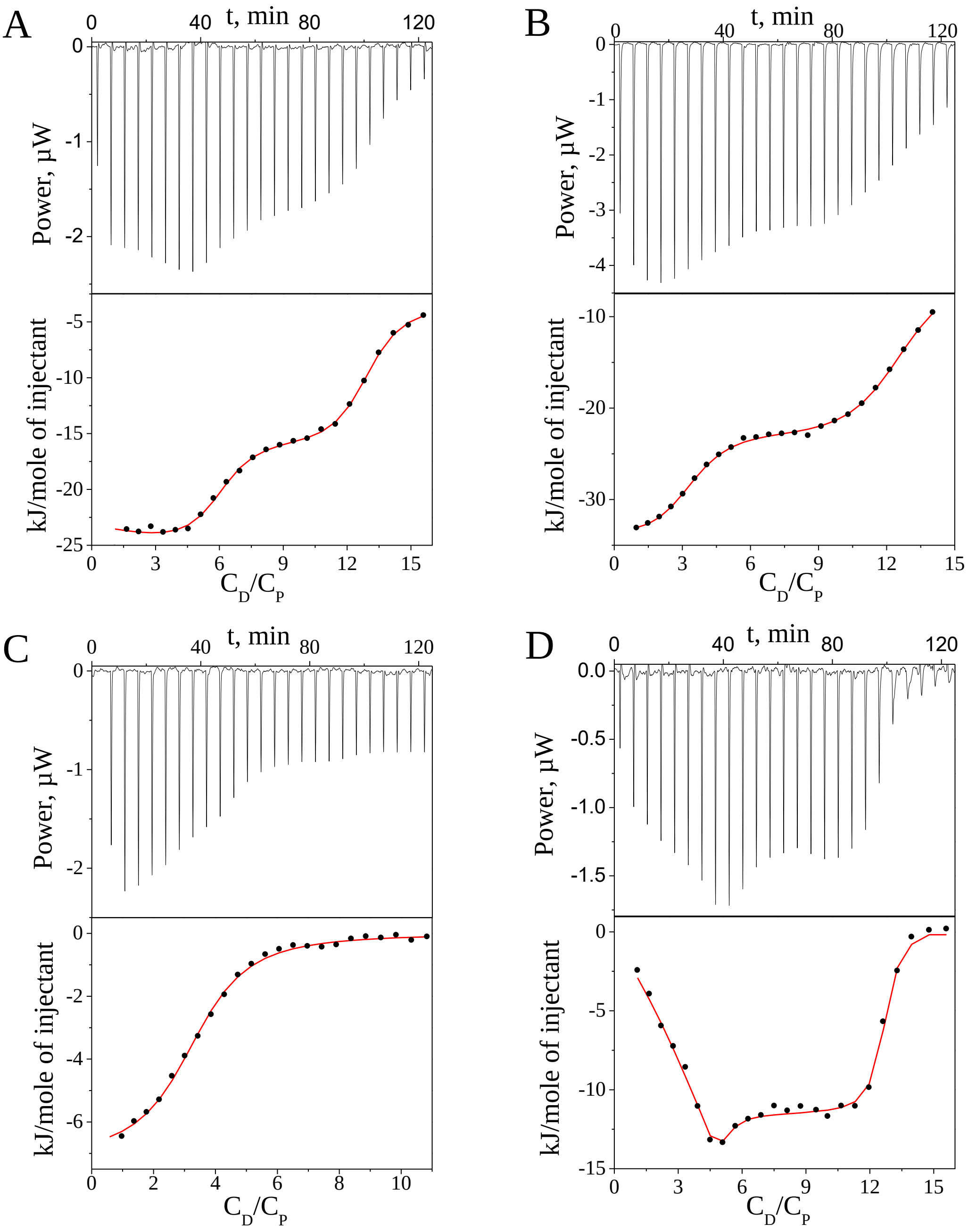

Figure 13. ITC titrations of Tel22 with complexes **1** (**A**), **2** (**B**), **3** (**C**) and **4** (**D**). Fittings corresponding to one, two or three binding modes are represented as a red line. C^0_P = 40 µM, 50 mM Tris-HCl (pH = 7.0), 10 mM KCl, T = 25 ºC.

The thermodynamic parameters obtained by fitting one-, two- or three-binding site models to the experimental data are gathered in **Table 2**. The thermodynamic constant for the first mode of binding, K_1, follows the trend **4** > **1** > **2** > **3**, which concurs well with the trend observed for the thermal stabilization of Tel22 in **Figure 10**. This trend suggests that the mode of binding of K_1 corresponds to the external stacking of the complexes with the G-quartet of the G-quadruplexes, as this binding mode is responsible for the thermal stabilization of the G-quadruplex structures. For complexes **1-3**, ΔH_1 corresponds to exothermic processes. In the case of complex **4**, two processes with high thermodynamic constants (K_1 and $K_2 > 1 \times 10^8$ M^{-1}) but with very different thermodynamic nature are observed; the first one is entropically driven, whereas the second one is enthalpically driven. Entropically favoured processes are often related to modes of binding that imply the displacement of water molecules from the binding site by the ligand [225,226]. This difference with complexes **1-3** could be one of the reasons for its much higher thermal stabilization.

Table 2. Thermodynamic parameters obtained for the interaction between complexes **1-4** and Tel22. K_i is the thermodynamic constant, and ΔH_i and ΔS_i the variation in the enthalpy and the entropy, respectively.

	1	**2**	**3**	**4**
$K_1 \times 10^{-5}$, M^{-1}	270 ± 60	49 ± 5	0.9 ± 0.1	3600 ± 900
ΔH_1, kJ mol^{-1}	-135 ± 3	-99 ± 1	-7.1 ± 0.2	1.2 ± 0.3
$T\Delta S_1$, kJ mol^{-1}	-93.8	-60.4	21.1	50
$K_2 \times 10^{-5}$, M^{-1}	5.7 ± 0.9	1.8 ± 0.9		1100 ± 700
ΔH_2, kJ mol^{-1}	-89 ± 3	-161 ± 2		-70 ± 10
$T\Delta S_2$, kJ mol^{-1}	-56.3	-131.2		-23.5
$K_3 \times 10^{-5}$, M^{-1}				50 ± 10
ΔH_3, kJ mol^{-1}				-11 ± 1
$T\Delta S_3$, kJ mol^{-1}				27

2.6. Polymerase Stop Assay.

The Polymerase Stop Asay was carried out to test the ability of the complexes to inhibit the activity of a DNA polymerase (*Taq* polymerase) through the stabilization of a G-quadruplex. The method used in this work is an adaptation from one described before in the literature[158]. As the human telomeric G-quadruplex DNA could not be used for this assay, the c-Myc sequence was chosen instead. This method has been described in detail in **section 2.2, Chapter II** and **Figure 14** summarizes the process. Briefly, a template oligonucleotide of 65 deoxinucleotides containing a G-quadruplex sequence derived from the c-Myc promoter region is mixed with a short labelled oligonucleotide that matches with the 3' overhang of the template. Different concentrations of the ligand and a positive control (10 mM KCl) are added to this mix, heated to 95 ^{o}C for 5 min and then allow to reach ambient temperature overnight. Then, the DNA polymerase is added and incubated for a short period of 30 min, after which the sample is denaturated and the products visualized in the FAM fluorescence channel after running polyacrylamide gel electrophoresis. In addition, the same procedure is performed using a template with a mutated c-Myc sequence, unable to form the G-quadruplex structure. **Table 3** summarizes all the oligonucleotide sequences used in this assay.

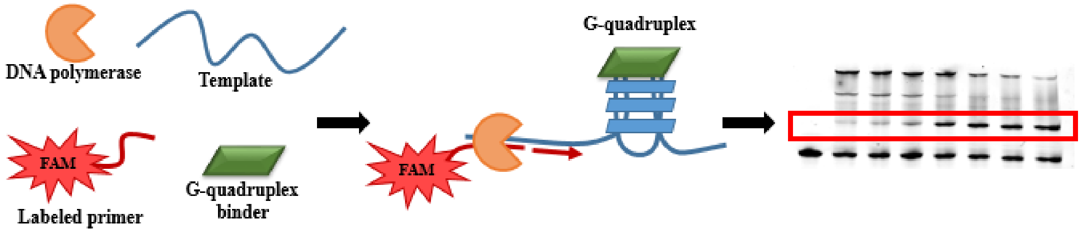

Figure 14. Schematic representation of the PSA.

Table 3. Sequences used for the Polymerase Stop Assay.

Template	Sequence (5' → 3')
Labeled primer	AGCATAATTCATGAGATCGGAA-FAM
c-Myc	GCGGC CCTGT G AGG GTG GGG AGG GTG GGG AAG ATTCCCGACT**TCGTATTAAGTACTCTAGCCTT**
Mutant c-Myc	GCGGCTCCTGT G AGG GTG **AA**G AGG GTG GGG AAG ATTCCCGACT**TCGTATTAAGTACTCTAGCCTT**

Figure 15 presents the example of the PSA carried out with complex **4**. The bands visualized in the gels correspond to the labeled primer that can present different lengths: the primer that has not been elongated by the *Taq* polymerase, the pausing product and the full-length product. The intensity of these bands is proportional to the oligonucleotide concentration and can be quantified using the GelAnalyzer software. The intensity of the positive control band (10 mM KCl) corresponds to a 100 % of G-quadruplex stabilization. The relative intensity of the pausing product band can be represented against the metal complex concentration as shown in **Figure 16**, and fitted to obtain the EC_{50} values (concentration of metal complex needed to reach a 50 % of relative intensity). These EC_{50} values are summarized in **Table 4** in order to compare the behaviour of the four metal complexes and they follow the trend **4** < **1** < **2** < **3**. These results demonstrate the correlation between the previous thermodynamic studies and this modificated polymerase stop assay, which has been described in this work for the first time.

Primer (1 µM)	+	+	+	+	+	+	+	+
Template c-MYC (1 µM)	-	+	+	+	+	+	+	+
Complex (µM)	-	-	0.3	1	5	10	20	-
KCl (10 mM)	-	-	-	-	-	-	-	+

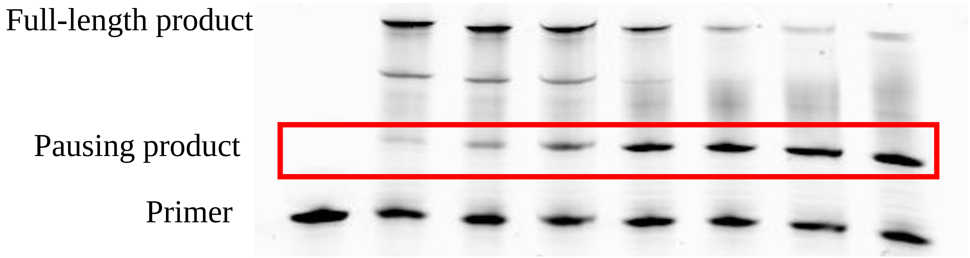

Figure 15. PSA of the c-Myc sequence with complex **4**. The band corresponding to the pausing product appears highlighted in red.

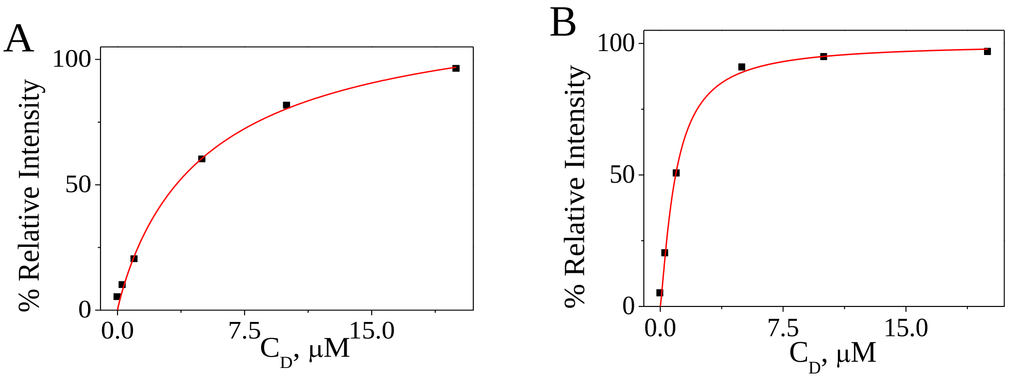

Figure 16. Examples of analysis of the PSA for complexes **3** (**A**) and **4** (**B**) and the non-linear curve fit (red).

Table 4. EC_{50} values obtained in the PSA for complexes **1-4** expressed as mean values ± standard deviation (SD). Data were obtained from two independent experiments.

Complex	**1**	**2**	**3**	**4**
EC_{50} (µM)	1.3 ± 0.1	1.5 ± 0.2	3.8 ± 0.4	0.92 ± 0.03

The same protocol was carried out using a template containing a mutant sequence of c-Myc (**Table 3**) in which two guanine residues were replaced by two adenine residues, which prevents the formation of the G-quadruplex. The most stabilizing complex, **4**, was used under the same experimental conditions than those described in **Figure 10**. In this case, the pausing product was not observed, so we can confirm that its presence is only due to the stabilization of a G-quadruplex structure in the c-Myc sequence by the metal complexes.

Primer (1 µM)	+	+	+	+	+	+	+	+
Mutant c-MYC (1 µM)	-	-	+	+	+	+	+	+
Template c-MYC (1 µM)	-	+	-	-	-	-	-	-
Complex (µM)	-	-	-	0.3	1	5	10	20
KCl (10 mM)	-	+	+	-	-	-	-	-

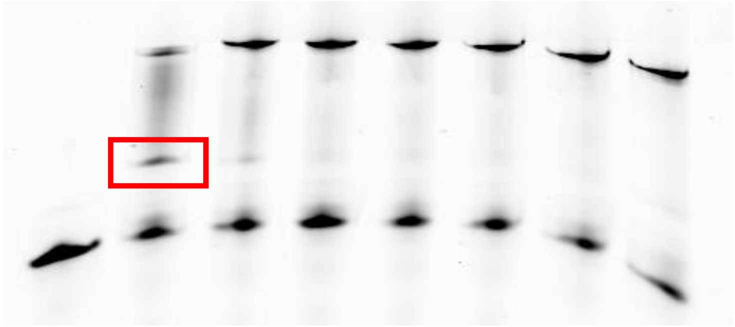

Figure 17. PSA of the mutant c-Myc sequence with complex **4**. The band corresponding to the pausing product in the normal c-Myc sequence appears highlighted in red.

3. Conclusions.

On one hand, the FRET melting measurements demonstrate that the new bipyridine-complex, **4**, presents a greater stabilizing effect compared to the salphen complexes. However, this modification also implies a slight stabilization of the duplex DNA, probably due to a partial intercalation of the extended aromatic core of the complex. ITC measurements demonstrates that **4** is also the complex that displays the highest thermodynamic constants for the binding to Tel22 G-quadruplex. In summary, we can conclude that the new bipyridine ligand represents a remarkable improvement over the previous salphen scaffold, thanks to the larger planar aromatic surface.

In addition, the PSA could not be performed with Tel22, so the sequence derived from the oncogene promoter c-Myc was chosen instead for this assay. In highly good agreement with the thermodynamic observations, the complexes were shown to inhibit the activity of the *Taq* DNA polymerase through the stabilization of a G-quadruplex in the c-Myc sequence following the same trend than that observed with the thermodynamic techniques: **4** > **1** > **2** > **3**. These results put forward that these G-quadruplex binders could interfere with important biological processes such as replication.

PARTE 3

Otras Dianas Terapéuticas: Actividad Biológica de Complejos de Ir(III) y Rh(III) Selectivos de Mitocondria.

CAPÍTULO IX

Aim of Part 3

As explained in **Chapter I**, traditional anticancer drugs targeting DNA make use of the fact that malignant cells divide rapidly. The evident drawback of this strategy is that dividing healthy cells are affected as well, causing severe toxic side-effects [227]. Because of this, there are several trends in chemotherapy research that deal with the development of new drugs with different mechanisms of action.

In this Part of the thesis, we aimed at exploring new species with alternative cellular targets. Mitochondria, besides being the centres of energy production in the cell, are key regulators of cell death, as they regulate the translocation of pro-apoptotic agents from the mitochondrial intermembrane space to the cytosol, which initiates the intrinsic pathway of apoptosis. Cancer cell mitochondria are structurally and functionally different from those in normal cells, and so targeting mitochondria has emerged as a promising alternative to be explored [96], as shown here in **Chapter IX**.

Capítulo IX

Actividad Anticancerígena de Complejos Ciclometalados de Ir(III) y Rh(III). ¿Qué Papel Juega el Centro Metálico?

Summary

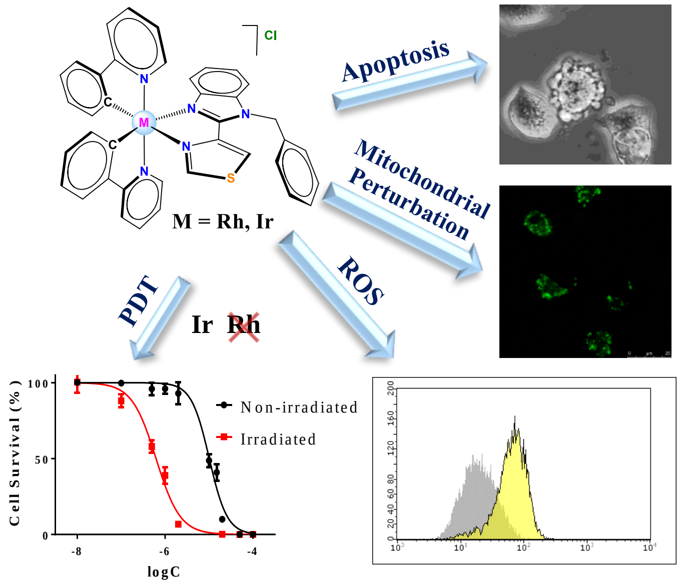

Figure 1. The biological activity of thiabendazole-based Ir and Rh complexes has been studied in the dark and upon visible irradiation.

In this work, the biological activity of two pairs of cyclometalated thiabendazole-based Ir(III) and Rh(III) complexes as well as their potential as photodynamic therapy agents were explored. The synthesis and characterization of these four metal complexes was carried out by the group of Prof. Gustavo Espino (Universidad de Burgos, Spain). Most of the biological results present in this work were obtained during the predoctoral stay at CiMUS (Center for Research in Molecular Medicine and Chronic Diseases, Santiago de Compostela, Spain) under the supervision of Prof. Fernando Domínguez.

Biscyclometalated Ir complexes with the general formula $[Ir(C^\wedge N)_2(N^\wedge N)]^+$ present a wide variety of cellular targets depending on the ancillary ligands, but the biological properties of Rh biscyclometallated complexes are much less studied. For this reason, the most cytotoxic pair of Rh and Ir complexes presented in this work were studied in detail to determine their biological mechanism of action (**Figure 1**). In spite of their different metal centre, they present a very similar biological behaviour, inducing the loss of mitochondrial functionality and the induction of apoptosis. On the other hand, the photodynamic activity of the four complexes was tested in tumour cells using visible blue light (460 nm). In this case, only the Ir complexes exhibit photodynamic therapy potential, which can be explained taking into account the very different photophysical properties or these Rh and Ir derivatives.

1. Introduction.

A great deal of effort has been invested over the past few decades to develop metal complexes with anticancer activity by mechanisms different from those of cisplatin to overcome the problems related to its severe side effects and cisplatin resistance. In line with this, cyclometalated complexes of various metal centres such as palladium(II), gold(III), ruthenium(II), platinum(II), rhodium(III) and iridium(III) constitute an interesting field of research due to their variety of cellular targets and mechanisms of action [228]. Among the former, mitochondria stands out, as it plays a key role in the cell metabolism and in the control of cell death. It is well-known that central metabolic pathways operating in malignant cells are different from those in normal cells [229,230]. Cancer cells exhibit various degrees of alterations in the mitochondria function, such as higher mitochondrial membrane potential (MMP) and increased oxidative stress [96]. Because of this, recent studies point to the potential benefits of targeting mitochondria metabolism for anticancer therapy [16] and several mitochondria-targeted drugs are currently in clinical trials. These drugs often act by directly disturbing mitochondrial function, which triggers the activation of mitochondrial cell death pathways.

Biscyclometalated complexes of the type $[Ir(C^\wedge N)_2(N^\wedge N)]^+$ present a wide variety of cellular targets depending on the ancillary ligands: mitochondria [231–236], lysosomes [237–239], endoplasmic reticulum [240,241], endosomes [242] or nucleus [243,244] have all been recognized as targeted organelles for different biscyclometalated Ir(III) derivatives. Nonetheless, cyclometalated Rh(III) complexes have not received as much attention so far, probably due to the lack of the exceptional photophysical properties typical of their analogous Ir(III) complexes. However, Rh complexes could also be a potential alternative to platinum metallodrugs [245], and their biological properties deserve further study.

In addition, Photodynamic Therapy (PDT) has also emerged as a prominent chemotherapeutic anticancer treatment, as it renders feasible local and transitory activation of drugs to achieve spatio-temporal control over its biological action and therapeutic effects [246]. The resulting selective activity over target (tumor) tissues eventually contributes to reducing systemic toxicity. PDT requires the combined action of three elements: light, oxygen and a photosensitizer (PS), in such a way that the excited PS agent (PS*) can generate singlet oxygen ($^1O_2$) from triplet oxygen ($^3O_2$) through energy transfer (ET) upon excitation with UV or visible light of specific wavelengths. $^1O_2$ is a very reactive species that can trigger cell death by different mechanims. Cyclometalated Ir(III) complexes are currently being studied as potential PDT agents due to their outstanding photophysical properties [247,248]. The crucial advantage of Ir complexes is the high spin-orbit coupling constant of the iridium metal core that favors the singlet-to-triplet intersystem crossing (see **section 1.4.2, Chapter I**) [249]. This peculiarity is responsible for features such as their long triplet excited state lifetimes and their appropriate energy gap that exceeds the excitation energy of $^3O_2$, which allow them to act as oxygen photosensitizers [250].

In this context, arylazoles are attractive ancillary N^N ligands, as they can be prepared and modified readily and can offer a remarkable structural and chemical diversity. Therefore, they can be used to tune the photophysical and chemical properties of organometallic compounds [251]. Specifically, the imidazole ring (**Figure 2**) can be functionalized through the reactive N−H bond [252]. In this work, the N-H function of thiabendazole (L^1) has been replaced with a benzyl group N-CH_2Ph (L^2) in an attempt to increase lipophilicity which, in turn, could improve their cytotoxic properties [253], and also their chemo-stability, since the N-H group can exhibit acid-base reactivity.

In summary, the potential use as anticancer and PDT agents of the two pairs of Rh(III) (**[Rh-a]Cl** and **[Rh-b]Cl**) and Ir(III) (**[Ir-a]Cl** and **[Ir-b]Cl**) complexes bearing N^N ligands based on the thiabendazole scaffold (L^1 and L^2) that are shown in **Figure 2** has beenexplored. First, we demonstrate that the benzyl modification in L^2 yields appreciable improvement of the cellular uptake and the cytotoxic activity in the dark. A deeper biological study demonstrates that both complexes bearing the L^2 ligand induce apoptosis via mitochondrial perturbation. Secondly, the PDT behavior of the four complexes was tested under soft irradiation conditions, using blue visible light with λ_{max} = 460 nm for short irradiation periods.

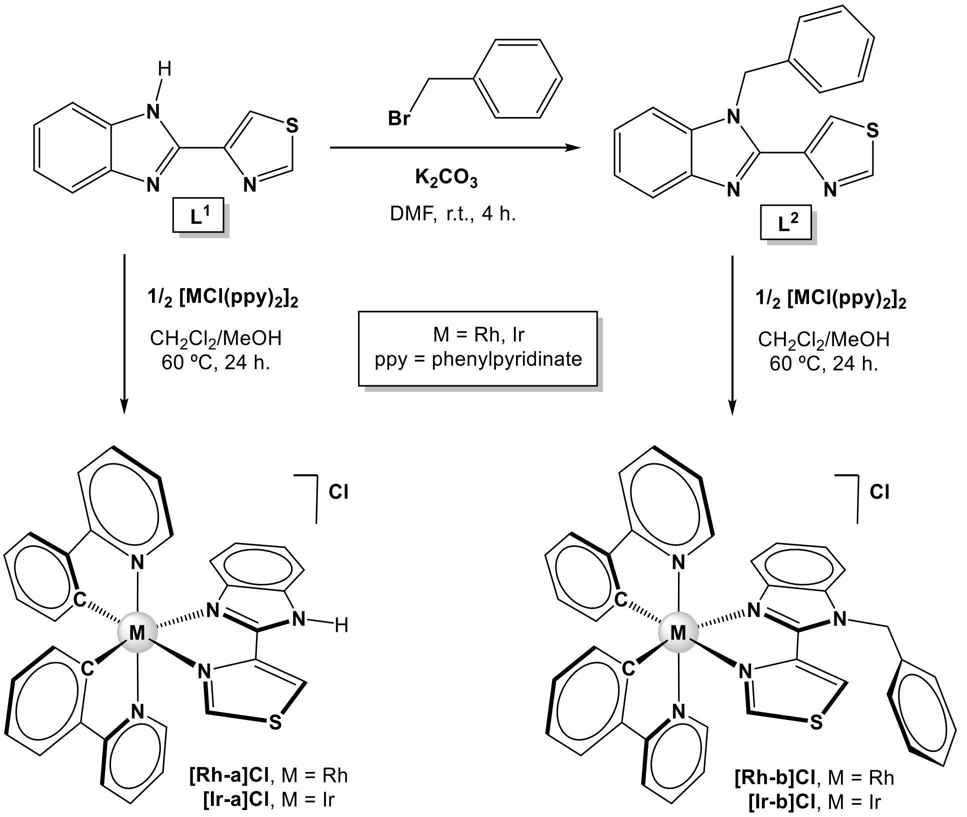

H
N
N
S
N
L1
Br
K2CO3
DMF, r.t., 4 h.
N
N
S
N
L2
1/2 [MCl(ppy)2]2
CH2Cl2/MeOH
60 ºC, 24 h.
M = Rh, Ir
ppy = phenylpyridinate
1/2 [MCl(ppy)2]2
CH2Cl2/MeOH
60 ºC, 24 h.
Cl
N
C
M
N
N—H
C
N
N
S
[Rh-a]Cl, M = Rh
[Ir-a]Cl, M = Ir
Cl
N
C
M
N
N
C
N
N
S
[Rh-b]Cl, M = Rh
[Ir-b]Cl, M = Ir

Figure 2. The synthesis and characterization of ligand L^2 as well as the Rh(III) and Ir(III) complexes studied in this work were carried out by the group of Prof. Gustavo Espino (Universidad de Burgos, Spain).

2. Results and discussion.

2.1. pK$_a$ study.

The pH effect on the four metal complexes was studied by means of UV-Vis spectroscopy. **[Rh-a]Cl** and **[Ir-a]Cl** undergo deprotonation of the N-H group when the pH is increased (**Figure 3**). **Eq. 1** [254] was fitted to the experimental data as shown in **Figure 3.B** and **3.D** and pK$_a$ values of 7.30 ± 0.01 for **[Rh-a]Cl** and 6.76 ± 0.03 for **[Ir-a]Cl** were obtained, which implies that at physiological pH these species will be partially deprotonated. On the other hand, **[Rh-b]Cl** and **[Ir-b]Cl** do not undergo acid-base processes over the whole pH range tested (pH = 3 - 12).

$$A = \frac{A_B - A_{HB^+}}{1 + 10^{(pK_a\ -\ pH)}} + A_{HB^+} \qquad (1)$$

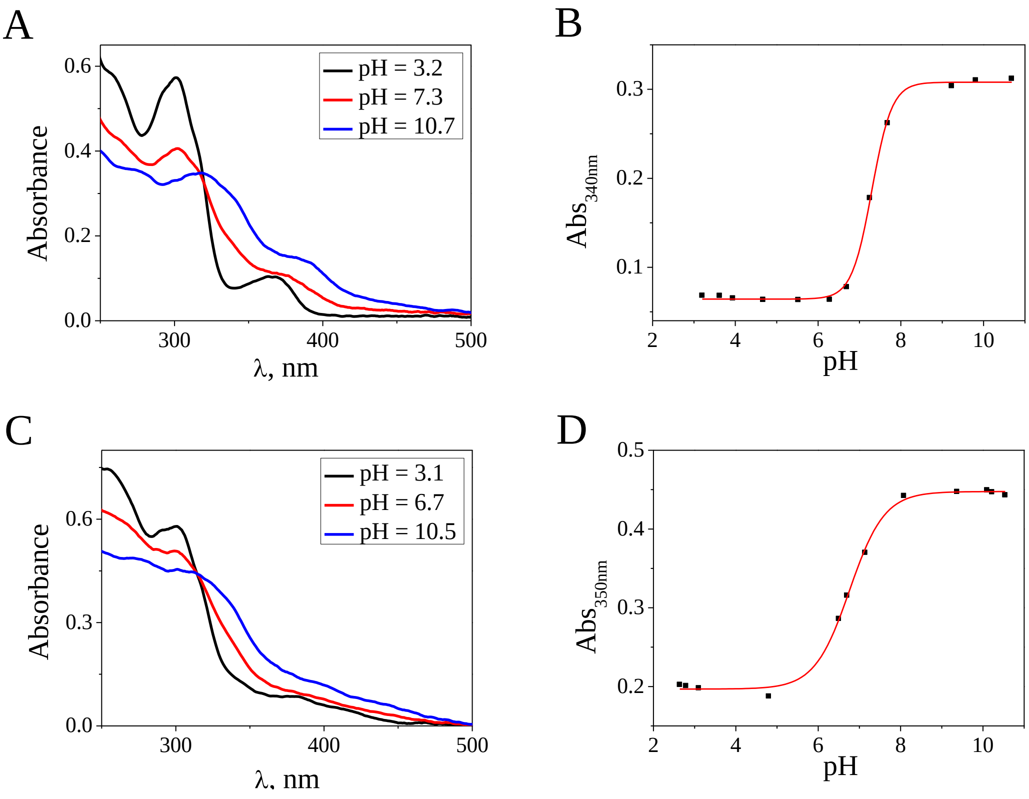

Figure 3. Representative absorbance spectra of **[Rh-a]Cl** (**A**) and **[Ir-a]Cl** (**C**) at different pH values in aqueous media and the corresponding fittings of **eq. 1** to the experimental data to obtain the pK$_a$ value for **[Rh-a]Cl** (**B**) and **[Ir-a]Cl** (**D**). C_D = 15 µM, H_2O, T = 25 ºC.

2.2. Photophysical properties.

The UV-Vis absorption spectra of the four metal complexes were recorded in air-saturated aqueous buffer solution (**Figure 4.A**). All the complexes exhibit intense ($\varepsilon > 30000\ M^{-1}\ cm^{-1}$), broad absorption bands in the UV region below 340 nm. The absorption of the Ir(III) complexes spreads into the visible region up to ~ 460 nm, where the Rh(III) derivatives barely absorb.

The emission spectra of the four complexes were also recorded in air-saturated aqueous solution (**Figure 4.B**). The Ir complexes present excitation bands at λ_{exc} = 305 nm and λ_{exc} = 385 nm and exhibit broad emission bands with one maximum for **[Ir-a]Cl** at 500 nm and two maxima for **[Ir-b]Cl** at 480 nm and 506 nm. On the contrary, the Rh complexes displayed no emission bands at any of the tested excitation wavelengths (λ_{exc} = 290 - 500 nm). This set of emission spectra in **Figure 4.B** evinces the noticeable dependence of the photophysical properties on the nature of the metal center.

The emission lifetimes ($\tau_{1/2}$), measured using a pulsed diode laser of λ_{exc} = 375 nm (**Figure 4.C**), and the quantum yields (ϕ) of the Ir(III) derivatives, were tested in air-saturated aqueous solution and the results are gathered in **Table 1**. Both Ir complexes display large Stokes shifts, moderate quantum yields (ϕ) and rather long emission lifetimes.

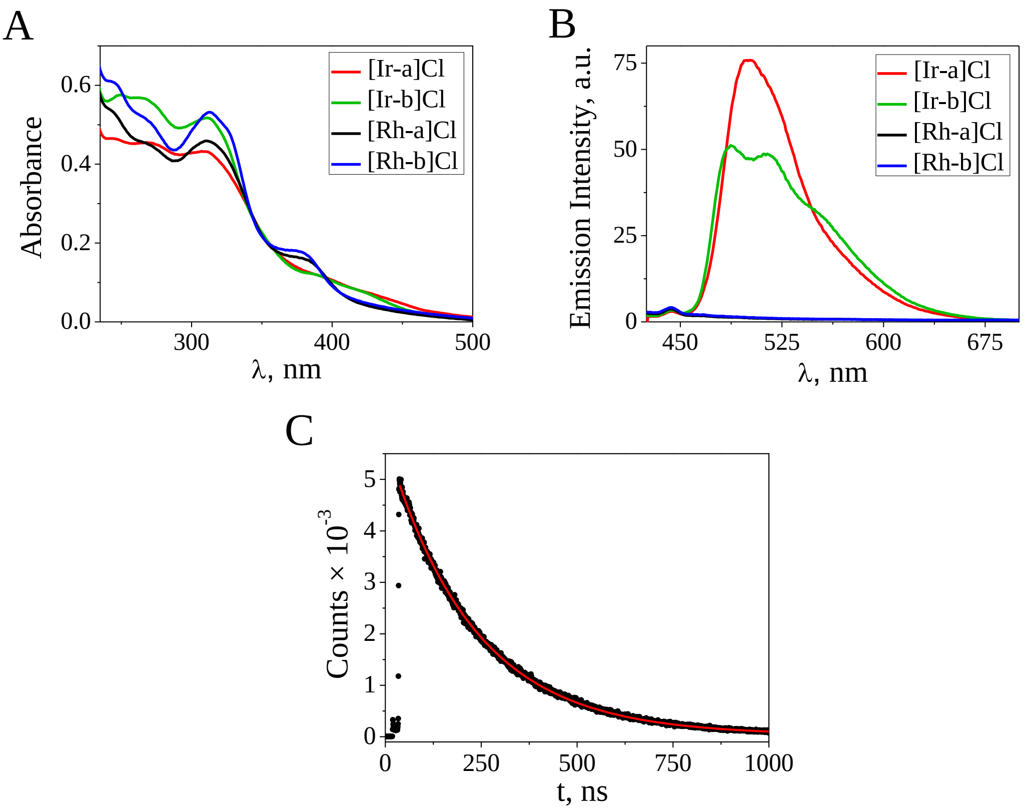

Figure 4. Absorption (**A**) and emission (**B**) spectra of the four metal complexes at a concentration $C_{complex}$ = 15 µM in aqueous buffered solution (2.5 mM NaCaC, pH = 7.0). **C)** Example of emission decay curve for **[Ir-b]Cl** at λ_{exc} = 375 nm and λ_{em} = 506 nm and fitting to a monoexponential decayment (red line) in aqueous buffer solution (2.5 mM NaCaC, pH = 7.0), T = 25 ºC.

Table 1. Photophysical parameters for complexes **[Ir-a,b]Cl** in aqueous buffer solution (2.5 mM NaCaC, pH = 7.0), T = 25 °C. [a)] In DMSO 100 %.

Compound	λ_{exc} (nm)	λ_{em} (nm)	ϕ^a (%)	$\tau_{1/2}$ (ns)
[Ir-a]Cl	375	500	2.3	187
[Ir-b]Cl	375	480, 506	6.1	228

2.3. *In vitro* cytotoxicity.

The antiproliferative activity of **[Ir-a,b]Cl** and **[Rh-a,b]Cl** was evaluated against human lung carcinoma (A549) and human colon adenocarcinoma (SW480) cell lines to compare the cytotoxic activity of the four metal complexes. The IC_{50} (half maximal inhibitory concentration) values are summarized in **Table 2**. The four metal complexes exhibit lower IC_{50} values than cisplatin against both cell lines. Moreover, the Ir and Rh complexes bearing the ligand L^2, **[Ir-b]Cl** and **[Rh-b]Cl**, exhibit greater cytotoxic activity than their analogous bearing the ligand L^1.

Table 2. IC_{50} (µM) of **[Ir-a,b]Cl**, **[Rh-a,b]Cl** and cisplatin against A549 and SW480 cancer cell lines after 24 h of treatment. Data were obtained from quadruplicates of three independent experiments and expressed as mean values ± standard deviation (SD).

	IC_{50} (µM)	
Compound	**A549**	**SW480**
[Ir-a]Cl	18.9 ± 0.2	10.0 ± 0.1
[Rh-a]Cl	10.3 ± 0.1	7.7 ± 0.4
[Ir-b]Cl	4.0 ± 0.4	2.9 ± 0.1
[Rh-b]Cl	4.1 ± 0.2	3.3 ± 0.1
Cisplatin	50 ± 3	37 ± 6

2.4. Cellular uptake.

The cellular uptake of the two pairs of complexes was evaluated to assess if the benzyl modification in L^2, which provides the complexes with stability against the deprotonation of the N-H group in L^1 at physiological pH, increased the cellular internalization of the complexes, which could explain their different cytotoxicity. A549 cells were treated with each complex at a concentration of 5 µM for 4 h and then harvested and analyzed by ICP-MS. **Figure 5** shows the relative uptake of the Ir and the Rh complexes bearing the ligand L^1 compared to those bearing L^2. Indeed, the uptake of **[Ir-b]Cl** and **[Rh-b]Cl** was greater than that of **[Ir-a]Cl** and **[Rh-a]Cl**, respectively, which is in good agreement with the cytotoxicity results and indicates that the benzyl modification improves the internalization of the complexes. The most cytotoxic pair, **[Ir-b]Cl** and **[Rh-b]Cl,** was selected to carry out a deeper biological study and determine the mechanism of action.

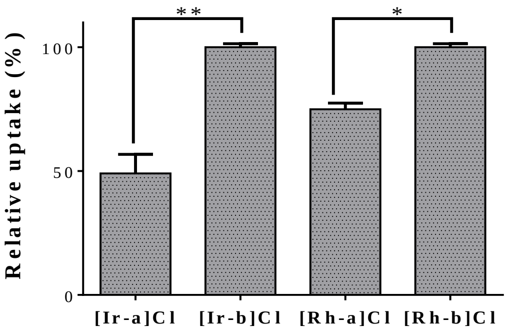

Figure 5. Relative metal accumulation in A549 cells exposed to 5 µM of complexes **[Ir-a,b]Cl** and **[Rh-a,b]Cl** for 4 h. Data were obtained from duplicates of two independent experiments. Difference between the relative uptake (%) of **[Ir-a]Cl** and **[Ir-b]Cl** is significant at **p = 0.02 and between **[Rh-a]Cl** and **[Rh-b]Cl** at *p = 0.05.

2.5. Cell cycle arrest.

The cytotoxicity of many anticancer drugs is often associated with DNA damage and cell cycle perturbation [87]. For instance, although cisplatin interacts with several cell components, its primary biological target is DNA [255]. As a result, this antitumor agent causes arrest at the G2-phase [58]. The effect of **[Ir-b]Cl** and **[Rh-b]Cl** on cell cycle distribution was investigated by flow cytometry and propidium iodide (PI) staining (**Figure 6**). Treatment of A549 cells with the complexes at a concentration close to their IC_{50} values (5 µM) caused a marked accumulation of cells in the G0/G1 phase. Compared with the vehicle-treated control, the percentage of cells in the G0/G1 phase increased by 32.8% and 33.3% at 24 h and 35.9% and 36.9% at 48 h for **[Ir-b]Cl** and **[Rh-b]Cl**, respectively (**Table 3**). Accordingly, the number of cells in the S-phase strongly decreased. These results point out that both complexes can act through mechanisms of action different from those of cisplatin [58]. Although some previously reported mitochondria-targeted compounds display no effects on the cell cycle distribution [103,256], our results concur well with recent studies on other Ir(III) complexes that also induce dose-dependent G0/G1 cell cycle arrest [231].

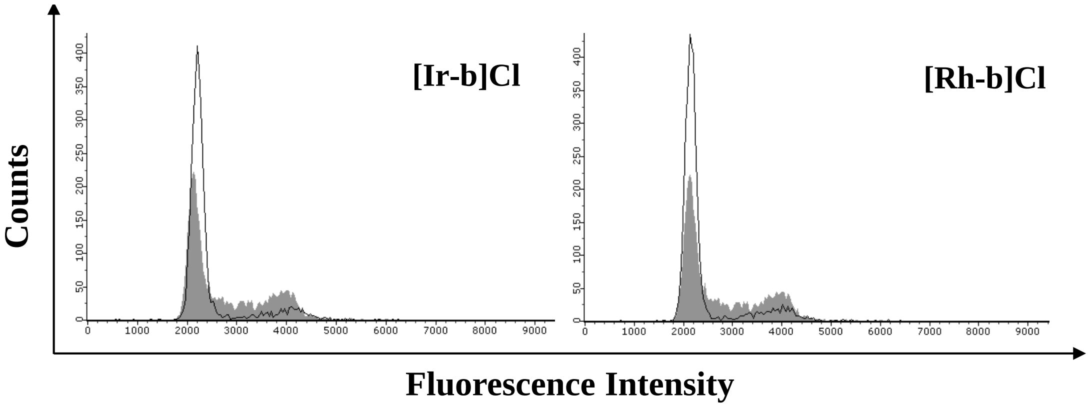

Figure 6. Effect of **[Ir-b]Cl** and **[Rh-b]Cl** on A549 cell cycle distribution analysed by PI staining with flow cytometry after treatment at $C_{complex} = 5$ µM for 24 h. Vehicle-treated cells are represented by the grey area and **[Ir-b]Cl** and **[Rh-b]Cl**-treated cells by the black line.

Table 3. Percentage (%) of cells in the G0/G1, S and G2-M phases of the cell cycle upon treatment with **[Ir-b]Cl** and **[Rh-b]Cl** at 5 µM for 24 h and 48 h. Differences between % of cells in G0/G1 phase for vehicle-treated cells and cells treated with **[Ir-b]Cl** or **[Rh-b]Cl** are significant at p = 0.0009 after 24 h and at p = 0.002 at 48 h. Data were obtained from duplicates of two independent experiments and expressed as mean values ± standard deviation (SD).

	24 h			**48 h**		
	G0/G1	**S**	**G2/M**	**G0/G1**	**S**	**G2/M**
Vehicle	49.7 ± 0.9	27.6 ± 0.1	22.7 ± 0.1	52.8 ± 0.8	25.5 ± 0.7	21.7 ± 0.5
[Ir-b]Cl	82 ± 1	7.4 ± 0.6	10.6 ± 0.5	89 ± 1	4.7 ± 0.3	6.3 ± 0.1
[Rh-b]Cl	83.0 ± 0.3	7.9 ± 0.6	9.1 ± 0.9	89.7 ± 0.7	1.8 ± 0.2	8.5 ± 0.5

2.6. Induction of apoptosis.

To determine if the cell death occurred via apoptosis, time-lapse fluorescence microscopy was used to detect activation of caspase-3/7. A549 cells were treated with **[Ir-b]Cl** or **[Rh-b]Cl** (5 µM) and co-treated with the CellEvent Caspase-3/7 Green Detection Reagent and images were recorded every 45 min for 24 h to monitor the process. During this procedure, the cells remained continuously under culture conditions at 37 °C and 5% CO_2. In the case of **[Ir-b]Cl**, its intrinsic green emission interfered with the fluorogenic probe used to detect the activation of caspase-3/7. However, this activation was clearly observed for **[Rh-b]Cl**, with the bulk amount of activation events starting 12 h after the treatment (videos in **Figure 7**).

A)

B)

Figure 7. QR codes that give access to the time-lapse videos of vehicle-treated A549 cells (**A**) and cells incubated with 5 µM of **[Rh-b]Cl** (**B**) for 24 h. Cells were co-treated with the CellEvent Caspase-3/7 Green Detection Reagent.

Additionally, A549 cells were treated with **[Ir-b]Cl** or **[Rh-b]Cl** for 24 h in the presence or absence of 20 µM of the Z-VAD-FMK caspase inhibitor. Indeed, **Figure 8** shows that caspase inhibition increases the survival rate after treatment with both **[Ir-b]Cl** and **[Rh-b]Cl** in a significant manner (p < 0.03) by 17.4 % and 18.1 %, respectively. These results confirm the role of apoptosis in the cell death induced by these complexes [257].

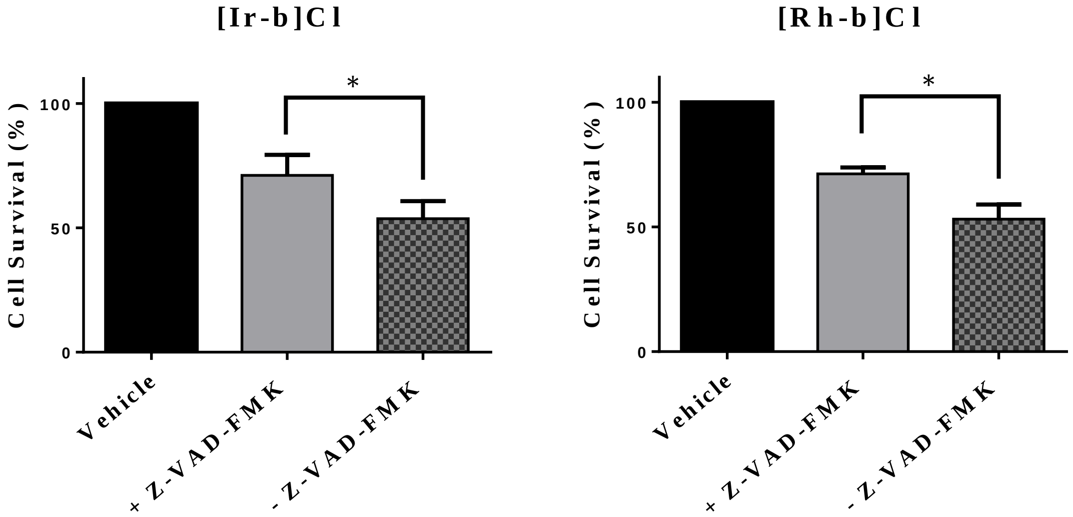

Figure 8. A549 cells were treated with 5 µM of **[Ir-b]Cl** or **[Rh-b]Cl** and co-treated (+ Z-VAD-FMK) or not (- Z-VAD-FMK) with caspase inhibitor Z-VAD-FMK for 24 h. Cell survival was assessed by flow cytometry through the Guava ViaCount Assay (Millipore). Difference significant at $^{*}p < 0.03$ compared to cells not treated with the caspase inhibitor.

2.7. Cellular localization.

The cellular localization of **[Ir-b]Cl** could be determined by confocal microscopy thanks to its intrinsic green emission properties. The colocalization experiments were performed after treatment with a low dose of **[Ir-b]Cl** (1.5 µM for 1 h), for which cell survival was nearly 100 %. Then, cells were stained with the commercial probe LysoTracker™ Red, a deep red-fluorescent dye for labeling and tracking lysosomes, which are acidic organelles, in live cells. After the staining, cells were washed twice with PBS and visualized by confocal microscopy. The same field of view was imaged sequentially with bright field, fluorescence emission at $\lambda_{em} = 460 - 515$ nm (green) for localization of **[Ir-b]Cl** and at $\lambda_{em} = 600 - 700$ nm (red) for localization of lysosomes. Representative images of these colocalization experiments are shown in **Figure 9.A**, in which we can clearly observe that the punctuate green emission pattern of **[Ir-b]Cl** is not correlated with the red emission pattern from the lysosomes.

On the other hand, the same procedure was carried out using the commercial probe tetramethylrhodamine methyl ester (**TMRM**), which is a cationic, red fluorescent dye that is readily sequestered by active mitochondria. **Figure 9.B** shows representative images of these mitochondrial colocalization experiments. The same experimental conditions as those described above were used to obtain the images in **Figure 9.B**, which demonstrate that **[Ir-b]Cl** selectively accumulates in mitochondria. In fact, Pearson's colocalization coefficient (PCC) with TMRM is 0.80, whereas with LysoTracker the PCC value is 0.09 (see **section 2.6.1, Chapter II**).

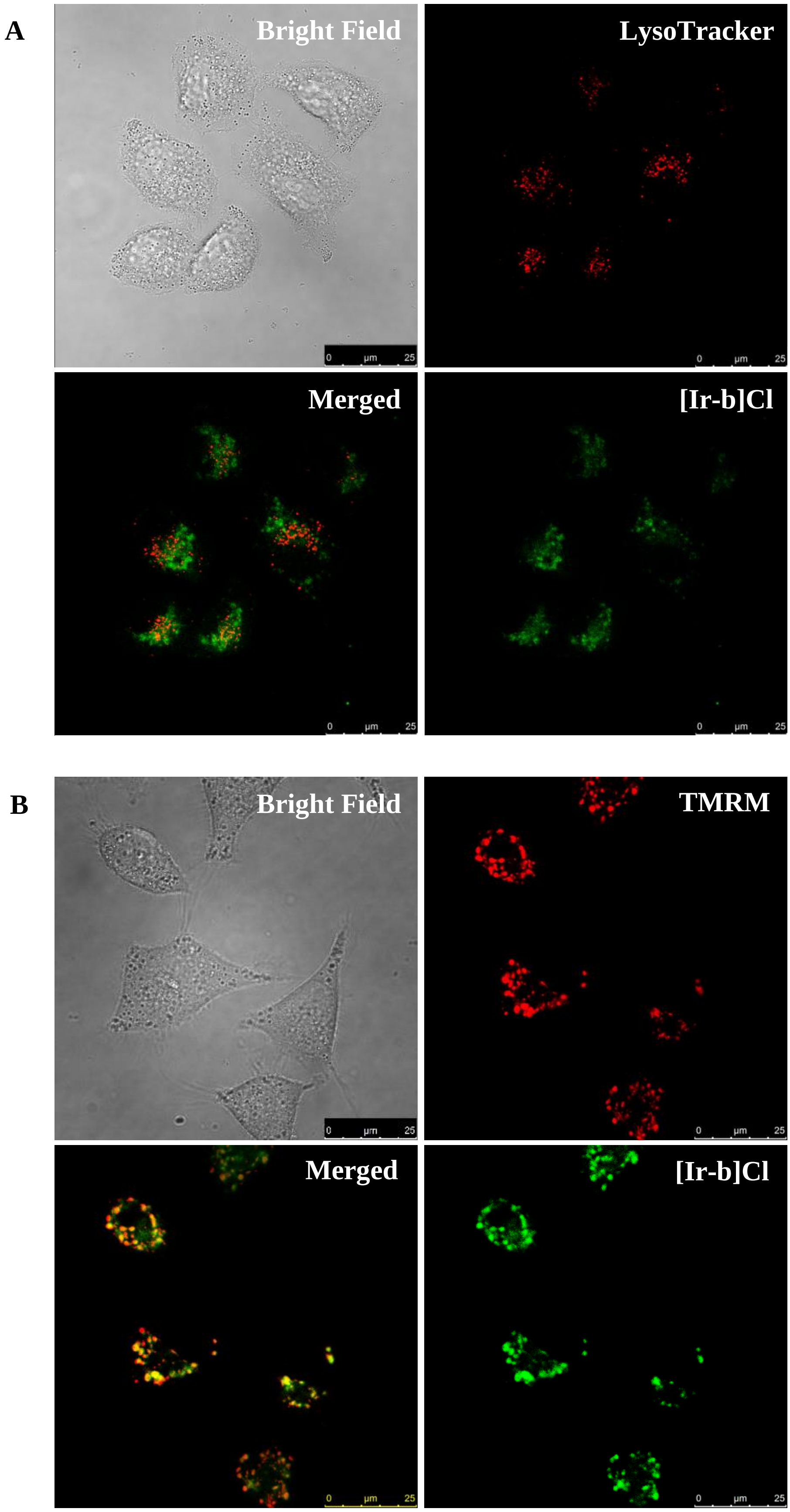
A
Bright Field
LysoTracker
Merged
[Ir-b]Cl
B
Bright Field
TMRM
Merged
[Ir-b]Cl
0 µm 25

Figure 9. A) Representative confocal images of A549 cells exposed to **[Ir-b]Cl** (1.5 µM, 1h) and to LysoTracker (75 nM, 30 min). **B)** Representative confocal images of A549 cells exposed to **[Ir-b]Cl** (1.5 µM, 1h) and to TMRM (100 nM, 30 min).

2.8. Effect on the mitochondrial membrane potential.

To assess if the accumulation of complex **[Ir-b]Cl** in mitochondria leads to an actual mitochondrial disfunction, mitochondrial membrane potential (MMP, $\Delta\Psi_m$) was analysed after staining living cells with the fluorescent cationic red dye TMRM, which accumulates only in active, polarized mitochondria due to their relatively negative charge. Depolarized or inactive mitochondria displays decreased membrane potential and fail to sequester TMRM. Treatment with 5 µM of **[Rh-b]Cl** or **[Rh-b]Cl** led to a quick loss of TMRM fluorescence in less than 2 h (**Figure 10**). These results indicate that both **[Ir-b]Cl** and **[Rh-b]Cl** cause mitochondrial depolarization.

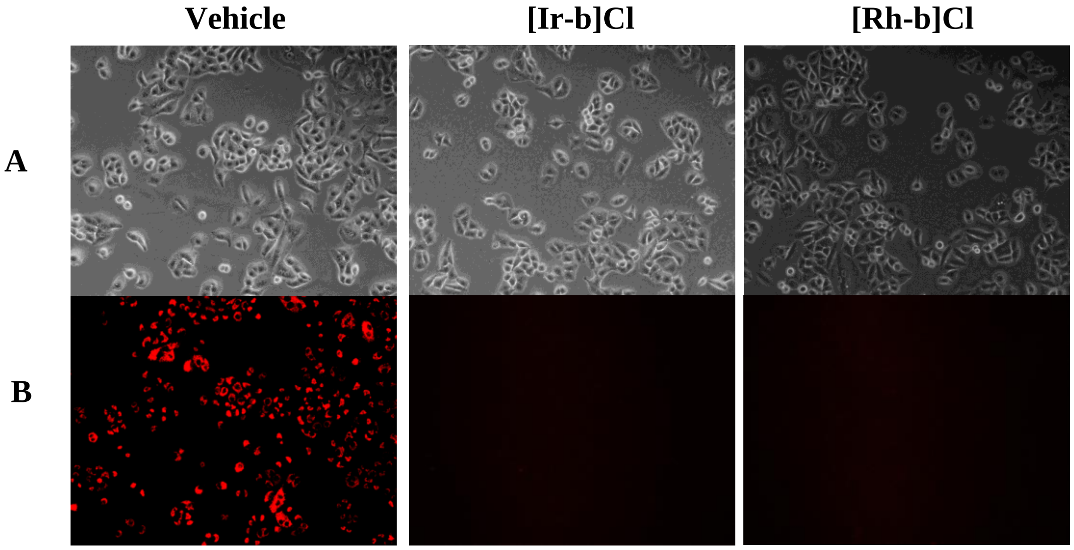

Figure 10. Effect of **[Ir-b]Cl** and **[Rh-b]Cl** treatment on the mitochondrial membrane potential observed by TMRM fluorescence (red). Representative images of A549 cells treated with DMSO (vehicle), **[Ir-b]Cl** (5 µM) and **[Rh-b]Cl** (5 µM) for 2 h under the same experimental conditions. **A)** Phase contrast image. **B)** Red fluorescence emission.

2.9. Intracellular ROS detection.

It is well known that mitochondrial depolarization is followed by other mitochondrial and non-mitochondrial perturbations. Mitochondria are the major source of intracellular reactive oxygen species (ROS), and mitochondrial dysfunction is closely related to ROS accumulation in the process of apoptosis [258]. To elucidate whether the depolarization of mitochondria observed in **Figure 10** led to ROS accumulation in the cell, the intracellular ROS levels were examined by using DHE (dihydroethidium) and H2DCFDA (2',7'-dichlorodihydrofluorescein diacetate). DHE allows one to measure cytosolic superoxide ($O_2^{\bullet-}$) and H2DCFDA other radical species including hydrogen peroxide (H_2O_2), in intact adherent cells [259]. These probes are oxidized by the reactive oxygen species to generate the corresponding fluorescent products in the cells, which can be measured by flow cytometry. **[Ir-b]Cl** could not be included in this assay due to its green emission that partially overlapped with the fluorescent probes. A549 cells were treated with **[Rh-b]Cl** (5 µM) for 2 or 4 h. Treatment with H_2O_2 (0.25 mM) was used as a positive control, as it causes oxidative stress that generates ROS overproduction in the cell. **Figure 11.A** shows that the population of cells with enhanced levels of superoxide after treatment with **[Rh-b]Cl** is even higher than after treatment with H_2O_2. The generation of other radical species was also detected (**Figure 11.B**), but this time the treatment with H_2O_2 induced a greater effect than the **[Rh-b]Cl** treatment. These results entail that superoxide is the main radical species generated in the cell by treatment with **[Rh-b]Cl**.

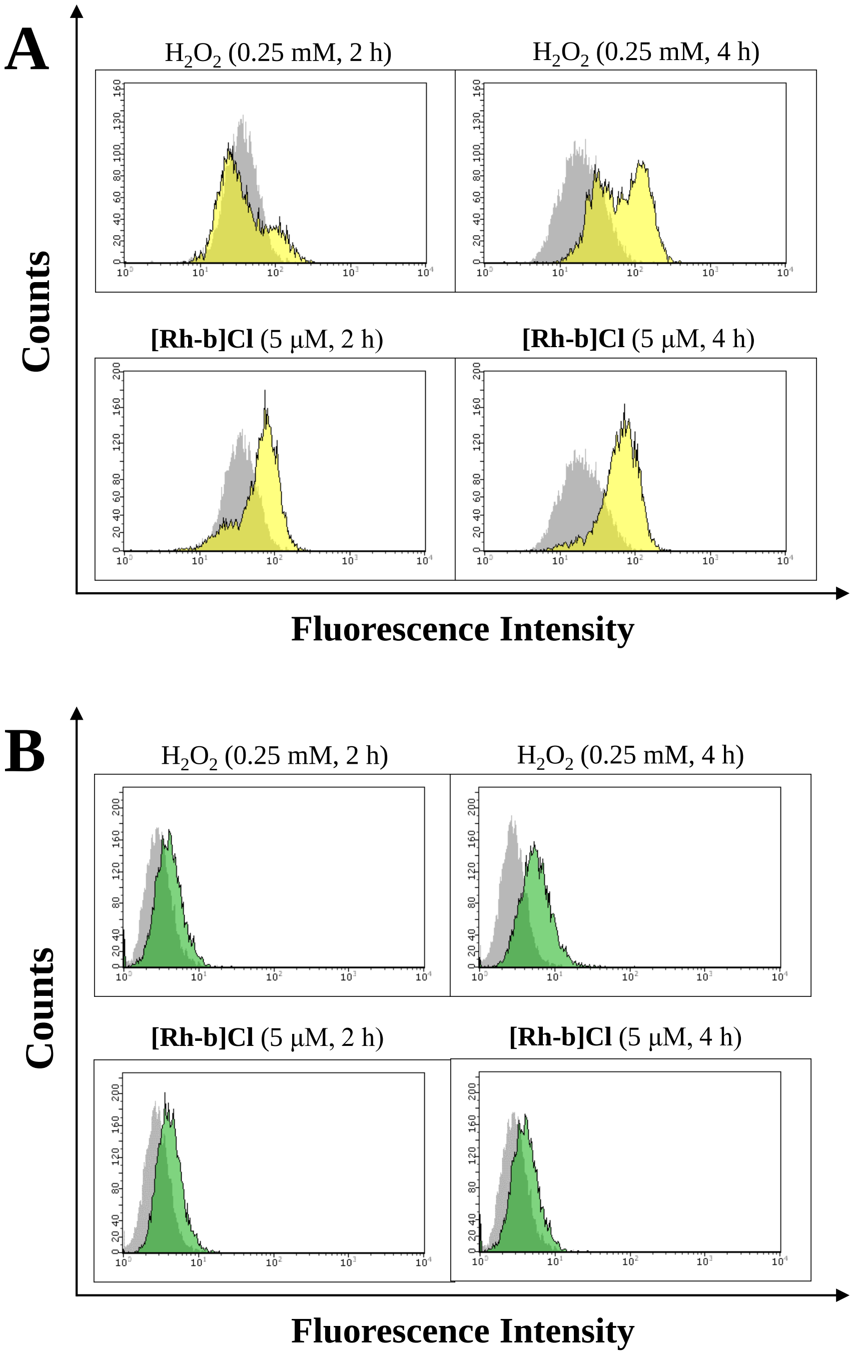

Figure 11. The level of intracellular ROS was detected by DHE (**A**, yellow) and H2DCFDA (**B**, green) assays using flow cytometric analysis in A549 cells treated with **[Rh-b]Cl** (5 µM) or H_2O_2 (0.25 mM) for 2 or 4 h. Grey: control cells; coloured: treated cells.

2.10. Oxidized cardiolipin study.

Because of depolarization, mitochondria overproduce ROS which, in turn, oxidize mitochondrial cardiolipins. The damage in mitochondria produced by ROS can be determined indirectly by assessing the oxidation state of cardiolipin, a molecule restricted to the inner mitochondrial membrane that plays a key role in the apoptotic cell death pathway [173]. The fluorescent dye 10-N-nonyl acridine orange (NAO) is extensively used for location and quantitative determination of cardiolipin in living cells. NAO interacts with intact, nonoxidized cardiolipin forming NAO dimers, which can be detected based on their red emission [175]. Therefore, a reduction in NAO fluorescence indicates a decrease in cardiolipin content [260]. A549 cells were preincubated with NAO and then treated for 4 h in the presence of different concentrations of **[Rh-b]Cl**. The fluorescence of NAO in the cells was then measured by flow cytometry (**Figure 12**). **[Rh-b]Cl** featured a great dose-dependent impact on NAO fluorescence intensity in agreement with cardiolipin oxidation. Again, **[Ir-b]Cl** could not be included in this study due to its emission features.

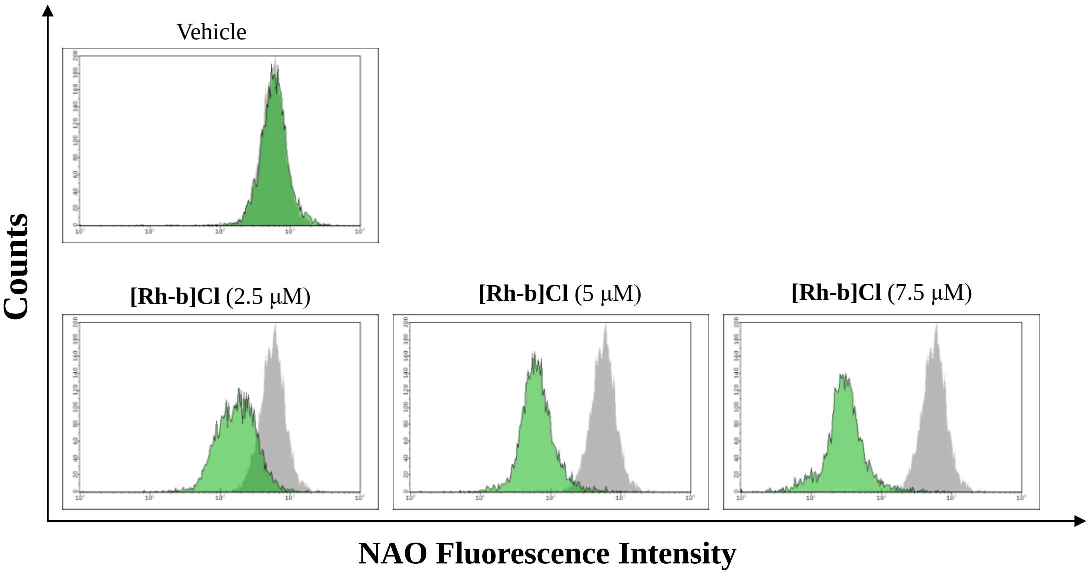

Figure 12. The decrease of NAO fluorescence upon treatment for 4 h with **[Rh-b]Cl** at different concentrations (2.5, 5 and 7.5 μM) was analysed by flow cytometry. Grey: control cells; coloured: treated cells.

2.11. Photodynamic activity.

The PDT effect of the **[Ir-b]Cl** and **[Rh-b]Cl** was first examined on A549 cells irradiated in the UV region at 365 nm (where the complexes present strong absorption) for a short period of 5 min at 20 mW cm^{-2}. Interestingly, the cytotoxicity of **[Ir-b]Cl** increased significantly, displaying a phototoxicity index (IC$_{50}$ non-irradiated/ IC$_{50}$ irradiated) of 18 ± 2, whereas no significant changes were observed for the **[Rh-b]Cl** complex that displayed a photoindex of 1.1 ± 0.1. Although the phototoxicity index quoted for **[Ir-b]Cl** is a promising result, the use of visible light and nontoxic compounds is preferable in photodynamic therapy. Hence, irradiation of cells treated with the four metal complexes initially included in this work with blue light (λ_{max} = 460 nm) was tested. **Figure 13** summarizes the cytotoxic activity of complexes **[Ir-a,b]Cl** and **[Rh-a,b]Cl** with and without irradiation for 20 min with blue LED light at 5.5 mW cm^{-2}. Control experiments were carried out to assess that irradiation alone under these experimental conditions did not affect the cell survival rate. The phototoxicity index values obtained for complexes **[Ir-a]Cl** and **[Ir-b]Cl** were 15.8 ± 0.7 and 3.6 ± 0.3, respectively, whereas **[Rh-a]Cl** and **[Rh-b]Cl** did not display significant differences in their IC_{50} values with and without irradiation. It is worth noting that the IC_{50} for **[Ir-a]Cl** and **[Ir-b]Cl** after blue light irradiation is nearly the same (1.2 ± 0.1 µM and 1.1 ± 0.1 µM, respectively). However, the phototoxicity index of **[Ir-a]Cl** is much higher due to its lower cytotoxicity in the dark.

Thus, despite the similar biological properties of the Ir and the Rh complexes in the dark, the different photophysical features give rise to a very distinct photodynamic activity. The explanation lies on the heavy atom effect that provides the Ir(III) complexes with long-lived triplet excited states, which favours the excitation of the triplet molecular oxygen molecule to generate singlet oxygen. This circumstance does not take place in the Rh complexes.

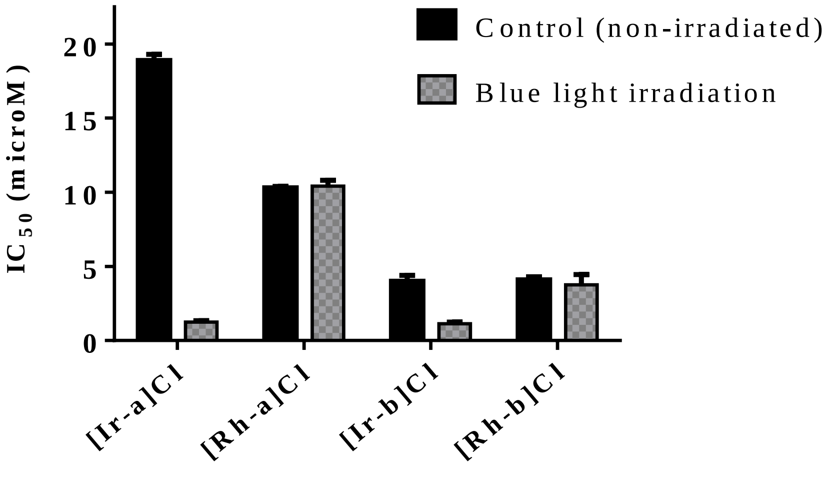

Figure 13. IC_{50} (µM) values obtained for A549 cells treated with **[Ir-a,b]Cl** and **[Rh-a,b]Cl** for 24 h with (grey columns) and without (black columns) irradiation for 20 min with blue LED light at 5.5 mW cm^{-2}. Data were obtained from quadruplicates of three independent experiments.

3. Conclusions.

The potential as anticancer and PDT agents of two pairs of Rh(III) and Ir(III) biscyclometalated complexes of general formula $[M(ppy)_2(N^\wedge N)]Cl$ (M = Rh, Ir) bearing N^N ligands based on the thiabendazole scaffold (L^1 and L^2) has been studied. In the dark, the Rh and Ir benzyl-derivatives are one order more cytotoxic against human lung carcinoma (A549) and human colon carcinoma (SW480) cell lines than cisplatin.

Additional biological studies with these Rh and Ir benzyl-derivatives show that both complexes interfere with mitochondria functionality causing the activation of apoptosis, which constitutes an alternative mechanism of action to that of classical antitumor agents. Moreover, the **[Ir-a]Cl** and **[Ir-b]Cl** complexes exhibit enhanced cytotoxic activity after irradiation with visible blue light, which could be useful in the rational design of new complexes with improved potential for PDT based in this scaffold.

Consideraciones Generales

GENERAL OVERVIEW

Although the conclusions of the different studies have already been described in each Chapter, some general conclusions can be drawn from the different parts of this thesis.

In **Part I**, the interaction of compounds of very different nature, including metal complexes, organic and metallic species, with biomolecules such as DNA and proteins, was explored. As stated before, DNA is one of the major targets in anticancer drug design. Hundreds of new organic and inorganic compounds have been developed in the past few decades and their interaction with DNA evaluated, trying to understand their structure – activity relationship in order to perform a rational design of new drugs. For example, the interaction of the silver atomic clusters Ag_3 with DNA and the distortion they introduce in its structure have a great biological impact, as shown in **Chapter IV**. However, it should also be taken into account that living organisms are complex systems, and oversimplification of this complexity may lead to misinterpretation of the experimental results. The behaviour of the Pt complexes in **Chapter V** is a good example of how different variables can influence the biological activity of a drug. These cisplatin analogues are capable of forming covalent bonds with DNA, but the interaction with proteins present in the extracellular medium can prevent them from reaching their target, thereby negatively affecting their cytotoxicity.

On the other hand, although DNA is one of the most interesting targets in anticancer drug design, several issues still need to be resolved, such as the high general toxicity related to the non-selectivity and the acquired resistance to these drugs. A popular approach to gain specificity has focused on the development of sequence-specific DNA-binding drugs [261]. Nonetheless, the recognition of a 16 base-pair (BP) sequence is needed to select a unique sequence in the human genome of 2.3×10^9 BP [21], and these drugs are often constituted by rather long polyamide chains that have not emerged as potential therapeutic agents yet [262,263]. G-quadruplex binders are a promising alternative that could also target specific sequences of interest based on their structural selectivity. G-quadruplexes, which can get formed in important regions of the human genome such as oncogene promoters, present a high degree of polymorphism and complex behaviours in solution, as evinced in **Chapters VI** and **VII** of **Part 2**. This high degree of polymorphism provides G-quadruplex sequences with very particular structural features that could be selectively targeted by small binders, such as those investigated in **Chapter VIII**. An important point to highlight is that the biological consequences of this type of interactions still need to be further explored.

Finally, despite the importance of DNA binding agents in anticancer research, other paths should not be discarded. As an example, the compounds studied in **Part 3**, **Chapter IX**, exert their cytotoxic activity through mitochondrial perturbation, which leads to cell-cycle arrest and apoptotic cell death. This approach represents a promising alternative for the future as it could help overcome resistance against classical anticancer agents. In addition, the potential use of these cyclometalated Ir(III) complexes as PDT agents constitutes another promising way to be investigated to achieve a higher degree of selectivity towards tumor cells.

ARTICLES AND CONFERENCES

To date, the work presented in this thesis is part of five articles published in peer-reviewed journals and of various contributions to national and international conferences:

- **Articles.**

C. Pérez-Arnaiz, J. Leal, N. Busto, María C. Carrión, Ana R. Rubio, I. Ortiz, G. Barone, B. D. Greñú, J. Santolaya, J. M. Leal, M. Vaquero, F. A. Jalón, B. R. Manzano, B. García, Role of seroalbumin in the cytotoxicity of cis-dichloro Pt(II) complexes with (N^N)-donor ligands bearing functionalized tails, Inorganic Chemistry, Accepted (**2018**).

C. Pérez-Arnaiz, N. Busto, J. Santolaya, J.M. Leal, G. Barone, B. Garcia, Kinetic evidence for interaction of TMPyP4 with two different G-quadruplex conformations of human telomeric DNA, Biochimica et Biophysica Acta,-General Subjects, 1862 (**2018**) 522–531.

C. Pérez-Arnaiz, N. Busto, J.M. Leal, B. Garcia, New microsecond intramolecular reactions of human telomeric DNA in solution, RSC Advances, 6 (**2016**) 39204–39208.

J. Neissa, C. Pérez-Arnaiz, V. Porto, N. Busto, E. Borrajo, J.M. Leal, M.A. Lopez-Quintela, B. Garcia, F. Dominguez, Interaction of silver atomic quantum clusters with living organisms: bactericidal effect of Ag_3 clusters mediated by disruption of topoisomerase-DNA complexes, Chemical Science, 6 (**2015**) 6717–6724.

C. Pérez-Arnaiz, N. Busto, J. M. Leal, B. Garcia, New insights into the mechanism of the DNA/Doxorubicin interaction, Journal of Physical Chemistry B, 118 (**2014**) 1288–1295.

- **Conferences.**

Oral Communication: Biological activity of two cyclometalated iridium and rodium complexes; what is the role of the metal centre? C. Pérez-Arnaiz, N. Busto, I. Echevarría, Mª I. Acuña, G. Espino, J. M. Leal, F. Domínguez, B. García. X Reunión Científica de Bioinorgánica (National), Bilbao, Spain, **2017**.

Flash Oral Communication: A novel dual-functional theranostic Ir(III) complex: biological and imaging properties. C. Pérez-Arnaiz, N. Busto, I. Echevarría, Mª I. Acuña, G. Espino, J. M. Leal, F. Domínguez, B. García. 14th International Conference on Applied Bioinorganic Chemistry (International), Toulousse, France, **2017**.

Poster: Bactericidal activity of silver clusters mediated by disruption of topoisomerase-DNA complexes. J. Neissa, C. Pérez-Arnaiz, N. Busto, V. Porto, E. Borrajo, J.M. Leal, M. A. Lopez-Quintela, B. García, F. Domínguez. EuroBIC13 (International), Budapest, Hungary, **2016**.

Poster: Selectivity of metal complexes towards specific G-Quadruplexes. C. Pérez-Arnaiz, J. González, A. Leczkowska, B. García, R. Vilar. The 11th Nucleic Acids Forum (International), London, UK, **2015**.

BIBLIOGRAPHY

[1] D. Hanahan, R.A. Weinberg, Hallmarks of cancer: the next generation, Cell, 144 (2011) 646–674.

[2] J. Ferlay, I. Soerjomataram, R. Dikshit, S. Eser, C. Mathers, M. Rebelo, D.M. Parkin, D. Forman, F. Bray, Cancer incidence and mortality worldwide: Sources, methods and major patterns in GLOBOCAN 2012, Int. J. Cancer, 136 (2015) E359–E386.

[3] L.A. Torre, F. Bray, R.L. Siegel, J. Ferlay, J. Lortet-Tieulent, A. Jemal, Global cancer statistics, 2012, CA. Cancer J. Clin., 65 (2015) 87–108.

[4] A. Sudhakar, History of Cancer, Ancient and Modern Treatment Methods, J. Cancer Sci. Ther., 1 (2009) 1–4.

[5] J.D. Watson, F.H.C. Crick, Molecular structure of nucleic acids A structure for deoxyribose nucleic acid, Nature, 171 (1953) 737–738.

[6] F.H.C. Crick, Central dogma of molecular biology, Nature, 227 (1970) 561–563.

[7] F.H.C. Crick, On protein synthesis, Symp. Soc. Exp. Biol., 12 (1958) 138–163.

[8] A. Urruticoechea, R. Alemany, J. Balart, A. Villanueva, F. Vinals, G. Capella, Recent advances in cancer therapy: an overview, Curr. Pharm. Des., 16 (2010) 3–10.

[9] M. Vanneman, G. Dranoff, Combining immunotherapy and targeted therapies in cancer treatment, Nat. Rev. Cancer, 12 (2012) 237–251.

[10] S. Farkona, E.P. Diamandis, I.M. Blasutig, Cancer immunotherapy: the beginning of the end of cancer?, BMC Med., 14 (2016) 1–18.

[11] C. Brown, Targeted therapy: An elusive cancer target, Nature, 537 (2016) 106–108.

[12] L. Benov, Photodynamic therapy: current status and future directions, Med. Princ. Pract., 24 (2015) 14–28.

[13] B.A. Chabner, T.G. Roberts, Chemotherapy and the war on cancer, Nat. Rev. Cancer, 5 (2005) 65–72.

[14] G.B. Jones, History of Anticancer Drugs, in: eLS, John Wiley & Sons, Ltd, 2014.

[15] V.T. DeVita, E. Chu, A History of Cancer Chemotherapy, Cancer Res., 68 (2008) 8643–8653.

[16] S.E. Weinberg, N.S. Chandel, Targeting mitochondria metabolism for cancer therapy, Nat. Chem. Biol., 11 (2015) 9–15.

[17] D. Dolmans, D. Fukumura, R.K. Jain, TIMELINE: Photodynamic therapy for cancer, Nat. Rev. Cancer, 3 (2003) 380–387.

[18] H. Abrahamse, M.R. Hamblin, New photosensitizers for photodynamic therapy, Biochem. J., 473 (2016) 347–364.

[19] B.W. Henderson, T.J. Dougherty, How does photodynamic therapy work?, Photochem. Photobiol., 55 (1992) 145–157.

[20] D.K. Deda, K. Araki, Nanotechnology, light and chemical action: an effective combination to kill cancer cells, J. Braz. Chem. Soc., 26 (2015) 2448–2470.

[21] L.H. Hurley, DNA and its associated processes as targets for cancer therapy, Nat. Rev. Cancer, 2 (2002) 188–200.

[22] Y. Huang, L. Li, DNA crosslinking damage and cancer - a tale of friend and foe, Transl. Cancer Res., 2 (2013) 144–154.

[23] G. Minotti, P. Menna, E. Salvatorelli, G. Cairo, L. Gianni, Anthracyclines: Molecular advances and pharmacologic developments in antitumor activity and cardiotoxicity, Pharmacol. Rev., 56 (2004) 185–229.

[24] C. Carvalho, R.X. Santos, S. Cardoso, S. Correia, P.J. Oliveira, M.S. Santos, P.I. Moreira, Doxorubicin: the good, the bad and the ugly effect, Curr. Med. Chem., 16 (2009) 3267–3285.

[25] M.F. Gellert, M.N. Lipsett, D.H. Davies, Helix formation by guanylic acid, Proc. Natl. Acad. Sci., 48 (1962) 2013–2018.

[26] R. Hansel-Hertsch, M. Di Antonio, S. Balasubramanian, DNA G-quadruplexes in the human genome: detection, functions and therapeutic potential, Nat. Rev. Mol. Cell Biol., 18 (2017) 279–284.

[27] D. Rhodes, H.J. Lipps, G-quadruplexes and their regulatory roles in biology, Nucleic Acids Res., 43 (2015) 8627–8637.

[28] M.L. Bochman, K. Paeschke, V.A. Zakian, DNA secondary structures: stability and function of structures, Nat. Rev. Genet., 13 (2012) 770–780.

[29] V.S. Chambers, G. Marsico, J.M. Boutell, M. Di Antonio, G.P. Smith, S. Balasubramanian, High-throughput sequencing of DNA G-quadruplex structures in the human genome, Nat. Biotechnol., 33 (2015) 877–881.

[30] E.Y.N. Lam, D. Beraldi, D. Tannahill, S. Balasubramanian, G-quadruplex structures are stable and detectable in human genomic DNA, Nat. Commun., 4 (2013) 1796.

[31] A.L. Moye, K.C. Porter, S.B. Cohen, K.G. Zyner, N. Sasaki, T.M. Bryan, T. Phan, G.O. Lovrecz, J.L. Beck, Telomeric G-quadruplexes are a substrate and site of localization for human telomerase, Nat. Commun., 6 (2015) 7643.

[32] D.L. Nelson, M.M. Cox, A.L. Lehninger, Principles of biochemistry, 6th ed., W.H. Freeman, New York, 2013.

[33] R.E. Dickerson, H.R. Drew, B.N. Conner, R.M. Wing, A. V Fratini, M.L. Kopka, The anatomy of A-, B-, and Z-DNA, Science, 216 (1982) 475–485.

[34] A.H.J. Wang, G.J. Quigley, F.J. Kolpak, J.L. Crawford, J.H. Van Boom, G. Van der Marel, A. Rich, Molecular structure of a left-handed double helical DNA fragment at atomic resolution, Nature, 282 (1979) 680–686.

[35] T. Biver, B. Garcia, J.M. Leal, F. Secco, E. Turriani, Left-handed DNA: intercalation of the cyanine thiazole orange and structural changes A kinetic and thermodynamic approach, Phys. Chem. Chem. Phys., 12 (2010) 13309–13317.

[36] T.J. Thamann, R.C. Lord, A.H.J. Wang, A. Rich, The high salt form of poly(dG-dC).poly(dG-dC) is left-handed Z-DNA: Raman spectra of crystals and solutions, Nucleic Acids Res., 9 (1981) 5443–5457.

[37] A. Rich, S. Zhang, Timeline: Z-DNA: The long road to biological function, Nat. Rev. Genet., 4 (2003) 566–572.

[38] T. Umehara, S. Kuwabara, S. Mashimo, S. Yagihara, Dielectric study on hydration of B-, A-, and Z-DNA, Biopolymers, 30 (1990) 649–656.

[39] A. Travers, G. Muskhelishvili, DNA structure and function, FEBS J., 282 (2015) 2279–2295.

[40] D.-B. Oh, Y.-G. Kim, A. Rich, Z-DNA-binding proteins can act as potent effectors of gene expression in vivo, Proc. Natl. Acad. Sci., 99 (2002) 16666–16671.

[41] H. Htun, J.E. Dahlberg, Topology and formation of triple-stranded H-DNA, Science, 243 (1989) 1571–1576.

[42] J. Bernues, F. Azorin, Triple-stranded DNA, Nucleic Acids Mol. Biol., 9 (1995) 1–21.

[43] J.T. Davis, G-quartets 40 years later: From 5’-GMP to molecular biology and supramolecular chemistry, Angew. Chem., Int. Ed., 43 (2004) 668–698.

[44] M. Malgowska, K. Czajczynska, D. Gudanis, A. Tworak, Z. Gdaniec, Overview of the RNA G-quadruplex structures, Acta Biochim. Pol., 63 (2016) 609–621.

[45] S. Burge, G.N. Parkinson, P. Hazel, A.K. Todd, S. Neidle, Quadruplex DNA: sequence, topology and structure, Nucleic Acids Res., 34 (2006) 5402–5415.

[46] T. Ou, Y. Lu, J. Tan, Z. Huang, K.-Y. Wong, L. Gu, G-quadruplexes: targets in anticancer drug design, ChemMedChem, 3 (2008) 690–713.

[47] A. Ambrus, D. Chen, J. Dai, T. Bialis, R.A. Jones, D. Yang, Human telomeric sequence forms a hybrid-type intramolecular G-quadruplex structure with mixed parallel/antiparallel strands in potassium solution, Nucleic Acids Res., 34 (2006) 2723–2735.

[48] M.A. Keniry, Quadruplex structures in nucleic acids, Biopolymers, 56 (2001) 123–146.

[49] A. Ambrus, D. Chen, J. Dai, R.A. Jones, D. Yang, Solution Structure of the Biologically Relevant G-Quadruplex Element in the Human c-MYC Promoter Implications for G-Quadruplex Stabilization, Biochemistry, 44 (2005) 2048–2058.

[50] J. Dai, T.S. Dexheimer, D. Chen, M. Carver, A. Ambrus, R.A. Jones, D. Yang, An Intramolecular G-Quadruplex Structure with Mixed Parallel/Antiparallel G-Strands Formed in the Human BCL-2 Promoter Region in Solution, J. Am. Chem. Soc., 128 (2006) 1096–1098.

[51] B. Alberts, A. Johnson, J. Lewis, D. Morgan, M. Raff, K. Roberts, P. Walter, Molecular Biology of the Cell, 6th ed., Taylor & Francis Group, New York, 2015.

[52] D.M. Livermore, D.F. Brown, Detection of beta-lactamase-mediated resistance, J. Antimicrob. Chemother., 48 (2001) 59–64.

[53] G. Bischoff, S. Hoffmann, DNA-binding of drugs used in medicinal therapies, Curr. Med. Chem., 9 (2002) 321–348.

[54] M.J. Horsfall, A.J.E. Gordon, P.A. Burns, M. Zielenska, G.M.E. Van der Vliet, B.W. Glickman, Mutational specificity of alkylating agents and the influence of DNA repair, Environ. Mol. Mutagen., 15 (1990) 107–122.

[55] S.R. Rajski, R.M. Williams, DNA Cross-Linking Agents as Antitumor Drugs, Chem. Rev., 98 (1998) 2723–2796.

[56] D.M. Noll, T. McGregor Mason, P.S. Miller, Formation and Repair of Interstrand Cross-Links in DNA, Chem. Rev., 106 (2006) 277–301.

[57] A.-M. Florea, D. Buesselberg, Cisplatin as an anti-tumor drug: cellular mechanisms of activity, drug resistance and induced side effects, Cancers, 3 (2011) 1351–1371.

[58] S. Dasari, P. Bernard Tchounwou, Cisplatin in cancer therapy: Molecular mechanisms of action, Eur. J. Pharmacol., 740 (2014) 364–378.

[59] A.H.J. Wang, Intercalative drug binding to DNA, Curr. Opin. Struct. Biol., 2 (1992) 361–368.

[60] S. Li, V.R. Cooper, T. Thonhauser, B.I. Lundqvist, D.C. Langreth, Stacking Interactions and DNA Intercalation, J. Phys. Chem. B, 113 (2009) 11166–11172.

[61] E.C. Long, J.K. Barton, On demonstrating DNA intercalation, Acc. Chem. Res., 23 (1990) 271–273.

[62] H.M. Berman, P.R. Young, The interaction of intercalating drugs with nucleic acids, Annu. Rev. Biophys. Bioeng., 10 (1981) 87–114.

[63] A.S. Biebricher, I. Heller, R.F.H. Roijmans, T.P. Hoekstra, E.J.G. Peterman, G.J.L. Wuite, The impact of DNA intercalators on DNA and DNA-processing enzymes elucidated through force-dependent binding kinetics, Nat. Commun., 6 (2015) 7304.

[64] S. Nafisi, A.A. Saboury, N. Keramat, J.-F. Neault, H.-A. Tajmir-Riahi, Stability and structural features of DNA intercalation with ethidium bromide, acridine orange and methylene blue, J. Mol. Struct., 827 (2007) 35–43.

[65] J.C. Francois, T. Saison-Behmoaras, C. Helene, Sequence-specific recognition of the major groove of DNA by oligodeoxynucleotides via triple helix formation Footprinting studies, Nucleic Acids Res., 16 (1988) 11431–11440.

[66] F. Hamy, U. Asseline, J. Grasby, S. Iwai, C. Pritchard, G. Slim, J.G. Butler, J. Karn, M.J. Gait, Hydrogen-bonding contacts in the major groove are required for human immunodeficiency virus type-1 tat protein recognition of TAR RNA, J. Mol. Biol., 230 (1993) 111–123.

[67] S.M. Nelson, L.R. Ferguson, W.A. Denny, Non-covalent ligand/DNA interactions: Minor groove binding agents, Mutat. Res. Fundam. Mol. Mech. Mutagen., 623 (2007) 24–40.

[68] G.S. Khan, A. Shah, Zia-ur-Rehman, D. Barker, Chemistry of DNA minor groove binding agents, J. Photochem. Photobiol. B Biol., 115 (2012) 105–118.

[69] A. Abu-Daya, K.R. Fox, Interaction of minor groove binding ligands with long AT tracts, Nucleic Acids Res., 25 (1997) 4962–4969.

[70] C.L. Kielkopf, S. White, J.W. Sewczyk, J.M. Turner, E.E. Baird, P.B. Dervan, D.C. Rees, A structural basis for recognition of A·T and T·A base pairs in the minor groove of B-DNA, Science, 282 (1998) 111–115.

[71] J.S. Ren, J.B. Chaires, Sequence and structural selectivity of nucleic acid binding ligands, Biochemistry, 38 (1999) 16067–16075.

[72] L. Strekowski, B. Wilson, Noncovalent interactions with DNA: An overview, Mutat. Res. Fundam. Mol. Mech. Mutagen., 623 (2007) 3–13.

[73] Y. Chen, D. Yang, Sequence, stability, and structure of G-quadruplexes and their interactions with drugs, Curr. Protoc. Nucleic Acid Chem., Chapter 17 (2012) Unit17.5.

[74] S. Bandeira, J. Gonzalez-Garcia, E. Pensa, T. Albrecht, R. Vilar, A Redox-Activated G-Quadruplex DNA Binder Based on a Platinum(IV)-Salphen Complex, Angew. Chemie, Int. Ed., 57 (2018) 310–313.

[75] A. Kotar, B. Wang, A. Shivalingam, J. Gonzalez-Garcia, R. Vilar, J. Plavec, NMR Structure of a Triangulenium-Based Long-Lived Fluorescence Probe Bound to a G-Quadruplex, Angew. Chemie, Int. Ed., 55 (2016) 12508–12511.

[76] Q. Cao, Y. Li, E. Freisinger, P.Z. Qin, R.K.O. Sigel, Z.-W. Mao, G-quadruplex DNA targeted metal complexes acting as potential anticancer drugs, Inorg. Chem. Front., 4 (2017) 10–32.

[77] J. Cuesta, M.A. Read, S. Neidle, The design of G-quadruplex ligands as telomerase inhibitors, Mini-Rev. Med. Chem., 3 (2003) 11–21.

[78] D. Monchaud, M.-P. Teulade-Fichou, A hitchhiker’s guide to G-quadruplex ligands, Org. Biomol. Chem., 6 (2008) 627–636.

[79] T.V.T. Le, S. Han, J. Chae, H.-J. Park, G-quadruplex binding ligands: from naturally occurring to rationally designed molecules, Curr. Pharm. Des., 18 (2012) 1948–1972.

[80] S. Balasubramanian, S. Neidle, G-quadruplex nucleic acids as therapeutic targets, Curr. Opin. Chem. Biol., 13 (2009) 345–353.

[81] S.N. Georgiades, N.H. Abd Karim, K. Suntharalingam, R. Vilar, Interaction of Metal Complexes with G-Quadruplex DNA, Angew. Chemie, Int. Ed., 49 (2010) 4020–4034.

[82] A.M. Burger, F. Dai, C.M. Schultes, A.P. Reszka, M.J. Moore, J.A. Double, S. Neidle, The G-quadruplex-interactive molecule BRACO-19 inhibits tumor growth, consistent with telomere targeting and interference with telomerase function, Cancer Res., 65 (2005) 1489–1496.

[83] K. Shin-ya, K. Wierzba, K. Matsuo, T. Ohtani, Y. Yamada, K. Furihata, Y. Hayakawa, H. Seto, Telomestatin, a novel telomerase inhibitor from Streptomyces anulatus, J. Am. Chem. Soc., 123 (2001) 1262–1263.

[84] F.X. Han, R.T. Wheelhouse, L.H. Hurley, Interactions of TMPyP4 and TMPyP2 with Quadruplex DNA Structural Basis for the Differential Effects on Telomerase Inhibition, J. Am. Chem. Soc., 121 (1999) 3561–3570.

[85] J. Dejeu, T. Lavergne, J. Della Nora, E. Defrancq, G. Pratviel, Binding of metalloporphyrins to G-quadruplex DNA: The role of the central metal, Inorganica Chim. Acta, 452 (2016) 98–103.

[86] C. Bertoli, J.M. Skotheim, R.A.M. de Bruin, Control of cell cycle transcription during G1 and S phases, Nat. Rev. Mol. Cell Biol., 14 (2013) 518–528.

[87] G.I. Shapiro, J.W. Harper, Anticancer drug targets: cell cycle and checkpoint control, J. Clin. Invest., 104 (1999) 1645–1653.

[88] Z.A. Stewart, M.D. Westfall, J.A. Pietenpol, Cell-cycle dysregulation and anticancer therapy, Trends Pharmacol. Sci., 24 (2003) 139–145.

[89] T. Kawabe, G2 checkpoint abrogators as anticancer drugs, Mol. Cancer Ther., 3 (2004) 513–519.

[90] C.M. Sorenson, M.A. Barry, A. Eastman, Analysis of events associated with cell cycle arrest at G2 phase and cell death induced by cisplatin, J. Natl. Cancer Inst., 82 (1990) 749–755.

[91] Y.-H. Ling, A.K. El-Naggar, W. Priebe, R. Perez-Soler, Cell cycle-dependent cytotoxicity, G2/M phase arrest, and disruption of p34cdc2/cyclin B1 activity induced by doxorubicin in synchronized P388 cells, Mol. Pharmacol., 49 (1996) 832–841.

[92] S. Neidle, Quadruplex Nucleic Acids as Novel Therapeutic Targets, J. Med. Chem., 59 (2016) 5987–6011.

[93] U. Herbig, W.A. Jobling, B.P.C. Chen, D.J. Chen, J.M. Sedivy, Telomere shortening triggers senescence of human cells through a pathway involving ATM, p53, and p21CIP1, but not p16INK4a, Mol. Cell, 14 (2004) 501–513.

[94] S. Victorelli, J.F. Passos, Telomeres and Cell Senescence - Size Matters Not, EBioMedicine, 21 (2017) 14–20.

[95] S. Neidle, Quadruplex nucleic acids as targets for anticancer therapeutics, Nat. Rev. Chem., 1 (2017) 1–10.

[96] S. Fulda, L. Galluzzi, G. Kroemer, Targeting mitochondria for cancer therapy, Nat. Rev. Drug Discov., 9 (2010) 447–464.

[97] C. Dumontet, M.A. Jordan, Microtubule-binding agents: a dynamic field of cancer therapeutics, Nat. Rev. Drug Discov., 9 (2010) 790–803.

[98] R. Lappano, M. Maggiolini, G protein-coupled receptors: novel targets for drug discovery in cancer, Nat. Rev. Drug Discov., 10 (2011) 47–60.

[99] C. Wang, R.J. Youle, The role of mitochondria in apoptosis, Annu. Rev. Genet., 43 (2009) 95–118.

[100] V. Gogvadze, S. Orrenius, B. Zhivotovsky, Mitochondria in cancer cells: what is so special about them?, Trends Cell Biol., 18 (2008) 165–173.

[101] P.E. Porporato, N. Filigheddu, J.M.B.-S. Pedro, G. Kroemer, L. Galluzzi, Mitochondrial metabolism and cancer, Cell Res., 28 (2018) 265–280.

[102] T. Dickerson, C.E. Jauregui, Y. Teng, Friend or foe? Mitochondria as a pharmacological target in cancer treatment, Future Med. Chem., 9 (2017) 2197–2210.

[103] Y. Li, C.-P. Tan, W. Zhang, L. He, L.-N. Ji, Z.-W. Mao, Phosphorescent iridium(III)-bis-N-heterocyclic carbene complexes as mitochondria-targeted theranostic and photodynamic anticancer agents, Biomaterials, 39 (2015) 95–104.

[104] J.H. Lee, K.Y. Kim, H. Jin, Y.E. Baek, Y. Choi, S.H. Jung, S.S. Lee, J. Bae, J.H. Jung, Self-Assembled Coumarin Nanoparticle in Aqueous Solution as Selective Mitochondrial-Targeting Drug Delivery System, ACS Appl. Mater. Interfaces, 10 (2018) 3380–3391.

[105] Y. Liu, X. Zhang, M. Zhou, X. Nan, X. Chen, X. Zhang, Mitochondrial-Targeting Lonidamine-Doxorubicin Nanoparticles for Synergistic Chemotherapy to Conquer Drug Resistance, ACS Appl. Mater. Interfaces, 9 (2017) 43498–43507.

[106] H. Wang, P. Agarwal, S. Zhao, X. He, H. Wang, J. Yu, X. He, H. Wang, P. Agarwal, S. Zhao, Z. Liu, X. He, Z. Gao, X. Li, X. Liu, Z. Liu, D.W. Conroy, C.P. Jaroniec, G. Ji, J. Yu, et al., Targeted production of reactive oxygen species in mitochondria to overcome cancer drug resistance, Nat. Commun., 9 (2018) 562.

[107] D. Buceta, N. Busto, G. Barone, J.M. Leal, F. Dominguez, L.J. Giovanetti, F.G. Requejo, B. Garcia, M.A. Lopez-Quintela, Ag2 and Ag3 Clusters: Synthesis, Characterization, and Interaction with DNA, Angew. Chem., Int. Ed., 54 (2015) 7612–7616.

[108] M.E. Reichmann, C.A. Rice, C.A. Thomas, P. Doty, A further examination of the molecular weight and size of deoxypentose nucleic acid, J. Am. Chem. Soc., 76 (1954) 3047–3053.

[109] K.W. Lim, V.C.M. Ng, N. Martin-Pintado, B. Heddi, A.T. Phan, Structure of the human telomere in Na+ solution: an antiparallel (2+2) G-quadruplex scaffold reveals additional diversity, Nucleic Acids Res., 41 (2013) 10556–10562.

[110] V. Kuryavyi, A.T. Phan, D.J. Patel, Solution structures of all parallel-stranded monomeric and dimeric G-quadruplex scaffolds of the human c-kit2 promoter, Nucleic Acids Res., 38 (2010) 6757–6773.

[111] K.W. Lim, P. Alberti, A. Guedin, L. Lacroix, J.-F. Riou, N.J. Royle, J.-L. Mergny, A.T. Phan, Sequence variant (CTAGGG)n in the human telomere favors a G-quadruplex structure containing a G·C·G·C tetrad, Nucleic Acids Res., 37 (2009) 6239–6248.

[112] S. Amrane, M. Adrian, B. Heddi, A. Serero, A. Nicolas, J.-L. Mergny, A.T. Phan, Formation of Pearl-Necklace Monomorphic G-Quadruplexes in the Human CEB25 Minisatellite, J. Am. Chem. Soc., 134 (2012) 5807–5816.

[113] J. Dai, T.S. Dexheimer, D. Chen, M. Carver, A. Ambrus, R.A. Jones, D. Yang, An Intramolecular G-Quadruplex Structure with Mixed Parallel/Antiparallel G-Strands Formed in the Human BCL-2 Promoter Region in Solution, J. Am. Chem. Soc., 128 (2006) 1096–1098.

[114] H. Martadinata, A.T. Phan, Structure of Human Telomeric RNA (TERRA): Stacking of Two G-Quadruplex Blocks in K+ Solution, Biochemistry, 52 (2013) 2176–2183.

[115] U. Kragh-Hansen, Molecular aspects of ligand binding to serum albumin, Pharmacol. Rev., 33 (1981) 17–53.

[116] C.N. Pace, F. Vajdos, L. Fee, G. Grimsley, T. Gray, How to measure and predict the molar absorption coefficient of a protein, Protein Sci., 4 (1995) 2411–2423.

[117] N. Busto, M. Martinez-Alonso, J.M. Leal, A.M. Rodriguez, F. Dominguez, M.I. Acuna, G. Espino, B. Garcia, Monomer-Dimer Divergent Behavior toward DNA in a Half-Sandwich Ruthenium(II) Aqua Complex Antiproliferative Biphasic Activity, Organometallics, 34 (2015) 319–327.

[118] J.D. McGhee, P.H. Von Hippel, Theoretical aspects of DNA-protein interactions Cooperative and noncooperative binding of large ligands to a one-dimensional homogeneous lattice, J. Mol. Biol., 86 (1974) 469–489.

[119] G. Scatchard, The attraction of proteins for small molecules and ions, Ann. N. Y. Acad. Sci., 51 (1949) 660–672.

[120] J.R. Lakowicz, Principles of Fluorescence Spectroscopy, 3rd ed., Springer US, 2006.

[121] N. Berova, K. Nakanishi, R. W. Woody, Circular Dichroism: Principles and Applications, 2nd ed., Wiley VCH, inc., 2000.

[122] J. Kypr, I. Kejnovska, D. Renciuk, M. Vorlickova, Circular dichroism and conformational polymorphism of DNA, Nucleic Acids Res., 37 (2009) 1713–1725.

[123] M.G. Varrica, C. Zagni, P.G. Mineo, G. Floresta, G. Monciino, V. Pistara, A. Abbadessa, A. Nicosia, R.M. Castilho, E. Amata, A. Rescifina, DNA intercalators based on (1,10-phenanthrolin-2-yl)isoxazolidin-5-yl core with better growth inhibition and selectivity than cisplatin upon head and neck squamous cells carcinoma, Eur. J. Med. Chem., 143 (2018) 583–590.

[124] N.C. Garbett, P.A. Ragazzon, J.B. Chaires, Circular dichroism to determine binding mode and affinity of ligand-DNA interactions, Nat. Protoc., 2 (2007) 3166–3172.

[125] N. Holmgaard List, J. Knoops, J. Rubio-Magnieto, J. Ide, D. Beljonne, P. Norman, M. Surin, M. Linares, Origin of DNA-Induced Circular Dichroism in a Minor-Groove Binder, J. Am. Chem. Soc., 139 (2017) 14947–14953.

[126] A. Garci, K.J. Castor, J. Fakhoury, J.-L. Do, J. Di Trani, P. Chidchob, R.S. Stein, A.K. Mittermaier, T. Friscic, H. Sleiman, Efficient and Rapid Mechanochemical Assembly of Platinum(II) Squares for Guanine Quadruplex Targeting, J. Am. Chem. Soc., 139 (2017) 16913–16922.

[127] H.K. Saeed, I.Q. Saeed, N.J. Buurma, J.A. Thomas, The structure of linkers affects the DNA binding properties of tethered dinuclear ruthenium(II) metallo-intercalators, Chem. - A Eur. J., 23 (2017) 5467–5477.

[128] J.P. Emerson, V.H. Le, E.A. Lewis, Calorimetry, in: eLS, John Wiley & Sons, Ltd, 2001.

[129] J.E. Ladbury, B.Z. Chowdhry, Sensing the heat: the application of isothermal titration calorimetry to thermodynamic studies of biomolecular interactions, Chem. Biol., 3 (1996) 791–801.

[130] G. Bruylants, J. Wouters, C. Michaux, Differential scanning calorimetry in life science: Thermodynamics, stability, molecular recognition and application in drug design, Curr. Med. Chem., 12 (2005) 2011–2020.

[131] C.M. Olsen, R. Shikiya, R. Ganugula, C. Reiling-Steffensmeier, I. Khutsishvili, S.E. Johnson, L.A. Marky, Application of differential scanning calorimetry to measure the differential binding of ions, water and protons in the unfolding of DNA molecules, Biochim. Biophys. Acta, Gen. Subj., 1860 (2016) 990–998.

[132] S. Krumova, S. Todinova, D. Mavrov, P. Marinov, V. Atanassova, K. Atanassov, S.G. Taneva, Intercriteria analysis of calorimetric data of blood serum proteome, Biochim. Biophys. Acta, Gen. Subj., 1861 (2017) 409–417.

[133] J. Murmur, P. Doty, Determination of the base composition of deoxyribonucleic acid (DNA) from its thermal denaturation temperature, J. Mol. Biol., 5 (1962) 109–118.

[134] P. Yakovchuk, E. Protozanova, M.D. Frank-Kamenetskii, Base-stacking and base-pairing contributions into thermal stability of the DNA double helix, Nucleic Acids

Res., 34 (2006) 564–574.

[135] D.W. Gruenwedel, Salt effects on the denaturation of DNA 3 A calorimetric investigation of the transition enthalpy of calf thymus DNA in Na2SO4 solutions of varying ionic strength, Biochim. Biophys. Acta, 340 (1974) 16–30.

[136] R. Palchaudhuri, P.J. Hergenrother, DNA as a target for anticancer compounds: methods to determine the mode of binding and the mechanism of action, Curr. Opin. Biotechnol., 18 (2007) 497–503.

[137] C. Spink, Differential scanning calorimetry, Methods Cell Biol., 84 (2008) 115–141.

[138] V. V Didenko, DNA probes using fluorescence resonance energy transfer (FRET): designs and applications, Biotechniques, 31 (2001) 1106–1121.

[139] D. Renciuk, J. Zhou, L. Beaurepaire, A. Guedin, A. Bourdoncle, J.-L. Mergny, A FRET-based screening assay for nucleic acid ligands, Methods, 57 (2012) 122–128.

[140] R. Vilar, V. Rakers, P. Cadinu, J. Edel, Development of microfluidic platforms for the synthesis of metal complexes and evaluation of their DNA affinity using online FRET melting assays, Chem. Sci., 9 (2018) 3459–3469.

[141] J. Medeiros-Silva, A. Guedin, G.F. Salgado, J.-L. Mergny, J.A. Queiroz, E.J. Cabrita, C. Cruz, Phenanthroline-bis-oxazole ligands for binding and stabilization of G-quadruplexes, Biochim. Biophys. Acta, Gen. Subj., 1861 (2017) 1281–1292.

[142] D. Suh, J.B. Chaires, Criteria for the mode of binding of DNA binding agents, Bioorg. Med. Chem., 3 (1995) 723–728.

[143] G. Cohen, H. Eisenberg, Viscosity and sedimentation study of sonicated DNA-proflavine complexes, Biopolymers, 8 (1969) 45–55.

[144] T. Biver, F. Secco, M. Venturini, Mechanistic aspects of the interaction of intercalating metal complexes with nucleic acids, Coord. Chem. Rev., 252 (2008) 1163–1177.

[145] G. Malgieri, G. D'Abrosca, L. Pirone, A. Toto, M. Palmieri, L. Russo, M.F.M. Sciacca, R. Tate, V. Sivo, I. Baglivo, R. Majewska, M. Coletta, P.V. Pedone, C. Isernia, M. De Stefano, S. Gianni, E.M. Pedone, D. Milardi, R. Fattorusso, Folding mechanisms steer the amyloid fibril formation propensity of highly homologous proteins, Chem. Sci., 9 (2018) 3290–3298.

[146] R. Rigler, C.R. Rabl, T.M. Jovin, Temperature-jump apparatus for fluorescence measurements, Rev. Sci. Instrum., 45 (1974) 580–588.

[147] K. Wilson, J. Walker, Principles and Techniques of Biochemistry and Molecular Biology, 7th Ed., Cambridge University Press, 2010.

[148] A. V Vologodskii, Distributions of topological states in circular DNA, Mol. Biol., 35 (2001) 240–250.

[149] S. Richter, S. Singh, D. Draca, A. Kate, A. Kumbhar, A.S. Kumbhar, D. Maksimovic-Ivanic, S. Mijatovic, P. Loennecke, E. Hey-Hawkins, Antiproliferative activity of ruthenium(II) arene complexes with mono- and bidentate pyridine-based ligands, Dalton Trans., 45 (2016) 13114–13125.

[150] G.L. Cohen, W.R. Bauer, J.K. Barton, S.J. Lippard, Binding of cis- and trans-

dichlorodiammineplatinum(II) to DNA: Evidence for unwinding and shortening of the double helix, Sci. (Washington, DC, United States), 203 (1979) 1014–1016.

[151] N.C. Stellwagen, Electrophoresis of DNA in agarose gels, polyacrylamide gels and in free solution, Electrophoresis, 30 (2009) 188–195.

[152] S.R. Gallagher, One-dimensional SDS gel electrophoresis of proteins, Curr. Protoc. Protein Sci., Chapter 10 (2012) 1–44.

[153] C. Arndt, S. Koristka, H. Bartsch, M. Bachmann, Native polyacrylamide gels, Methods Mol. Biol., 869 (2012) 49–53.

[154] T. Maniatis, A. Jeffrey, H. Van de Sande, Chain length determination of small double- and single-stranded DNA molecules by polyacrylamide gel electrophoresis, Biochemistry, 14 (1975) 3787–3794.

[155] F. Flett, H. Interthal, Separation of DNA Oligonucleotides Using Denaturing Urea PAGE, Methods Mol. Biol. (New York, NY, United States), 1054 (2013) 173–185.

[156] H.M.E. Azzazy, R.H. Christenson, All about albumin: biochemistry, genetics, and medical applications Theodore Peters, Clin. Chem. (Washington, D. C.), 43 (1997) 2014–2015.

[157] I. Wittig, H.-P. Braun, H. Schaegger, Blue native PAGE, Nat. Protoc., 1 (2006) 418–428.

[158] H. Han, L.H. Hurley, M. Salazar, A DNA polymerase stop assay for G-quadruplex-interactive compounds, Nucleic Acids Res., 27 (1999) 537–542.

[159] A. Siddiqui-Jain, C.L. Grand, D.J. Bearss, L.H. Hurley, Direct evidence for a G-quadruplex in a promoter region and its targeting with a small molecule to repress c-MYC transcription, Proc. Natl. Acad. Sci., 99 (2002) 11593–11598.

[160] R.K. Saiki, D.H. Gelfand, S. Stoffel, S.J. Scharf, R. Higuchi, G.T. Horn, K.B. Mullis, H.A. Erlich, Primer-directed enzymatic amplification of DNA with a thermostable DNA polymerase, Science, 239 (1988) 487–491.

[161] J. van Meerloo, G.J.L. Kaspers, J. Cloos, Cell sensitivity assays: the MTT assay, Methods Mol. Biol., 731 (2011) 237–245.

[162] C.A. Puckett, R.J. Ernst, J.K. Barton, Exploring the cellular accumulation of metal complexes, Dalton Trans., 39 (2010) 1159–1170.

[163] K.K.-W. Lo, Luminescent Rhenium(I) and Iridium(III) Polypyridine Complexes as Biological Probes, Imaging Reagents, and Photocytotoxic Agents, Acc. Chem. Res., 48 (2015) 2985–2995.

[164] R. Xu, Y. Wang, X. Duan, K. Lu, D. Micheroni, A. Hu, W. Lin, Nanoscale Metal-Organic Frameworks for Ratiometric Oxygen Sensing in Live Cells, J. Am. Chem. Soc., 138 (2016) 2158–2161.

[165] H.C. Ishikawa-Ankerhold, R. Ankerhold, G.P.C. Drummen, Advanced fluorescence microscopy techniques-FRAP, FLIP, FLAP, FRET and FLIM, Molecules, 17 (2012) 4047–4132.

[166] J. Jonkman, C.M. Brown, Any Way You Slice It-A Comparison of Confocal Microscopy Techniques, J. Biomol. Tech., 26 (2015) 54–65.

[167] V. Zinchuk, O. Grossenbacher-Zinchuk, Quantitative colocalization analysis of confocal fluorescence microscopy images, Curr. Protoc. Cell Biol., Chapter 4

(2011).

[168] K.W. Dunn, M.M. Kamocka, J.H. McDonald, A practical guide to evaluating colocalization in biological microscopy, Am. J. Physiol., 300 (2011) 723–742.

[169] Y. Shi, Mechanisms of caspase activation and inhibition during apoptosis, Mol. Cell, 9 (2002) 459–470.

[170] G. Kroemer, J.C. Reed, Mitochondrial control of cell death, Nat. Med., 6 (2000) 513–519.

[171] A. Adan, G. Alizada, Y. Kiraz, Y. Baran, A. Nalbant, Flow cytometry: basic principles and applications, Crit. Rev. Biotechnol., 37 (2017) 163–176.

[172] A. Krishan, Rapid flow cytofluorometric analysis of mammalian cell cycle by propidium iodide staining, J. Cell Biol., 66 (1975) 188–193.

[173] M. Ott, B. Zhivotovsky, S. Orrenius, Role of cardiolipin in cytochrome c release from mitochondria, Cell Death Differ., 14 (2007) 1243–1247.

[174] H.-U. Simon, A. Haj-Yehia, F. Levi-Schaffer, Role of reactive oxygen species (ROS) in apoptosis induction, Apoptosis, 5 (2000) 415–418.

[175] P. Kaewsuya, N.D. Danielson, D. Ekhterae, Fluorescent determination of cardiolipin using 10-N-nonyl acridine orange, Anal. Bioanal. Chem., 387 (2007) 2775–2782.

[176] M.I. Garcia Fernandez, D. Ceccarelli, U. Muscatello, Use of the fluorescent dye 10-N-nonyl acridine orange in quantitative and location assays of cardiolipin: a study on different experimental models, Anal. Biochem., 328 (2004) 174–180.

[177] C. Perez-Arnaiz, N. Busto, J.M. Leal, B. Garcia, New Insights into the Mechanism of the DNA/Doxorubicin Interaction, J. Phys. Chem. B, 118 (2014) 1288–1295.

[178] J. Neissa, C. Perez-Arnaiz, V. Porto, N. Busto, E. Borrajo, J.M. Leal, M.A. Lopez-Quintela, B. Garcia, F. Dominguez, Interaction of silver atomic quantum clusters with living organisms: bactericidal effect of Ag3 clusters mediated by disruption of topoisomerase-DNA complexes, Chem. Sci., 6 (2015) 6717–6724.

[179] Y. Pommier, E. Leo, H.-L. Zhang, C. Marchand, DNA Topoisomerases and Their Poisoning by Anticancer and Antibacterial Drugs, Chem. Biol., 17 (2010) 421–433.

[180] T. Oktay, S. Pornsak, D.C. R., Doxorubicin: an update on anticancer molecular action, toxicity and novel drug delivery systems, J. Pharm. Pharmacol., 65 (2012) 157–170.

[181] G. Franci, A. Falanga, S. Galdiero, L. Palomba, M. Rai, G. Morelli, M. Galdiero, Silver nanoparticles as potential antibacterial agents, Molecules, 20 (2015) 8856–8874.

[182] C. Marambio-Jones, E.M. V Hoek, A review of the antibacterial effects of silver nanomaterials and potential implications for human health and the environment, J. Nanopart. Res., 12 (2010) 1531–1551.

[183] F.Q. Schafer, G.R. Buettner, Redox environment of the cell as viewed through the redox state of the glutathione disulfide/glutathione couple, Free Radic. Biol. Med., 30 (2001) 1191–1212.

[184] L. Galluzzi, L. Senovilla, I. Vitale, J. Michels, I. Martins, O. Kepp, M. Castedo, G.

Kroemer, Molecular mechanisms of cisplatin resistance, Oncogene, 31 (2012) 1869–1883.

[185] K. Shekar, C.I. Mcdonald, D. V Mullany, J.F. Fraser, J.A. Roberts, S.C. Wallis, S. Ghassabian, C. Anstey, Y.L. Fung, Protein-bound drugs are prone to sequestration in the extracorporeal membrane oxygenation circuit: results from an ex vivo study, Crit. Care, 19 (2015) 164.

[186] M. V Babak, M. Pfaffeneder-Kmen, S.M. Meier-Menches, M.S. Legina, S. Theiner, C. Licona, C. Orvain, M. Hejl, M. Hanif, M.A. Jakupec, B.K. Keppler, C. Gaiddon, C.G. Hartinger, Rollover Cyclometalated Bipyridine Platinum Complexes as Potent Anticancer Agents: Impact of the Ancillary Ligands on the Mode of Action, Inorg. Chem., 57 (2018) 2851–2864.

[187] E. Gabano, S. Gama, F. Mendes, F. Fregonese, A. Paulo, M. Ravera, Application of microwave-assisted heating to the synthesis of Pt(II) complexes, Inorganica Chim. Acta, 437 (2015) 16–19.

[188] C. Mock, I. Puscasu, M.J. Rauterkus, G. Tallen, J.E.A. Wolff, B. Krebs, Novel Pt(II) anticancer agents and their Pd(II) analogues: syntheses, crystal structures, reactions with nucleobases and cytotoxicities, Inorganica Chim. Acta, 319 (2001) 109–116.

[189] J.S. Casas, A. Castiñeiras, E. García-Martínez, Y. Parajó, M.L. Pérez-Parallé, A. Sánchez-González, J. Sordo, Synthesis and cytotoxicity of 2-(2′-pyridyl)benzimidazole complexes of palladium(II) and platinum(II), Zeitschrift Fur Anorg. Und Allg. Chemie, 631 (2005) 2258–2264.

[190] M. Serratrice, L. Maiore, A. Zucca, S. Stoccoro, I. Landini, E. Mini, L. Massai, G. Ferraro, A. Merlino, L. Messori, M.A. Cinellu, Cytotoxic properties of a new organometallic platinum(II) complex and its gold(I) heterobimetallic derivatives, Dalton Trans., 45 (2016) 579–590.

[191] S. Labadie, P.S. Dragovich, K. Barrett, W.S. Blair, P. Bergeron, C. Chang, G. Deshmukh, C. Eigenbrot, N. Ghilardi, P. Gibbons, C.A. Hurley, A. Johnson, J.R. Kenny, P.B. Kohli, J.J. Kulagowski, M. Liimatta, P.J. Lupardus, R. Mendonca, J.M. Murray, R. Pulk, et al., Structure-based discovery of C-2 substituted imidazo-pyrrolopyridine JAK1 inhibitors with improved selectivity over JAK2, Bioorg. Med. Chem. Lett., 22 (2012) 7627–7633.

[192] G.A. Fernandez, M.S. Vela Gurovic, N.L. Olivera, A.B. Chopa, G.F. Silbestri, Antibacterial properties of water-soluble gold(I) N-heterocyclic carbene complexes, J. Inorg. Biochem., 135 (2014) 54–57.

[193] M. Marinelli, M. Pellei, C. Cimarelli, H.V.R. Dias, C. Marzano, F. Tisato, M. Porchia, V. Gandin, C. Santini, Novel multicharged silver(I)-NHC complexes derived from zwitterionic 1,3-symmetrically and 1,3-unsymmetrically substituted imidazoles and benzimidazoles: Synthesis and cytotoxic properties, J. Organomet. Chem., 806 (2016) 45–53.

[194] K.A. Smith, J.C. Conboy, Using micropatterned lipid bilayer arrays to measure the effect of membrane composition on merocyanine 540 binding, Biochim. Biophys. Acta, Biomembr., 1808 (2011) 1611–1617.

[195] R.A. Schlegel, B.M. Phelps, A. Waggoner, L. Terada, P. Williamson, Binding of merocyanine 540 to normal and leukemic erythroid cells, Cell, 20 (1980) 321–328.

[196] A. Ecker, A.M. Lehane, J. Clain, D.A. Fidock, PfCRT and its role in antimalarial drug resistance, Trends Parasitol., 28 (2012) 504–514.

[197] S. Das, R. Preet, S. Siddharth, A. Nayak, C.N. Kundu, N. Tripathi, P. V Bharatam, Quinacrine induces apoptosis in cancer cells by forming a functional bridge between TRAIL-DR5 complex and modulating the mitochondrial intrinsic cascade, Oncotarget, 8 (2017) 248–267.

[198] J. Zhu, Y. Zheng, H. Zhang, J. Zhu, H. Sun, J. Zhu, Y. Zheng, H. Zhang, J. Zhu, Low concentration of chloroquine enhanced efficacy of cisplatin in the treatment of human ovarian cancer dependent on autophagy, Am. J. Transl. Res., 9 (2017) 4046–4058.

[199] L.R. Kelland, Preclinical perspectives on platinum resistance, Drugs, 59 (2000) 1–8.

[200] B. Michalke, Platinum speciation used for elucidating activation or inhibition of Pt-containing anti-cancer drugs, J. Trace Elem. Med. Biol., 24 (2010) 69–77.

[201] A.S. Fridman, E.N. Galyuk, V.I. Vorob’ev, A.N. Skvortsov, D.Y. Lando, Melting of crosslinked DNA: VI Comparison of influence of interstrand crosslinks and other chemical modifications formed by antitumor compounds on DNA stability, J. Biomol. Struct. Dyn., 26 (2008) 175–185.

[202] M.P. Sullivan, H.U. Holtkamp, C.G. Hartinger, Antitumor Metallodrugs that Target Proteins, Met. Ions Life Sci., 18 (2018) 351–386.

[203] C. Schmidt, B. Karge, R. Misgeld, A. Prokop, R. Franke, M. Broenstrup, I. Ott, Gold(I) NHC complexes: antiproliferative activity, cellular uptake, inhibition of mammalian and bacterial thioredoxin reductases, and gram-positive directed antibacterial effects, Chem. - A Eur. J., 23 (2017) 1869–1880.

[204] J.F. Neault, H.A. Tajmir-Riahi, Interaction of cisplatin with human serum albumin Drug binding mode and protein secondary structure, Biochim. Biophys. Acta, Protein Struct. Mol. Enzymol., 1384 (1998) 153–159.

[205] V. Novohradsky, Z. Liu, M. Vojtiskova, P.J. Sadler, V. Brabec, J. Kasparkova, Mechanism of cellular accumulation of an iridium(iii) pentamethylcyclopentadienyl anticancer complex containing a C,N-chelating ligand, Metallomics, 6 (2014) 682–690.

[206] O.S. Markovic, I.N. Cvijetic, M. V Zlatovic, I.M. Opsenica, J.M. Konstantinovic, N. V Terzic Jovanovic, B.A. Solaja, T.Z. Verbic, Human serum albumin binding of certain antimalarials, Spectrochim. Acta, Part A Mol. Biomol. Spectrosc., 192 (2018) 128–139.

[207] R.D. Gray, J.B. Chaires, Kinetics and mechanism of K+- and Na+-induced folding of models of human telomeric DNA into G-quadruplex structures, Nucleic Acids Res., 36 (2008) 4191–4203.

[208] A.T. Phan, Human telomeric G-quadruplex: structures of DNA and RNA sequences, FEBS J., 277 (2010) 1107–1117.

[209] K.W. Lim, S. Amrane, S. Bouaziz, W. Xu, Y. Mu, D.J. Patel, K.N. Luu, A.T. Phan, Structure of the Human Telomere in K+ Solution: A Stable Basket-Type G-Quadruplex with Only Two G-Tetrad Layers, J. Am. Chem. Soc., 131 (2009) 4301–4309.

[210] S. Dhakal, Y. Cui, D. Koirala, C. Ghimire, S. Kushwaha, Z. Yu, P.M. Yangyuoru, H. Mao, Structural and mechanical properties of individual human telomeric G-quadruplexes in molecularly crowded solutions, Nucleic Acids Res., 41 (2013) 3915–3923.

[211] C. Perez-Arnaiz, N. Busto, J.M. Leal, B. Garcia, New microsecond intramolecular reactions of human telomeric DNA in solution, RSC Adv., 6 (2016) 39204–39208.

[212] C. Perez-Arnaiz, N. Busto, J. Santolaya, J.M. Leal, G. Barone, B. Garcia, Kinetic evidence for interaction of TMPyP4 with two different G-quadruplex conformations of human telomeric DNA, Biochim. Biophys. Acta, Gen. Subj., 1862 (2018) 522–531.

[213] C.B. Harley, A.B. Futcher, C.W. Greider, Telomeres shorten during ageing of human fibroblasts, Nature, 345 (1990) 458–460.

[214] N.W. Kim, M.A. Piatyszek, K.R. Prowse, C.B. Harley, M.D. West, P.L.C. Ho, G.M. Coviello, W.E. Wright, S.L. Weinrich, J.W. Shay, Specific association of human telomerase activity with immortal cells and cancer, Science, 266 (1994) 2011–2015.

[215] D.M. Feldser, C.W. Greider, Short telomeres limit tumor progression in vivo by inducing senescence, Cancer Cell, 11 (2007) 461–469.

[216] P. Stadlbauer, L. Trantirek, T.E. Cheatham III, J. Koca, J. Sponer, Triplex intermediates in folding of human telomeric quadruplexes probed by microsecond-scale molecular dynamics simulations, Biochimie, 105 (2014) 22–35.

[217] J. Amato, A. Pagano, S. Cosconati, G. Amendola, I. Fotticchia, N. Iaccarino, J. Marinello, A. De Magis, G. Capranico, E. Novellino, B. Pagano, A. Randazzo, Discovery of the first dual G-triplex/G-quadruplex stabilizing compound: a new opportunity in the targeting of G-rich DNA structures?, Biochim. Biophys. Acta, Gen. Subj., 1861 (2017) 1271–1280.

[218] M. Boncina, C. Podlipnik, I. Piantanida, J. Eilmes, M.-P. Teulade-Fichou, G. Vesnaver, J. Lah, Thermodynamic fingerprints of ligand binding to human telomeric G-quadruplexes, Nucleic Acids Res., 43 (2015) 10376–10386.

[219] J.E. Reed, A.A. Arnal, S. Neidle, R. Vilar, Stabilization of G-Quadruplex DNA and Inhibition of Telomerase Activity by Square-Planar Nickel(II) Complexes, J. Am. Chem. Soc., 128 (2006) 5992–5993.

[220] A. Arola-Arnal, J. Benet-Buchholz, S. Neidle, R. Vilar, Effects of metal coordination geometry on stabilization of human telomeric quadruplex DNA by square-planar and square-pyramidal metal complexes, Inorg. Chem., 47 (2008) 11910–11919.

[221] A. Shivalingam, M.A. Izquierdo, A. Le Marois, A. Vysniauskas, K. Suhling, M.K. Kuimova, R. Vilar, The interactions between a small molecule and G-quadruplexes are visualized by fluorescence lifetime imaging microscopy, Nat. Commun., 6 (2015) 8178.

[222] R.F. Pasternack, L. Francesconi, D. Raff, E. Spiro, Aggregation of nickel(II), copper(II), and zinc(II) derivatives of water-soluble porphyrins, Inorg. Chem., 12 (1973) 2606–2611.

[223] A. De Cian, L. Guittat, M. Kaiser, B. Sacca, S. Amrane, A. Bourdoncle, P. Alberti, M.-P. Teulade-Fichou, L. Lacroix, J.-L. Mergny, Fluorescence-based melting

assays for studying quadruplex ligands, Methods, 42 (2007) 183–195.

[224] J.B. Chaires, A thermodynamic signature for drug–DNA binding mode, Arch. Biochem. Biophys., 453 (2006) 26–31.

[225] I. Jelesarov, H.R. Bosshard, Isothermal titration calorimetry and differential scanning calorimetry as complementary tools to investigate the energetics of biomolecular recognition, J. Mol. Recognit., 12 (1999) 3–18.

[226] C. Giancola, B. Pagano, Energetics of ligand binding to G-quadruplexes, Top. Curr. Chem., 330 (2013) 211–242.

[227] P.C. Bruijnincx, P.J. Sadler, New trends for metal complexes with anticancer activity, Curr. Opin. Chem. Biol., 12 (2008) 197–206.

[228] N. Cutillas, G.S. Yellol, C. de Haro, C. Vicente, V. Rodriguez, J. Ruiz, Anticancer cyclometalated complexes of platinum group metals and gold, Coord. Chem. Rev., 257 (2013) 2784–2797.

[229] R.A. Cairns, I.S. Harris, T.W. Mak, Regulation of cancer cell metabolism, Nat. Rev. Cancer, 11 (2011) 85–95.

[230] R.J. De Berardinis, N.S. Chandel, Fundamentals of cancer metabolism, Sci. Adv., 2 (2016) 1–18.

[231] J.-J. Cao, C.-P. Tan, M.-H. Chen, N. Wu, D.-Y. Yao, X.-G. Liu, L.-N. Ji, Z.-W. Mao, Targeting cancer cell metabolism with mitochondria-immobilized phosphorescent cyclometalated iridium(III) complexes, Chem. Sci., 8 (2017) 631–640.

[232] L.K. McKenzie, I. V Sazanovich, E. Baggaley, M. Bonneau, V. Guerchais, J.A.G. Williams, J.A. Weinstein, H.E. Bryant, Metal Complexes for Two-Photon Photodynamic Therapy: A Cyclometallated Iridium Complex Induces Two-Photon Photosensitization of Cancer Cells under Near-IR Light, Chem. - A Eur. J., 23 (2017) 234–238.

[233] W. Lv, Z. Zhang, K.Y. Zhang, H. Yang, S. Liu, A. Xu, S. Guo, Q. Zhao, W. Huang, A Mitochondria-Targeted Photosensitizer Showing Improved Photodynamic Therapy Effects Under Hypoxia, Angew. Chemie, Int. Ed., 55 (2016) 9947–9951.

[234] M.-H. Chen, F.-X. Wang, J.-J. Cao, C.-P. Tan, L.-N. Ji, Z.-W. Mao, Light-Up Mitophagy in Live Cells with Dual-Functional Theranostic Phosphorescent Iridium(III) Complexes, ACS Appl. Mater. Interfaces, 9 (2017) 13304–13314.

[235] J. Liu, C. Jin, B. Yuan, X. Liu, Y. Chen, L. Ji, H. Chao, Selectively lighting up two-photon photodynamic activity in mitochondria with AIE-active iridium(III) complexes, Chem. Commun., 53 (2017) 2052–2055.

[236] C. Jin, J. Liu, Y. Chen, R. Guan, C. Ouyang, Y. Zhu, L. Ji, H. Chao, Cyclometalated Iridium(III) Complexes as AIE Phosphorescent Probes for Real-Time Monitoring of Mitophagy in Living Cells, Sci. Rep., 6 (2016) 22039.

[237] L. He, C.-P. Tan, R.-R. Ye, Y.-Z. Zhao, Y.-H. Liu, Q. Zhao, L.-N. Ji, Z.-W. Mao, Theranostic Iridium(III) Complexes as One- and Two-Photon Phosphorescent Trackers to Monitor Autophagic Lysosomes, Angew. Chemie, Int. Ed., 53 (2014) 12137–12141.

[238] L. He, Y. Li, C.-P. Tan, R.-R. Ye, M.-H. Chen, J.-J. Cao, L.-N. Ji, Z.-W. Mao, Cyclometalated iridium(III) complexes as lysosome-targeted photodynamic

anticancer and real-time tracking agents, Chem. Sci., 6 (2015) 5409–5418.

[239] F.-X. Wang, M.-H. Chen, Y.-N. Lin, H. Zhang, C.-P. Tan, L.-N. Ji, Z.-W. Mao, Dual Functions of Cyclometalated Iridium(III) Complexes: Anti-Metastasis and Lysosome-Damaged Photodynamic Therapy, ACS Appl. Mater. Interfaces, 9 (2017) 42471–42481.

[240] R. Cao, J. Jia, X. Ma, M. Zhou, H. Fei, Membrane Localized Iridium(III) Complex Induces Endoplasmic Reticulum Stress and Mitochondria-Mediated Apoptosis in Human Cancer Cells, J. Med. Chem., 56 (2013) 3636–3644.

[241] S. Mandal, D.K. Poria, R. Ghosh, P.S. Ray, P. Gupta, Development of a cyclometalated iridium complex with specific intramolecular hydrogen-bonding that acts as a fluorescent marker for the endoplasmic reticulum and causes photoinduced cell death, Dalton Trans., 43 (2014) 17463–17474.

[242] V. Novohradsky, A. Zamora, A. Gandioso, V. Brabec, J. Ruiz, V. Marchan, Somatostatin receptor-targeted organometallic iridium(III) complexes as novel theranostic agents, Chem. Commun., 53 (2017) 5523–5526.

[243] X. Tian, Y. Zhu, M. Zhang, L. Luo, J. Wu, H. Zhou, L. Guan, G. Battaglia, Y. Tian, Localization matters: a nuclear targeting two-photon absorption iridium complex in photodynamic therapy, Chem. Commun., 53 (2017) 3303–3306.

[244] C. Li, M. Yu, Y. Sun, Y. Wu, C. Huang, F. Li, A Nonemissive Iridium(III) Complex That Specifically Lights-Up the Nuclei of Living Cells, J. Am. Chem. Soc., 133 (2011) 11231–11239.

[245] C.-H. Leung, H.-J. Zhong, D.S.-H. Chan, D.-L. Ma, Bioactive iridium and rhodium complexes as therapeutic agents, Coord. Chem. Rev., 257 (2013) 1764–1776.

[246] Z. Huang, H. Xu, A.D. Meyers, A.I. Musani, L. Wang, R. Tagg, A.B. Barqawi, Y.K. Chen, Photodynamic therapy for treatment of solid tumors-potential and technical challenges, Technol. Cancer Res. Treat., 7 (2008) 309–320.

[247] W. Lin, Q. Zhao, H. Sun, K.Y. Zhang, H. Yang, Q. Yu, X. Zhou, S. Guo, S. Liu, W. Huang, An Electrochromic Phosphorescent Iridium(III) Complex for Information Recording, Encryption, and Decryption, Adv. Opt. Mater., 3 (2015) 368–375.

[248] A. Zamora, G. Vigueras, V. Rodriguez, M.D. Santana, J. Ruiz, Cyclometalated iridium(III) luminescent complexes in therapy and phototherapy, Coord. Chem. Rev., 360 (2018) 34–76.

[249] R.D. Costa, E. Orti, H.J. Bolink, F. Monti, G. Accorsi, N. Armaroli, Luminescent Ionic Transition-Metal Complexes for Light-Emitting Electrochemical Cells, Angew. Chemie, Int. Ed., 51 (2012) 8178–8211.

[250] J.S. Nam, M.-G. Kang, J. Kang, S.-Y. Park, S.J.C. Lee, H.-T. Kim, J.K. Seo, O.-H. Kwon, M.H. Lim, H.-W. Rhee, T.-H. Kwon, Endoplasmic Reticulum-Localized Iridium(III) Complexes as Efficient Photodynamic Therapy Agents via Protein Modifications, J. Am. Chem. Soc., 138 (2016) 10968–10977.

[251] J. Pracharova, G. Vigueras, V. Novohradsky, N. Cutillas, C. Janiak, H. Kostrhunova, J. Kasparkova, J. Ruiz, V. Brabec, Exploring the Effect of Polypyridyl Ligands on the Anticancer Activity of Phosphorescent Iridium(III) Complexes: From Proteosynthesis Inhibitors to Photodynamic Therapy Agents, Chem. - A Eur. J., 24 (2018) 1–14.

[252] L. He, J. Qiao, L. Duan, G. Dong, D. Zhang, L. Wang, Y. Qiu, Toward Highly Efficient Solid-State White Light-Emitting Electrochemical Cells: Blue-Green to Red Emitting Cationic Iridium Complexes with Imidazole-Type Ancillary Ligands, Adv. Funct. Mater., 19 (2009) 2950–2960.

[253] K.K.-W. Lo, A.W.-T. Choi, W.H.-T. Law, Applications of luminescent inorganic and organometallic transition metal complexes as biomolecular and cellular probes, Dalton Trans., 41 (2012) 6021–6047.

[254] H.N. Po, N.M. Senozan, The Henderson-Hasselbalch equation: its history and limitations, J. Chem. Educ., 78 (2001) 1499–1503.

[255] E.R. Jamieson, S.J. Lippard, Structure, recognition, and processing of cisplatin-DNA adducts, Chem. Rev., 99 (1999) 2467–2498.

[256] S.P. Wisnovsky, J.J. Wilson, R.J. Radford, M.P. Pereira, M.R. Chan, R.R. Laposa, S.J. Lippard, S.O. Kelley, Targeting Mitochondrial DNA with a Platinum-Based Anticancer Agent, Chem. Biol., 20 (2013) 1323–1328.

[257] S.A. Susin, H.K. Lorenzo, N. Zamzami, I. Marzo, B.E. Snow, G.M. Brothers, J. Mangion, E. Jacotot, P. Costantini, M. Loeffler, N. Larochette, D.R. Goodlett, R. Aebersold, D.P. Siderovski, J.M. Penninger, G. Kroemer, Molecular characterization of mitochondrial apoptosis-inducing factor, Nature, 397 (1999) 441–446.

[258] D. Trachootham, J. Alexandre, P. Huang, Targeting cancer cells by ROS-mediated mechanisms: a radical therapeutic approach?, Nat. Rev. Drug Discov., 8 (2009) 579–591.

[259] A. Wojtala, M. Bonora, D. Malinska, P. Pinton, J. Duszynski, M.R. Wieckowski, Methods to monitor ROS production by fluorescence microscopy and fluorometry, Methods Enzymol., 542 (2014) 243–262.

[260] N. Zamzami, C. Maisse, D. Metivier, G. Kroemer, Measurement of membrane permeability and the permeability transition of mitochondria, Methods Cell Biol., 80 (2007) 327–340.

[261] P.B. Dervan, Design of sequence-specific DNA-binding molecules, Science, 232 (1986) 464–471.

[262] J.S. Kang, J.L. Meier, P.B. Dervan, Design of sequence-specific DNA binding molecules for DNA methyltransferase inhibition, J. Am. Chem. Soc., 136 (2014) 3687–3694.

[263] Y. Kawamoto, A. Sasaki, A. Chandran, K. Hashiya, S. Ide, T. Bando, K. Maeshima, H. Sugiyama, Targeting 24 bp within Telomere Repeat Sequences with Tandem Tetramer Pyrrole-Imidazole Polyamide Probes, J. Am. Chem. Soc., 138 (2016) 14100–14107.